FACULTY OF SCIENCE

Development of Novel Electrode Materials for Li-ion Batteries and Na-ion Batteries

This thesis is presented in fulfilment of the requirements for the degree of

DOCTOR OF PHILOSOPHY

of the

University of Technology, Sydney

By Dawei Su B. Eng., M. Eng.

2013

CERTIFICATE OF ORIGINAL AUTHORSHIP

I certify that the work in this thesis has not previously been submitted for a degree nor has it been submitted as part of requirements for a degree except as fully acknowledged within the text.

I also certify that the thesis has been written by me. Any help that I have received in my research work and the preparation of the thesis itself has been acknowledged. In addition, I certify that all information sources and literature used are indicated in the thesis.

Dawei Su

ACKNOWLEDGEMENTS

I wish to express my deep appreciation for the encouragement, understanding, invaluable advice and constant support of my supervsior, Prof. Guoxiu Wang, director of Centre for Clean Energy Technology, during my study in University of Technology, Sydney (UTS).

I also wish to thank A/Prof. Mike Ford, my co-supervisor, at the School of Physics and Advanced Materials, A/Prof. Alison Ung, Dr. Ronald Shimmon and Dr. Linda Xiao, Berry Liu from School of Chemistry and Forensic Science in UTS for their friendly support and kind discussions during my study. I would like to give my thanks to Katie McBean and Mark Berkahn from the Microstructural Analysis Unit in UTS for their help on material characterization.

I am very grateful to Dr. David Wexler, Dr. Zhixin Chen from University of Wollongong, and Prof. Paul Munroe from University of New South Wales, for assistance with the TEM work, and A/Prof. Josip Horvat, in University of Wollongong for spenting time with me on the magnetic measurements.

Special thanks go to Dr. Yueping (Jane) Yao for her support in many ways.

I wish to thank our group members: Dr. Hao Liu, Dr. Xiaodan Huang, Dr. Bing Sun, Mr. Bei Wang, Ms. Ying Wang, Mr. Kefei Li, Mr. Jinqiang Zhang, Mr. Anjon Kumar Mondal, Mr. Ali Reza Ranjbartoreh and Mr. Shuangqiang Chen.

I would like to thank the financial support provided by the Australian Research Council (ARC) through the ARC linkage project.

Finally, I would like to thank my wife, Wenyuan Wu, my son, Siwen Su and my whole family for their love, support, and encouragement during my PhD study. Their love is the mental strength that supported me to fulfil my study abroad.

LIST OF PUBLICATION

[1]. **D. W. Su**, M. Ford and G. X. Wang. Mesoporous NiO crystals with dominantly exposed {110} reactive facets for ultrafast lithium storage. *Scientific Reports* 2:924 | DOI:10.1038/srep00924, (2012) (Nature Publishing Group: Impact factor is not available until 2013.)

[2]. **D. W. Su**, H. J. Ahn and G. X. Wang. SnO_2@graphene nanocomposites as anode materials for Na-ion batteries with superior electrochemical performance. *Chemical Communications* DOI: 10.1039/c3cc40448j. (Impact factor: 6.169)

[3]. **D. W. Su**, H. J. Ahn and G. X. Wang. Hydrothermal synthesis of α-MnO_2 and β-MnO_2 nanorods as high capacity cathode materials for Na-ion batteries. *Journal of Materials Chemistry A* DOI: 10.1039/c3ta00031a (Impact factor: 5.968)

[4]. **D. W. Su**, C. Y. Wang, H. J. Ahn and G. X. Wang. Single Crystalline $Na_{0.7}MnO_2$ Nanoplates as Cathode Materials for Sodium Ion Batteries with Enhanced Performance. *Chemistry-A European Journal* Accepted (2013). (Impact factor: 5.925)

[5]. **D. W. Su**, J. Horvat, P. Munroe, H. Ahn, A. R. Ranjbartoreh and G. X. Wang. Polyhedral Magnetite Nanocrystals with Multiple Facets: Facile Synthesis, Structural Modelling, Magnetic Properties and Application for High Capacity Lithium Storage. *Chemistry-A European Journal* 18, 488-497, (2012). (Impact factor: 5.925)

[6]. **D. W. Su**, H. S. Kim, W. S. Kim and G. X. Wang. Mesoporous Nickel Oxide Nanowires: Hydrothermal Synthesis, Characterisation and Applications for Li-ion batteries and Supercapacitors with Superior Performance. *Chemistry-A European Journal* 18, 8224-8229, (2012). (Impact factor: 5.925)

[7]. **D. W. Su**, H. S. Kim, W. S. Kim and G. X. Wang, A study of Pt_xCo_y alloy nanoparticles as cathode catalysts for lithium-air batteries with improved catalytic activity. *Journal of Power Sources,* DOI:10.1016/j.jpowsour.2012.11.024 (2012) (Impact factor: 4.951)

[8]. **D. W. Su**, H. J. Ahn and G. X. Wang, One-dimensional magnetite Fe_3O_4 nanowires as electrode material for Li-ion batteries with improved electrochemical performance. *Journal of Power Sources,* DOI:10.1016/j.jpowsour.2012.11.058 (2012) (Impact factor: 4.951)

[9]. **D. W. Su**, H. J. Ahn and G. X. Wang. Ab initio calculations on Li-ion migration in Li_2FeSiO_4 cathode material with a P2(1) symmetry structure. *Applied Physics Letters,* 99, 14909(1)-14909(3) (2011). (Impact factor: 3.844)

[10]. **D. W. Su**, H. S. Kim, W. S. Kim and G. X. Wang. Synthesis of tuneable porous hematit (alpha-Fe_2O_3) for gas sensing and lithium storage in Li-ion batteries. *Microporous and Mesoporous Materials,* 149, 36-45, (2012). (Impact factor: 3.285)

[11]. **D. W. Su**, H. J. Ahn and G. X. Wang. Octahedral Tin Dioxide Nanocrystals as High Capacity Anode Materials for Na-ion Batteries. *Physical Chemistry Chemical Physics* Accepted (2013). (Impact factor: 3.573)

[12]. **D. W. Su**, H. T. Fu, X. C. Jiang and G. X. Wang. ZnO nanocrystals with a high percentage of exposed $\{4\bar{2}\bar{2}3\}$ reactive facets for enhanced gas sensing performance. *Sensors & Actuators, B Chemical* Accepted (2013). (Impact factor: 3.898)

[13]. **D. W. Su**, H. Liu, H. J. Ahn and G. X. Wang. Synthesis of Highly Ordered Mesoporous Co_3O_4 for Gas Sensing. *Journal of Nanoscience and Nanotechnology,* 13, 3354-3359, (2013) (Impact factor: 1.563)

[14]. **D. W. Su**, H. J. Ahn and G. X. Wang. β-MnO_2 Nanorods with Exposed Tunnel Structures as High Performance Cathode Materials for Sodium-ion Batteries. *NPG Asia Materials, Accepted,* (2013) (Impact factor: 9.042)

[15]. H. Liu, **D. W. Su**, R. F. Zhou, B. Sun, G. X. Wang and S. Z. Qiao. Highly Ordered Mesoporous MoS_2 with Expanded Spacing of the (002) Crystal Plane for Ultrafast Lithium Ion Storage. *Advanced Energy Materials* 2, 970-975, (2012).

[16]. H. Liu, **D. W. Su**, G. X. Wang and S. Z. Qiao. An ordered mesoporous WS_2 anode material with superior electrochemical performance for Li-ion batteries. *Journal of Materials Chemistry* 22, 17437-17440, (2012). (Impact factor: 5.968)

[17]. B. Wang, J. Park, **D. W. Su**, C. Y. Wang, H. J. Ahn and G. X. Wang. Solvothermal synthesis of CoS_2-graphene nanocomposite material for high-performance supercapacitors. *Journal of Materials Chemistry* 22, 15750-15756, (2012). (Impact factor: 5.968)

[18]. B. Sun, B. Wang, **D. W. Su**, L. D. Xiao, H. J. Ahn and G. X. Wang. Graphene nanosheets as cathode catalysts for lithium-air batteries with an enhanced electrochemical performance. *Carbon* 50, 727-733, (2012). (Impact factor: 5.378)

[19]. K. F. Li, B. Wang, **D. W. Su**, J. Park, H. J. Ahn and G. X. Wang. Enhance electrochemical performance of lithium sulfur battery through a solution-based processing technique. *Journal of Power Sources* 202, 389-393, (2012). (Impact factor: 4.951)

[20]. Y. Wang, **D. W. Su**, C. Y. Wang and G. X. Wang. SnO_2@ MWCNT nanocomposite as a high capacity anode material for Na-ion batteries." *Electrochemistry Communications* 29 (2013): 8-11. (Impact factor: 4.859)

[21]. B. Wang, K. F. Li, **D. W. Su**, H. J. Ahn and G. X. Wang. Superior Electrochemical Performance of Sulfur/Graphene Nanocomposite Material for

High-Capacity Lithium-Sulfur Batteries. *Chemistry-an Asian Journal* 7, 1637-1643, (2012). (Impact factor : 4.5)

[22]. Y. Wang, **D. W. Su**, A. Ung, J. H. Ahn and G. X. Wang. Hollow $CoFe_2O_4$ nanospheres as a high capacity anode material for Li-ion batteries. *Nanotechnology* 23, (2012). (Impact factor: 3.979)

[23]. B. Wang, **D. W. Su**, J. Park, H. J. Ahn and G.X. Wang, Graphene-supported SnO_2 nanoparticles prepared by a solvothermal approach for an enhanced electrochemical performance in Li-ion batteries, *Nanoscale Reseach Letters* 7:215 (2012). (Impact factor: 2.726)

[24]. H. T. Fu, X. C. Jiang, X. H. Yang, A. B. Yu, **D. W. Su** and G. X. Wang. Glycothermal synthesis of assembled vanadium oxide nanostructures for gas sensing. *Journal of Nanoparticle Research* 14, (2012). (Impact factor: 3.287)

[25]. Y. Wang, N. Sharma, **D. W. Su**, D. Bishop, H. J. Ahn and G. X. Wang. High capacity spherical $Li[Li_{0.24}Mn_{0.55}Co_{0.14}Ni_{0.07}]O_2$ cathode material for Li-ion batteries. Solid State Ionics, Accepted on December 5, (2012) (Impact factor: 2.646)

[26]. A. R. Ranjbartoreh, **D. W. Su** and G. X. Wang,Consideration of Critical Axial Properties of Pristine and Defected Carbon Nanotubes Under Compression. *Journal of* Nanoscience *and Nanotechnology* 12, 5025-5029, (2012). (Impact factor: 1.563)

[27]. A. K. Mondal, B. Wang, **D. W. Su**, Y. Wang, X. G. Zhang and G. X. Wang. Preparation and Enhanced Electrochemical Performance of MnO_2 Nanosheets for Supercapacitors. *Journal of the Chinese Chemical Society* 59, 1275–1279, (2012) (Impact factor: 0.678)

[28]. Y. Wang, **D. W. Su** and G. X. Wang. The effect of Carbon Coating on the

Electrochemical Performance of Nanosized Li_2FeSiO_4 Cathode Materials. the 2nd International Advances in Applied Physics and Materials Science (APMAS 2012), 26th – 29th Apr. 2012, Antalya, Turkey.

[29]. A. K. Mondal, **D. W. Su**, Y. Wang, S. Q. Chen and G. X. Wang. Hydrothermal synthesis of nickel oxide nanosheets for lithium-ion batteries and supercapacitors with excellent performance. *Chemistry - An Asian Journal* DOI: 10.1002/asia.201300708, (2013) (Impact factor: 4.5)

[30]. A. K. Mondala, **D. W. Su**, Y. Wang, S. Q. Chen, Q. Liu and G. X. Wang. Microwave hydrothermal synthesis of urchin-like NiO nanospheres as electrode materials for lithium-ion batteries and supercapacitors with enhanced electrochemical performances. *Journal of Alloy and Compounds*, DOI: 10.1016/j.jallcom.2013.08.085 (2013) (Impact factor: 2.39)

RECEIVED AWARDS

[1]. 2012 Chinese Government Award for Outstanding Self-financed Students Abroad, April 2013. ($ 6000 USD)

[2]. ARC Postgraduate Award (Industry) (APAI) April 2010

[3]. University of Wollongong International Postgraduate Tuition Fee Waiver Award (UOW IPTA) April 2010

[4]. University of Technology, Sydney International Research Scholarship (UTS IRS) June 2010

TABLE OF CONTENTS

LIST OF FIGURES

LIST OF TABLES

ABSTRACT

Li-ion batteries have dominated the global market for electronic devices, and are considered to be the most promising power system for electric vehicles (EVs), and hybrid electric vehicles (HEVs). However current Li-ion battery systems are still far from reaching the demands of the high energy density on EVs and HEVs due to limitations on the capacity of the electrodes. Moreover, they cannot match the high charge/discharge current requirements of the next generation of batteries. This doctoral work aims to address these problems by designing nanotechnology and nanomaterials with high power performance. Herein, a series of nanostructured materials with designed morphology: polyhedral nanoparticals, nanowires, 2-dimention nanoplate and mesoporous structure have been developed. By using theoretical calculations, X-ray diffraction, and *Ex-situ* SEM, TEM observation techniques, the relationship between the electrode crystal structure and electrochemical performance was established.

In addition, to overcome the controversial debates regarding the size of reserves and higher cost of obtaining Li, the counterpart to Li-ion batteries, Na-ion batteries, have been researched in this work due to the low cost, abundant supply and widespread terrestrial reserves of sodium mineral salts. However, the analogue intercalation compounds for Li-ion batteries are not appliable for Na-ion batteries due to the higher ionization potential and larger ionic diameter of the Na ((1.02 Å *vs*. Li (0.76 Å)). Consequently, suitable electrode materials for Na-ion batteries were also developed and optimised in this study. Appropriate active materials having sufficiently large interstitial space within their crystallographic structure to host Na ions and achieve a satisfactory electrochemical performance were created.

Following are the corresponding brief introductions to each research task:

The crystal structure and electronic structure of Li_2FeSiO_4 and its delithiated products, $LiFeSiO_4$ and $FeSiO_4$, were systematically investigated through the ab initio calculation based on a monoclinic supercell with the $P2_1$ symmetry. The expansion of the unit cell volume during the lithium extraction process, and the two-step voltage profiles of Li_2FeSiO_4 corresponding to the $Fe^{+2/+3}$ and $Fe^{+3/+4}$ redox couples, respectively, have been studied. Furthermore, the diffusion mechanism of Li ions in Li_2FeSiO_4 and its delithiated product $LiFeSiO_4$ was established base on the energy barriers calculation: the lithium will diffuse along the [101] direction and Li ion layer in the ac plane.

Tuneable porous α-Fe_2O_3 materials were prepared using a novel selective etching method. It was found that the pore size and pore volume can be controlled by adjusting the etching time during the synthesis process. When the porous hematite was applied for lithium storage in lithium ion cells, it demonstrated a reversible lithium storage capacity of 1269 mA h g^{-1}.

Atomistic simulation and calculations on surface attachment energy predicted the polyhedral structure of magnetite nanocrystals with multiple facets. Through a low temperature hydrothermal method, polyhedral magnetite nanocrystals with multiple facets were successfully synthesised and identified by the X-ray diffraction (XRD), field emission scanning electron microscopy (FESEM), and high resolution transmission electron microscopy (HRTEM). When applied as an anode material in lithium ion cells, magnetite nanocrystals demonstrated outstanding electrochemical performance with a high lithium storage capacity, satisfactory cyclability, and excellent high rate capacity.

One-dimensional single crystal magnetite nanowires were synthesized by the low temperature hydrothermal method. XRD and transmission electron microscopy (TEM) confirmed the cubic structure of Fe_3O_4 nanowires with a space group of $Fd\bar{3}m$. Electrochemical measurement showed as-prepared Fe_3O_4 nanowires exhibited an excellent reversible lithium storage capacity and a satisfactory cycling performance.

Mesoporous nickel oxide nanowires were synthesized by a hydrothermal reaction with subsequent annealing at 400 ºC. When applied as the anode material in Li-ion batteries, nickel oxide nanowires demonstrated an outstanding electrochemical performance with a high lithium storage capacity, adequate cyclability, and outstanding rate capacity. In addition, it also exhibited a high specific capacitance of 348 F g^{-1} as electrodes in supercapacitors.

Mesoporous NiO crystals with dominantly exposed {110} reactive facets was prepared by thermal conversion of hexagonal $Ni(OH)_2$ nanoplatelets. When applied as anode materials in Li-ion batteries, mesoporous NiO crystals exhibited a high reversible lithium storage capacity of 700 mA h g^{-1} at 1 C rate in 100 cycles and excellent cyclability. In particular, the dominantly exposed {110} reactive facets and mesoporous nanostructure of NiO crystals lead to ultrafast lithium storage, which mimics the high power delivery of supercapacitors.

Two types of MnO_2 polymorphs, α-MnO_2, β-MnO_2 nanorods, have been synthesized as cathode materials for Na-ion batteries. Although both can achieve high initial sodium ion storage capacities (278 mA h g^{-1} and 298 mA h g^{-1}, respectively), β-MnO_2 nanorods exhibited a better rate capability and cyclability than that of α-MnO_2 nanorods attributable to its more compact tunnel structure and the one-dimensional architecture of

nanorods which could facilitate sodium ion diffusion in the charge and discharge process.

Through an *In-situ* synthesis approach, SnO_2@Graphene nanocomposite was synthesized. FESEM and TEM revealed the homogeneous distribution of octahedral SnO_2 nanoparticles (60 nm in size) on a graphene matrix. When used as an anode for Na-ion batteries the SnO_2@Graphene nanocomposite exhibited a high reversible sodium storage capacity of above 700 mA h g^{-1} and an excellent cyclability. After 100 cycles, the capacity still maintained at 628 mA h g^{-1} at 20 mA g^{-1}due to the 3D architecture of the SnO_2@Graphene nanocomposite.

INTRODUCTION

Background

It is now universally recognised that the world is facing energy challenges. Two main frontiers are being considered to address this major issue: shifting electricity production from burning of fossil fuels and biomass to sustainable energy sources, and moving ground transportation towards electrical propulsion.[1] To answer the former concern, solar radiation, wind, waves, and geothermal energy have been developed. However these sources fluctuate during the time, day, and location. Hence, all require the availability of suitable energy storage technologies. Hereinto, the most convenient form of energy storage is portable chemical energy, which is the premise for our instrest in battery research. For the latter concern, of transportation, the solution lies in the adoption of electric vehicles (EVs), hybrid electrical vehicles (HEVs), or car powered by other portable devices which can provide both high power and high energy density instead of internal combustion engines (ICEs). To obtain the breakthrough on these substitute devices, batteries, especially the lithium ion batteries (Li-ion batteries are the most promising power source for the EVs and HEVs), must be developed. Therefore, battery technology lies at the heart of the solution to our energy crisis. This doctoral study is based on electrode materials, the core technology of Li-ion batteries.

Currently, the commercialized Li-ion batteries are composed of the lithium cobalt oxide or lithium iron phosphate cathode and graphite anode, which suffer from a low energy density problem due to the low capacity of the electrode materials. They also cannot meet the requirements of large-scale and high-power applications due to the

sizeable cost, safety and environmental concerns of cobalt. Lithium manganese oxides (either spinel or layered structure) have been explored as alternative cathode materials for large-size Li-ion batteries, but suffer from relatively low specific capacity and poor cyclability.[2-4] Transition metal oxides have been proposed as high capacity anode materials based on a "conversion" reaction, which is different from the classical insertion/de-insertion mechanism.[5] The theoretical capacity of the transition metal anode is almost 3-4 times higher than the graphite anode. However, the rate performance and cyclability of these potential substitute anode materials are poor, owing to slow kinetics of the conversion reaction and large volume change in the electrode (the volume change due to the expansion in the discharge process and contraction in the charge process can be up to 100 %). To circumvent these disadvantages, many approaches have been investigated, including the use of carbon materials as a conductive matrix, synthesis of nanostructured materials (nanocone,[6] nanotubes,[7] nanofilm,[8] and nanowires[9] *etc.*), and preparation of porous architecture.[9-13] So far, the achievement is still unsatisfactory and the development of an efficient electrode is still a huge challenge for Li-ion batteries.

Moreover, recently, it was realized that Li-ion batteries might also meet another barrier, relating to the controversial debates regarding the size of reserves and high costs of obtaining Li.[14] In light of the projected orders-of magnitude increase in lithium usage in batteries for low emission hybrid and electric vehicles (EV),[15] concerns have surfaced regarding the resource availablity of lithium and hence future cost. While modest expansion of Li production can support 1 MM 40 kW h vehicle batteries, to meet a long-term target of 100 MM 40 kW h Li-based EV batteries per year, a dramatic expansion of annual production will be necessary

(more than one order of magnitude).[16] The issue is not the insufficiency lithium on a global scale, but what fraction can be used and still be economically effective.[17] Consequently, Na-based compounds have made a comeback due to the low cost,[18,19] abundant supply (4th most abundant element in the earth crust) and widespread terrestrial reserves of sodium mineral salts. In addition, sodium ion batteries (Na-ion batteries) have similar features to Li-ion batteries: non-aqueous electrolytes, alkali insertion electrodes,[15] stable diffusion barrier of Na-ion.[20] However, the higher ionization potential[3] and larger ionic diameter of the Na ((1.02 Å) *vs.* Li (0.76 Å))[21] limit the structural variability and choice of Na insertion materials in crystalline materials. Therefore, finding and optimizing suitable electrode materials are crucial for the development of Na-ion batteries. These remains a lack of appropriate active materials with sufficiently large interstitial space within their crystallographic structure to host Na ions and present the satisfied electrochemical performance.

Innovation of this doctoral study

Creating novel nanomaterials and nanotechnology is the best way to achieve a breakthrough in the intercalation batteries (Li-ion batteries and Na-ion batteries). Many strategies have been used to design the special morphology in electrode materials, which can offer a high reversible capacity and unprecedented cyclability. It is worth noting that the promising performance of these electrodes in Li-ion cells have warranted the evaluation as commercially viable. Although the move to nanometer-sized materials can improve performance to a certain extent,[22-24] much less attention is paid to crystal structure controlled mechanism compared to the morphogenesis of active materials. Essentially, the exposed heterogeneous crystal planes of inorganic single crystals play a critical role in determining fascinating surface dependent properties, which not only

impacts the final shape of the particles themselves but also generates obviously different effects on their promising applications in a variety of technologically important areas. Therefore, understanding the nanoscale topography of surface sites, such as terraces, steps, kinks, adatoms and vacancies, and their effects on physicochemical properties is the key to designing nanoscale functional materials by nanotechnology. Therefore, the structure of the materials, especially the surface structure, is a crucial factor in determining the rate of alkaline metal cation (Li^+ or Na^+) insertion/extraction. This is because nanomaterials are generally bound by close-packing facets, which intrinsically present different ability in furnishing suitable channels or the active energy for Li^+ or Na^+ transportation. Following this strategy, recent reports have evidenced that the surface structure for Li^+ transportation is critical to the rate capability.[25-30] It was also reported that in layered cathode materials with α-$NaFeO_2$ structure, such as $Li[Li_{1/3-2x/3}Ni_xMn_{2/3-x/3}]O_2$,[31] Li^+ can only intercalate into the bulk of a crystal along the direction parallel to the Li^+ layers.

Consequently, it is necessary to investigate the mechanism and understand the affecting of exposed heterogeneous crystal planes of nanoscale single crystals on electrochemical properties. These points are major research contents in this doctoral work. Hereinto, theoretical calculation, X-ray diffraction, and *Ex-situ* SEM, TEM observation techniques have been combined to establish the relationship between the electrode crystal structure and electrochemical performance. Following this, we aimed to optimize the electrochemical properties of these electrode materials, including:

1: Improved cycling stability, the designed nanoparticles will more easily accommodate the mechanical strains and buffer the volume changes during cycling.

2: Enhanced of power capability, this benefits from the shorten diffusion length of ions and enhanced transfer of electrons.

3. Increased the rate performance through designing electrode materials with exposed high energy facets, profiting kinetics of the conversion reaction.

Outline of this work

An outline of the content is briefly presented as follows:

1. A literature review of Li-ion batteries and Na-ion batteries is presented in Chapter 1. In detail, the basic concepts, principles, conventional and recent developments in the cathode materials, electrolyte, and anodes materials of Li-ion batteries are summarized. In addition, the review on the Na-ion batteries' cathode and anode materials are also introduced in this Chapter.

2. The experimental parts, including introduction on synthesis, characterisations, electrochemical testing methods, relevant equipment and facilities, and the theoretical calculation methods used in this doctoral study, are presented in Chapter 2. Briefly, hydrothermal and solid state synthesis methods are the major preparation strategy in this study. X-ray diffraction (XRD), scanning electron microscopy (SEM), transmission electron microscopy (TEM), N_2 sorption and thermogravimetric analysis (TGA) were used to identify the phase, crystal structure and morphology of as-prepared electrode materials. Other physical properties, like the optical and magnetic features were researched using Fourier Transform Infrared (FT-IR) Spectroscopy, Ultraviolet-Visible Spectroscopy (UV), and magnetometer, respectively. Ab initio calculations based on the density function theory (DFT) was used to assist the analysis of the experimental work.

The electrochemical performance was evaluated by galvanostatic charge-discharge, cyclic voltammetry (CV) and electrochemical impedance spectra.

3. Chapter 3 describes the study of the new potential generation cathode material, Li_2FeSiO_4, for Li-ion batteries according to the theoretical calculations based on the Ab initio method. The expansion of the unit cell volume during the lithium extraction process, the electron transfer process, and the diffusion mechanism of Li ions in Li_2FeSiO_4 and its delithiated product $LiFeSiO_4$ are all discussed based on the $P2_1$ symmetry unit.

4. From Chapter 4 to Chapter 8, tuneable porous hematite (α-Fe_2O_3), polyhedral magnetite (Fe_3O_4) nanocrystals with multiple facets, one-dimensional single crystal magnetite (Fe_3O_4) nanowires, mesoporous nickel oxide (NiO) nanowires, and NiO mesocrystals exposed with high energy facet {110} worked as the well-defined anode candidates for the Li-ion batteries are presented, respectively. In these Chapters, the facile synthesis route, phase, crystal structure, morphology, theoretical calculation, physical and electrochemical properites of the as-prepared electrode materials are all disscussed deeply.

5. Chapter 9 introduces the preparation of two types of MnO_2 polymorphs: α-MnO_2, β-MnO_2 nanorods by a simple hydrothermal method, characterization, and their electrochemical performance as the cathode materials for the Na-ion batteries. The electrochemical properties of α-MnO_2 and β-MnO_2 nanorods are compared in detail in this Chapter.

6. To achieve the requirements for high power Na-ion batteries, an *In-situ* hydrothermal synthesis approach to prepare SnO_2@graphene nanocomposites is

described in Chapter 10. As an anode material, the as-prepared nanocomposite exhibited a high reversible sodium storage capacity and excellent cyclability for Na-ion battery.

7. The conclusions of this dissertation are summarized in Chapter 11. Some challenges and suggestions for further research are also presented in this Chapter.

CHAPTER 1 LITERATURE REVIEW

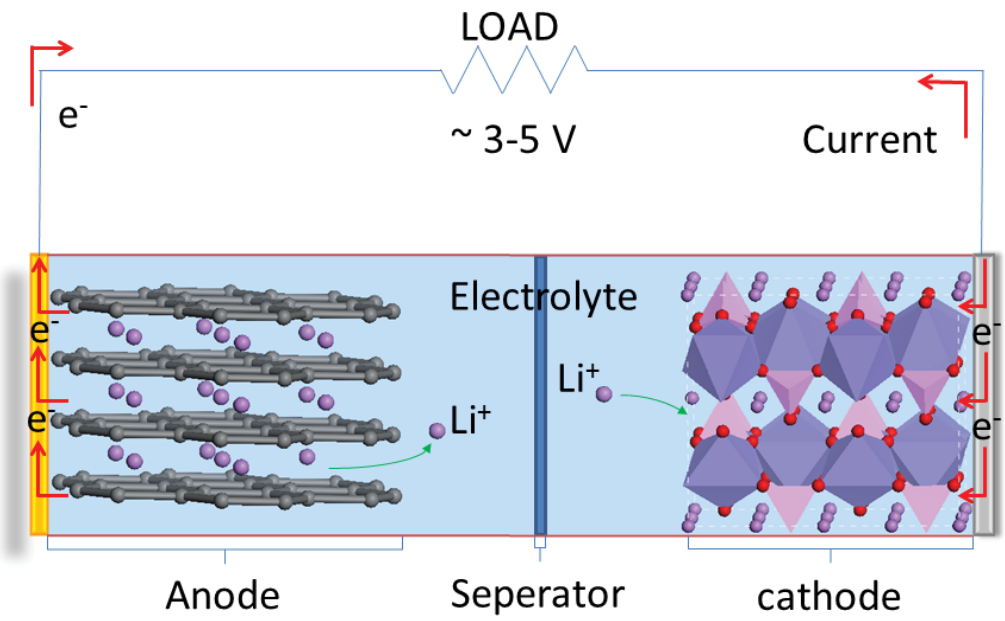

Figure 1-1 A schematic illustration of a Li-ion battery during discharge.

The unique properties of lithium, such as its low weight and large negative electrode potential, give the Li-ion battery its high energy density, which is superior to all other types of battery. Therefore, Li-ion batteries are the most advanced power source for portable electronic devices. They are also currently being considered as the state-of-the-art candidate to power electric vehicles (EVs) and hybrid electric vehicles (HEVs).[32] The Li-ion battery can be divided into three major components: the cathode, the anode (in some papers they are called as positive and negative electrode, respectively), and the electrolyte. In today's commercial Li-ion batteries, the cathode typically contains the active material $LiNi_xCo_{1-x}O_2$ or $LiFePO_4$, while the anode is usually made from graphite or carbon-based materials.

On discharge, electrons leave the anode via an external circuit where they do useful work before entering the cathode. To retain charge neutrality in the electrodes, cations

(Li^+) are released from the anode to the electrolyte. The working cation of the electrolyte carries positive charge to the cathode to provide charge neutrality in the cathode. It is drawn schematically in Figure 1-1. The process is reversed on charge in a rechargeable (secondary) battery.

The electrolyte is very often an aprotic, organic solvent with a dissociated lithium salt. It can also be a gel or a solid polymer. However, liquid electrolytes are still the most employed because of their superior conductivity. Much of the research on Li-ion batteries is devoted to the electrode materials. Ideally, these should combine high Li-ion conduction with high electronic conductivity in order to facilitate fast discharge. They should also have a favourable structure in which a large number of lithium ions can be inserted and extracted reversibly to yield the high capacity. Furthermore, the electrode materials should tolerate lower and elevated temperatures without significant loss of performance and without unwanted side effects. This is particularly important for the stability of the battery. Although the benefits to the Li-ion battery, the cost, safety, stored energy density, charge/discharge rates and service life are issues that continue to hinder the development of the lithium battery, especially for the potential mass market of electric vehicles. Three components of the Li-ion batteries have been discussed in detail as follows.

1.1 Electrolytes for Li-ion batteries

In general, the electrolyte is specifically designed for the particular battery application. Figure 1-2 is a schematic of the relative electron energies in the electrodes and the electrolyte of a thermodynamically stable battery cell. The suitable "window" of the electrolyte is the crucial selection criterion for the battery system, and can be evaluated by the energy separation E_g, which is the deviation between the lowest unoccupied

molecular orbital (LUMO) and the highest occupied molecular orbital (HOMO) of the electrolyte.[33] The two electronic conductors (anode and cathode) having corresponding electrochemical potentials μ_A and μ_C (their Fermi energies ε_F) should be within the

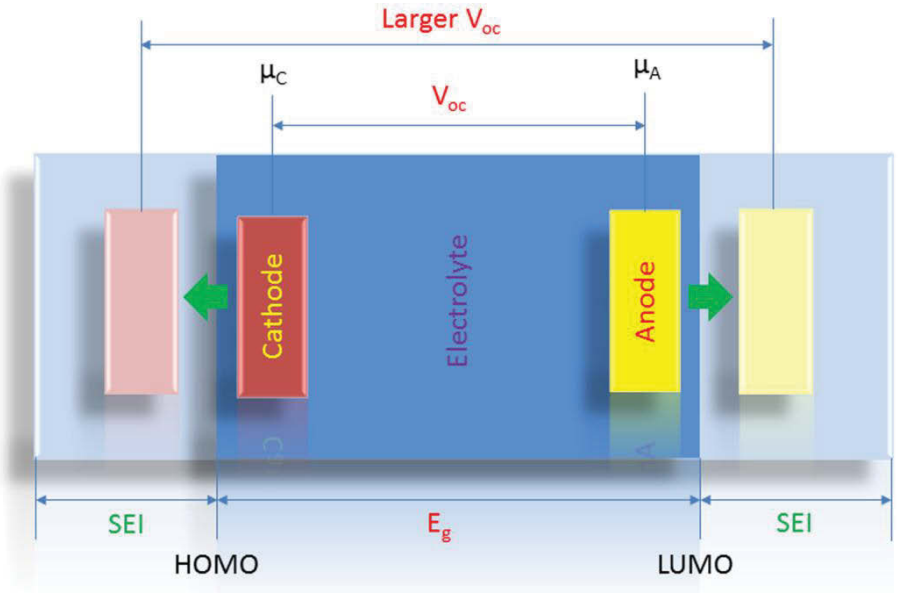

Figure 1-2 Schematic open-circuit energy diagram of electrolyte. E_g is the window of electrolyte thermodynamic stability. A μ_A > LUMO and/or a μ_C < HOMO requires a the formation of an SEI layer for kinetic stability.[33]

range of E_g for thermodynamic stability requirements. Otherwise, the anode will reduce the electrolyte when the μ_A is above the LUMO. Similarly, a cathode with a μ_C below the HOMO will oxidize the electrolyte. Therefore, the constrains for the open circuit voltage V_{oc} of a battery cell are expressed as:

$$eV_{oc} = \mu_A - \mu_C \leq E_g \tag{1-1}$$

where e is the magnitude of the electron charge. It should be noted that a passivating solid/electrolyte-interface (SEI) layer at the electrode/electrolyte boundary can provide kinetic stability to a larger V_{oc} provided that eV_{oc} - E_g is not too large because the

passivation layer can create a barrier which impedes the electron transfer between the electrodes and the electrolyte, thereby, protecting the electrolyte from reduction by the electron from the anode, and oxidization by losing electron to cathode.

Another key factor which estimates the electrolyte and the value of a battery cell is the energy density, ΛV_{oc}, where Λ is the capacity of reversible charge transfer per unit weight (Ah g^{-1}) between the anode and cathode. Most of time Λ was directly used to evaluate the electrolyte. Normally, the rate of ion transfer across the electrode/electrolyte interface is much smaller than the electronic current density because the electrodes and electrolyte are thin with a large surface area and. Nevertheless, at high current densities, it is hard to reach equilibrium for charge distribution due to the slow ionic motion within an electrode and/or across an electrode/electrolyte interface. This results in the reversible capacity decreasing with increasing rate of charge or discharge in the battery. Herein, the magnitude of the electronic current in the external circuit must be matched by the internal ionic current within the battery. However, through improving the ion conductivity, it can achieve high reversible capacity Λ and therefore higher energy density ΛV_{oc} at high current density. Obtaining a cell with a higher V_{oc} also can profit with a higher energy density. These observations, in turn, have led to a nonaqueous electrolyte, because they have a larger E_g compared to the aqueous electrolyte. The following summarises additional selection criterion for a nonaqueous electrolytes, besides the requirements on the large electrolyte window E_g and high ion conductivity:[33]

(1) Retention of the electrode/electrolyte interface during cycling when the electrode particles are changing their volume.

Table 1-1 Nonaqueous electrolytes for Li-ion batteries.[33]

Electrolytes	Example of classical electrolytes	Ionic conductivity ($\times 10^{-3}$ S cm^{-1}) at room temp	Electrochemical window (V) *vs.* Li/Li$^+$		Remark
			Reduction	Oxidation	
Liquid organic	1M $LiPF_6$ in EC:DEC (1:1)	7[34]	1.3[35]	4.5[36]	Flammable
	1M $LiPF_6$ in EC:DMC (1:1)	10[34]	1.3[35]	>5.0[34]	
Ionic liquids	1M LiTFSI in EMI-TFSI	2.0[37]	1.0[37]	5.3[37]	Non-flammable
	1M $LiBF_4$ in EMI-BF_4	8.0[37]	0.9[38]	5.3[38]	
Polymer	LiTFSI-P(EO/MEEGE)	0.1[39]	<0.0[39]	4.7[39]	Flammable
	$LiClO_4$-PEO_8 + 10 wt % TiO_2	0.02[40]	<0.0[40]	5.0[40]	
Inorganic solid	$Li_{4-x}Ge_{1-x}P_xS_4$ (x = 0.75)	2.2[41]	<0.0[41]	>5.0[41]	Non-flammable
	$0.05Li_4SiO_4 + 0.57Li_2S + 0.38SiS_2$	1.0[42]	<0.0[42]	>8.0[42]	
Inorganic liquid	$LiAlCl_4 + SO_2$	70[43]	-	4.4[43]	Non-flammable
Liquid organic + Polymer	$0.04LiPF_6$+0.2EC+0.62DMC +0.14PAN	4.2[44]	-	4.4[44]	Flammable
	$LiClO_4$ + EC + PC + PVdF	3.0[45]	-	5.0[45]	
Ionic liquid + Polymer	1M LiTFSI + P_{13}TFSI + PVdF-HFP	0.18[46]	<0.0[46]	5.8[46]	Less flammable
Ionic liquid + Polymer + Liquid organic	56 wt % LiTFSI-Py_{24}TFSI + 30 wt % PVdF-HFP + 14 wt % EC/PC	0.81[47]	1.5[47]	4.2[47]	Less flammable
Polymer + Inorganic solid	2 vol % $LiClO_4$-TEC-19 + 98 vol%95 ($0.6Li_2S + 0.4Li_2S$) + $5Li_4SiO_4$	0.03[48]	<0.0[49]	>4.5[49]	Non-flammable

(2) A Li^+ ion conductivity $\sigma_{Li} > 10^{-4}$ S cm^{-1} over the temperature range of battery operation.

(3) An electronic conductivity $\sigma_e < 10^{-10}$ S cm^{-1}.

(4) Chemical stability over ambient temperature ranges and temperatures in the battery under high power.

(5) Chemical stability with respect to the electrodes, including the ability to rapidly form passivating solid/electrolyte-interface (SEI) layer where kinetic stability is required because the electrode potential lies outside the electrolyte window.

(6) Safe materials, i.e., preferably nonflammable and nonexplosive if short-circuited.

(7) Low toxicity and low cost.

Meeting all these requirements proves to be a formidable challenge.

Partial sorts of electrolyte are discussed at here as listed by Table 1-1.

1.1.1 Organic liquid electrolytes

The most commonly used organic liquid electrolytes are carbonates or carbonate blends consisting of one or more of propylene carbonate (PC), ethylene carbonate (EC), diethyl carbonate (DEC), dimethyl carbonate (DMC), or ethylmethyl carbonate (EMC). They have an oxidation potential at ca. 4.7 V (*vs.* Li/Li^+)[36,50,51] and a reduction potential near 1.0 V (*vs.* Li/Li^+).[35] These electrolytes also exhibit low viscosity, benefiting low activation energy for Li^+ ion diffusion. For the carbonaceous anode materials, the pure carbonate is not suitable for serving as the electrolyte because carbon has a higher electrochemical potential than the LUMO of a carbonate. Therefore, a passivating

solid/electrolyte-interface (SEI) layer on the surface of a carbonaceous anode is required to protect the electrolytes from reduction by the electron transferred from carbon.[52,53] In most cases, the carbonate blend consisting of ethylene carbonate (EC) was used as solvent for the electrolyte, because the EC can provides the SEI layer.[52,53] However, the highly flammable nature of carbonate-based electrolyte is a safety issue.[54] Moreover, the lithium salt in the electrolyte, $LiPF_6$, can decompose into LiF and PF_5 automatically: the latter further reacts irreversibly with any water present ($PF_5 + H_2O = PF_3O + 2HF$) at temperature above 60 ºC.[55] Obviously, these reactions degrade the battery and lead to safety hazards. The use of thermally stable additives, such as $LiBF_4$ and LiBOB salts, can lower the operating temperature to prevent the autocatalytic decomposition of $LiPF_6$ salt.[56]

Table 1-2 Important families of ionic liquids and their physical properties.[1]

Cation	Anion	Melting point (°C)	Density (g cm^{-3} at 20 °C)	Viscosity (mPa s at 25 °C)	Conductivity, (10^{-4} S cm^{-1} at 25 °C)
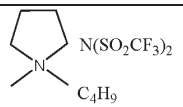	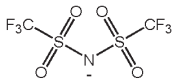	-18	1.41	85	22
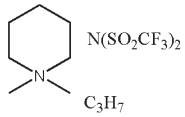	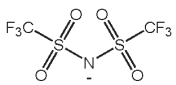	8.7	1.43	117	15.1
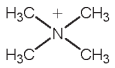	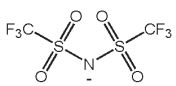	-14	1.41	83	12
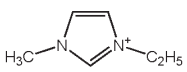	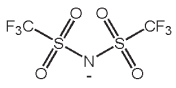	-15	1.52	34	87
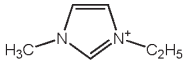	BF_4	13	1.28	37	140

1.1.2 Ionic liquids

Room-temperature ionic liquids (RTILs)[37,38,57,58] offer several advantages over carbonate-based electrolytes: a high oxidation potential (~ 5.3 V *vs* Li/Li^+), non-flammability, low vapour pressure, better thermal stability, low toxicity, high boiling point, and high Li-salt solubility. These have been recently considered as alternative electrolytes for Li-ion batteries.[59-61] Several important families of relevant RTILs are provided including structural formulae and physical properties (Table 1-2).

The limiting reactions of important IL solutions in the anodic (cathodes) and the cathodic (anodes) sides of their electrochemical windows were thoroughly explored.[62,63] Unfortunately, they have higher viscosity, which leads to poor wettability of the porous active mass of the composite electrodes and reduces Li^+ ion conductivity. An alternative approach is to increase Li^+ ion conductivity σ_{Li} by adding a liquid carbonate to an ionic liquid, but at a concentration that retains the non-flammability of the ionic liquid. With this strategy, it is also possible to increase the oxidation voltage of the hybrid electrolyte from that of the carbonate. In spite of extensive research, no RTILs have yet been introduced into large power batteries. Further drawbacks, include very high prices and incompatibility with graphite electrodes due to detrimental co-intercalation of the IL cations together with Li ions.[62] The latter problem can be solved by enhancing the passivation of graphite electrodes (stable SEI layer) by the use of special surface active additives in solutions,[64] such as EC or VC.

1.1.3 Inorganic liquid electrolytes

The inorganic liquid electrolyte based on $LiAlCl_4$ and SO_2 [65] has a good room-temperature Li-ion conductivity ($\sigma_{Li} = 7 \times 10^{-2}$ S cm^{-1}) and is non-flammable, but its electrolyte window appears to be too small to be competitive.

1.1.4 Solid polymer electrolytes

Solid polymer electrolytes, with low-cost, non-toxic, good chemical stability features, are usually comprised by polyethylene oxides (PEOs) and lithium salts ($LiClO_4$, $LiPF_6$, or $LiAsF_6$).[39] They can work as the separator of the electrodes, and also retain contact over an electrode/electrolyte interface during modest changes of the electrode volume with the state of charge of the battery. The main drawback of the solid polymer electrolytes is the low Li^+ ion conductivity. Normally, the value of σ_{Li} is less than 10^{-5} S cm^{-1} at room temperature, which is far from the demand of the power-battery system. It was found that fast ion transport can be realized in cooperation with the fast side chain motion with a (2-methoxyethoxy) ethyl glycidyl ether (MEEGE) composition.[39] Solid polymer electrolytes complexed with lithium bis(trifluoromethylsulfonyl)imide (LiTFSI) exhibit higher conductivity than those complexed with a conventional salt, lithium perchlorate ($LiClO_4$). For instance, the polymer electrolytes, (PEO/MEEGE) containing 9 mol % of MEEGE complexed with LiTFSI, exhibit high ionic conductivities of 10^{-4} S cm^{-1} at 30 °C and 10^{-3} S cm^{-1} at 80 °C, and achieved a 4 V electrochemically stable potential window was achieved. The introduction of oxide particles (e.g., Al_2O_3, TiO_2, SiO_2, or ZrO_2) can further enhance the σ_{Li} and Li^+ ion transference number by creating a more amorphous polymer matrix to inhibit chain crystallisation and attract Li^+ from its salt. However, the σ_{Li} is still not comparable to that of the carbonate electrolytes, which explains why little research is based on this type of electrolyte.

1.1.5 Inorganic solid electrolytes

Inorganic solid Li^+ ion conducting materials have been considered as alternative for Li-based electrolytes due to their two superior features: higher ionic conductivity ($\sigma_{Li} > 10^{-4}$ S cm^{-1})[41,42,66,67] and wider electrochemical window (have been extensively reviewed[68]). For these reasons, laboratory-size all-solid-state Li-ion batteries have been investigated[48,68,69] and used in thin-film battery applications.[70] However, from consideration for large-scale batteries application, the additional electrolyte requirements have excluded inorganic solid Li-ion electrolytes. [33]

1.1.6 Hybrid electrolyte system

Hybrid electrolytes represent a shortage to combine the desirable qualities of the electrolytes described above. They are blends of organic liquid electrolytes, ionic liquids, polymer electrolytes, and/or inorganic solid electrolytes based on the following compositions:

Polymer + organic liquid (polymer gel)[44,45,71]

Ionic liquid + polymer electrolyte (ionic liquid polymer gel)[46,72-75]

Ionic liquid + polymer electrolyte + liquid organic electrolyte[46]

Polymer electrolyte + inorganic solid electrolyte[48,49,76]

Although the strategy of mixing electrolytes aims to exploit the advantages of each constituent, the disadvantages of each also appear. For example, the ionic conductivity is increased in polymer gel electrolytes, but they are still flammable and have the irreversible capacity loss below 1 V associated with formation of a passivation layer. So far, the most optimal electrolyte is a hybrid ionic liquid and organic liquid as the

electrolyte solvent, which can be made non-flammable without too great a compromise of the electrolyte σ_{Li}.

1.2 Cathode materials for Li-ion batteries

The key requirements for a material to be successfully used as a cathode in a rechargeable lithium battery are as follows.[77]

(1) The material contains a readily reducible/oxidisable ion, for example a transition metal.

(2) The material reacts with lithium in a reversible manner. This dictates an intercalation-type reaction in which the host structure essentially does not change as lithium is added.

(3) The material reacts with lithium with a high free energy of reaction and allow high-energy storage with:

- high capacity, preferable at least one lithium per transition metal.

- high voltage, preferably around 4 V (as limited by stability of electrolyte).

(4) The material reacts with lithium very rapidly both on insertion and removal.

This leads to high power density, which is needed to replace the Ni/Cd battery or for batteries that can be recharged using HEV regenerative braking.

(5) The material is a good electronic conductor, preferably a metal.

- easy addition or removal of electrons during the electrochemical reaction.

- reaction should proceed at all contact points between the cathode active material and the electrolyte rather than at ternary contact points between the cathode active material, the electrolyte, and the electronic conductor (such as carbon black).

- minimal need for inactive conductive diluents, which take away from the overall energy density.

(6) The material is stable, and does not change structure or otherwise degrade, causing over discharge and overcharge.

(7) The material is low cost and environmentally benign.

Almost all of the research and commercialisation of cathode materials have centred on two classes of materials. The first contains layered compounds with an anion close-packed or almost close-packed lattice in which alternate layers between the anion sheets are occupied by a redox-active transition metal and lithium then inserts itself into the essentially empty remaining layers. This group is exemplified by $LiTiS_2$, which is depicted in Figure 1-3, $LiCoO_2$, $LiNi_{1-y}Co_yO_2$, and $LiNi_yMn_yCo_{1-2y}O_2$. (The spinels may be considered as a special case where the transition-metal cations are ordered in all the layers). The materials in the second group have more open structures, and include vanadium oxides, the tunnel compounds of manganese dioxide, and the recently developed transition-metal phosphates, such as the olivine $LiFePO_4$. The first group will have an inherent advantage in energy stored per unit of volume owing to their more compact lattices, however some in the second group, such as $LiFePO_4$, are potentially much lower cost. The following discussion will centre predominantly on these two classes of materials.

1.2.1 Layered structure cathode materials

The earliest cathodes of rechargeable lithium cells in several prototypes and commercial products are a variety of chalcogenides (TiS_2, MoS_2, etc.),[77] co-operating with the metallic lithium or Li-Al alloys as anode. Later, manganese and vanadium oxides were utilized. Hereinto, one of the earliest lithium batteries with the Li/MnO_2 system was initially sold in solar rechargeable calculators (Sanyo, Lithium Battery Calculator, Model CS-8176L.) by the Sanyo manufacturer.[78-80] However, Lithium metal as an anode material in rechargeable batteries was ultimately rejected due to safety concerns, owing to dendrite growth on the metal surface after repeated Li plating that led to internal short circuits.

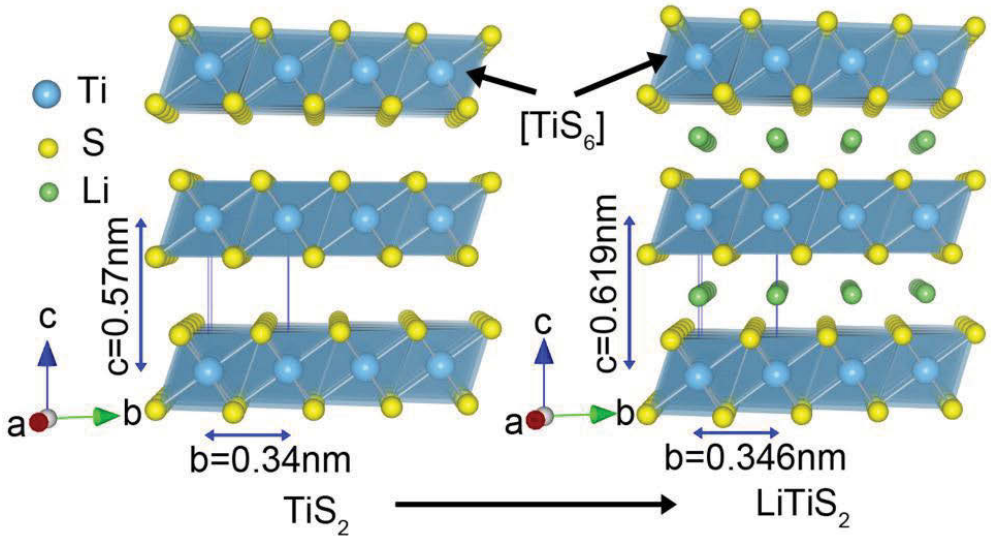

Figure 1-3 Crystal structure of TiS_2 and lithiated $LiTiS_2$.

1.2.1.1 Chalcogenides

Around 1970 researchers at Stanford[81] discovered that a range of electron-donating molecules and ions could be intercalated into the layered dichalcogenides. These guest-host intercalation reactions modified the physical properties and, in particular, were

found to enhance the superconducting transition temperature from 0.8 to over 3 K. It was also discovered that such compounds remained superconducting even when the guest molecules were paramagnetic.[82] Of all the layered dichalcogenides, titanium disulphide (as shown in Figure 1-3) was the most appealing for consideration as an energy storage electrode,[83-85] because it was the lightest. Thus was subsequently discovered to be a semimetal,[86] so no conductive diluent was needed in the cathode structure, and any such addition was found to be detrimental to the electrochemical behaviour. It was also found to form a single phase with lithium over the entire composition range of Li_xTiS_2 for $0 \leq x \leq 1$.[87] This lack of phase change enables all the lithium to be removed reversibly, without the need for energy wastage associated with the nucleation of new phases or sluggish reactions when massive rearrangement of the host must occur as the lithium content is changed. Exxon marketed button cells with LiAl anodes[88] and TiS_2 cathodes for watches and other small devices in 1977-1979; the LiAl anode improved the safety of the cells. Some of the largest lithium single cells built to date are those exhibited by Exxon at the Electric Vehicle Show in Chicago in 1977.

1.2.1.2 $LiCoO_2$

Goodenough recognized that $LiCoO_2$ had a structure similar to the layered structures of the dichalcogenides and showed that the lithium could be removed electrochemically, thus making it a viable cathode material.[89] $LiCoO_2$ has the α-$NaFeO_2$ structure with the oxygen in a cubic close-packed arrangement as shown in Figure 1-4. On complete removal of the lithium, the oxygen layers rearrange themselves to give hexagonal close packing of the oxygen in CoO_2.[90] Between these composition limits several phases are formed with varying degrees of distortion of the cubic close packed (ccp) oxygen lattice.

The composition $Li_{0.5}CoO_2$ can also be formed in the spinel form,[91] though it appears to be metastable and is not normally formed during the cycling of the Li_xCoO_2 electrode. Further TEM study[92] has identified the spinel phase originating on the surface of heavily cycled $LiCoO_2$ cathodes.

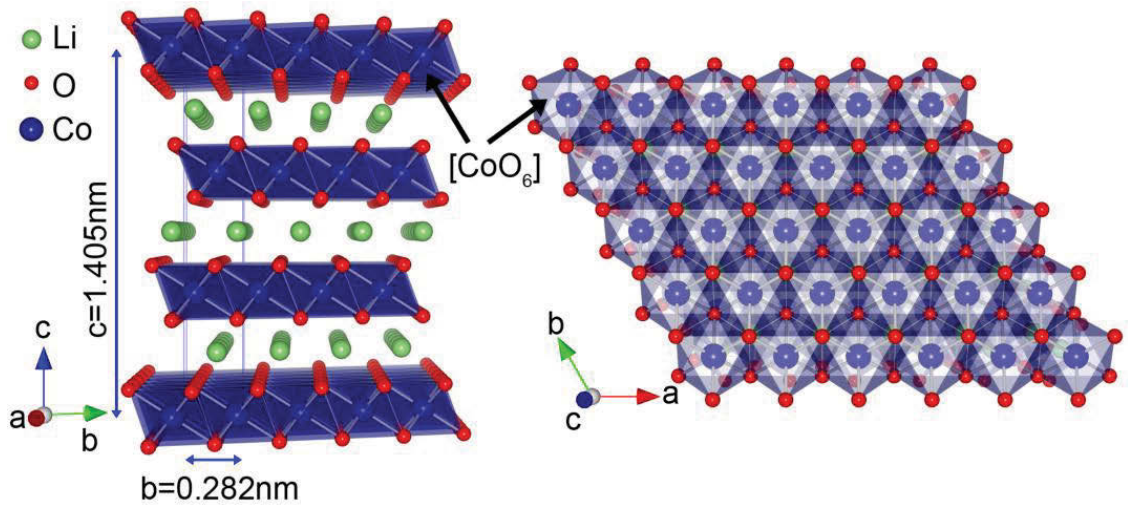

Figure 1-4 Crystal structure of $LiCoO_2$, (a) depicted along a axis and (b) see along c axis.

SONY combined the $LiCoO_2$ cathode with a carbon anode to make the first successful Li-ion battery,[93,94] which now dominates the lithium battery market. The carbon anode, which provides a host for Li^+ ions at low potential, forms the compound LiC_6 on reaction with lithium. Thus makes for a much safer battery than pure lithium as there is much less chance of dendritic lithium formation, which can lead to cell shorting. The use of graphitic carbon can result in the loss of 100-300 mV in cell potential, which is feasible with the higher potential $LiCoO_2$ cathode but not with the lower potential of the TiS_2 cathode. The reaction mechanism of Li_xCoO_2 on Li extraction can be summarized as follows:[95] first, the interlayer c axis expands as a result of electrostatic repulsion of the oxygen layers $x \leq 0.5$;[96,97] second, a hexagonal-monoclinic transformation occurs at

$x \approx 0.5$ that represents an order-disorder transition,[96,98] lastly, transforms the O3 $LiCoO_2$ phase (close-packed oxygen layers with an ABCABC stacking sequence) into the O1 Li_xCoO_2 phase (ABAB stacking sequence) occurs at $x \approx 0.05$.[97,99] The transformation proceeds via an intermediate phase, $Li_{0.12}CoO_2$, (H1-3)[100,101] a hybrid host structure that encompasses both the O3 and O1 stacking sequences. Although almost all of the Li can be extracted to give a theoretical capacity of 274 mA h g^{-1}, only a little over half of the capacity is practically reversible for insertion/extraction ($\leq$ 4.2 V vs Li/Li^+). Capacity fading is severe upon extraction of > 0.7 Li because of loss of oxygen (resulting from reduced stability of lithium poor phases) result in low reaction rates and poor stability of the electrode at low lithium contents,[102] electrolyte decomposition,[103,104] and the problem of cobalt dissolution in typical electrolytes.[105] In addition, reactive nanosize materials/components may not be viable for commercial batteries because of safety and durability.[77]

The diffusion of lithium in $LiCoO_2$ is 5×10^{-9} cm^2 s^{-1}, which compares with 10^{-8} cm^2 s^{-1} for $LiTiS_2$.[106] These high diffusivity values are consistent with the ability to cycle these two cathodes at current density 4[106] and 10 mA cm^{-2},[107] respectively.

Cho et al. reported in a pioneering series of papers,[94,108-111] that the $LiCoO_2$ capacity could be increased to 170 mA h g^{-1} without capacity fading over 70 cycles by coating a metal oxide or phosphate on the surface of the $LiCoO_2$ particles. Benefits of surface coatings were quickly confirmed by other research groups.[112-114] The mechanism of protection is related to minimizing the reactivity of Co^{4+} on charge with the acidic HF in the electrolyte coming from the interaction of moisture with the electrolyte salt $LiPF_6$.[115] Another method of maintaining capacity is replacing the $LiPF_6$ salt by LiBOB to remove the source of HF.[116] It was shown that completely drying the $LiCoO_2$ by heating

to temperature 550 °C can improve the capacity retention at 180 mA h g^{-1} at a 4.5 V cutoff. However, above a 4.5 V level, substantial movement of the oxygen layers from ABCA to ABA stacking sequence, occurs as a result of the conversion of three block cubic close-packed Li_xCoO_2 to a 1T one-block hexagonal close-packed structure of CoO_2, causing a significant disruption of structure. Hereinto, it cannot achieve capacities for $LiCoO_2$ much above 180 mA h g^{-1} over hundreds of cycles.

Although the $LiCoO_2$ cathode dominates the rechargeable lithium battery market, a limited availability of cobalt is responsible for its high price. Moreover, cobalt is biologically toxic and non-environment friendly element. The conductivity of Li_xCoO_2 is reported to change dramatically with composition,[94] behaving like a metal at $x = 0.6$ and a typical semiconductor at $x = 1.1$ (the typical lithium-rich material used in commercial cells), changing by 2^{117} (for the $x = 1.1$ compound) to 4^{118} (for the $x = 1.0$ compound) orders of magnitude at ambient temperatures and up to 6 orders of magnitude at lower temperatures.[118] This causes a challenge and limits its use. An alternative cathode is necessary for large-scale applications, as envisioned in HEV or for load level. Therefore, some other layered lithium transition metal oxides cathode materials have also been developed vigorously as discussed below:

1.2.1.3 $LiNiO_2$

Isostructural $LiNiO_2$[119] was considered as an alternative to $LiCoO_2$ because of its lower cost, higher reversible capacity (ca. 200 mA h g^{-1}) and better environmental compatibility. However, it is difficult to synthesize stoichiometric $LiNiO_2$. Most reports suggest excess nickel as in $Li_{1-y}Ni_{1+y}O_2$; thus, nickel is being found in the lithium layer, which pins the NiO_2 layers together, giving rise to cation site disorder because of the similar size of Ni^{2+} and Li^+ ($R_{Ni}^{3+} = 0.56$ Å, $R_{Ni}^{2+} = 0.69$ Å , $R_{Li}^{+} = 0.76$ Å, where R is

Radius).[95] Exchange of Li^+ and Ni^{2+} in the 3b and 3a sites results in materials that can be formulated as $[Li_{1-y-\alpha}Ni^{2+}_{y+\alpha}]$-$[Ni^{3+}_{1-y}Ni^{2+}_{y-\alpha}Li_\alpha]O_2$ (α: cation disorder between Ni^{2+} and Li^+, $\alpha < y$),[120,121] where α increases as the amount of Ni^{2+} increases ($\alpha \approx 0$ at $y \leq 0.07$, $\alpha = 0.02$ at $y = 0.25$).[121] The cation disorder has important consequences for Li^+ transport. The presence of Ni^{2+} in the interlayer Li^+ sites induces local reduction of spacing between the transition-metal layers because the Ni^{2+} is oxidized into the smaller Ni^{3+} cation during charging. This results in a reduction of the lithium diffusion coefficient and the power capability of the electrode.[120] Furthermore, compounds with low lithium contents appear to be unstable due to the high effective equilibrium oxygen partial pressure, making cells inherently unstable and therefore dangerous when in contact with organic solvents. In addition, the position of the $Ni^{3+/4+}$ couple in $LiNiO_2$ can result in preferential oxidation of the lattice oxide ions and hence evolution of O_2 on charging of the electrode, with concomitant safety issues. The phase transformations exhibited on (de)lithiation of Li_xNiO_2 are as complicated as those of $LiCoO_2$. They can be summarized as consisting of three single-phase reactions and three two-phase reactions: (H1 ($0 < x < 0.15$) ↔ H1 + M ($0.15 < x < 0.25$) ↔ M ($0.25 < x < 0.5$) ↔ M+H2($0.5 < x < 0.57$) ↔ H2($0.57 < x < 0.68$) ↔ H2 + H3 ($0.68 < x$), H: hexagonal, M: monoclinic phase).[122,123]

Many different elements can be substituted into the $LiNiO_2$, which impact the layeredness of the structure, its stability on lithium removal, and the retention of capacity on cycling. Hereinto, the substitution of Ni^+ by Co^{3+} was mostly examined.

In a series of papers, the Delmas group[124-127] and Zhecheva et al.[128] determined the structural details and physical properties of the $LiNi_{1-y}Co_yO_2$ system and showed that there is an increased ordering as the cobalt concentration increases; they found that the

c/3*a* ratio increases monotonically from 1.643 to 1.652 as *y* increases from 0 to 0.4 and that there is no nickel content on the lithium sites for $y \geq 0.3$ due to lower levels of $Ni^{2+} \leftrightarrow Li^{+}$ site exchange[128] as well as greater structural stability at high temperature.[129] Thus, cobalt has the ability to supress the migration of nickel to the lithium site in the mixed Li nickel/cobalt compounds. In addition, studies have shown that the cobalt-substituted nickel oxides are more stable and are thus less likely to lose oxygen than the pure nickel oxide. Cobalt is also reported to facilitate the oxidation of iron atoms in the structure.[130] Other ions, such as iron, do not have the same positive effect as cobalt; thus, in the compound $LiNi_{1-y}Fe_yO_2$ the capacity is reduced with increasing iron content and the iron has no positive effects on the layeredness of the structure.[131] Specifically, for $y = 0.10$, 0.20, and 0.30 the amount of 3d metal in the lithium layer is 6.1 %, 8.4 %, and 7.4 %, respectively, for samples formed at 750 °C. Although a $LiFeO_2$ compound would be ideal for a low-cost battery, it has been reported[132] that the lithium cannot be deintercalated within the normal potential ranges used in lithium batteries; this is explained[133] by the lack of compression of the FeO_6 octahedra which makes the reduction of one electron from Fe^{3+} very difficult. The addition of a small amount of a redox-inactive element, such as magnesium, can reduce the capacity fading on cycling.[134] NiO_2 by itself is thermodynamically unstable at 25 °C, as the equilibrium oxygen partial pressure exceeds 1 atm. In $LiNi_{1-y}Mg_yO_2$;[135] the inert element prevents the complete removal of lithium and thus minimizes the possibility of structural collapse and development of high oxygen partial pressures.

Stability can be further improved by Al (and other metal) doping, such as in $Li[Ni_{0.8}Co_{0.15}Al_{0.05}]O_2$, which has experienced tremendous commercial success as the cathode of advanced lithium batteries for use in large-scale systems such as hybrid electric vehicles,[136-139] Co assists in ordering the structure, to retain the nickel in the

nickel layer, while Al, being redox inactive, prevents the complete removal of all the lithium, thus additionally stabilizing the structure and preventing any phase changes that might occur at very low or zero lithium content. On charging these mixed oxides the nickel is oxidized first to Ni^{4+} then the cobalt to Co^{4+}.[140]

An issue with all these layered oxides is their electronic conductivity, which is not uniformly high across the lithium composition range. Thus, cobalt substitution in $LiNiO_2$, as in $LiNi_{0.8}Co_{0.2}O_2$, reduces the conductivity.[127] In addition, as lithium is removed from the phase $Li_xNi_{0.1}Co_{0.9}O_2$[126] or from Li_xCoO_2,[118] the conductivity was increases dramatically by some 6 orders of magnitude to around 1 S cm^{-1} from $x = 1$ to 0.6. These dramatic changes require a conductive diluent to be added to the cathode-active material, however this would reduce both the energy storage and the power capabilities.

In addition, it was reported that anion doping with F^- and S^{2-} on the O^{2-} sites[141] can improve cycling performance as a result of reduced Ni migration into the Li layer.

1.2.1.4 $LiMnO_2$

Much interest has been placed on the layered $LiMnO_2$ compound for its low-cost and environmentally benign properties.[142,143] However, unlike cobalt and nickel, manganese does not form a stable $LiMnO_2$ phase with the layered α-$NaFeO_2$ structure under normal conditions. The spinel structure is the stable phase in the $Li_{0.5}MnO_2$ composition. As there are a myriad of structures[144] with Mn : O in a 1 : 2 ratio, other structures may be stable at different lithium contents. It is not thermodynamically stable at elevated temperature and thus cannot be synthesized by one step solid state method like $NaMnO_2$. Therefore, brand new approaches are needed to obtain the layered structure $LiMnO_2$.

Ion exchange the sodium compound in the $NaMnO_2$, giving $LiMnO_2$, was successfully accomplished independently by Bruce[143] and Delmas.[145] Starting with different layered structures maintains the stacking order of the parent manganese oxide, thus allowing the impact of stacking sequence on electrochemical performance to be studied. An alternative preparative approach is to synthesize the structure at low temperatures, as, for example, by hydrothermal synthesis/decomposition of alkali permanganates,[142,146,147] which, in the case of lithium, results in a $Li_{0.5}MnO_2 \cdot H_2O$ composition. Mild warming results in the loss of water to give the desired layered Li_xMnO_2, while overheating to 150 °C results in the formation of the spinel $LiMn_2O_4$.

Regardless of overheating, the layer structured $LiMnO_2$ will easily convert to the thermodynamically stable spinel on the first charge cycle. This conversion does not require oxygen diffusion as both structures have ccp oxygen lattices. The layered-to-spinel phase transition in Li_xMnO_2 has been explained through Ab initio calculations,[148] which suggest that partially lithiated layered Li_xMnO_2 transforms to spinel in a two-stage process. In the first stage, a significant fraction of the Mn and Li ions rapidly occupy tetrahedral sites, forming a metastable intermediate. The second stage involves a more difficult coordinated rearrangement of Mn and Li ions to form the spinel. This behaviour is contrasted to Li_xCoO_2. The susceptibility of Mn to migration into the Li layer is controlled by oxidation state, which suggests various means of inhibiting the transformation.

Two approaches to stabilising the layered $LiMnO_2$ have been taken. In the geometric stabilization approach, non ccp structures such as tunnel structures,[149,150] or "pillars", are placed between the layers to provide the stabilization.[142,146,151] The former is stable during spinel formation at low current densities, and the latter shows excellent stability

but poor rate capability. The groups of Dahn and Doeff among others have pursued non-ccp structures by examining tunnel structures such as $Li_{0.44}MnO_2$.[149] They also ion-exchange layered sodium manganese oxide compounds with non ccp stacking of the oxygen sheets.[152-157] These sheets cannot readily reorganize after ion exchange to give ccp stacking. This results in the two block rather than the three-block structures such as O3, which describes $LiMnO_2$. This ion exchange process also results in much faulting in the stacking of the layers, which prevents the layers from reordering into the thermodynamically stable O3 phase. However, these phases intercalate lithium over a rather wide range of potential and in some cases over two potential steps.[154]

In the electronic stabilisation approach, the goal is to make the electronic properties of Mn cobalt-like by substitution of the Mn with more electron rich elements such as Ni, which work as the electrochemically active ion. The first studies on $LiNi_{1-y}Mn_yO_2$, for $0 < y < 0.5$, indicated low capacities and poor reversibility.[158] However, Spahr et al. later demonstrated a high capacity and reversibility for $LiNi_{0.5}Mn_{0.5}O_2$[159] with a discharge curve typical of that of $LiNiO_2$. These compounds are thus best described as substituted nickel oxides in which the manganese remains in the tetravalent state and the nickel is redox active between the +2 and +4 oxidation states; the manganese helps in reducing the cost and stabilising the lattice.

1.2.1.5 $LiMn_{0.5}Ni_{0.5}O_2$

The $LiNi_{1-x}Mn_xO_2$ ($x \leq 0.5$) system was first studied by Dahn et al. in 1992.[158] After being revisited by Ohzuku et al,[160] in 2001, $LiNiMnO_2$ demonstrated greatly improved electrochemical performance, exhibiting 200 mA h g^{-1} capacity (2.5 - 4.5 V window *vs.* Li/Li^+) with little fading rate.[161] $LiNi_{0.5}Mn_{0.5}O_2$ has other advantages: lower thermal runaway, better structural thermal stability and greater inhibition to reaction with

electrolytes in the charged state compared to $LiCoO_2$ or $LiNiO_2$.[161,162] Cycled $Li_xNi_{0.5}Mn_{0.5}O_2$ (x = 0.2, 0.9) also show a higher onset temperature of oxygen release and reduced oxygen loss as a result of increased structural stability.[163]

There are 2 possible valence states of the metal accommodated in $LiNi_{0.5}Mn_{0.5}O_2$ one is Ni^{3+} and Mn^{3+} as originally thought,[159] another is Ni^{2+} and Mn^{4+} as speculated[164] and proven by X-ray adsorption spectroscopy[165] and first principles calculations.[166] Spin density calculations indicate that the Mn ion has oxidation state +4 independently of the Li content in the material, while Ni is oxidized from Ni^{2+} to Ni^{4+} upon removal of Li. The high insertion voltage for the $LiNi_{0.5}Mn_{0.5}O_2$ can be partly attributed to the change in Mn-Ni interaction upon Li cycling. However, it has been proposed that most charge compensation actually occurs at hybridized 2p-like levels with local weight near the oxygen atoms.[167] The "formally invariant" valence state of Mn^{4+} in the range of $0 < x < 1$ accounts for some of the stability of the material upon cycling;[165] The redox potential of $Li_xNi_{0.5}Mn_{0.5}O_2$ is very similar to that of Li_xNiO_2, although it should be lower because of the greater span of oxidation states. This discrepancy may be to the energy difference in the attractive interaction (mixing) between Ni and Mn at x = 1 and the repulsive interaction between them at x = 0 in $Li_xNi_{0.5}Mn_{0.5}O_2$.[166] The other assumes that Mn and O contribute ~ 10 % and ~ 5 %, respectively, for charge compensation in the range of $0 < x < 1$ of $Li_xNi_{0.5}Mn_{0.5}O_2$, which reflects the covalent mixing in the system.[168]

$LiNi_{0.5}Mn_{0.5}O_2$ possesses 8 - 10 % cation disorder between the 3a and 3b sites due to the similar size of Ni^{2+} and Li^+, which impedes the kinetics of Li diffusion.[160] The effect of this disorder on Li ion diffusivity in layered transition metal oxides implies that[169,170] the site-exchanged transition metal (M) ions within the Li slabs (i) disrupt the lithium-

ion diffusion path, (ii) increase electrostatic repulsion between M and Li, resulting in a lower Li mobility, and (iii) reduce the Li slab space, resulting in a higher activation barrier to lithium diffusion.[95] Li diffusivity in the layered metal oxides takes place by migration through a tetrahedral site (octahedral-tetrahedral-octahedral), which is determined by the c-lattice parameter. And the high reversible capacity (200 mA h g^{-1}) of $LiNi_{0.5}Mn_{0.5}O_2$ is achieved only at slow current densities (0.17 mA cm^{-2}).[171]

There are several strategies which can address the problem of cation disorder in $LiNi_{0.5}Mn_{0.5}O_2$. Preparing the material via ion exchange from $NaNi_{0.5}Mn_{0.5}O_2$,[172] which decreases the amount of cation disorder to 4.3 %. $NaNi_{0.5}Mn_{0.5}O_2$ exhibits no cation disorder due to the larger size difference between Na^+ (R_{Na}^+ = 1.02 Å) and Ni^{2+} (R_{Ni}^{2+} = 0.69 Å), Mn^{4+} (R_{Mn}^{4+} = 0.53 Å). This method of material synthesis demonstrates substantially improved rate capability (183 mA h g^{-1} at a 6 C rate). Adjusting the stoichiometry to $LiNi_{0.5+\delta}Mn_{0.5-\delta}O_2$ also reduced the nickel content in the lithium layer to 5.6 %.[173] It was proposed that better cation ordering is induced because the elastic energy related to the different ionic sizes can overcome the entropy associated with cation disorder.[174] This material also presented better rate performance (ca. 110 mA h g^{-1} at 4 C). From a combination of neutron diffraction, ^{6}Li MAS NMR, first principle calculations, Ni was proven to migrate from the Li layer to transition metal (TM) sites vacated by Li at > 4.6 V *vs.* Li/Li^+ (the octahedral Li in TM sites is electrochemically extractable).[175,176] Therefore, charging to high voltages (5.3V *vs.* Li/Li^+) reduces the cation disorder.[177] Finally, complete delithiation to $Ni_{0.5}Mn_{0.5}O_2$ on charging to 5.3 V *vs.* Li/Li^+ results in conversion of the O3 to the O1 phase, similar to the case of $LiNiO_2$.[177]

1.2.1.6 $LiCo_{1/3}Ni_{1/3}Mn_{1/3}O_2$

The $LiNi_{1-y-z}Mn_yCo_zO_2$ compound, in which the metals Co, Ni, and Mn all are accommodated in the layered metal oxide structure, was been extensively investigated in the last few years and found to have properties that qualify them as possible candidates, for the replacement of $LiCoO_2$,[178-193] especially $LiCo_{1/3}Ni_{1/3}Mn_{1/3}O_2$ which was reported in 2001 by Ohzuku et al.[178] In addition to their high lithiation capacities and reversibility, these compounds show higher thermal stabilities, promising electrochemistry and intriguing structural behaviour compared to the Co-free compounds. $LiCo_{1/3}Ni_{1/3}Mn_{1/3}O_2$ possesses the same α-$NaFeO_2$-type layer structure,[178] which can be considered as a 1:1:1 solid solution of $LiCoO_2$, $LiNiO_2$, and $LiMnO_2$ [194] or a 1:2 solid solution between $LiCoO_2$ and $LiNi_{0.5}Mn_{0.5}O_2$ (i.e., $LiCo_{1-2x}Ni_xMn_xO_2$),[195] with Ni, Co, and Mn adopting valence states of 2^+, 3^+, and 4^+, respectively.[196] In addition, $Li_{1-x}Co_{1/3}Ni_{1/3}Mn_{1/3}O_2$ exhibits a very tiny volume change (1 – 2 %) within 0 and 0.7 range for x.[181,197-199] It also shows a low level of cation disorder.[197,198,200-203] Both the stable structure and regular cation order contribute to its excellent electrochemical performance. The material shows high rate capability (200 mA h g^{-1} at 18.3 mA g^{-1} and 150 mA h g^{-1} at 1600 mA g^{-1}).[204] Moreover, $LiCo_{1/3}Ni_{1/3}Mn_{1/3}O_2$ has excellent safty at a high state of charge compared to $LiNiO_2$, $LiCoO_2$, and $LiNi_{0.8}Co_{0.15}Al_{0.05}O_2$,[204,205] which is another attractive property suitable for the large-scale practical applications, especially as a potential cathode candidate for electric vehicles.

On the basis of the combined NMR, soft and hard X-ray absorption spectroscopy (XAS) studies,[206-208] the major charge compensation of $LiCo_{1/3}Ni_{1/3}Mn_{1/3}O_2$ at the metal site on Li deintercalation is achieved by the oxidation of Ni^{2+} to Ni^{3+} (surface) and Ni^{4+} (bulk),

and the oxygen site associated with the presence of Co, while Co^{3+} and Mn^{4+} remain in their original valence states. Hwang et al. used a combined computational calculation and experimental XANES study to show that the redox couples in $Li_{1-x}Co_{1/3}Ni_{1/3}Mn_{1/3}O_2$ are Ni^{2+}/Ni^{3+}, Ni^{3+}/Ni^{4+}, and Co^{3+}/Co^{4+}, are in the range of $0 \leq x \leq 1/3$, $1/3 \leq x \leq 2/3$, and $2/3 \leq x \leq 1$, respectively.[196] This prediction is consistant with XAS study,[198] which indicated that the Ni^{2+}/Ni^{4+} redox couple is near 3.75 V and the Co^{3+}/Co^{4+} couple occurs over the entire range of charge/discharge. The reaction mechanism of $LiCo_{1/3}Ni_{1/3}Mn_{1/3}O_2$ is additional debate for this material. X-ray and neutron diffraction studies show that $Li_{1-x}Co_{1/3}Ni_{1/3}Mn_{1/3}O_2$ is chemically stable as the O3 structure type without the loss of any oxygen from the lattice at $(1-x) > 0.35$.[181,197] It undergoes a phase transition from the starting O3 phase ($R\bar{3}m$) to the O1 phase of $Li_{0.04}Co_{1/3}Ni_{1/3}Mn_{1/3}O_2$ ($P\bar{3}m1$) at $(1-x) = 0.3$ without oxygen loss.

However, some research[178,201] based on first-principle calculations claimed the structure of $LiCo_{1/3}Ni_{1/3}Mn_{1/3}O_2$ to be a $[\sqrt{3} \times \sqrt{3}]$ R30°-type superlattice with long-range ordering. On the basis of subsequent electron diffraction, XRD, and XAS studies, the same group suggested that this superlattice adopted a $P\bar{3}12$ space group.[209] This point was supported by other studies on the local ordering within the transition metal layers, but further evidence for the long-range superstructure remains elusive.[95] Diffraction data were reported to be consistent with a random distribution of Mn, Ni, Co in the 3a site.[201] Through the solid state ^6Li NMR study,[203,210] it was show that local ordering of the transition metal layers is driven by local charge balance (Pauling's electroneutrality), related to Ni^{2+}-Mn^{4+}. In addition, electron paramagnetic resonance (EPR) spectroscopy[211] and XAS[208] also supported short-range ordering.

1.2.2 Polyanion-Based Positive Electrodes

Although transition metal oxides as energy storage materials dominate the modern portable devices market today, concerns over safety and cost have promoted research into alternative electrode materials for Li-ion batteries. Some compounds have been studied as possible new cathode materials, including those polyanion-based positive electrodes with large polyanions of the form $(XO_4)^{y-}$ (X = S, P, Si, As, Mo, W) in the lattice. An inductive effect from $(PO_4)^{3-}$ and $(SO_4)^{2-}$ ions raises redox energies compared to those in oxides and stabilizes the structure.[212] Furthermore the strong X-O covalent bonds within polyanion $(XO_4)^{y-}$ can increase the potential, resulting in the strong polarization of oxygen ions toward the X cation, which decrease the covalence of the M-O bond, generating relatively high operating potential for Li^+ ion insertion and extraction. Research shows that the redox centres have potentials as the redox centre have potentials in the range of 2.8-3.5 V *vs.* Li/Li^+.[213] Therefore, lithium metal phosphate and sulfate compounds contain XO_4 tetrahedron surrounded by four MO_6 octahedrons.

1.2.2.1 $LiFePO_4$

The advantage in using iron-based compounds is that, in addition to being naturally abundant and inexpensive, they are less toxic than vanadium, cobalt, manganese, and nickel compounds. $LiFePO_4$ is thermally and mechanically stable. The material is stable in overcharge or discharge, and is compatible with most electrolyte systems.[214,215] It also has a very flat voltage plateau at 3.45 V *vs.* Li/Li^+, which is easy to work with and has a high theoretical capacity of 170 mA h g^{-1} (based on the extraction of all lithium), which gives a cell made of the material a high energy density, particularly suited for high power application.[216,217] $LiFePO_4$ is also environmentally friendly, for it is found in

nature as the mineral triphylite and is made from plentiful elements, reducing its cost of production.

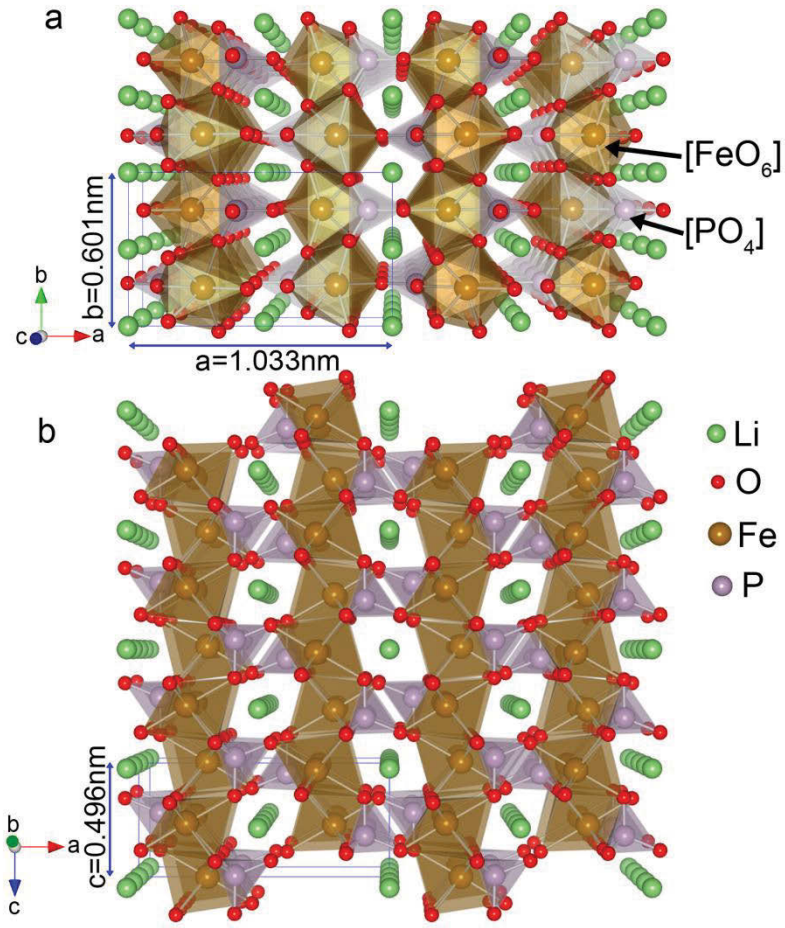

Figure 1-5 Crystal structure of $LiFePO_4$ (a) see along c axis and (b) see along b axis.

The structure of $LiFePO_4$ is shown in Figure 1-5 and belongs into the category of olivines, consisting of a distorted hexagonal close-packed (hcp) oxygen framework with 1/8 of the tetrahedral holes occupied by P, and 1/2 of the octahedral holes occupied by various metal atoms (in this case Li and Fe). $LiFePO_4$ crystallizes in space group 62 (Pnma). Each PO_4 tetrahedron is surrounded by four FeO_6 octahedrons (three corner-sharing and one edge-sharing), with lithium ions occupying the large open channels. These chains are bridged by edge and corner-sharing phosphate tetrahedrons, creating a

stable three-dimensional structure. $LiFePO_4$ has some drawbacks, especially its physical properties, such as its poor ionic and electronic conductivity. Many strategies have been devoted to solve this problem, such as coating $LiFePO_4$ particles with a highly conductive agent,[218,219] decreasing the actual size of the $LiFePO_4$ particles,[220 221,222] and cycling the batteries at a higher temperature than room temperature.[222] Another method of increasing the electronic conductivity is doping the $LiFePO_4$ with other elements.[223-225] When these methods are combined, the utilisation of the $LiFePO_4$ cathodes approaches its theoretical value.

1.2.2.2 Ion and electron transport in $LiFePO_4$

In the early stage, $LiFePO_4$ was thought to have a two dimension Li^+ ions diffusion pathway, similar to the layered oxides material $LiCoO_2$,[216] because it has 2 possible directions for Li^+ ions transport as shown in Figure 1-5. One Li tunnel is parallel to the b-axis of the crystal (Figure 1-5 a), while another possible direction of Li transport is along the c-axis (Figure 1-5 b). Later, first-principles calculations of Li transport in olivine structures with a Li_xMPO_4 composition (M = Mn, Fe, Co, Ni; $x \approx 0$ and 1),[226] showed that Li moves rapidly through a 1D channel with little possibility for crossing between channels. The calculated diffusion coefficient in the [010] direction (along with b-axis, Figure 1-5 b) was several orders of magnitude higher than the [001] direction (along with c-axis, Figure 1-5 a). The activation energy for [010] lithium transport is also found to be 0.27 eV compared to 2.5 eV in the [001] direction for $LiFePO_4$. These results clearly indicate a preference for Li^+ ion transport along the b-axis. These mobility results are also expected to apply to other olivine materials, because the transport properties are largely determined by the topology of the olivine structure. The olivine structure has high intrinsic ionic conductivity and could achieve good rate

capacity if defects blocking the 1D channel and the electrical conductivity problems of Fe were avoided. This is consistent with the conventional belief that rate problems in Li_xFePO_4 materials are due to electron conductivity limitations.[226] The high activation energy for the pathway along c-axis is likely to be due to the LiO_6 octahedrally coordinated interstitial site which is face-shared with two PO_4 tetrahedrons, causing Li occupation of this site to be highly unfavourable.[95]

Islam et al.[27] further confirmed the possible 1D diffusion pathway for Li transport along the [010] direction with the lowest activation energy (0.55 eV). He also clearly demonstrated that the migration between adjacent Li sites in the [010] direction occur along a curved pathway instead of linear hopping, which was later confirmed by performing maximum entropy method (MEM) modelling on neutron diffraction data of $Li_{0.6}FePO_4$.[227] Li et al. performed AC impedance measurements on different axes of $LiFePO_4$ single crystals. The total conductivity of each axial orientation of the crystal was measured. The results agree with the calculations of Morgan: the ionic resistivity along the [010] direction is about 1000 times less than that in the [100] direction and 3000 times less than in the [001] direction.[228] Through the theoretical calculation,[229] the equilibrium morphology predominated with {201}, {011}, and {100} faces. The calculated growth morphology exhibits the {010}, {100} and {101} faces, with an elongated hexagonal prism-like shape, which is consistent with experimentally observed $LiFePO_4$ particles. Almost all of the low energy surfaces are lithium-deficient relative to the bulk lattice, requiring Li vacancies at the surface.

1.2.2.3 Delithiation mechanisms of $LiFePO_4$

The typical electrochemical profile of $LiFePO_4$ remained flat over a large compositional range, indicating that both the extraction and insertion reactions proceeded by the

motion of a two-phase interface. The second phase was identified to be orthorhombic $FePO_4$, which has the same space group as $LiFePO_4$ (Pnma). There is 6.8 % difference in the unit cell volume between these two phases. Initially, intercalation of Li into $FePO_4$ was proposed as a simple shrinking core model, in which lithium insertion proceeds from the surface moving the two phase interface. A critical phase boundary surface area may be reached where the rate of lithium transported across the interface is not able to sustain the applied current. Thus, ion transport becomes diffusion-limited. [230]

Nevertheless, the nature of Li^+ ion transport in $LiFePO_4$ is highly anisotropic. Furthermore, first-principles calculations show that the (010) surface has a lower potential (2.95 V) compared to bulk $LiFePO_4$ (3.55 V), suggesting that Li will be extracted from the (010) surface first upon charging the electrode material.[229] As the (010) surface is initially extracted and this facet is the terminus of the 1D Li channels in the material, the maximization of its surface area would be key to the optimization of $LiFePO_4$ electrodes.[231] Ethylene glycol was reported to be a structural directing agent to orient crystal growth and control $LiFePO_4$ size. The as-prepared $LiFePO_4$ nanoplates with large exposure of the (010) face exhibit low polarization, fine reversible capacity, good cycling performance and high rate capability. [231]

Moreover, partially oxidized $LiFePO_4$ large particles were shown to have ordered domains of $FePO_4$ situated between domains of $LiFePO_4$.[232] An electron energy loss spectroscopy (EELS) study on the O-K edge of a particle from a bulk sample delithiated to $Li_{0.45}FePO_4$ proved that the core of the particle comprised $FePO_4$, whereas areas of the particle closer to the surface are $LiFePO_4$.[233] At the interfaces between $FePO_4$ and $LiFePO_4$, linear combinations of the spectra from $LiFePO_4$ and $FePO_4$ were represented. As a consequence, it was proposed that the interface is in fact a concurrence of the two

phases and not a solid solution. On the basis of these observations, it was proposed Lgi^{+} and electrons are removed from the b-axis tunnels based on two factors: (1) the number of Li^{+}/electron pairs displaced by hopping: shortest and most empty tunnels should delithiate first, and (2) the energy gain due to the proximity of the growing $FePO_4$ nucleus, thus minimizing the area and number of grain boundary interfaces. As delithiation progresses, the $FePO_4$ core formed in the particle interior extends in the a-direction through the entire particle. The process is effectively reversed for the case of relithiation. Based on this mechanism, reduction of particle dimension is not only along the b-axis, but also along the a-axis which is critical for good electrochemical performance.

Delmas et al.[233] also studied the partial electrochemical delithiation of smaller particles (< 100 nm in diameter) prepared by solid state method. The results demonstrated that electrochemically delithiated individual particles have single phase. The phenomenon is totally different from the hydrothermal samples which exhibit clear regions of Li-rich and Li-poor phases.[232] On the basis of these observation and experience, it was thus concluded that when lithium extraction is nucleated, it proceeds very rapidly through the whole crystallite. After a Li_xFePO_4 region is nucleated and a phase boundary is formed in a "domino-cascade" fashion. The boundary moves rapidly along the a-axis of the Pnma crystal. However, because of the different potential of particles on this scale, it is conceivable that redox reactions between larger deintercalated particles and pristine nanoparticles within the positive electrode itself could account for the anisotropy of Li^{+} ion transport within these morphologies and possible nanosize effects.[234] The $LiFePO_4$ prepared by various methods generated a vast array of particle morphologies and inherent difficulty of imaging the small iron phosphate particle, underline the difficulty

in determining a single global model which can depicts the electrochemical performance of the $LiFePO_4$.

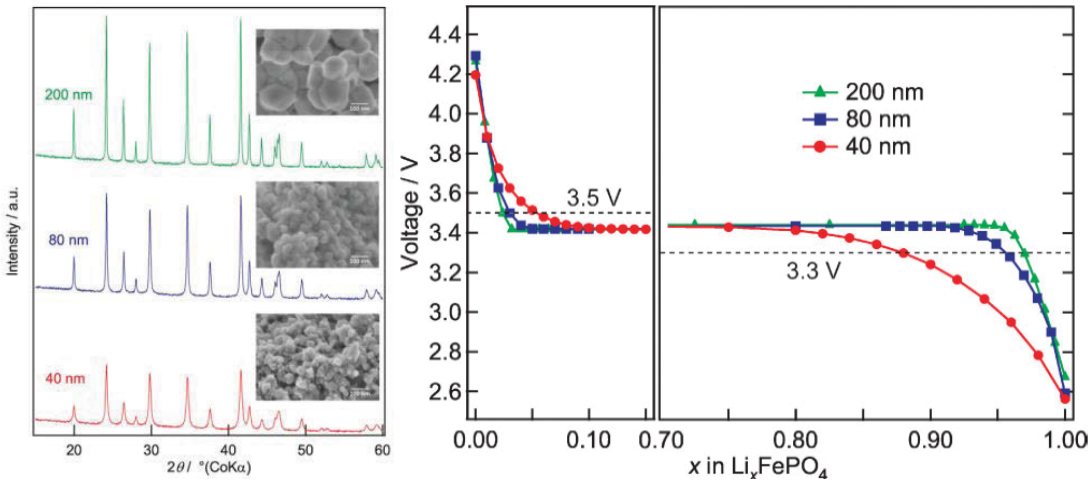

Figure 1-6 OCV curves measured for Li_xFePO_4 with various mean particles sizes of 200, 80, and 40 nm, showing the particle size dependence of the room-temperature miscibility gap.[235]

Large studies were proposed on the solid solution behaviour of the $LiFePO_4$. An early model predicted the existence of two single compositional regimes, $Li_{1-y}FePO_4$ and Li_xFePO_4, close in composition to the $LiFePO_4$ and $FePO_4$.[230] This point was later confirmed by X-ray diffraction studies on bulk oxidized $LiFePO_4$ particles.[236] Various compositions of the chemically olivine confirmed the presence of two phases: a Li-rich phase (unit cell volume of 290.7 $Å^3$), and a Li-deficient phase (unit cell volume of 272.6 $Å^3$). All fall in between pure $LiFePO_4$ (291.1 $Å^3$) and pure $FePO_4$ (271.9 $Å^3$).[236] Further neutron diffraction study on lithium content presents the miscibility gap to be narrower, $y = 0.11$ and $x = 0.05$.[235] This miscibility gap shorten with decreasing particle size: values of $y = 0.12$ and $x = 0.06$ are obtained for 40 nm particles, as shown in Figure 1-6.[235] When the $LiFePO_4$ particle size decreases to 34 nm, the values of y is 0.17 and x is 0.12.[237] Rietveld refinement revealed a significant amount of stress existing within the

Li-rich and Li-deficient regions, which accounts for the average bond lengths for Fe^{2+}-O and Fe^{3+}-O within each phase. There are no coherence stresses in the bulk particles. Wagemaker et al. claimed that the difference in lattice parameters of the two crystallographic phases coexisting within one particle results in a slight phase boundary energy penalty.[238] The two-phase coexistence in smaller particles becomes unstable due to the strain-induced energy, resulting in an increase in the phase boundary fraction in the particle volume. As a consequence, it will decrease the energetic benefits from phase separation for smaller particles and gradually narrow the miscibility gap for particles with decreasing size.

If the $LiFePO_4$ is exposured to air, it can induce the formation of Li_xFePO_4 solid solutions.[239] From X-ray diffraction and Mössbauer spectroscopy studies, it observed a reduction in the lattice parameters of the lithium-rich phase and Fe^{3+} after one day of air exposure at room temperature was observed. This effect is more obvious for particles less than 100 nm in size.

By a low-temperature precipitation method, Gibot et al. prepared highly defective $LiFePO_4$: $Li_{0.89}Fe_{0.96}PO_4$ (70 nm) and $Li_{0.79}Fe_{0.969}PO_4$ (40 nm).[240] There are substantial deviations between these and the typical olivine stoichiometry, as revealed by chemical analysis. The presence of Fe^{3+} in each of the samples was disclosed by Mössbauer measurements. 15 % of vacancies on the M1 site, and 10 % vacancies on the M2 site were observed by Rietveld analysis, which is commonly deficient under low temperature (below 120 °C) synthetic methods.[165] Although the Li channels were partially blocked by iron ions due to the 6 % anti-site mixing happening at Fe on the M1 site and only having a stoichiometry of 0.79 Li, the majority of the theoretical capacity of $LiFePO_4$ (82 %) was still achieved. The electrochemical curve had a sloping profile,

indicative of solid-solution behaviour in the material. More insight is needed into the role of defects, and the nature of ionic conductivity in this $LiFePO_4$-like material. So far it is still uncertain what the critical particle size is for the full removal of miscibility gap. The synthetic procedure plays a crucial role in the formation of lattice defects that may increase ionic conductivity in these materials and thus maybe addressed.

To overcome the low conductivity drawback, there are many studies on coating $LiFePO_4$ with carbon. Based on the comparison of different types of carbon produced from various organic additives, the performance of $LiFePO_4$ was improved with high sp2 carbon content, derived from organic compounds that contained a high percentage of sp2-hybridized carbon.[241,242] However, a thick carbon coating may be detrimental to electrode performance.[219] As well carbon reduces the volumetric energy density. Therefore, to keep high energy density with superior electrochemical performance, it is important to maximize conductivity and minimize carbon content.

Aliovalent cation doping of $LiFePO_4$ is another electrochemical performance enhancing strategy. The compounds of the type $Li_{1-x}M_x^{z+}FePO_4$ ($z \geq 2$), sintered at 800 °C, were found to have exceptional electronic conductivity, of more than 1×10^8 times higher than in pure $LiFePO_4$.[243] It was shown that iron valence was less than Fe^{2+}. Charge was compensated by Fe^{3+}, as the basis of the dramatic conductivity increase. The dopant was thought to reside on the lithium (M1) site and create additional lithium vacancies. This finding induced debates over the source of the increased conductivity and the sustainability of lithium vacancies in the structure. A subsequent study reveals that Zr and Nb-doped $LiFePO_4$ do not demonstrate good conductivity.[244] It is only when carbon is added, the conductivity can be increased. A further study by Delacourt et al. confirmed that Nb-doped $LiFePO_4$ can achieve high conductivity only when prepared

with high carbon content.[245] In addition, Nb was detected on the surface of the olivine particles as crystalline β-$NbOPO_4$, further questioning the validity of doping claims. Theoretical calculations further demonstrated that the accommodation of an aliovalent dopant on either the M1 or M2 site is highly unfavourable.[27,246] Based on energetics, there is also no evidence that a highly valent cation can occupy the M1 site. However, Wagemaker et al. combined X-ray and neutron diffraction data to demonstrate a preference of the dopant for occupying the M1 site, although the quantity of dopant in the lattice is much less than targeted.[247] Targeting the higher dopant concentrations will cause impurities to be clearly detected by diffraction. Most importantly, the refinements show the incorporation of the aliovalent dopant is balanced by lithium vacancies, resulting in the charge of the iron ion in the lattice to remain at +2, ruling out the presence of Fe^{3+} holes.

The nature of the dopant lattice site, doping limits, the resultant physical properties of $LiFePO_4$ has been rigorously debated. In addition, the presence of small quantities of immobile dopants in the lithium channels of $LiFePO_4$ (typically less than 3 %) would likely hinder lithium transport, also deteriorating the $LiFePO_4$ electrochemical performance, assuming 1D transport.

1.2.2.4 Other $LiMPO_4$ (M = Mn, V, Co) compounds

Some other $LiMPO_4$ (M = Mn, V, Co) compounds also were researched during last few years. Hereinto, the olivine $LiMnPO_4$ has a similar theoretical electrochemical capacity (170 mA h g^{-1}) with $LiFePO_4$, however $LiMnPO_4$ presents a higher voltage (4.1 V *vs.* Li^+/Li).[216] The flat voltage profile during both charge and discharge process of $LiMnPO_4$ suggests a reverse two-phase conversion process (the conversion between $LiMnPO_4$ and $MnPO_4$), to occur during the lithiation and delithiation process.

The challenge facing the $LiMnPO_4$ system is: I: very low electrical conductivity and II: structural distortions upon oxidation to $MnPO_4$ which hinder ionic transport. This is the reason why many initial electrochemical reports of the material show poor capacity as well as very poor reversibility.[248-250] Reducing particle size and carbon coating to improve surface conductivity are common strategies to improve its electrochemical property. Reduced particle size in sol-gel prepared $LiMnPO_4$ demonstrates improved electrochemical performance.[251] When the $LiMnPO_4$ particles exceptionally thin, < 30 nm in the b-direction, synthesised by polyol method,[251] it achieved a high rate discharge capacity (113mA h g^{-1} in 1 h) due to the short diffusion pathway of the Li^+ ions. Furthermore, this material demonstrated stable cyclability over 200 cycles. The Mn^{3+} ion did not degrade the material as was the case of the spinel $LiMn_2O_4$. Furthermore, the carbon coating on the particle surface, produced by the carbothermal reduction method, enhanced the surface conductivity and electrochemical performance of $LiFePO_4$; however, it was reported that carbothermal reduction of $LiMnPO_4$ is difficult because it only occurs at temperatures of ≥ 1000 °C.[252] At such high temperatures, the prepared $LiMnPO_4$ particle size is large and prohibit electrochemistry.[253] Another drawback of $LiMnPO_4$ is the much larger volume difference between $LiMnPO_4$ and $MnPO_4$ (9.5 %) compared with the Fe olivine.[254] Divalent cation substitution in $LiMnPO_4$ can reduce this volume difference between lithiated and delithiated phases. For instance, the difference can be reduced to 7.8 % for $LiMn_{0.9}Mg_{0.1}PO_4$. The presence of redox inactive magnesium maintains lithium ions in the delithiated phase.[254] Moreover, the magnesium also helps to stabilise the Jahn-Teller distortions of the delithiated phase. As a consequence, the substitution $LiMnPO_4$ can achieve improved electrochemical performance without the conductive additive.

Research has shown that when Li_xMnPO_4 is near full oxidation ($x < 0.2$) status, it will generate solid-solution behaviour.[255] The domains of the solid solution regime were determined to be < 45 nm, suggesting that many domains coexist within the same particle. Chemical delithiation of $LiMnPO_4$ resulted in small pores appearing on the surface of the particles and, unfortunately, the original morphology of as-prepared $LiMnPO_4$ were preserved.[256] The degradation of particle morphology clearly indicates poor ionic transport in $LiMnPO_4$, which results from a large lattice mismatch between the $LiMnPO_4$ and $MnPO_4$ phases and Jahn-Teller distortions. Furthermore, $MnPO_4$ phase could be easily dissolved due to the well-known disproportionation of $2Mn^{3+} \rightarrow Mn^{2+} + Mn^{4+}$. On the basis of above discussion, minimization of the lattice mismatch in $LiMnPO_4$, particle size reduction, and conductive surface coatings are crucial factor to optimising this promising material.

1.2.2.5 NASICON type cathode materials

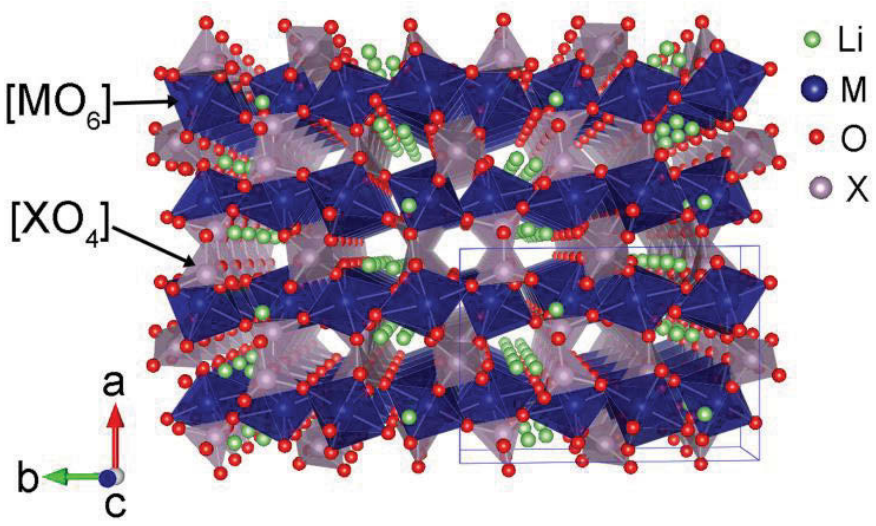

Figure 1-7 Crystal structure of $Li_3M_2(XO_4)_3$.

The NASICON type material is potentially promising cathode material for Li-ion batteries. It is a family of compounds with a $A_3M_2(XO_4)_3$ (A = Alkali cations, M =

transition metal, X = P, Si, As, etc.) framework made up of a XO_4 tetrahedron sharing corners with MO_6 octahedrons and vice versa as shown in Figure 1-7. The $M_2(XO_4)_3$ host framework is chemically versatile; it can be stabilised with a variety of transition metal cations M and XO_4 polyanions. Such framework oxides have been known to undergo topotactic insertion/extraction of a mobile atom[257-260] and therefore are candidates as electrode materials for rechargeable batteries. The open structure of $M_2(XO_4)_3$ supports fast Li ionic conduction and allows up to at least four Li cations per formula unit in the interstitial space. The NASICON framework is thus a promising host for Li battery cathodes. However, this framework structure with a large interstitial space tends to be unstable if the large cations that form are replaced by smaller Li^+ ions. On the other hand, the NASICON $M_2(XO_4)_3$ framework is capable of receiving reversibly up to 5 Li atoms and the $M_2(PS_4)_3$ framework of $AgTi_2(PS_4)_3$ has been shown to accommodate up to 10 Li atoms;[261 262] although reduction of the PS_4 groups and the Ti^{4+} to Ti destabilises the framework. Moreover, $LiV_2(PS_4)_3$ dissolves in the electrolyte $LiPF_6$ in EC/DEC. So the host must be stable in the electrolyte.

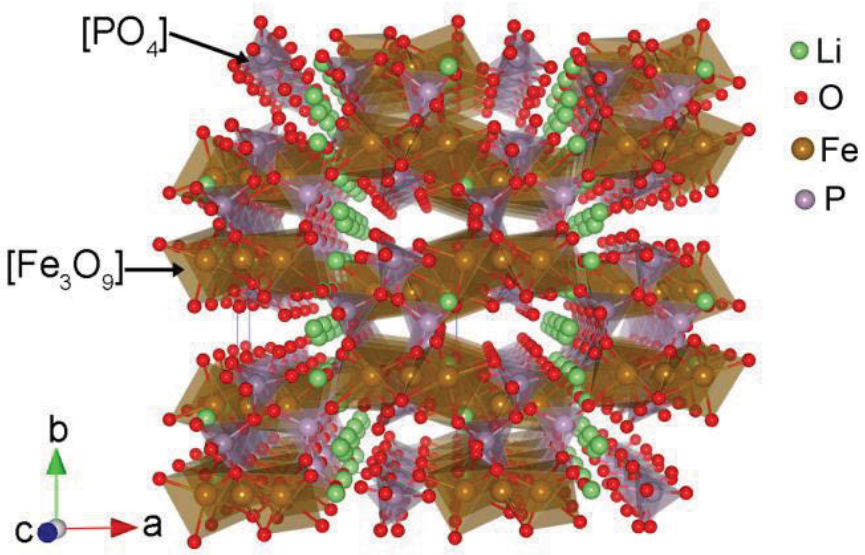

Figure 1-8 Crystal structure of pyrophosphate ($Li_2FeP_2O_7$).

1.2.2.6 Pyrophosphate

Recently, pyrophosphate ($Li_2FeP_2O_7$), as shown in Figure 1-8,[263-265] and related compounds[266-268] have been proposed as new electrode materials, because $Li_2FeP_2O_7$ is easy to synthesize by a conventional solid-state reaction and displays reversible electrode operation at 3.5 V *vs.* Li/Li^+ without nanosizing or carbon coating. The chemical composition of $Li_2MP_2O_7$ allows for the possibility of a two-electron reaction where the theoretical capacity could reach 220 mA h g^{-1}.[269] Islam and Yamada et al.[269] used a combination of neutron diffraction and atomistic simulation techniques to provide a systematic survey into the crystal structure, defect chemistry, and Li^+ ion migration pathways of the $Li_2FeP_2O_7$ cathode material. They found that the stoichiometric $Li_2FeP_2O_7$ has a monoclinic structure with $P2_1/c$ space group. The simulations suggest that the most favourable intrinsic defect of $Li_2FeP_2O_7$ is the Li/Fe antisite, especially for the mixed-occupied sites (Li4/Fe2 and Li5/Fe3), which would be sensitive to synthesis conditions. In the crystal, Li^+ ion diffusion is predicted to occur through a 2D network in the bc-plane following curved paths via Li1/Li3 sites. $Li_2FeP_2O_7$ shows low migration energies (0.40 eV). Therefore, compared to 1D diffusion in $LiFePO_4$, fast 2D Li^+ ion transport in $Li_2FeP_2O_7$ is important for achieving good rate capability and for the function of particles without nanosizing. The results suggest that synthetic approaches to minimize Li/Fe mixed-occupied sites would enhance the diffusion pathways. The practical capacity of $Li_2FeP_2O_7$ is limited to a one-electron theoretical value of approximately 110 mA h g^{-1}.

1.2.3 Silicates

Within the family of $(XO_4)^{n-}$ polyanion compounds, orthosilicates Li_2MSiO_4 (where M^{+2} is a transition metal) have been considered as attractive cathode materials due to

their potential ability to extract more than one Li^+ ion per formula.[270-273] These silicates crystallize in various polymorphs, all of which are structurally similar to β-Li_3PO_4[274] or γ-Li_3PO_4[275] where all the cations occupy tetrahedral sites. One typical material belonging to this group is Li_2FeSiO_4, which was found in 2003. Lithium ions were extracted and inserted reversibly according to the reaction[276]:

$$Li_2FeSiO_4 \leftrightarrow LiFeSiO_4 + Li^+ + e^- \quad (1\text{-}2)$$

This gives a theoretical capacity of 166 mA h g^{-1}, which is very close to that of $LiFePO_4$. Many of the positive attributes of $LiFePO_4$ also apply to Li_2FeSiO_4, especially the low cost of raw materials and environmental acceptability. Furthermore, this type of material generally allows a wide range of solid solutions with various compositions. Therefore, Li_2FeSiO_4 presents an exciting platform to explore new cathode materials for next generation high power Li-ion batteries. While there is a problem of low electronic conductivity for Li_2FeSiO_4 as with $LiFePO_4$, the same approaches used for $LiFePO_4$ may be applied to develop full utilisation of Li_2FeSiO_4 cathodes.

Although Li_2FeSiO_4 has been successfully synthesised by various techniques,[277-282] its crystal structure is still not completely clear. Nytén et al. performed Rietveld refinements on a conventional powder X-ray diffraction profile of pristine Li_2FeSiO_4 and suggested a β-Li_3PO_4-based structure with $Pmn2_1$ symmetry. In this proposed structure, all the cations occupy half of the tetrahedral sites in a slightly distorted hcp oxygen array, forming a corner-sharing network of tetrahedron with an identical upward direction. Li^+ ions occupy tetrahedral sites in between layers comprising chains of alternating corner-shared FeO_4 and SiO_4 tetrahedron, which run in the a-direction. This structural model has been used by many other research groups. Furthermore, most of the first principle calculations on Li_2FeSiO_4 were based on the

β-Li_3PO_4 structure.[283] Wu et al.[284] investigated structural stabilities, electronic structures and lithium deintercalation in Li_xMSiO_4 (M = Mn, Fe, Co, Ni) based on the $Pmn2_1$ symmetry structure using GGA and GGA+U study. They suggested that the structural stability of Li_2MSiO_4 is a consequence of the strong covalent Si-O bonding in the SiO_4 tetrahedron, which is similar to the P-O bond in the phosphate. Li_2MSiO_4 materials with M = Fe, Co and Ni (which undergo large volume expansion when Li^+ ions are extracted) would be unlikely to reversibly extract both two Li^+ ions per formula unit, although the electronic conductivity is enhanced during the process of delithiation. $LiMSiO_4$ is shown to be a stable non-stoichiometric structure, while the compound $Li_{1.5}MSiO_4$ is unstable relative to a two-phase form containing Li_2MSiO_4 and $LiMSiO_4$. For $Li_{0.5}MSiO_4$, though the formation energies are negative for a Mn-system and Ni-system, although the absolute values are so small that they would be likely to also undergo phase separation at room temperature. It was also reported that $LiMSiO_4$ (M = Mn, Fe, Co and Ni) and $CoSiO_4$, are both semiconductors, however, $MnSiO_4$, $FeSiO_4$ and $NiSiO_4$ are shown to be spin-polarised half metals. J. O. Thomas' group completed a series of studies on Li_2FeSiO_4 by the density functional theory (DFT) calculations based on the $Pmn2_1$ symmetry structure, including three possible Li arrangements in the delithiated structure ($LiFeSiO_4$) and their corresponding voltages, possible Li^+ ion migration pathways, and diffusion barriers for Li^+ ions.[285] They concluded that the Li/Fe site-mixing observed during the electrochemical cycling of Li_2FeSiO_4 does not lead to any noticeable loss in performance. The Li/Fe site-interchange does not increase the activation barriers of Li vacancy. Instead, it opens alternative pathways allowing 3D percolation of the corner-sharing tetrahedral sites available for Li^+ ion migration. They further reported the structural and electrochemical aspects of Mn

substitution into Li_2FeSiO_4,[286] indicating that capacity increase in $Li_2Fe_{1-y}Mn_ySiO_4$ through > 1 Li^+ ion per formula unit redox reaction may not be so readily attainable in practice, either for high or low Mn concentrations.

Shin-ichi Nishimura et al. recently indicated elaborate three major problems associated with the $Pmn2_1$ structure for Li_2FeSiO_4. They adopted a $P2_1$ symmetry with a monoclinic super cell with respect to the systematic extinction and observed reflections, which has been confirmed by the powder HR-XRD and SAED patterns along various zone axes.[287]

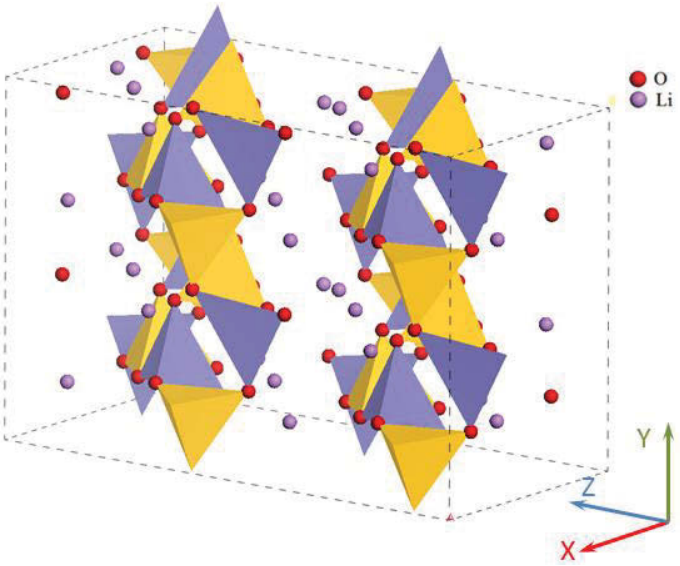

Figure 1-9 Crystal structure of Li_2FeSiO_4 based on $P2_1$ symmetry with a monoclinic super cell.

Figure 1-9 shows the crystal structure of Li_2FeSiO_4 based on the $P2_1$ symmetry. The structural modulation leads to variation in the orientation of trigonal pyramids, particularly those in the corner-shared one-dimensional FeO_4 and SiO_4 chains along the $[\bar{1}01]$ direction. In detail, in the $P2_1$ model, FeO_4 and SiO_4 trigonal pyramids periodically take opposite orientations. It is strikingly contrasted to the previous

orthorhombic Pnma model, where the orientations of all trigonal pyramids are identical. N. Kuganathan and M. S. Islam[288] examined both monoclinic and orthorhombic polymorphs of Li_2MnSiO_4. As reported, the most favorable intrinsic defect type is found to be the cation anti-site defect, in which Li and Mn ions exchange positions, and the differences in the intrinsic Li mobility between the monoclinic and orthorhombic polymorphs would affect their rate capability as rechargeable electrodes. They also discussed curved Li diffusion paths and confirmed the anisotropic nature of Li transport, which can probably be general used for the Li_2MSiO_4 (M = Mn, Fe, Co) family of compounds. Zhong et al.[289] investigated the delithiated transition metal (Mn, Fe, and Co) orthosilicates based on the $P2_1$ symmetry structure and indicated that the fully lithiated compounds are all stabilised in their ferromagnetic phase, while the delithiated compounds are all stabilised in the antiferromagnetic phase. Compared with $Pmn2_1$, the fully delithiated $MSiO_4$ with $P2_1$ structure has better stability. Li_2MSiO_4, delithiated $LiMSiO_4$ and $MSiO_4$ are all semiconducting, and the band gap lowers with the extraction of Li^+ ions. In Li_2FeSiO_4, the possibility of reversibly extracting more than one Li^+ ion is enhanced because of the lower stability of the intermediate phase $LiFeSiO_4$ compared with the $Pmn2_1$ symmetry situation.

Li_2FeSiO_4 had a 3.10 V *vs.* Li initial potential, while subsequent charges were at 2.84 V *vs.* Li/Li^+. A reversible capacity of 140 mA h g^{-1} was displayed over 8 cycles.[276] The decrease in voltage indicated a structural rearrangement after the first cycle induced from Li and Fe site exchange occurred.[290] The high voltage of the initial charge was later determined to be a result of an impurity, as pure Li_2FeSiO_4 will deintercalate at a voltage of 2.8 V.[291]

The isostructure of the Li_2FeSiO_4 compound, Li_2MnSiO_4, is found to have a high redox potential near 4.0 V *vs.* Li/Li^+.[270] However this material shows substantial irreversible capacity loss, even when coated with carbon.[270,292] The poor performance of Li_2MnSiO_4 a result of amorphization of the delithiated manganese silicate.[293] Thermodynamic stability of four Li_2MnSiO_4 polymorphs can be synthesized at various temperatures and pressures, which was predicted by the calculations.[294]

1.3 Anode materials for Li-ion batteries

Graphite or carbon-based materials are among the most attractive anode materials for commercial Li-ion batteries.[295] The main reasons for this are good cycling performance for carbonaceous materials and low cost. Graphite can accommodate up to one lithium atom per six carbon atoms in forming the compound LiC_6. This gives a gravimetric capacity of 372 mA h g^{-1}.[296] Single layer graphene synthesised by Novoselov et al. opened new avenues for the field of secondary rechargeable batteries because of its remarkable storage capacity for lithium ions,[297-300] promoting the lithium ion storage capacity to 784 mA h g^{-1}.[301] This characteristic can be attributed to its strictly two dimensional, flat, and single-layer structure where lithium ions can be adsorbed on both sides of its surface equally, forming a LiC_3 compound. The interaction between lithium ions and graphene has been investigated theoretically by several groups.[302-307]

1.3.1 Transition metal compounds based on the conversion reaction

Increasing interest in large-scale applied energy storage technique and aspiring the alternative power sources for electric vehicles, brought a new reactivity concept with the reversible electrochemical reaction of lithium with transition metal compounds

(conventionally generalized referred to as "conversion reaction") attention. It can transfer two-six electrons,[308,309] according to the reactions as follows:

$$M_aX_b + (b \cdot n)\ Li \leftrightarrow aM + bLi_nX \qquad (1\text{-}3)$$

Where M = transition metal, X = anion, and n = formal oxidation state of X.[310]

Before being extensively studied, many transition metal compounds that do not have any vacant sites in the structure were disregarded because of the impossibility of intercalating lithium. It was not until it was proven that several oxides can deliver stable gravimetric capacities as much as three times that of carbon that these phases were considered as promising alternatives in rechargeable batteries. These brand new anode materials can reach markedly high specific capacities of more than 600 mA h g^{-1} due to more than two electrons transferring. Therefore, the "conversion reaction" concept has now become a strategy. It must be noted that the conversion reactions are not limited to the oxides, they can extend to the sulphides, nitrides, fluorides, phosphides, and even H has boomed with different degrees of reversibility.[311-314] The key to the reversibility of the conversion reaction was proposed to depend on the formation, and complete reduction of the metal embedded into the decomposition of the matrix of the lithium binary compound (Li_nX) when a reverse polarization is applied.[315] The actual potential at which conversion occurs to depends on both the transition metal and the anionic species (Table 1-3), so that, in principle, the reaction potential can easily be tuned to the application requirements.[316] This is an important part of consideration.

Table 1-3 Experimental values of potential for the plateaus associated with conversion reactions in binary transition metal compounds, M_aX_b.[310]

	X = O		X = S		X = N		X = P		X = F	
	Phase	E_{conv}/V	Phase	E_{conv}/V	Phase	E_{conv}/V	Phase	E_{conv}/V	Phase	E_{conv}/V
M = Ti									TiF_3	0.95[317]
M = V									VF_3	0.4[317]
M = Cr	Cr_2O_3	0.2[318]	CrS	0.85[319]	CrN	0.2[320]			CrF_3	1.8[c][321]
M = Mn	MnO_2	0.4[322]	MnS	0.7[323]			MnP_4	0.2[d][324]		
	Mn_2O_3	0.3[325]								
	MnO	0.2[326]								
M = Fe	Fe_2O_3	0.8[327]	FeS_2	1.5[328]			FeP_2	0.3[329]	FeF_3	2.0[c][330]
	Fe_3O_4	0.8[331]	FeS	1.3[332]	Fe_3N	0.7[333]	FeP	0.1[329]		
	FeO	0.75[296]								
M = Co	Co_3O_4	1.1[334]	CoS_2	1.65-1.3[b][335]	CoN	0.8[336]	CoP_3	0.3[337]	CoF_2	2.2[c][338]
	CoO	0.8[334]	$Co_{0.92}S$	1.4[319]	Co_3N	1.0[333]				
			Co_9S_8	1.1[339]						
M = Ni	NiO	0.6[296]	NiS_2	1.6[340]	Ni_3N	0.6[341]	NiP_3	0.7[342]	NiF_2	1.9[c][338]
			NiS	1.5[343]			NiP_2	0.5-0.3[b][344]		
			Ni_3S_2	1.4[345]			Ni_3P	Slope[a][346]		
M = Cu	CuO	1.4[347]	CuS	2.0-1.7[b][348]	Cu_3N		CuP_2	0.7[349]	CuF_2	3.0[350]
	Cu_2O	1.4[351]	Cu_2S	1.7[352]			Cu_3P	0.8[353]		
M = Mo	MoO_3	0.45[354]	MoS_2	0.6[355]						
	MoO_2	Slope[a][356]								
M = W			WS_2	0.8-0.6[b][357]						
M = Ru	RuO_2	0.9[358]								

[a] Slope indicates the absence of distinct voltage plateau in the electrochemical profile.

[b] Two plateaus were observed in the electrochemical profile.

[c] Data collected for nanocomposites with carbon at 70 °C.

[d] Conversion of Li_7MnP_4 to Li_3P and Mn.

In contrast to the intercalation mechanism that occurs in graphite, the transition metal compounds are reduced in a conversion reaction to small metal clusters leading to large volume expansion and destruction of the structure upon electrochemical cycling, especially at high rates, and experience poor capacity sustainability on cycling that prohibits their practical applications.[359,360] Several other issues present these compounds from use in commercial applications, such as an unacceptable, round-trip energy density loss, in the large voltage hysteresis that is observed between the discharge and charge step. Furthermore, a virtually ubiquitous large Coulombic inefficiency observed in the first cycle is also a drawback. Hence, despite the promise of this concept and the progress that has been made since it was first proposed, several fundamental obstacles to making these materials a viable alternative remain. Consequently, optimising particle size and mixing the particles with various carbon additives have been employed to improve the reversible capacity and rate capability of metal oxide electrodes.[361-365]

1.3.1.1 Manganese oxide

Among the transition metal compounds, the oxides, unsurprisingly, attracted the majority attention. Among the vast numbers of binary transition metal oxides, MnO_2 has the highest theoretical capacity, 1233 mA h g^{-1}.[310] However, this did not attract research interest, possibly because manganese is the most difficult to reduce into a metallic state among the 1st row transition metals.[366]

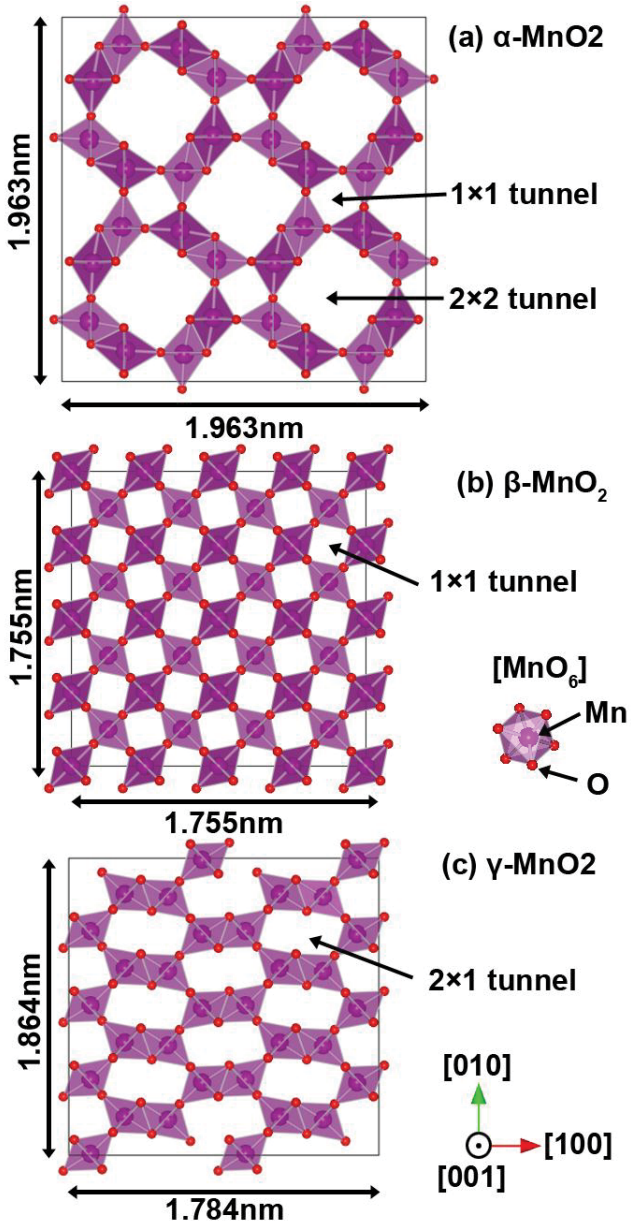

Figure 1-10 Crystal structure of the polymorph MnO_2 (a) α-MnO_2, (b) β-MnO_2, and (c) γ-MnO_2.

There is a long voltage plateau observed around 0.4 V for the first MnO_2 reduction process by lithium, followed by a sloping region, which is commonly expected to ascribed to the lithium insertion in MnO_2.[367] This might be related to the special tunnel structure existing in all the MnO_2 polymorphs since the MnO_6 octahedral units can be linked in different ways,[368] which can provide spare space to allow lithium insertion (as

shown in Figure 1-10). α-MnO_2 is constructed from the double chains of edge-sharing MnO_6 octahedron that are linked at the corners to form (2 × 2) + (1 × 1) tunnel structure (Figure 1-10 a), while β-MnO_2 shows 1D channel (1 × 1) structure composed of individual chains of the MnO_6 octahedral units (Figure1-10 b). β-MnO_2 is more stable phase compare with α-MnO_2, and the β-MnO_2 with its compact (1 × 1) tunnel is more readily than the α-MnO_2 in the absence of a big guest cation. γ-MnO_2 presented with 1D channel (2 × 1) tunnel along c-axis, as shown in Figure 1-10 c. It has been reported that γ-MnO_2 can achieve large capacities, well above 1000 mA h g^{-1} and, in some cases, close to 2000 mA h g^{-1}, upon the first reduction by lithium.[369,370]

Some other manganese oxides, such as Mn_3O_4,[371,372] MnO,[373,374] and Mn_2O_3[325,371] all achieved first reduction capacities higher than 1000 mA h g^{-1}. However, all the samples demonstrate rather low Coulombic efficiencies in the first cycle and rapid capacity decays with cycling. The better results reported are 600 mA h g^{-1} after 100 cycles for a γ-MnO_2 film deposited on nickel metal[369] and after 150 cycles for MnO powder.[374] Until now few studies have focused on the reaction mechanism of manganese oxides. Both X-ray diffraction (XRD) patterns acquired after the reduction of MnO in a molten salt cell at 400 °C[311] and Li 1s and Mn 2p X-ray photoelectron spectroscopy (XPS) results for γ-MnO_2 electrodes[369] are consistent with the presence of Mn and Li_2O. Electrochemical reduction for Mn^{2+} to Mn for $Mn_{0.6}Mo_{0.8}V_{1.2}O_6$ has also been proven by X-ray absorption spectroscopy (XAS).[375] According to the analysis of electron energy loss spectroscopy (EELS) data on β-MnO_2 and electron diffraction (ED), the manganese is indeed not completely reduced and that $LiMn_3O_4$ is formed upon discharge down to 0 V.[376] Since the formation of such an oxide cannot explain the huge capacity of 1600 mA h g^{-1} observed for this process, an alternative mechanism of interfacial storage is speculated.

1.3.1.2 Iron oxide

Among the transition metal oxides, iron oxides are no doubt are the most attractive candidate due to their environment-friendly, low cost, and abundant supply features. Magnetite (Fe_3O_4) has a high theoretical reversible capacity (926 mA h g^{-1})[377] when discharging to 0 V *vs.* Li metal. This is because one Fe_3O_4 can react with about eight lithium ions. It is therefore considered as one of the most promising electrode materials.[378,379] Nevertheless, Fe_3O_4 anode materials also have poor cyclic performance owing to agglomerations and huge volume changes of active materials during lithium insertion/extraction. Several strategies to reduce this problem have been pursued, including the preparation of nano-architectured materials and core-shell structured materials: Taberna et al. fabricated the self-supported Fe_3O_4/Cu nano-architectured electrodes and demonstrated a factor of improvement in power density over planar electrodes while maintaining the same total discharge time.[380] Wang et al. prepared C/Fe_3O_4 composite nano-fibers by electro spinning and subsequent carbonisation processes, which exhibits superior electrochemical performance with a high reversible capacity of 1007 mA h g^{-1} at the 80th cycle and excellent rate capability.[381] Liu et al. synthesised carbon coated nano-rods magnetite, with an initial lithium storage capacity of 1120 mA h g^{-1} and a reversible capacity of 394 mA h g^{-1} after 100 cycles.[379] Kim et al. have demonstrated that Fe/Fe_3O_4 core-shell nanostructure electrodes can release a reversible capacity of about 600 mA h g^{-1} after 50 cycles.[382] Guo et al. synthesised Fe_3O_4 nano-crystals@C composite that can exhibit 600 mA h g^{-1} (around 30 cycles).[378] Zhang et al. reported that carbon-coated Fe_3O_4 nano-spindles were synthesised by partial reduction of mono dispersed hematite nano-spindles with carbon coatings. This showed high reversible capacity in the first cycle (745 mA h g^{-1} at C/5 and 600 mA h g^{-1} at C/2), as well as significantly enhanced cycle performance and high rate capability.[383]

Banov et al. prepared the nano-size Fe_3O_4/carbon composites, whose reversible capacity was measured in the range 400 - 550 mA h g^{-1} in the 15th charge/discharge cycle.[384]

Hematite (α-Fe_2O_3) is also a stable iron oxide under ambient conditions, and has non-toxicity, low cost, high resistance to corrosion and environment-friendly features, with 1007 mA h g^{-1} theoretical capacity. The performance of α-Fe_2O_3 strongly depends on the particle size, morphology, and structure.[364,385,386] α-Fe_2O_3 with one-dimensional nanowire/nanotube structures,[387,388] two-dimensional flake/film structures,[389,390] and three-dimensional hollow/porous structures[391] have already been synthesised by a variety of methods, such as the sol-gel method,[392] electrostatic spray deposition,[393] hydrothermal treatment[394,395] and template method.[388,396] All obtained improved electrochemical performance. In addition, porous structure can generate a high rate specific capacity and good cycling stability, and reversibility of lithium intercalation for use as an anode material in Li-ion battery. Therefore, many strategies have been explored to prepare α-Fe_2O_3 with porous or hollow nanostructures, including the hard templates method, using porous alumina,[387] carbon nanotubes,[397] and porous silica,[398] or surfactants (sometimes called soft templates)[399] as template. Suslick et al[399] produced an iron/carbon composite by first using ultrasound to create a mixture of carbon nano-particles and iron pentacarbonyl in hexadecane, and then obtained hollow hematite particles by elaborately controlling the oxidation of the resulting composite. Xu and co-workers[400] prepared α-Fe_2O_3 hollow nanospheres by controlled precipitation of Fe^{3+} with urea in the presence of carbonaceous saccharide nanospheres as hard templates. However, the template-direct synthesis suffers from the disadvantages of low yield and high cost. As an alternative route, template-free solution-based synthetic methods have also been reported as preparation methods for porous α-Fe_2O_3 nanostructures,[401,402] such as nanotubes, nanorings, and porous nanorods. In this case, the presence of some

inorganic salts, such as $NH_4H_2PO_4$, Na_2SO_4, Na_2SO_3, NH_4Cl, KCl, etc, is a prerequisite. In addition, the sort and amount of additives, as well as other experimental parameters, must be carefully selected and controlled. Therefore, it still remains a challenge to develop a facile approach to synthesise α-Fe_2O_3 porous or hollow structures.[403-407]

1.3.1.3 Cobalt oxide

Cobalt oxides (CoO and Co_3O_4) are also most explored transition metal oxides as anodes in Li-ion batteries due to their high theoretical capacity (715 and 890 mA h g^{-1}, respectively). They will form metallic Co and Li_2O with lithium metal, which was observed in earlier studies,[408,409] but it was not until the report of the high degree of cyclability of the conversion reaction in 2000[296] that intensive efforts to evaluate the performance of these phases were triggered. Several authors have now shown that CoO can efficiently re-form after one or more full discharge-charge cycles between 0 and 3 V, albeit in a nanometric state regardless of the microstructure of the initial samples.[296,410-413] Particular significance is that this phase can be cycled up to a hundred, even a thousand, times at high rates with very good capacity retention values.[315]

The performance has now been evaluated for Co_3O_4 prepared in powder form with controllable microstructures through diverse methods, such as hydrothermal[414,415] and solvothermal[416] methods, ultrasound-assisted nanocasting fabrication,[417] solid state,[418] microwave-assisted reflux method,[419] precursor conversion processes,[420] and chemical vapour deposition synthesis routes.[421] Various morphologies including 3D structure: nanocubes,[420,422] nanodisc,[420] sphere,[423,424] 2D structure: nanobelts,[425] nanosheets,[426] and 1D structure: nanotubes,[427,428] nanowires,[429-431] and nanorods[431,432] have been prepared directly targeting improvements in electrochemical properties.

The mechanism of Co_3O_4 as anode material for Li-ion battery has also been discussed in recent years. It was found that depending on the crystallite size and surface area of Co_3O_4, and the applied current, the electrochemical reaction with the first 1or 2 moles of lithium can proceed through insertion to form $Li_xCo_3O_4$ (small domains and/or low current densities) or through the conversion to Li_2O and CoO (large domains and/or high current densities),[433,434] which, upon further reduction, indistinctively decompose into Co and Li_2O.[429,435-437] However, a unique path is generally observed upon oxidation of the nanometric composite, generally appearing to lead to the partial oxidation of cobalt to form CoO, which becomes the active material upon further cycling, instead of Co_3O_4.[429,434,435,437,438]

1.3.1.4 Nickel oxide

Spinel NiO has also been reported as an available anode for reversible electrochemical conversion into Ni and Li_2O.[439,440] After several cycles of NiO powder samples, close to theoretical capacity (718 mA h g^{-1}) values have been achieved.[441,442] Even more outstanding high rate performance of NiO on the mesh substrates have been reported, which demonstrate 700 mA h g^{-1} capacity after 20 cycles at rates as high as 10 A g^{-1} due to the reticular design of the electrode.[443]

As discussed above, the specific capacity and cycling performance of NiO electrodes are also closely related to its morphology and microstructure. Therefore, great efforts have been devoted towards the synthesis of NiO with controllable complex morphologies and hierarchically porous structures:[10] such as single crystalline NiO nanoflakes,[444] NiO nanotubes,[7,445] concave polyhedron shaped NiO,[446] NiO hollow spheres.[447] Moreover it was reported that mesoporous NiO nanowire electrodes delivered a capacity of 435 mA h g^{-1} at 1 A g^{-1}.[9] Hierarchically ordered porous NiO

array film[448] delivered 518 mA h g^{-1} specific capacity after 50 cycles at 0.7 A g^{-1} current density, maintaining 72 % of the theoretical capacity. Porous NiO film prepared by chemical bath deposition exhibited even higher coulombic efficiency and weaker polarization and its specific capacity after 50 cycles was 490 mA h g^{-1} at the 0.5 A g^{-1}, and 350 mA h g^{-1} at 1.5 A g^{-1}.[449] Two-layer porous NiO film is found to sustain and deliver 570 mA h g^{-1} at 70 mA g^{-1}, 501 mA h g^{-1} at 350 mA g^{-1}, and 409 mA h g^{-1} at 1.4 A g^{-1} after 50 cycles, corresponding to 79 %, 70 %, and 57 % of the theoretical value, respectively, demonstrating the capability for a high cycling rate.[11] Sandwich-like NiO film electrode after 50 cycles has 400 mA h g^{-1} capacity at a discharge current density of 1.4 A g^{-1}.[446] NiO nanocone arrays were fabricated by a two-step approach which can deliver a capacity up to 1058 mA h g^{-1} after 100 cycles at 0.3 A g^{-1} and a capacity higher than 436 mA h g^{-1} even at a current density as high as 15 A g^{-1}.[6] The presence of monodispersed open macropores in the nickel-oxide film might facilitate the electrolyte penetration, diffusion, and migration. [8]

Recently, research on NiO anode materials have focused on how to improvements to the cycling stability. For example, many strategies have emerged, forming composites with conductive materials such as metals and carbon can remarkably improve the conductivity of active materials, facilitate the lithiation and delithiation process, and meanwhile buffer the volume changes to alleviate the pulverization of active materials.[450] Following this strategy, many studies focused on the self-supported nickel-coated NiO or NiO directly grown on the foam Ni. The Ni particles in the composites provide a highly conductive medium for electron transfer during the conversion reaction of NiO with Li^+ and facilitate a more complete decomposition of Li_2O during charge with increased reversibility of conversion reaction. For instance, nanocrystalline and mesoporous NiO film was formed based on the nickel mesh via self-template method,

in which frameworks of the nickel mesh and mesopores of NiO film filled with electrolyte provide ideal electrolyte and Li^+ ion paths. The nickel wires with low resistivity play a role in the electronic path. Moreover, the high surface area of the NiO film reduces the required diffusion length in the active materials and the effective specific current density. The resultant NiO anode achieved high specific capacities (695 mA h g^{-1}) at high current densities (10 A g^{-1}).[451] Nickel-coated NiO arrays prepared by chemical bath deposition of NiO flake arrays followed by magnetron sputtering of nickel nanoparticles delivered a reversible capacity of 455, 316 and 187 mA h g^{-1} at a current density of 2, 4 and 7.18 A g^{-1}, respectively, higher than the bare NiO array electrode.[452] Nanoporous NiO films directly grown on the foam Ni, fabricated via a facile ammonia-induced route, exhibit an outstanding rate capacity of 280 mA h g^{-1} at 7.18 A g^{-1} current density and high reversible capacity of 543 mA h g^{-1} after 100 cycles at 1 A g^{-1} current density.[12] The nickel foam-supported porous NiO-Ni nanocomposite synthesised by electrostatic spray deposition (ESD) technique exhibited improved cycle performance as well as good rate capability.[453] 3D structured foam NiO anode was also prepared by simple solid phase oxidation method with Ni foam as the substrate and metal nickel sources.[454] Electrochemical testing obtained a high capacity of 950 mA h g^{-1} at 1.5 A g^{-1} current density was obtained, with excellent capacity retention of up to 40 cycles.[455]

Other metals have been also attempted as a vconductivity improvement method, like Ag and Co. NiO/Ag film was prepared by loading the NiO film with Ag nanoparticles. The specific capacity after 50 cycles for the NiO/Ag film is 550 mA h g^{-1} at 0.5 A g^{-1}, 450 mA h g^{-1} at 1.5 A g^{-1}, and 420 mA h g^{-1} at 3 A g^{-1}.[456] Co-doped NiO nanoflake arrays with a cellular-like morphology were fabricated by low temperature chemical bath deposition, which results in a capacity of 600 mA h g^{-1} after 50 discharge/charge cycles

at low current density of 100 mA g^{-1}, and it retains 471 mA h g^{-1} when the current density is increased to 2 A g^{-1}. [457]

The metal-coated NiO array electrode, however, suffers from a large voltage hysteresis, indicating that the enhanced electronic conductivity is not effective on decreasing this hysteresis. Therefore, carbon coating NiO, or carbon and NiO composites have emerged as a new strategy to improve the electrochemical performance. So far different carbons have been tried. The specific capacities of the porous NiO/C microspheres after 10 cycles at 0.1, 0.5, 1, and 3 A g^{-1} are about 698, 608, 454 and 352 mA h g^{-1} respectively.[10] Mesoporous carbon-encapsulated NiO nanocomposite presented a charge capacity of 808 mA h g^{-1} at a C–rate as high as 3.2 A g^{-1} owning to the contribution of NiO nanoparticles in CMK-Ni, which shows excellent rate capability for NiO, with utilization close to 100 %. The result suggests fast kinetics of conversion reaction for NiO with Li^{+}. [458] The functionalized graphene sheets-NiO composite sample exhibits a high capacity of about 700 mA h g^{-1} at a discharge current density of 100 mA g^{-1} and a good cycling ability due to advantageous combination of the highly conductive graphene, which provides a sufficient electrode/electrolyte contact area and facilitates fast and continuous conducting pathways for electrons through the electrodes during the lithiation/delithiation process.[459] [460] NiO nanosheets grown on graphene nanosheets[461] have a large initial charge capacity of 1056 mA h g^{-1} at 0.7 A g^{-1}, which decreased by only 2.4 % to 1031 mA h g^{-1} after 40 cycles. NiO/MWCNT composites also were considered to be potential electrode material for Li-ion batteries. The lithium storage properties could be maintained at ~800 mA h g^{-1} after 50 discharge/charge cycles at a constant current density of 50 mA g^{-1}.[462]

1.3.1.5 Copper oxide

CuO was already well known to the lithium battery community in the 1980s as an attractive electrode for primary cells.[463] So far plenty studies on the optimization of the performance of these devices have been reported.[464-466] Like the other transition metal oxides, both CuO and Cu_2O are proven to transform into Cu nanoparticles and amorphous Li_2O matrix when reduced by lithium.[351,467-469] It has been found that after a full discharge-charge cycle, certain cycling inefficiencies have been observed for CuO, which result in the presence of Cu_2O.[468] This phenomenon is quite similar to what has been described for Co_3O_4, which CoO will be generated after first discharge cycle. The capacities that are close to theoretical have indeed been obtained by several research groups after several tens of cycles using Cu_2O instead.[296,467,470-473] Nonetheless, the cycling capacities around 600 mA h g^{-1} have been achieved for CuO thin film electrodes,[474-478] which suggest CuO's full utilisation of potential. Oxidation of copper to its higher state as careful design of the electrodes shows much improvement of electrochemical properties. For instance, *In-situ* formation of CuO has been reported upon cycling of Li_2O/Cu_2O composite films.[479]

1.3.1.6 Other transition metal composites

1.3.1.6.1 Manganese

Stable rock-salt-type structure α-MnS submicrocrystals has been prepared by the simple low temperature hydrothermal synthesis method,[480] which show initial discharge capacities of 900 - 1300 mA h g^{-1} depending on the synthesis temperature, after 20 cycles the capacity will be decreased to 400 - 600 mA h g^{-1}. MnP_4 was also prepared that demonstrate a huge specific capacity of more than 1400 mA h g^{-1}.[481] It shows a

conversion reaction to Li_3P and Mn in the reduction in a lithium battery. However, the reversibility of this material is poor, and half of the capacity is already lost during the first cycle. XRD proved that $Mn_{0.75}H_5$ also can fully form reversible metal particles and LiH with very low polarization (ca. 0.25 V) observed in the electrochemical profiles, which is the lowest reported to date for reversible conversion reactions. Poor retention was still observed, unless capacity-constrained cycling was performed,[482] but no data upon extended cycling was provided.

1.3.1.6.2 Iron

Both FeS_2 and FeS are well known within the lithium battery field. As already stated, they were the object of very intensive research in the 1980's and early 1990's because of their attractive performance as positive electrodes in high temperature (375 - 500 °C) batteries with molten salt electrolytes to be used to power electric vehicles.[314]

1.3.2 Silicon and tin anode materials based on the alloying mechanism

There is also a group of anode materials that has been investigated extensively for several years now, but has not yet reached commercialisation. These are metals and semimetals that can electrochemically form alloys with lithium with high capacity.[483] It was first reported in 1971 by Dey that Li metal can electrochemically alloy with other metals at room temperature in the organic electrolyte cell.[484] Since then, Li-alloying reactions with metallic or semi-metallic elements and various alloy compounds have been investigated. The capacities achieved from these alloying reactions which generate the lithium metal alloys, Li_xM, where M is typically Al, Sn, Si, Ge, Pb, or Sb, can reach extremely high values, both by weight and volume.[484] One problem, however, is a consequence of their ability to accommodate large amounts of lithium atoms: namely,

the high volume expansion and contraction during cycling associated with the (de)alloying process, which results in the introduction of large strains in the particles of active material and, in general, in the composite electrode. This resulted in structural degradation, progressive decohesion, particle shuffling, and severely reduced cycle life.[485,486] In 1997, Fuji announced its Stalion battery, which employed an amorphous tin composite oxide anode,[487] but it was not commercialized because of its large irreversible capacity during the first cycle. If the microstructure of the electrode material can be designed properly, the volume change during discharge (lithiation) and charge (delithiation) would be compromised to some extent. Composite materials, as well nanosized particles and nanostructured materials have also been suggested in order to alleviate the mechanical strain generated from volume change, as the Li^+ ions are inserted to and extracted from the host electrode materials. Another solution to this problem invlove the intermetallic compounds: AlSb,[488] Cu_6Sn_5,[489] and Cu_2Sb.[490] The volume changes in these compounds are much less compared to the lithium metal alloys. The reason is that intermetallic compounds contain a second element that is usually not electrochemically active (Al in AlSb, Cu in Cu_6Sn_5 and Cu_2Sb) but can buffer the volume expansion and contraction during cycling. It also entails limiting the effects of these volume changes, mainly through the modification of the content ratios of active material, conductive additive and polymeric binder in the electrode formulation, which, nonetheless, typically reduce the final electrode capacities (including all components). The efforts in this direction proved to be successful, and batteries containing composite anodes based on Sn became a commercial reality.

1.3.2.1 Silicon

Among the various Li alloy elements, Si has been the main focus as Li alloying metals owing to the high capacity Li-rich binary alloys. Based on the maximum Li-containing phase of the Li-Si binary phase diagram ($Li_{22}Si_5$),[491] the theoretical capacities of Si can reach 3590 mA h g^{-1} for gravimetric energy and 8365 mA h cm^{-3} for volumetric energy. More important, Si is abundant, cheap, and environmentally benign. However, it easily displays capacity fading after a few cycles due to the large volume expansion/contraction during the discharge/charge reactions causing mechanical failure of the active material. In order to overcome this problem, various approaches have been applied such as the use of active-inactive binary alloys and Si dispersion in active and/or inactive matrices.

The electrochemical lithiation of Si electrodes at elevated temperatures have been investigated by several groups.[492-500] It follows the equilibrium Li-Si binary phase diagram, forming intermetallic compounds such as $Li_{12}Si_7$ ($Li_{1.7}Si$), Li_7Si_3 ($Li_{2.3}Si$), $Li_{13}Si_4$ ($Li_{3.25}Si$), and $Li_{22}Si_5$ ($Li_{4.4}Si$). For each two-phase region there are distinct voltage plateaus.[492] Through the *In-situ* XRD measurement it was confirmed that crystalline silicon becomes an amorphous Li-Si alloy when Si reacts electrochemically with Li.[495,496,501] Limthongkul et al. proposed an electrochemically driven solid-state amorphization mechanism.[495] Combining the *Ex-situ* and *In-situ* XRD analyses, the reaction mechanism was proposed as follows:[497,498,500]

During discharge:

$$Si\ (crystalline) + xLi^+ + xe^- \rightarrow Li_xSi\ (amorphous) \qquad (1\text{-}4)$$

$$Li_xSi\ (amorphous) + (3.75 - x)\ Li^+ + (3.75 - x)\ e^- \rightarrow Li_{15}Si_4\ (crystalline) \qquad (1\text{-}5)$$

During charge:

$$Li_{15}Si_4 \text{ (crystalline)} \rightarrow Si \text{ (amorphous)} + yLi^+ + ye^- + Li_{15}Si_4 \text{ (residual)} \quad (1\text{-}6)$$

Crystalline Si becomes an amorphous Li-Si alloy (1-4) and the amorphous phase suddenly crystallizes as a $Li_{15}Si_4$ phase around 50 mV *vs.* Li/Li^+ (1-5). During the delithiation process crystalline $Li_{15}Si_4$ is reversed back to the amorphous Si (1-6). Due to electrical disconnection of the active material caused by a severe volume change, there are some amounts of the residual $Li_{15}Si_4$ phase after the first delithiation, which results in a large irreversible capacity. During the second cycle, Li^+ ions will insert into the amorphous Si, accompanying by two slope voltage plateaus, which indicates single phase regions. After the second cycle, reactions (1-5) and (1-6) shown above are repeated.

The failure mechanism of the Li-Si alloying was investigated.[500] It was found that dealloying reaction is not completed during the Li extraction process due to the increased internal resistance. This is caused by volume contraction of the Si particles after expansion in the previous Li-Si alloying process which results in a loss of the contact between Si and the conducting agent carbon. Therefore, applying pressure on the cells to relieve the Si expansion during the alloying process or loading more conductive agent materials could improve cyclability of Si. The particle size and architecture also can affect cycling stability of Si.[502-504]

1.3.2.1.1 Si Nanowires

Numerous research efforts have been spent on Si architectures. It was reported that the Si Nanowires (NWs) exhibited significantly improved electrochemical performance compared to thick films and large particles.[505] They claimed such Si NW electrodes

have several superior features compared with the counterpart: i). There is sufficient empty space between adjacent nanowires to accommodate the volume change. ii). Si NWs have efficient charge transport due to the continuous one-dimensional electronic pathways, which is in contrast to the inefficient hopping of electrons between particles in traditional slurry-coated battery electrodes. Iii): The stress-relief volume accompanying crack growth is not significant enough to overcome the surface energy penalty associated with the crack growth for the nanostructured Si anodes. The Si NWs can maintain a discharge capacity close to 75 % of its maximum over 10 cycles with little fading. After observing the NW morphology after electrochemical reactions, it was found that despite the large volume change, the Si NWs remained intact and did not break into smaller particles, suggesting minimal capacity fading.

Since the first report on the rational Si NW design, many other studies on the Si NW synthesized by different methods have emerged, such as the vapour-liquid-solid (VLS) method, scalable supercritical fluid-liquid-solid (SFLS) method, electrospinning method.[506-516] Coating with carbon improved the electrochemical performance of Si NWs, after 30 cycles, it still maintained reversible capacities of 1500 mA h g^{-1}.[517] Carbon-coated Si NW electrodes exhibited a stable reversible capacity of 1326 mA h g^{-1} after 40 cycles.[518] Si nanowire prepared by metal-induced chemical etching of Si wafers[508,519,520] shows the potential for precise control of crystal orientation and doping.[521]

1.3.2.1.2 Core-shell Si NWs

Cui' s research group proposed the concept of the core-shell Si NW maintaining its electrical connection without pulverization, where the core material is structurally stable and electrically conducting and the shell material is the active Si for storing lithium

ions.[522] They developed a simple method to grow crystalline amorphous core-shell Si NWs without changing the growth temperature to form the crystalline and amorphous regions using CVD furnace.[523] Different core materials, including metal silicides,[508,524] nitride,[508] and carbon nanotubes[508,509,525] have been realised, all presenting satisfactory electrochemical performance.

1.3.2.1.3 Si nanoparticles

It was found that if Si has small enough diameters, it will undergo large volumetric strains without mechanical fracture.[526] Improvement and maintenance of the electrically connection to the current collector after repetitive volume changes need to be addressed. Simply increasing amount of conductive carbon and PVDF binder additive cannot work well for this improvement. Therefore, developing other novel methods are necessary for figure out electrically connecting Si nanoparticles. For instance, the amorphous Si, can be used as an inorganic glue to fuse all the particles together and bind them onto the current collector,[527] which can help solve the issue of the loss of electrical contact in Si particle anodes effectively. Using this method, the prepared Si particle with a 200 nm particle-size showed stable cycling of up to 130 cycles. The Si particles with 8 μm particle size can be cycled for over 200 cycles.

Recently, new polymer binder materials were invented showing dramatic enhanced electrochemical cycling performance of Si nanoparticle electrodes.[528,529] Liu et al. developed a conductive binder which can address the volume change problems in Si. Their integrated experimental and theoretical results show that the developed polymer features greatly improved electronic conductivity and robust mechanical binding forces, which simultaneously maintains electrical connectivity and accommodates the Si volume change. Yushin et al. reported that alginate, a natural polysaccharide extracted

from brown algae, can yield stable Si nanoparticle anodes for more than thousands cycles without obvious capacity fading.[528] These applications of new high performance binders attract much attention due to its low-cost and compatiblity with current slurry manufacturing.

1.3.2.1.4 Hollow Si nanostructures

Specific hollow structured Si nanoparticle which can provide empty interior space for the volume expansion is another novel strategy to Si architecture design. The major merit lies in its low level of diffusion-induced stresses. Cui et al. used a finite element model to calculate the stress induced by diffusion during lithiation of hollow Si nanospheres. The results show that the maximum tensile stress (that which would affect fracture) in a hollow Si sphere is five times lower than that in a solid sphere with an equal volume of Si,[530] which means that the hollow nanostructures will fracture less readily, proving a unique advantage. Through a series of experiments, the authors demonstrated the great cycling stability of hollow Si nanostructures.[530,531] Since then, different methods have been explored to prepare this advantage structured Si nanoparticles. One method involves employing solid silica nanospheres as a template for fabricating interconnected Si nanospheres with an inner radius of ~ 175 nm and an outer radius of ~ 200 nm. This material can achieve 2725 mA h g^{-1} initial discharge capacity. The discharge value only degrades 8 % per 100 cycles,[531] it can maintain 57 % of the 0.2 C capacity when tested at 10 C rate due to the lower stresses present.[531]

Some other hollow structured Si were also studied, such as hollow Si tubes,[532-534] which also showed the good performance on electrochemical characteristics. For instance, Cho's group synthesized the Si nanotube by reductive decomposition of Si precursor inside anodic alumina templates.[530] It presented with a greater than 3000 mA h g^{-1}

reversible charge capacity, and capacity retention of 89 at a rate of 1 C after 200 cycles. They claimed that the hollow nanotubes structure can increase the surface area accessible to the electrolyte, allowing lithium ions to intercalate from both the interior and the exterior of the nanotubes.[534]

1.3.2.1.5 The problem of the unstable SEI of Si

One serious problem facing the use of Si anode is the unstable SEI layer out of the active particles. The SEI layer is an electronic insulator, but a lithium ion conductor; ideally, this results in the SEI eventually terminating its growth at a certain thickness.[535] However, realistically, the interface between the Si nanostructure and the electrolyte is not static due to continuous expansion and contraction accompanying with the charge and discharge process.[498,534,536,537] Therefore, the SEI formed in the lithiated expanded state can be broken as the nanostructure shrinks during delithiation. Then, a fresh Si surface will be exposed to the electrolyte, forming more SEI. This process accumulates a thicker and thicker SEI film outside of the Si nanostructure upon charge/discharge cycling, resulting in degradation of battery performance. During this continuous SEI formation process electrolyte and lithium ions will be consumed, and the electrical contact between the current collector and anode material will be degraded due to insulating nature of the SEI film. In addition, lithium must diffuse a greater distance to access to the active Si nanoparticles because of the increased thickness of SEI layer. Therefore, achieving a stable SEI out of the active Si nanoparticles is critical for realizing long cycle life. Yushin et al. reported a successful control of SEI growth on Si nanotubes with a rigid carbon outer shell,[538] which showed high electrochemical performance, possibly owning to the management of SEI formation.

A surface-clamped hollow Si nanostructure, termed double walled Si nanotubes was also reported, which can overcome this unstable SEI problem.[539] The as-prepared continuous Si nanotubes have an oxide coating layer on the outer surface, fabricated based on electrospun nanofiber templates. Their SiO_x coating layer can successfully prevent the direct contact between Si and electrolyte. Therefore, the outer surface of the nanotubes interfaced with the electrolyte is static, allowing for a stable SEI to be built on the outer surface. The electrochemical property test results show that these Si nanotubes have extremely high cyclability at high rates (6000 cycles with 88 % capacity retention, ~ 2970 mA h g^{-1} at C/5, ~ 1000 mA h g^{-1} at 12 C).

Other nanoscale Si materials, such as the yolk-shell structured Si, have been explored to overcome the SEI problem.[540,541] This is feature in commercial Si nanoparticles, which are sealed inside thin, self-supporting carbon shells. The rationally designed void space between Si particles and the carbon shells allows free expansion during lithiation process. The SEI layers can only be generated out of the carbon shell surface, and avoid being broken due to dramatic volume change of Si particles. This kind of material electrode have achieved high capacity (2800 mA h g^{-1} at C/10), long cycle life (1000 cycles with 74 % capacity retention), and high Coulombic efficiency (99.84 %).

1.3.2.2 Si-M systems (M: active/inactive metal or compound)

Another important strategy to overcome the poor cyclability caused by huge volume variation of Si electrode the use of using intermetallic compounds (M-active metal or M-inactive metal, M = Si) instead of pure Si electrodes.[542-548] It has been reported that Li ternary silicides (Li-Metal-Si) have a more favourable voltage profile and a higher reversible capacity than Li-Si binary alloys based on thermodynamic calculations.[542,543] The following are some examples using the alloy as anode for the Li-ion batteries.

Metallic magnesium is active to Li, forming Li-Mg alloys electrochemically. The electrochemical characteristics of Mg_2Si were investigated serially at ambient temperature.[544-546] Based on XRD and Auger electron spectroscopy (AES) measurements, the reaction mechanism of Li insertion into Mg_2Si was proposed as follows:[544]

$$Mg_2Si + xLi^+ + xe^- \rightarrow Li_xMg_2Si \quad (1\text{-}7)$$

$$Li_xMg_2Si + xLi^+ + xe^- \rightarrow Li_{critical}Mg_2Si \rightarrow Li_{saturated}Mg_2Si + Mg + \text{Li-Si alloy} \quad (1\text{-}8)$$

$$Mg + xLi^+ + xe^- \rightarrow \text{Li-Mg alloy} \quad (1\text{-}9)$$

In detail, Li is inserted into the Mg_2Si antifluorite structure to form Li_xMg_2Si, occupying the octahedral site until the amount of inserted Li reaches the critical value. Then $Li_{critical}Mg_2Si$ decomposes into $Li_{saturated}Mg_2Si$, Mg, and Li-Si alloy phases (1-8). Finally, further Li will alloy with Si to form Li-Mg alloy (1-9). During the charge process, the reverse reactions are expected to occur. Subsequently, Moriga et al. and Roberts et al.[545,546] proposed the Li_2MgSi will be formed during the first stage instead of Li_xMg_2Si. The Mg_2Si electrodes suffered from the same rapid capacity fading problem due to material pulverization by the large volume expansion and shrinkage.

$CaSi_2$, as another Si-active metal intermetallic compound anode, was also evaluated from the electrochemical aspect.[547] Both sieved and ball-milled $CaSi_2$ demonstrated potential as an alternative anode material. The following reaction is proposed based on the predicted Ca-Si-Li phase diagram at ambient temperature.

$$10.8Li + CaSi_2 - Li_2Ca + 2Li_{4.4}Si \quad (1\text{-}10)$$

In contrast to the Si-active metal compounds, Si-inactive metal compounds such as NiSi and FeSi were also examined as a substitute for the Li-ion batteries.[548] Because Ni and Fe are inactive elements to Li, they are expected to act as a buffering matrix for the formation of Li_xSi and the following reaction mechanisms were proposed for the reactions of NiSi and FeSi with Li.

$$xLi^+ + xe^- + NiSi \rightarrow Li_xSi + Ni \leftrightarrow Ni + Si + xLi^+ + xe^- \quad (1\text{-}11)$$

$$xLi^+ + xe^- + FeSi \rightarrow Li_xSi + Fe \leftrightarrow Fe + Si + xLi^+ + xe^- \quad (1\text{-}12)$$

For NiSi, the first discharge capacity was 1180 mA h g^{-1}, corresponding to 3.82 mol of Li insertion into the Si. The other similar intermetallic compounds, $CoSi_2$, $FeSi_2$, $NiSi_2$, and SiB_3 were also reported as alternative anode materials for the Li-ion batteries.[496] Although these intermetallic compound electrodes showed better cyclability than a Si powder electrode, there was still capacity fading caused by the large volume change.

Therefore, the approach to addressing Si volume expansion during cycling is to generate composite materials which consist of finely dispersed Si particles in an inactive matrix.

This inactive matrix is expected to act as a buffering material to accommodate the volume change of Si, resulting in enhanced cycle performance, such as TiN and TiB_2.[549,550] This kind of composite anode material showed reversible capacities of 300-400 mA h g^{-1} up to 15 - 20 cycles with a relatively good capacity retention. However, the reversible capacities were low compared to their theoretical values of 700 - 900 mA h g^{-1} because some of the Si particles were embedded in the nanocomposite after prolonged milling which led to electrochemical inactivity of the Si.[551]

1.3.2.3 Tin

Electrochemical lithiation process of Sn at elevated temperatures is quite similar to Si, which carries out different phase transitions between Li-Sn binary alloy, yielding seven different Li-Sn line phases within the Li-Sn phase diagram: Li_2Sn_5 ($Li_{0.4}Sn$), LiSn, Li_7Sn_3 ($Li_{2.33}Sn$), Li_5Sn_2 ($Li_{2.5}Sn$), $Li_{13}Sn_5$ ($Li_{2.6}Sn$), Li_7Sn_2 ($Li_{3.5}Sn$), and $Li_{17}Sn_4$ ($Li_{4.25}Sn$) orderly. Based on the final product of the Li-Sn alloy phase ($Li_{17}Sn_4$), maximum gravimetric capacity of Sn is calculated to 959.5 mA h g^{-1}. Although this value is less than Si, Sn is an attractive anode material due to its high volumetric capacity (about 2000 mA h cm^{-3}), which is even higher than that of metallic Li and is comparable to Si.[552]

Noriyuki reported that the electroplated Sn electrode can deliver close to the theoretical capacity (940 mA h g^{-1}).[552,553] However, like the Li-Si alloying process, Sn also suffer from dramatic capacity fading problem caused by mechanical degradation such as cracking and pulverization due to large volume variation between lithiation and de-lithiation during cycling.[483] Some *In-situ* studies showed the morphological changes of the Sn electrode with their underlying mechanics during cycling. According to the *In-situ* atomic force microscopy observations it was found that Sn electrode exhibited irreversible morphological changes and the above mentioned electrochemical pulverization of Sn during discharge and charge led to the breakdown of the electrical conduction pathways in the electrode as well as physical degradation of Sn, thereby causing its poor capacity retention.[554] Further *In-situ* stress measurements revealed that Sn film electrode actually underwent a stress transition during cycling and the induced stresses were released by creating cracks.[555] Therefore, the main reason for the drastic

capacity fading of the Sn electrode can be attributed to non-homogenous large volume changes associated with the formation of a Li-Sn intermetallic phase.

1.3.2.4 Sn–M systems

Sn-based intermetallic compounds M_xSn (M = Co, Cu, Mn, Fe, Ce, Mg, Sb, etc. . .) and multiphase Sn-M alloys have been studied broadly over the past decades.[556-566] Their electrochemical reactions are similar and can be summarised as follow:

Initial discharge process:

$$M_xSn + 4.25Li^+ + 4.25e^- \rightarrow xM + Li_{4.25}Sn \quad (1\text{-}13)$$

Following charge and subsequent cycles:

$$xM + Li_{4.25}Sn \leftrightarrow M_xSn + Sn + 4.25\ Li^+ + 4.25\ e^- \quad (1\text{-}14)$$

It can be seen that during the first discharge process, the Sn-Metal is decomposed into pure M and Sn. The latter will react with lithium forming a Li-Sn alloy phase. If the M can react with lithium, such as Sb and Mg, further Li-M alloying reactions will proceed.[559-561,565]

The detailed lithiation mechanism is very complicated and depends on the crystal structure of the mother compounds. Cu_6Sn_5 will transfer to fcc Li_2CuSn (lithiated zinc-blende structure) at the first stage and, thereafter, form an intermediate solid solution of $Li_{2+x}Cu_{1-x}Sn$ ($0 \leq x \leq 1$). Then, all the Cu will be extracted to yield a Li-Sn alloy phase.[567] The subsequent delithiation process is accompanying the reconstruction of a Cu_6Sn_5 intermetallic phase, as indexed by *In-situ* XRD analysis. Of course, this whole cycle causes extreme volume variation in the electrode. In contrast to the reversible

structural changes of Cu_6Sn_5, in Sn_2Fe alloy, partial Sn and Fe can be re-alloyed during charging process, which suggest that some of the Fe atoms acted as an inactive phase.[557]

Although Sn intermetallic compounds showed a higher initial coulombic efficiency, their capacity retention was not satisfactory for utilization in commercial Li-ion batteries.

Large volume variation can bother the Sn-based intermetallic compounds during cycling, which accounts for their poor cyclability. Because of this, multiphase Sn-M alloys have emerged. They can be classified into two groups: (i) active/inactive composite, in which the inactive ingredient acts as an inert matrix phase holding Sn-based reacting components, such as Sn_2Fe and $SnFe_3C$.[568,569] (ii) all-active multiphase alloys such as Sn-Sb, Sn-Ag, and Sn-Sb-Ag alloys.[570-573] A comparison of these two classified composites shows the latter to have more stable capacity retention.

As explained above, large expansion of a more reactive phase in the composite can be buffered by an inactive matrix. Therefore, the extent of mechanical degradation can be relieved. For instance, the active/inactive composite alloy proposed by Mao et al.[569] showed improved cycle performance by buffering the expansion of the Sn-based active component with an inert matrix phase. Sn_2Fe intermetallic phase/inert $SnFe_3C$ intermetallic phase prepared by HEMM demonstrated relatively stable cycling over several tens of cycles. The composite with 24 wt % Sn_2Fe, 72 wt % SnFe+C, and 4 wt % C can achieve about 200 mA h g^{-1} discharge capacity and no capacity fade over 80 cycles.[569] *In-situ* XRD and electrochemical characterization reveal that Sn in $SnFe_3C$ did not react with lithium, while Sn atoms in the Sn_2Fe component did react with lithium. It was also found that the cycle performances of such composite were directly proportional to the amount of $SnFe_3C$. Besides of those active/inactive composites

materials, other various inert phases have been tried and some of them significantly improved cycling performance over one hundred cycles.[574-577] For instance, Ag-Sn-Fe nanocomposites can maintain about 280 mA h g^{-1} over 300 cycles.[576] However, the use of inert matrix phases, especially intermetallic phase and transition metals, tended to decrease the gravimetric capacity of Sn-based nanocomposite materials.

1.4 Na-ion batteries

Li-ion battery has dominated the portable electronic market as an energy storage technology, and the prime candidate to power the next generation of electric vehicles. However, with respect to the long term goal of vehicle batteries and large scale applications, lithium reserves are limiting,[16] raising concerns about cost challenges.[578,579] Additionally, debate over the feasibility and environmental impact of lithium carbonate production,[580] drive the exploration of new low-cost and reliable electrochemical energy storage technologies.[579] Hereinto, Na-ion batteries have attracted more attention recently due to low cost, abundant supply and widespread terrestrial reserves of sodium mineral salts.[580] Moreover, the computational studies on voltage, stability and the diffusion barrier of Na-ion and Li-ion materials indicate that Na-ion systems can be competitive with Li-ion systems.[581]

The use of Na instead of Li in rocking chair batteries could address the shortage of lithium reserves. Furthermore, the development of a rechargeable Na-ion battery with good performance characteristics could have the advantage of using electrolyte systems of lower decomposition potential due to the higher half-reaction potential for sodium relative to lithium. This low voltage operation would make Na-ion cells cheaper, because water-based electrolytes could be used instead of organic ones.[582]

There is, however, an important shortcoming of Na-ion batteries: they fall short of meeting energy densities compared to Li-ion batteries. This is because of the higher equivalent weight of Na than Li, and because there are two competing factors regarding the formation of sodium-based intercalation compounds: the ionization potential and the size of the alkali metal.[582] The ionic diameter decreases from 4 Å to 2 Å from Cs to Li in the series of alkali metal elements in the periodic table. In spite of these considerations, there exists growing interest on Na-ion technology. In any case, Na-ion batteries would be interesting for very low cost systems for grid storage, which could make renewable energy a primary source of energy rather than just a supplemental one. Progress the on Na-ion battery has involved development of framework materials based on the phosphate polyanion: 147 mA h g^{-1} specific capacity of olivine $NaFePO_4$ has been obtained by Zaghib et al.[583] However, its reversibility is poor (50.6 mAh g^{-1} in the second cycle).[584] Fluoride-based cathode materials, $NaMF_3$ (M = Fe, Mn, V and Ni), have been prepared with specific capacities ranging from 30 to 170 mA h g^{-1}.[585,586] Moreover, layered transition metal oxide, such as P2-Na_xCoO_2,[587,588] P2-$Na_{2/3}[Fe_{1/2}Mn_{1/2}]O_2$,[589] $Na_{2/3}(Ni_{1/3}Fe_{1/3}Mn_{2/3})O_2$,[590] $NaCrO_2$,[591,592] Na_xMnO_2,[593,594] Na_xVO_2,[595] with stable capacities were reported. Fluorophosphate[596] and fluorosulfate[597-599] materials were also developed as a cathode material for Na-ion batteries. The major issue lies in the higher ionization potential[580] and bigger ionic diameter of the Na, and lack of appropriate active materials with sufficiently large interstitial space within their crystallographic structure to host Na ions [600] Nanomaterials and nanotechnology have been explored to address this problem. For instance, $Na_4Mn_9O_{18}$ nanowires offered a high reversible capacity and exhibited unprecedented cyclability has been reported.[601]

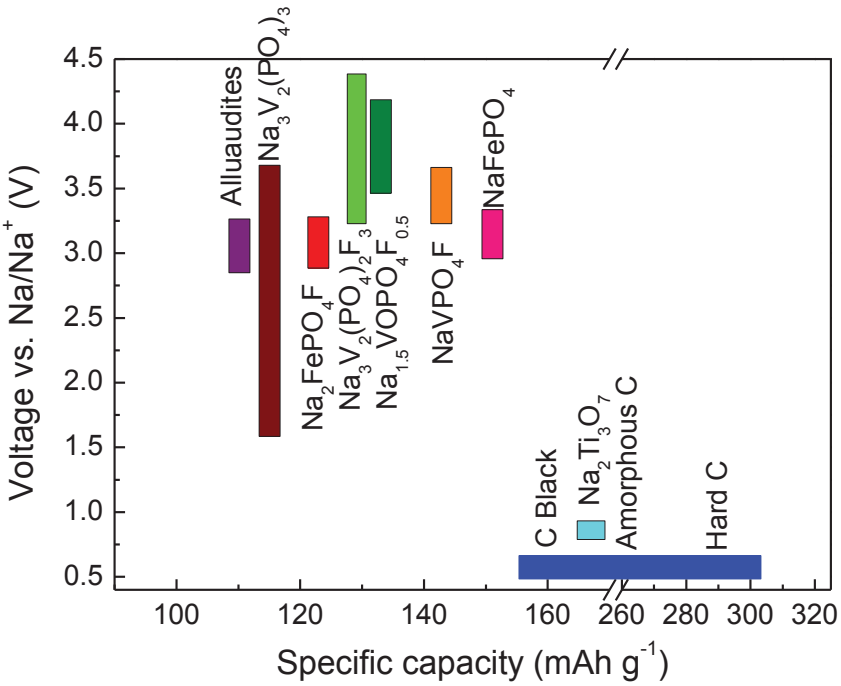

Figure 1-11 Most important cathode and anode materials studied for their application in Na-ion batteries, represented by their specific capacity and operating voltage *vs.* a sodium metal anode.

A summary of potentials as well as theoretical and achieved capacities for cathode and anode electrode materials for Na-ion batteries is presented in Figure 1-11.[602] Unsurprisingly, many of the materials suitable for Na-ion batteries are similar to those which have been exhaustively researched over the past two decades for Li-ion batteries, including layered transition metal oxides, olivines and compounds with the NASICON framework.

1.5 Cathode materials for Na-ion batteries

1.5.1 Layered oxides

Layered oxides of the type AMO_2 (A = Li, Na; M = Co, Mn, Ni and combinations thereof),[160,603] are sought after for their high intercalation potentials and energy densities.

They are known for their commercial domination of the Li-ion battery market. Similar to the lithium metal oxides, the alkali cation Na is reversibly de/intercalated between the layers of transition metal MO_6 octahedron on electrochemical cycling. Sodium oxides can exist as one of several poly types. They differ in the stacking of the oxygen layers, resulting in different intercalation sites for the alkali cation.[604] In the nomenclature used to distinguish these phases, O and P represent octahedral or trigonal prismatic coordination of the sodium ions and 3 or 2 represents the number of distinguishable sodium layers. This way, ABCABC for O3, ABBA for P2 and ABBCCA for P3 were defined. For instance, in Na_xCoO_2 bronzes, x may be varied in the range $0.4 < x < 1$. These compounds are layered oxides with the sequence OMOAOMOA, where O = oxygen, M = Co and A = Na. Within the composition range $0.5 < x < 1$, up to four phases have been identified in which the sodium coordination is either octahedral or trigonal prismatic.[605-608] O3, O'3, P3 and P2 phases are comprised in the mentioned x range. Although all these four phases have been shown to react reversibly *vs.* sodium insertion, P2 bronze offers better cycle life and better energy efficiency.[609]

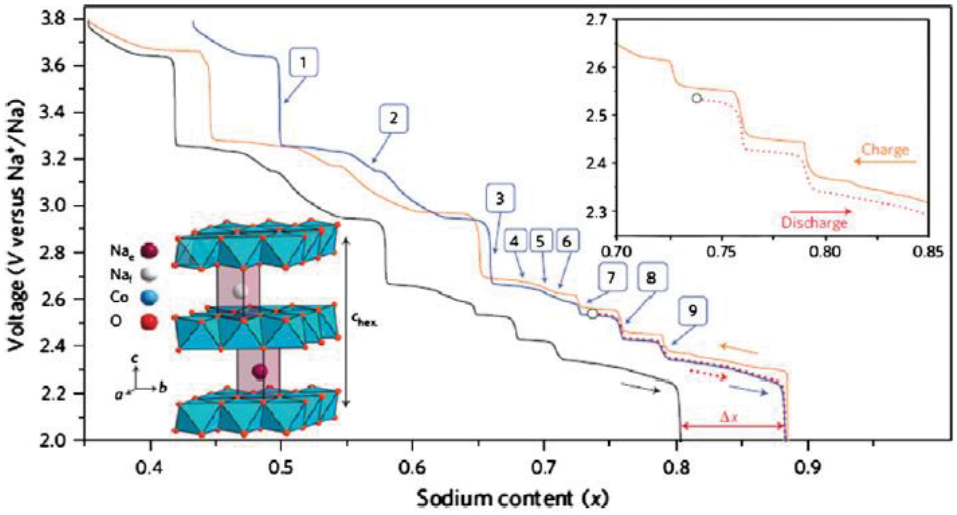

Figure 1-12 Galvanic cycling of $Na_{0.7}CoO_2$, showing phase transitions on electrochemical cycling. Close up of the region between $Na_{0.7}CoO_2$ and $Na_{0.85}CoO_2$ shown in right inset. Structure of $Na_{0.7}CoO_2$ shown in left inset.[610]

In 1993, Doeff et al. prepared P2-Na_xCoO_2 electrode sodium electrochemical cells, which showed an open circuit potential of about 2.8 V when operated at 90 - 100 °C.[611] The voltage profile (Figure 1-12) shows that sodium extraction and reintercalation into Na_xCoO_2 occurs via several steps due to ordering transitions of the Na ions between the layers. Thus, cationic distribution in P2-Na_xCoO_2 phase changes with sodium content, leading to diverse Na^+/vacancy ordered distributions for definite sodium concentrations. Registered cationic exchange was of 0.5 - 0.6, which would correspond to ca. 141 mA h g^{-1}. Cyclability limitations associated with cathodic material were observed. Cells run at higher temperature (40 °C) retain the most stable electrochemical features (# 3, 8 and 9 from Figure 1-12) and also maintain a similar capacity, which indicates greater sodium mobility (disorder) and phase stability. Reduction of particle size of the synthesized compounds was found to improve electrochemical performance.[612]

The crystal structure change of P2-Na_xCoO_2 phase during cycling *vs.* Na/Na^+ showed a multistep voltage-composition curve with several reversible biphasic and single-phase domains from 2 to 3.8 V.[604]

In contrast to the complicated mechanism of sodium extraction from the P2 phase for pure Co, the P2 phase of $Na_{0.66}Co_{0.66}Mn_{0.33}O_2$ displayed solid solution behaviour on sodium extraction, except at the composition $Na_{0.50}Co_{0.66}Mn_{0.33}O_2$ where an ordered line-phase was found.[613] On the other hand, Na insertion and extraction into and from P2-$Na_{0.66}Co_{0.66}Mn_{0.33}O_2$ phase showed that all the sodium can be reversibly extracted from the phase, unlike its Li counterpart that only extracts 1/3 of the Li ions. This way, a specific capacity of 161 mA h g^{-1} was achieved, very close to the theoretical one, of 173 mA h g^{-1}. Several voltage plateaux were observed from 3 to 4.1 V *vs*. Na/Na^+.[614]

Another important cathode electrode material with layered structure is sodium-manganese oxide. Manganese oxides form a very rich and versatile structural family enlisting materials having either 1D, 2D, or 3D type tunnel structures, causing the diversity of the $NaMnO_2$ phases.[367] The known phases of Na_xMnO_2 also demonstrated different poly phases (x = 0.2, 0.40, 0.44, 0.70, and 1).[615] The phase α-$NaMnO_2$, prepared at lower temperatures, displays an O3 layered structure with a monoclinic structural distortion due to the Jahn–Teller distortion of the Mn^{3+} ion, whereas high temperature orthorhombic β-$NaMnO_2$ adopts a double stacked sheet structure. Compared with β-$NaMnO_2$, α-$NaMnO_2$ is more energetically stable according to computational studies.[616] Back in 1985, the electrochemical behaviour of both α- and β-$NaMnO_2$ were first researched by Mendiboure.[617] He reported that only 0.22 and 0.15 Na could be extracted and re-intercalated into the α-$NaMnO_2$, and β-$NaMnO_2$ crystals, respectively. Recently, the electrochemical properties of the monoclinic α-$NaMnO_2$

have been revisited. It showed a significant improvement, with 0.8 Na able to be reversibly de/intercalated with good capacity retention, corresponding to a 200 mA h g^{-1} capacity.[618] The voltage profiles of monoclinic $NaMnO_2$ reveal very pronounced structural transitions on desodiation,[618] which have also been observed in $NaCoO_2$. This might be due to Na-vacancy ordering or transitions that involve the gliding of oxygen planes, especially as Na likes to adopt both octahedral and trigonal prismatic environments and the latter can only be achieved in an O3 stacking by sliding some of the oxygen layers.[602]

The sodium manganese bronze Na_xMnO_2 phase was compared by Doeff et al. as a cathode material for both sodium and lithium secondary batteries. A reversible intercalation of 0.6 Na^+ or Li^+ ions per manganese, 160-180 mA h g^{-1} specific capacity, was observed at moderate current densities and 85 °C in a solid polymer electrolyte battery.[619]

Another layered oxide, based on nickel (II)/manganese (IV), $Na_{0.85}Li_{0.17}Ni_{0.21}Mn_{0.64}O_2$, also displays promising electrochemistry.[620] It was proposed that the electrochemical processes are driven by the Ni^{2+}/Ni^{4+} redox reaction, therefore, its corresponding theoretical capacity is based on extraction of 0.42 Na (112 mA h g^{-1}). In contrast to the pure layered structure P2 Na_xCoO_2 phase, the voltage profile on discharge/charge of $Na_{0.85}Li_{0.17}Ni_{0.21}Mn_{0.64}O_2$ was a relatively smooth curve, indicating intercalation within a single phase. Impressive high rate performance was demonstrated within this material: the obtained discharge capacity of 65 mA h g^{-1} at high rate of 25 C (discharge in about 3 min) corresponds to a competitive power density of about 670 W kg^{-1}. Other layered structured transition metal oxide, such as P2-$Na_{2/3}[Fe_{1/2}Mn_{1/2}]O_2$,[589]

$Na_{2/3}(Ni_{1/3}Fe_{1/3}Mn_{2/3})O_2$,[590] $NaCrO_2$,[591,592] Na_xVO_2,[595] with stable capacities were also reported.

The layered metal oxide structures are certainly amenable to sodium insertion and extraction. Besides layered oxides, other structure sodium intercalation compounds, like the olivines and NASICONs have exhibited phase stability and activation energy for ion mobility with respect to voltage from the theoretical calculations.[621]

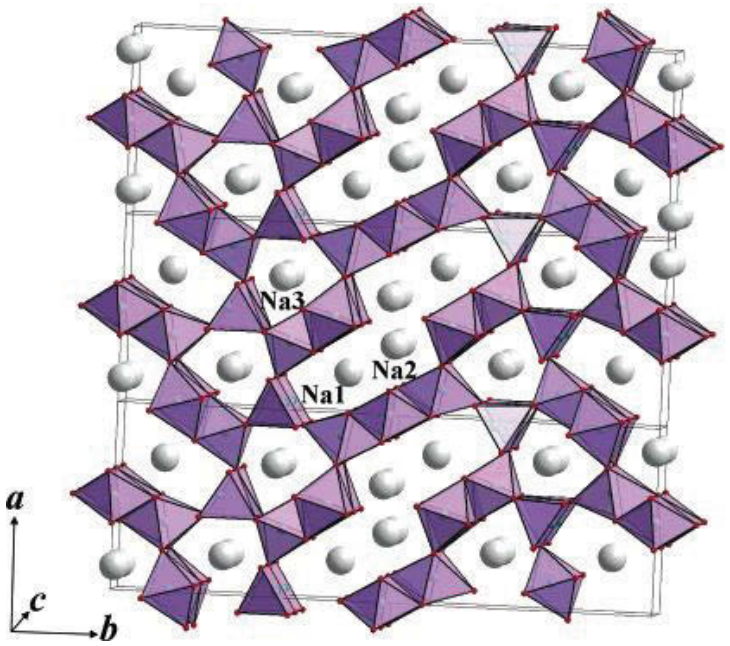

Figure 1-13 Structure of $Na_{0.44}MnO_2$ perpendicular to the ab plane.[622]

$Na_{0.44}MnO_2$ is a particularly attractive candidate for the Na-ion batteries because its crystal structure forms suitable large-sized tunnels for sodium incorporation.[623] $Na_{0.44}MnO_2$ crystallizes in an orthorhombic lattice cell with Pbam space group (Figure 1-13). The manganese ions are located in two different environments: all Mn^{4+} cations and half of the Mn^{3+} cations are in octahedral sites (MnO_6), while the other Mn^{3+} are gathered in a square-pyramidal environment (MnO_5). The latter forms edge-linked chains linked to two double and one triple octahedral chain(s) by the vertices, leading to

the formation of two types of tunnels. Two sodium sites (referenced as Na1 and Na2) are situated in large S-shaped tunnels, while another sodium site (Na3) is found in smaller tunnels. According to this structure, the c direction is the main path for sodium diffusion. The entitled $Na_{0.44}$/Mn ratio corresponds to a filling of the Na3 sites, whereas the S-shaped tunnels are only half filled.

The mechanism of the $Na_{0.44}MnO_2$/C composite electrodes in a Na-ion batteries during cycling was recently reported by Tarascon et al.,[622]. It was proposed that Na content varied in the range 0.18 - 0.64 between 2 and 3.8 V *vs*. Na/Na^+ through the *In-situ* XRD measurement technique. The potential profiles also presented multisteps, suggesting multitransition processes, which indicate that $Na_{0.44}MnO_2$ processes the complexity of the insertion/extraction mechanism.

At very low current rates (C/200), $Na_{0.44}MnO_2$ can achieve 140 mA h g^{-1} specific capacity. When the current rate was increased at C/10, the capacity retention of this oxide was not good, as only half of the capacity was only retained after 50 cycles. It was found that when this material was cycled faster than C/20, a drastic decrease in the capacity occurs, demonstrating its kinetic limitations. Whitacre investigated this type of sodium intercalation compound in an aqueous electrolyte (1 M Na_2SO_4) solution.[624] In his electrochemical cell, activated carbon was chosen as an anode material. This hybrid system showed a specific capacity of 45 mA h g^{-1} through a 0.6 V range from $Na_{0.44}MnO_2$ to $Na_{0.22}MnO_2$.[625] At the same time, the cathodic material demonstrated to be fully stable in an aqueous environment, and electrochemical device demonstrated very good cyclability for 1000 cycles.

1.5.2 Phosphates

Another framework material is based on the phosphate polyanion, like which, lithium phosphate polyanion intercalation compounds, has also been identified to be potential electro active materials for sodium metal and Na-ion battery applications. The metal phosphates can be further divided to two main groups: olivine structured or NASICON structured. In both species, the strong inductive effect of the PO_4^{3-} polyanion moderates the energetics of the transition metal redox couple to generate relatively high operating potentials.[626] Following are some typical phosphate polyanion cathode materials for the Na-ion batteries.

1.5.3 Olivine $NaFePO_4$

Olivine $NaFePO_4$ has a high theoretical specific capacity (154 mA h g^{-1}). The most stable polymorph of $NaFePO_4$ is maricite, which is structurally analogous to $LiFePO_4$. In maricite $NaFePO_4$, Na^+ cations occupy the 4(c) Wyckoff sites and the Fe^{2+} species are situated in 4(a) sites. In this way, maricite presents one-dimensional, edge sharing FeO_6 octahedron and no cationic channels, thus hindering cation exchange, while in olivine $LiFePO_4$ the Li^+ and Fe^{2+} ions occupy 4(a) and 4(c) sites, respectively. Burba et al.,[627] explained that this might be due to the larger ionic radius of Na^+ compared to that of Li^+.

Morean et al.,[628] prepared olivine $NaFePO_4$ and $Na_{0.7}FePO_4$ phases by a two step process, involving: I, chemical oxidation of $LiFePO_4$ to heterosite $FePO_4$ by using NO_2BF_4 in acetonitrile[629] or bromine dissolved in water,[630] and II, electrochemical Na insertion by using $FePO_4$ as the positive electrode and metallic Na foil as anode. Using this method prepared $NaFePO_4$ demonstrated reversible insertion and extraction of Na

into olivine $FePO_4$ at 2.8 V. A discontinuity in the potential-composition curve has been detected in the vicinity of $Na_{0.65}FePO_4$, both on discharge and on charge, which corresponds to an electrochemical biphasic process involving a $Na_{0.7}FePO_4$ phase in equilibrium with $FePO_4$, as confirmed by *Ex-situ* X-ray diffraction measurement.

Although a high initial discharge specific capacity (147 mA h g^{-1}) of $NaFePO_4$ has been reported at C/24 rate, poor reversibility (50.6 mA h g^{-1} in the second cycle) still limited practical application of $NaFePO_4$. Moreau et al. could cycle reversibly 0.9 Na in the first charge/discharge cycle (139 mA h g^{-1}), but the cycle life of the produced material was not investigated. Much more work on this material is required in order to develop a high capacity olivine Na-based cathodic material.

Nazar et al.[631] has extended the research on olivine structure materials for Na-ion batteries to $Na[Mn_{1-x}M_x]PO_4$ (M = Fe, Ca, Mg). Preliminary galvanostatic tests at low cycling rates indicated that electrochemical reaction takes place in a single-phase, with a sloping voltage profile.[631] A series of sodium fluorophosphates, for example, $NaVPO_4F$, $Na_3V_2(PO_4)_2F_3$, $Na_{1.5}VOPO_4F_{0.5}$ and Na_2FePO_4F, also showed to be promising candidates.

1.5.4 Sodium vanadium fluorophosphates

As shown in Figure 1-11, there is another branch of the potential cathodic material candidates for Na-ion batteries: the sodium vanadium fluorophosphates, involving $NaVPO_4F$, $Na_3V_2(PO_4)_2F_3$, and $Na_{1.5}VOPO_4F_{0.5}$, which have features of low-cost raw materials, and safe.

$NaVPO_4F$, with a tetragonal symmetry structure (space group I4/mmm), was first prepared in 2003 by Barker et al.[632] He proposed that this compound represents one of

the first examples of fluorophosphate-based compounds that have been recognized as alkali ion insertion hosts. When this compound was electrochemically tested using hard carbon anode with a sodium electrolyte at 23 °C and C/10 current rate between 2.5 and 4.25 V, 82 mA h g^{-1} discharge specific capacity was achieved at the first cycle. Repeated cycling at this current rate demonstrated that the discharge capacity decayed to less than 50 % of the initial one after 30 cycles. Therefore, improvements are needed towards the $NaVPO_4F$ in Na-ion cells.

Some other research showed that $NaVPO_4F$ has another polymorph phase, which has a monoclinic crystal structure with a space group of C2/c,[633] [634,635] which is consistent with the related $Na_3Al_2(PO_4)_2F_2$ phase. The structure of this material is made up of two $[PO_4]$ tetrahedrons that share two corner-oxygen atoms with two different $[VO_4F_2]$ octahedrons. Zhao et al.,[635] used the sol–gel synthesis method and subsequent firing at 700 °C, and described the generation of a monoclinic $NaVPO_4F$ polymorph phase, and tetragonal phase formation at 750 °C. The monoclinic polymorph can obtain a specific capacity of 80 mA h g^{-1}, and cycling performance was improved with doping.

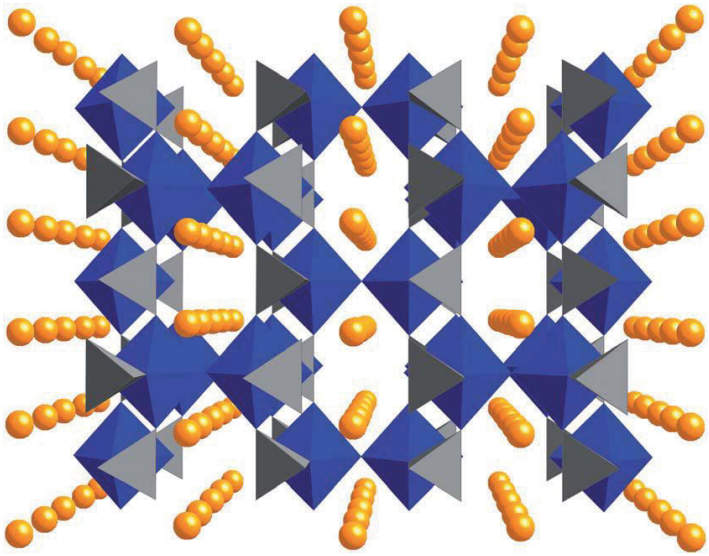

Figure 1-14 Crystal structure of $Na_3(VO)_2(PO_4)_2F$.[636]

Furthermore, Sauvage et al.[637] produced a new compound, $Na_3(VO)_2(PO_4)_2F$, from the same precursors used to make ''$NaVPO_4F$''. Its space group is I4/mmm, and it is formed by layers of alternating [VO_5F] octahedron and [PO_4] tetrahedron sharing O vertices parallel to the ab plane (Figure 1-14). Along the c direction the V octahedron are joined pairwise through common F vertices in the inversion centres. The sixth O vertex of the V octahedron is the terminal O $\times$ O ligand of a vanadyl group. Thus, the structure is described as a mixed para frame work of octahedron and tetrahedron {$V_2O_2F[PO_4]_2$} with disordered Na atoms in the interstices.[636] This new vandyl compound exhibited a reversible capacity of 87 mA h g^{-1} over the course of two different voltage plateaus at 3.6 V and 4.0 V *vs*. Na/Na^+.[637] The lower voltage plateau (3.6 V) process showed a sustained reversibility over 50 cycles. This capacity fading was associated with a cell polarization increase that could be consistent with the formation of a surface layer resulting from electrolyte degradation at the surface of the materials.

1.5.5 Sodium iron fluorophosphates

Na_2FePO_4F was first reported in 2007,[14] to adopt a layered structure isostructural with the previously reported Mg[638] and Co[639] sodium fluorophosphates. Linda et al.,[20] proposed that these 2D iron phosphate sheets house two Na^+ cations: Na (1), which sits exactly between the layers, and the Na (2) which resides close to the phosphate sheets. The comprised bioctahedral $Fe_2O_7F_2$ units made of face-sharing FeO_4F_2 octahedron that are connected via bridging F atoms to form chains, and joined by PO_4 tetrahedron to form [$FePO_4F$] infinite layers. The two Na cations located in the interlayer space possess facile two-dimensional migration pathways. Moreover, the layered structure of Na_2FePO_4F allows for minimal structural modification on sodium deintercalation. The

unit cell of the oxidized compound ($NaFePO_4F$) is only 3.7 %,[14] smaller than that of sodium olivine (~ 15 %).[20], which makes this compound a low strain material. This superior feature benefits from the effect of the Na (1) ion, which cannot be electrochemically removed by oxidation due to the inaccessibly high potential of the Fe^{3+}/Fe^{4+} couple, and remains as a "pillar" between the layers to prop them apart. The kinetics of transport is also enhanced as the layers do not collapse. The electrochemical profile of Na_2FePO_4F cycled *vs.* sodium presented two-phase plateaus, (2.90 V and 3.05 V *vs.* Na/Na^+). Higher cyclablity has been achieved: 80 % of the 120 mA h g^{-1} theoretical capacity was sustained on cycling.[640] An intermediate phase, $Na_{1.5}FePO_4F$, is obtained with intermediate lattice parameters lying between the two end members. Its structure undergoes a slight change in symmetry to a monoclinic unit cell (P2/c, β = 91.22 °). Nanosized Na_2FePO_4F particles improved electrochemical performance slightly by showing better initial capacity, lower irreversible capacity, lower polarization and better capacity retention.[640] The discharge specific capacity for this sample was over 100 mA h g^{-1} for 10 cycles.

Na_2MnPO_4F was also reported by the ionothermal synthesis process. It presents a tunnel structure formed by MnO_4F_2 entities, in which manganese octahedrons share only one common F vertex to form $Mn_2F_2O_8$ chains parallel to the b-axis of the monoclinic unit cell. These chains are linked by PO_4 tetrahedron in a and c directions and creat to tunnels for possible cationic Na transport.

Ellis et al.[641] reported that Na_2CoPO_4F phase, having isostructure with Na_2FePO_4F, can get higher voltage. Furthermore, Ellis et al. also prepared the Na_2NiPO_4F phase, which is a structural analogue of Fe. It was presumed that this compound has a Ni^{2+}/Ni^{3+} redox

couple above 5 V, because it did not show any electrochemical activity below 5 V, similar to that of other nickel phosphates such as $LiNiPO_4$[642] and Li_2NiPO_4F.[643]

Substitutional solid solutions such as $Na_2(Fe_{1-x}Mn_xPO_4)F$ ($0 < x < 0.2$),[16] $Na_2(Fe_{1-x}Co_x)PO_4F$ ($0 < x < 1$), and $Na_2(Fe_{1-x}Mg_x)PO_4F$ ($x < 0.15$) were also prepared,[17] but all presented minimal reversibility. Electrochemical performance of substituted samples decreased with increasing the substitute content. Mn based species showed worse performance, even in the same structure as the Fe-based compound.

1.5.6 NASICON-type materials

NASICON-related compounds, with the highest ionic mobility possessing rhombohedral R-3 symmetry, have been extensively studied for their structural stability and fast ion conduction, initially as solid electrolytes and more recently as insertion materials.[644-646] They have been shown to be promising cathode materials for Li-ion batteries, exhibiting high Li^+ ion mobility and reasonable discharge capacities. Na^+ ions also can be inserted into a series of compounds having a general formula $A_nM_2(XO_4)_3$ because they have a large sodium site based on a 3D framework. In this structure, alkali ions can occupy two different sites. At low alkali content ($x < 1$ in $A_xM_2(XO_4)_3$) an octahedral site, A(1), is selectively occupied. With $x > 1$, the alkali ions are randomly distributed among the A(1) and three 8-coordinate sites, A(2). This way, the open 3D nature of the structure allows easy migration of the alkali ions between A(1) and A(2).

Sodium intercalation in $Na_3V_2(PO_4)_3$ was first reported in 2002.[647] It was proposed that the initial discharge capacity of this compound was 50 mA h g^{-1} at 1.6 V *vs*. Na/Na^+. When the material was charged to the original stoichiometry, it could be further charged at 3.4 V *vs*. Na/Na^+ and the discharge capacity at this step was 90 mA h g^{-1}. In the same

work, the $Na_3Fe_2(PO_4)_3$ compound was also tested as a positive electrode material *vs.* sodium, but it only showed a plateau around 2.5 V, and a discharge specific capacity of 45 mA h g^{-1} for the first cycle. Moreover, $Na_3V_2(PO_4)_3$ is an ideal candidate for fabrication of symmetric cells with other V^{3+} phosphates such as $LiVPO_4F$,[648] because of the range of oxidation states of vanadium. Therefore, it was further studied in 2010,[649] although cycling stability over several cycles was poor. Symmetric $Na_3V_2(PO_4)_3$//1 M $NaClO_4$/PC//$Na_3V_2(PO_4)_3$ cells were found to work as reversible Na-ion batteries with coulombic efficiency of 75 % for the first cycle. When change the electrolyte was changed to a non-flammable electrolyte based on $EMIBF_4$ ionic liquid (1-ethyl-3-methyl imidazolium tetrafluoroborate) the examined symmetric cell showed decreased first discharge capacity and rate capability at high current densities, but exhibited better cycling performance due to the lower reactivity of the ionic liquid used.

Compounds based on the NASICON framework are remarkable because of their compatibility with aqueous electrolytes. This makes these phases very interesting from the economical point of view. In combination with the affordable price of Na, it would produce a low cost battery.

1.6 Anodic materials for Na-ion batteries

Much less works has centred on the anode materials compared to cathode materials. Pure metallic sodium is not a perfect anode material, because it will generate dendrite formation, as for metallic lithium. Besides, the safety of sodium anodes has been further put into question by its low melting point of 97.7 °C compared to 180.5 °C for lithium.[650] Furthermore, theoretical calculations based on the DFT method proved that current strategies and technologies are unlikely to be able to compete with their Li-ion

analogous in terms of volumetric energy density.[650] These findings highlight the need for new approaches in anodes for Na-based energy storage technologies.

Indeed, the search for appropriate anodes for Na-ion batteries is complex, and, although a great variety of phases that can potentially be used as cathode have been identified, few studies have shown suitable anode materials for Na-ion batteries.[651] Right now, the majority research has been devoting to carbon-based composites.[652-654] Among a variety of carbon materials only can the hard carbons sustain a capacity as large as 300 mA h g^{-1} due to their large interlayer distance and disordered structure.[652-654]

1.6.1 Carbon materials

Graphite, the common commercialized anode in Li-ion batteries, cannot be used as an insertion electrode in Na-ion batteries because Na atoms do not intercalate between the carbon sheets.[655-657] Most of the intercalation methods of alkali metals in graphite like vapor-phase reaction, high pressure reaction, electrochemical reaction and reaction in a solvent have been used and rendered a much lower amount of Na^+ ions between the graphene layers than for Li^+ ions. This is due to the fact that sodium hardly forms staged intercalation compounds with graphite.[658] Graphite electrochemical insertion of sodium into graphite is also expected to occur below the sodium plating potential ($\leq$ 0.1 V), thus the reductive or charging process cannot be observed.[15]

Other carbonaceous materials have been investigated, for instance, Doeff et al. studied the petroleum-coke carbon in 1993.[659] They observed that electrochemical insertion of sodium into a petroleum-coke carbon can result in reversible capacity of 85 mA h g^{-1}. Thus, they evidenced the highest value reported for electrochemical “intercalation” of

Na^+ ion on carbonaceous materials (NaC_{15}). At the same time, they also claimed that a stoichiometry of NaC_{24} (using coke) exhibited a reversible intercalation.

Subsequently, Tirado et al. observed the reversible insertion of 0.0155 moles of Na per cm^3 of amorphous carbon black, corresponding to capacity values of 121 mA h g^{-1}, and 200 mA h g^{-1} considering only the discharge.[660] They proposed that Na was stored between the bent graphene layers in the amorphous carbon black. Some years later, they optimized the amorphous carbon prepared from the pyrolysis of a polymeric resin forming microspheres with high surface area.[661] It showed improved electrochemical performance towards the Na-ion batteries. When ether type solvents were added to the liquid electrolyte, the capacity value for reversible insertion of Na^+ ion in this material was 285 mA h g^{-1}. As ether-type solvents have shown higher chemical stability against metallic sodium than carbonate based-electrolytes, the optimization of liquid and solid electrolytes containing ether groups could also be the key to improving the electrochemical efficiency.

Recently, a carbon template, which was prepared from mesophase pitch carbon precursor base on the porous silica template, was reported having 130, 120 and 100 mA h g^{-1} at C/5, 2C and 5C rates, respectively.[662] The first capacity value corresponds to a NaC_{17} nominal composition (17 carbon atoms are needed to accommodate one sodium atom). The authors claimed that the remarkable result is attributed to the hierarchical pore system in the material, which consists of interconnected pores in the macro- and mesopore range that enable fast ion transport and short diffusion lengths and a well-defined conductive carbon microstructure compared to other carbons.

Other sodium intercalation compounds were observed in soft carbons (small regions of ordered graphene) and hard (disordered) carbons.[657,663] The potential of Na insertion

into hard carbon is close to that of the metal itself, which indicates there was very little carbon to sodium charge transfer. This would occur if the sodium inserted into the carbon via pores at the surface. Sodium was found to insert between the disordered layers of the hard carbon. Hard carbon prepared from glucose demonstrated a capacity of 300 mA h g^{-1} at a slow current rate (C/80). Sodium insertion enhancement can also be achieved with heteroatoms like hydrogen and oxygen after pyrolysis of cellulose to produce hard carbons for intercalation. This method has evidenced higher reversible capacities for sodium intercalation than outgassed samples.[664]

1.6.2 Low potential metal phosphates

Recently Park et al. reported he use of NASICON-type $NaTi_2(PO_4)_3$ as possible anodes for both aqueous and non-aqueous Na-ion batteries at room temperature.[665] They proposed that Na intercalates into this compound following a two-phase mechanism at 2.1 V *vs.* Na/Na^+. In non-aqueous and aqueous electrolytes, $NaTi_2(PO_4)_3$ can obtain 120 and 123 mA h g^{-1} capacity respectively, corresponding to over 90 % of its theoretical capacity (133 mA h g^{-1}). It was also found that in the aqueous electrolyte, the polarization was substantially smaller than that in non-aqueous electrolyte, especially at a large current density due to the lower impedance and viscosity of the aqueous electrolyte. The aqueous electrolyte also benefit long cycle life, and sustainability for $NaTi_2(PO_4)_3$.

1.6.3 Low potential sodium metal oxides

Sodium intercalation into amorphous TiO_2 nanotubes was reported in 2011, which describes the use of transition metal oxide as possible anodes for a room temperature Na-ion battery.[666] This compound allows the intercalation of two Na^+ ions in a plateau

around 0.3 V *vs*. Na/Na^+, which corresponds to a 200 mA h g^{-1} specific capacity and accompanying reduction of 2/3 of the Ti^{4+} to Ti^{3+}. In this way, other titanate compounds that have been tested in Li-ion batteries, such as $Na_2Ti_6O_{13}$ or $Na_4Ti_5O_{12}$, could be applied to sodium ion technology. Similarly, vanadium oxides are also found to have low potential alkali intercalation property. For the O3 phase $NaVO_2$, many of the complex structural changes have taken place in the intercalation process.[667] On extraction process, the phase adopts a monoclinic distortion to form an O'3 structure where the octahedral site occupation of Na^+ is preserved.[668] Later, Hamani et al. confirmed the existence of these phases.[669] The voltage profile also demonstrated several steps on both charge and discharge processes between 1.2 V and 2.4 V. Electrochemical deintercalation can generate a capacity of 126 mA h g^{-1}. In addition, $Na_{0.7}VO_2$ was reported that exhibited very low polarization and presented a good high rate performance. A tunnel structured sodium vanadium oxide, NaV_6O_{13}, was synthesised with nanorod morphology, which presented three distinct plateaus at 2.7 V, 2.3 V and 1.7 V *vs*. Na/Na^+ in its voltage profile curve. It showed a substantial capacity loss at low cycling rates.

1.6.4 Alloys

Recently, the focus on the anode material for Na-ion batteries has shifted to sodium alloy materials, because it was released that Na^+/Na has a higher potential value compared with Li^+/Li, which can relieve electrolyte degradation on the surface of the electrode material. This critical point can benefit conversion reactions and alloying/dealloying processes with interface driven and through the continuous restructuration of the electrode material.[670] Na can alloy with many metallic elements such as Sn, Sb, germanium (Ge), lead (Pb), and the calculated theoretical specific

capacities are 847 ($Na_{15}Sn_4$), 660 (Na_3Sb), 1108 (Na_3Ge), and 484 ($Na_{15}Pb_4$) mA h g^{-1} respectively.[671] The first attempt of using an alloying reaction was reported based on the SnSb/C nanocomposite, which achieved 544 mA h g^{-1} capacity, good rate capacity and cyclability.[672] Later it was reported that pure micrometric antimony can sustain a capacity close to 600 mA h g^{-1} at a high rate in Na-ion batteries.[20] Antimony-based nanocomposites have demonstrated reversible capacities between 500 and 600 mA h g^{-1} over numerous cycles.[673]

Monconduit et al.,[670] recently, proposed that the alloy reaction mechanism with Na does not simply go through the alloying mechanism observed for Li where the intermediate species are those expected from the phase diagram. In the case of Na, the intermediate phases are mostly amorphous and could not be precisely identified. Through *In-situ* XRD analysis it was shown that a competition takes place at the end of the discharge of the Sb/Na cell between the formation of the hexagonal and the cubic polymorphs of Na_3Sb, the latter being described in the literature as unstable at atmospheric pressure and only synthesized under high pressure (1-9 GPa). They even demonstrated commercial micrometric Sb shows outstanding cycling performances *vs.* Na at a high rate, largely superior to the better known ones for Li. A capacity of 600 mA h g^{-1}, very close to the theoretical one (610 mA h g^{-1}), is maintained over 160 cycles with a constant Coulombic efficiency exceeding 98 %. They ascribed the very well-defined electrochemical features to the high crystallinity of the Sb material.

CHAPTER 2 EXPERIMENTAL METHODS

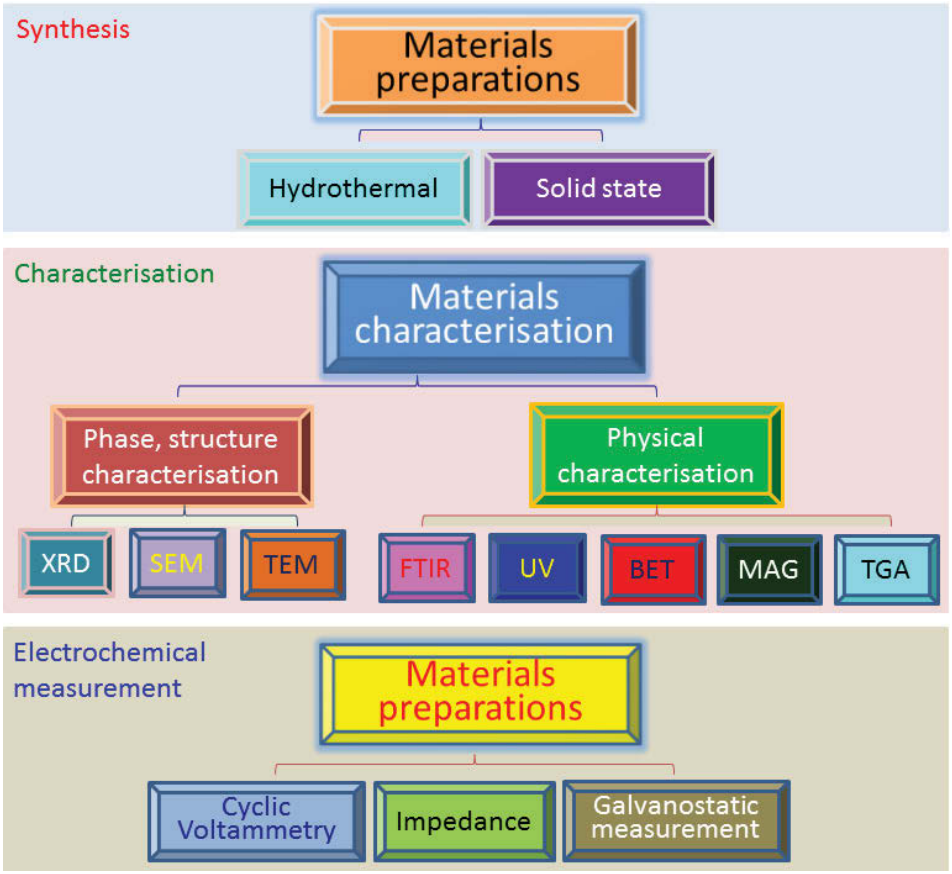

Figure 2-1 Flow chart of the research strategy in this thesis.

2.1 Overview

The design of nanostructured materials for electrochemical applications is based on the three main steps as shown by the flow chart (Figure 2-1). It includes: A) synthesis of active materials, B) characterisation of the as-prepared materials, and C) evaluation of their electrochemical performance. As shown in Figure 2-1, hydrothermal method and solid state method are the main synthesis strategies used in this study. The phase, morphology, and crystal structure of the as-prepared materials were seriously characterized by the X-ray Diffraction (XRD), scanning electron microscopy (SEM), transmission electron microscopy (TEM), and energy dispersive spectroscopy (EDS).

The other physical performances, such as magnetic and optical properties, were measured by the magnetometer, FT-IR, ultraviolet-visible (UV-vis), N_2 sorption (BET), and thermogravimetric and differential thermal analysis (TGA-DTA) etc. Following is the rough introduction of each step using in this thesis.

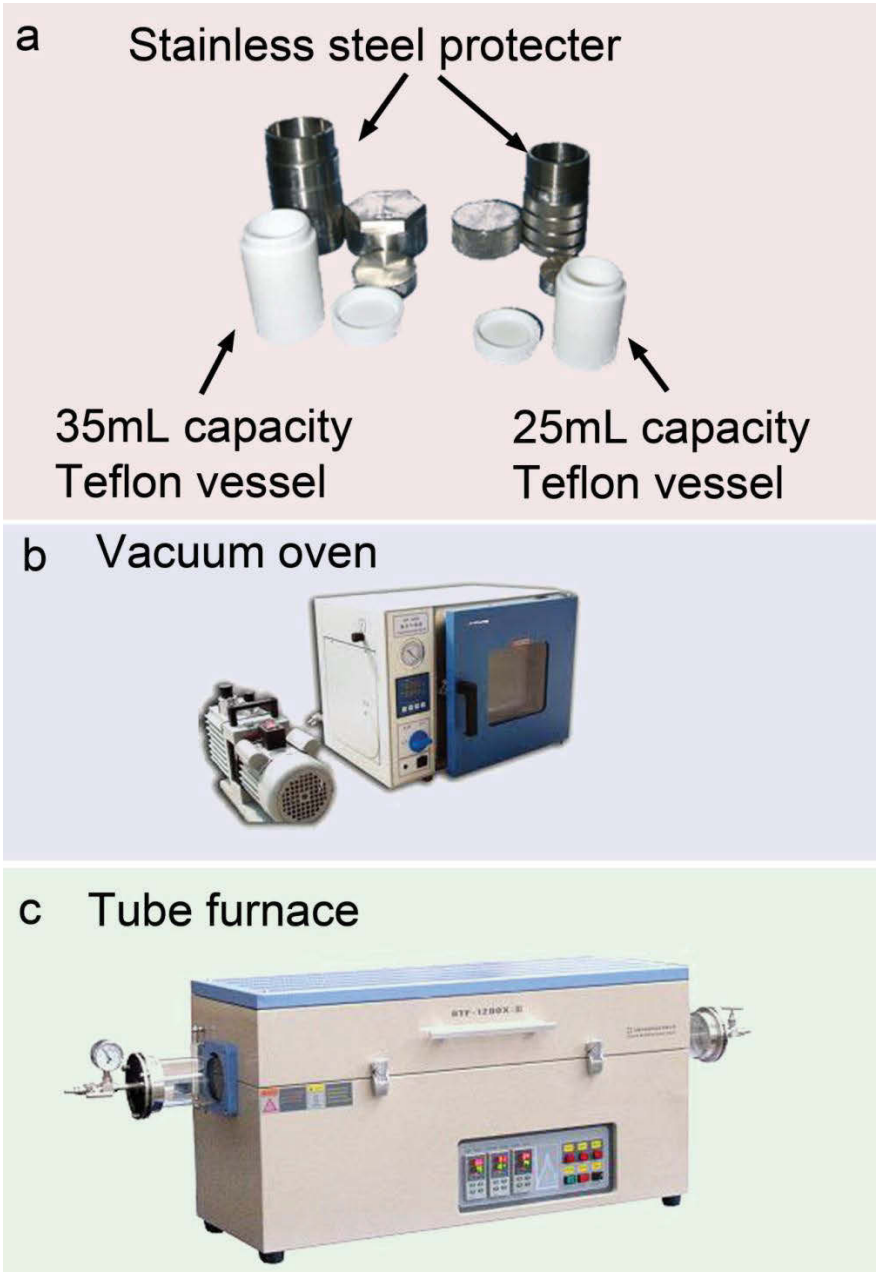

Figure 2-2 Photograph of the equipment used in this thesis.

2.2 Materials Preparation

In this research, hydrothermal method and solid state method were mainly used to synthesize nanostructure materials for the active electrode materials.

2.2.1 Hydrothermal Method

The hydrothermal synthesis process can prepare various single crystal materials from a high-temperature aqueous solution at a high vapour press. The crystal growth is performed in a gradient of temperature vessel, which is maintained at the opposite ends of the growth chamber so that the hotter end dissolves the nutrient and the cooler end causes seeds to undergo additional growth. There are several advantages of this synthesis method, including the ability to create crystalline phases which aren't stable at the melting point and prepare materials which have a high vapour pressure near their melting points. In addition, it does not need too high temperature. It is especially suit to the growth of large-scale, good-quality crystals while maintaining good control of their morphologies. As the aim of this study is to establish a relationship between the crystal structure of the electrode material and their electrochemical properties, the hydrothermal process is the appropriate method to synthesize crystalline active materials.

The hydrothermal synthesis procedure depends on the solubility of minerals in hot water or any other solvent, such as ethylene glycol (EG),[674] which the term should be named as solvothermal method. The experimented temperature is usually higher than 100 °C, so a well closed vessel such as a Teflon-lined autoclave or the well-sealed glassware is needed to avoid evaporation of the solvent. In this study, two capacities, 25 and 35 mL, of polytetrafluoroethylene (PTFE)-lined autoclaves have been used as shown in Figure 2-2 a. The upper limit of the reaction temperature is 220 °C. In addition, the whole experiment procedure involves the high pressure (generated by the high

temperature in the closed vessel), so the autoclaves must be placed a stainless steel protection shell, as shown in the Figure 2-2 a. There is a blowhole at the top part of the stainless steel protector, which releases gas and avoids explosion when the interior pressure is extremely high (might be due to the dramatic increase of evaporation pressure generated by the decomposition of the reaction chemical, such as the urea or ammonia, etc.).

To control the morphology and crystal structure of the products, several of the basic parameters can be adjusted: I the concentration of the precursors (density of the crystal seeds), II the volume of the solvent (control the inner pressure), III temperature (make the reaction happen properly), IV experiment time (maintain the growth of the crystal). Usually, other conditions also can be used to influence the final products, such as the use of a surfactant and the use of a solvent other than water. The heating apparatus for the hydrothermal reaction is the electronic oven as shown in Figure 2-2 b.

2.2.2 Solid-state reaction

The solid-state reaction route is the most widely used method to prepare polycrystalline solids from a mixture of solid starting materials. Solids cannot react together at ambient temperature over normal time scales, therefore it is necessary to heat them to much higher temperatures, often more than 500 to 1500 °C, in order for the reaction to occur at an appreciable rate. The tube furnace is used for the heating and maintaining the reaction at the appropriate temperature, as shown in Figure 2-2 c (36" Three Zones Split Tube Furnace with Optional Quartz Tube Flanges, product of MTI corporation[674]).

There are several factors on which the feasibility and rate of a solid state reaction change, including reaction conditions, structural properties of the reactants, surface area of the solids, their reactivity and the thermodynamic.[675,676]

The reagents are solid reactants from which solid crystalline compound are prepared. Prior to use, the reactants must be dried thoroughly and weighed according to the expected nature of the product. Usually in order to enhance reaction extension, fine grained materials should be used. After being weighed out in the required amounts, the reactants are mixed. For manual mixing of small quantities, usually an agate mortar and pestle are employed. Sufficient amount of some volatile organic liquid – preferably acetone or ethanol – is added to the mixture to aid homogenization. This forms a paste which is mixed thoroughly. During the process of grinding and mixing, the organic liquid gradually volatilizes and has usually evaporated completely after 10 to 15 minutes. For quantities much larger than ~ 20 g, mechanical mixing is usually adopted using a ball mill and the process may take several hours. Then the mixture will be pelleted to increase the surface area of contact between the grains and placed into a suitable container. The heating programme to be used depends very much on the form and reactivity of the reactants. According to the demand of the final products, the proper protection gas (argon, helium, nitrogen, hydrogen, etc.) will be selected to avoid oxidization. In the control of temperature, atmosphere, and nature of the reactant chemicals will be considered in detail.

In this thesis, solid state reaction route was employed for the phase transaction in chapter 7 and chapter 8.

2.3 Structural and Physical Characterization Method

2.3.1 X-ray Diffraction (XRD)

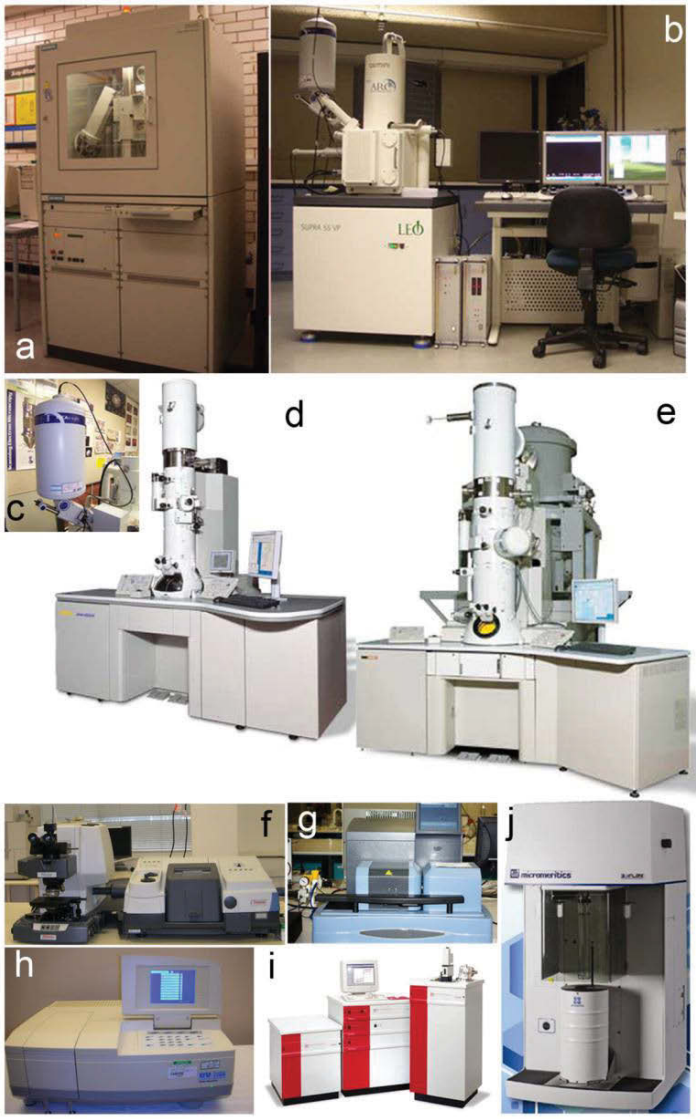

Figure 2-3 Instruments for the characterization of the as-prepared materials used in this thesis. a is XRD, b is SEM, c is EDS, d and e are the TEM, f is FT-IR, g is TGA, h is UV-Vis, i is SQUID, and j is N_2 adsorption/desorption instrument.

The XRD instrument used in this doctoral work to identify the phase and crystallographic structure of as-prepared materials was a Siemens D5000 diffractometer equipped by a Cu Kα1 radiation (λ = 1.54056 Å), as shown in Figure 2-3 a. Different 2θ range and scanning step were operated dependent on different demands.

Broadening the Full Width of single peak in the XRD patterns data was used to estimate the average size of the polycrystalline particles according to the Scherrer formula which was used by reference[22]:

$$\text{Crystallite Size} = K \times \lambda / FW(S) \times \text{Cos}(\theta) \quad (2\text{-}1)$$

where θ is the peak position, λ is the wavelength of the radiation and K is the shape factor of the average crystallite, and $FW(S)^D = FWHM^D - FW(I)^D$, where FWHM is the Full Width at Half Maximum and FW(I) is calculated from the current FWHM curve and D is called the deconvolution parameter.

2.3.2 Electron microscopy (EM)

2.3.2.1 Scanning Electron microscopy (SEM)

In this study, the morphology was analysed by high resolution field emission scanning electron microscopes (FESEM, Zeiss Supra 55VP) as shown in Figure 2-3 b. The microscope was operated at a working distance of 2 mm with an acceleration voltage of 20 kV. Inlens secondary detector was used to collect the filtered secondary electrons generated from the samples to give the final image. The Oxford Energy Dispersive Spectroscopy (EDS) was attached in the Supra 55VP for the elemental analysis or chemical characterization of as-prepared materials as shown in Figure 2-3 c.

2.3.2.2 Transmission electron microscopy (TEM)

The structured information of as-prepared materials in this thesis was acquired by transmission electron microscopy (TEM) and high-resolution transmission electron microscopy (HRTEM, JEOL JEM-2011) worked at an accelerating voltage of 200 kV.

The bright field image (BF) and selected area electron diffraction (SAED) patterns were recorded by a Gatan CCD camera in a digital format as shown in Figure 2-3 d. Some atomic resolution TEM images were collected by the transmission electron microscopy (HRTEM) FEGTEM 3000 (JEOL 300KV Atomic Resolution Transmission Electron Microscope (0.192 nm resolution)) worked at an accelerating voltage of 300 kV as shown in Figure 2-3 e.

2.4 Other physical characterization

2.4.1 Optical property measurement

2.4.1.1 Fourier Transform Infrared (FTIR) Spectroscopy

Fourier transform infrared spectroscopy (FTIR)[677] is a technique which is used to obtain an infrared spectrum of absorption, emission, photoconductivity scattering of a solid, liquid or gas. An FTIR spectrometer simultaneously collects spectral data in a wide spectral range. This confers a significant advantage over a dispersive spectrometer which measures intensity over a narrow range of wavelengths at a time. FTIR has made dispersive infrared spectrometers all but obsolete (except sometimes in the near infrared), opening up new applications of infrared spectroscopy.

FTIR spectra of the as-prepared materials in this doctoral work were recorded on a Bruker Tensor 27 IR spectrometer (as shown in Figure 2-3 f) by using KBr as the dispersant to assist in distinguishing the phase transaction.

2.4.1.2 Ultraviolet-Visible Spectroscopy

Ultraviolet-visible spectroscopy (UV-Vis) refers to absorption spectroscopy or reflectance spectroscopy in the ultraviolet-visible spectral region. It measures the

intensity of light passing through a sample (I), and compares it to the intensity of light before it passes through the sample (I_0). The ratio I/I_0 is called the transmittance, and is usually expressed as a percentage (%T). The absorbance, A, is based on the transmittance:

$$A = -\log(\%T/100\ \%) \qquad (2\text{-}2)$$

The UV-visible spectrophotometer can also be configured to measure reflectance. In this case, the spectrophotometer measures the intensity of light reflected from a sample (I), and compares it to the intensity of light reflected from a reference material (I_0) (such as a white tile). The ratio I/I_0 is called the reflectance, and is usually expressed as a percentage (%R).

The absorption or reflectance in the visible range directly affects the perceived color of the chemicals involved. In this region of the electromagnetic spectrum, molecules undergo electronic transitions. This technique is complementary to fluorescence spectroscopy, in that fluorescence deals with transitions from the excited state to the ground state, while absorption measures transitions from the ground state to the excited state.[678]

The band gap energy of the as-prepared Fe_2O_3 nanocrystals in this study Chapter 4 has been determined by ultraviolet-visible (UV-visible) spectroscopy using a Shimadzu UV-1700 spectrophotometer as shown in Figure 2- 3 h.

2.4.2 Magnetic property measurement

Magnetic measurements were performed using the Quantum Design MPMS-5 superconducting quantum interference device (abbreviation as SQUID) magnetometer in Chapter 5 to identify the crystal facets depended magnetic property as shown in

Figure 2-3 i. A SQUID is a very sensitive magnetometer used to measure extremely subtle magnetic fields, based on superconducting loops containing Josephson junctions.[679]

The magnetic moment was measured as a function of temperature under three different protocols: zero-field-cooled (ZFC), field-cooled upon cooling the sample (FCC), and field-cooled upon warming the sample (FCW). In the ZFC measurements, the sample was cooled in a zero magnetic field to 10 K. A magnetic field was then applied and the magnetic moment was measured upon warming the sample to 300 K in a constant field with a constant sweep rate of temperature. The FCC measurement was then performed by measuring the magnetic moment as the temperature was decreased from 300 K to 10 K without changing the field. The FCW measurement was followed by measuring the moment upon warming from 10 K to 300 K in the same magnetic field.

2.4.3 Thermogravimetric Analysis (TGA)

In this work, TGA was used to determine the carbon content of in the carbon composite materials. The TGA instrument used was Simultaneous TG-DTA (SDT 2960 as shown in Figure 2-3 g) with a platinum plate as the sample holder. The temperature can increase up to 1000 °C in air or N_2 atmosphere with a speed of 5-10 °C min^{-1}.

2.4.4 N_2 sorption measurement

In this dissertation, N_2 adsorption/desorption isotherms were measured by using an Micromeritics 3Flex analyzer at 77 K as shown in Figure 2-3 j, which is a fully automated, three-station instrument capable of high-throughput surface area, mesopore, and micropore analyses with superior accuracy, resolution, and data reduction. BET surface area was calculated using the isothermal points at a relative pressure of P/P_0 =

0.05-0.25. The pore size distribution was calculated by the Barret–Joyner–Halenda (BJH) method.

2.5 Electrode Preparation and Cell Assembly

To prepare the working electrode, the appropriate ratio of as-prepared electrode materials, acetylene black, and poly (vinylidene fluoride) (PVDF) were mixed in N-methyl-2-pyrrolidone (NMP) to form a slurry. The mass of each electrode is around 1.4 mg (the active material is around 1 mg). For the cathode materials, the resultant slurry was pasted onto aluminium foil (size 1 cm × 1 cm), while anode materials were pasted onto copper foil (size 1 cm × 1 cm), with a blade. Following this, the electrode was dried at 100 °C for 12 h under the vacuum condition and followed by pressing at 200 kg cm^{-2}.

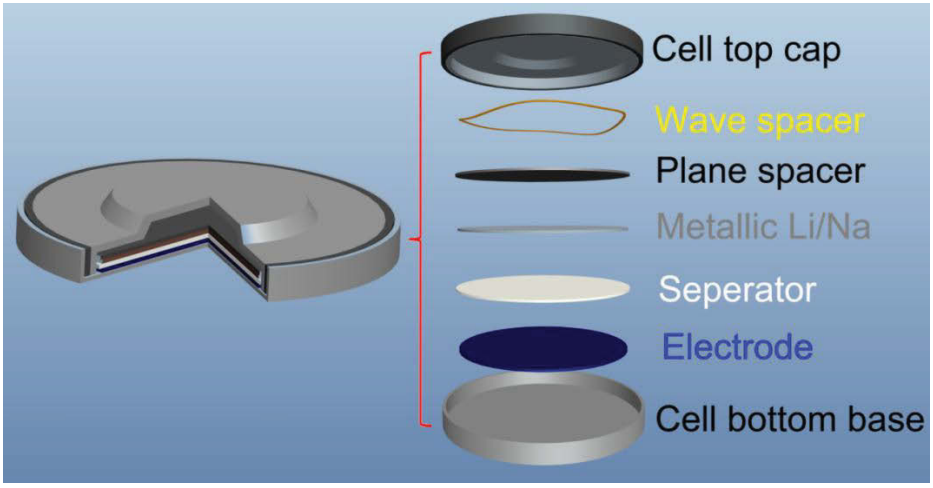

Figure 2-4 Schematic diagram of the CR2032 coin type cell configuration.

Electrochemical measurements were carried out using two-electrode coin cells (CR2032). A schematic diagram of the configuration of the coin-type cell is shown in Figure 2-4. For the Li-ion batteries, the cells contained the as-prepared electrode as the working electrode, lithium foil as the counter and reference electrode, a porous

polypropylene (Celgard 2300) as the separator. Two kinds of electrolyte solutions purchased from Zhangjiagang Guotai-Huarong New Chemical Materials Co., Ltd were used in this study. LB301 is 1M $LiPF_6$ in a 1:1 mixture of ethylene carbonate (EC) and dimethyl carbonate (DMC). LB303 is 1M $LiPF_6$ in a 1:1:1 mixture of ethylene carbonate (EC), diethyl carbonate carbonate (DEC) and dimethyl carbonate (DMC).

For the Na-ion batteries test, Na metal was worked as the counter and reference electrodes and using the glass microfiber (Whatman) works as the separator. The electrolyte solution was 1 M $NaClO_4$ dissolved in a mixture of ethylene carbonate (EC) and propylene carbonate (PC) with a volume ratio of 1:1.

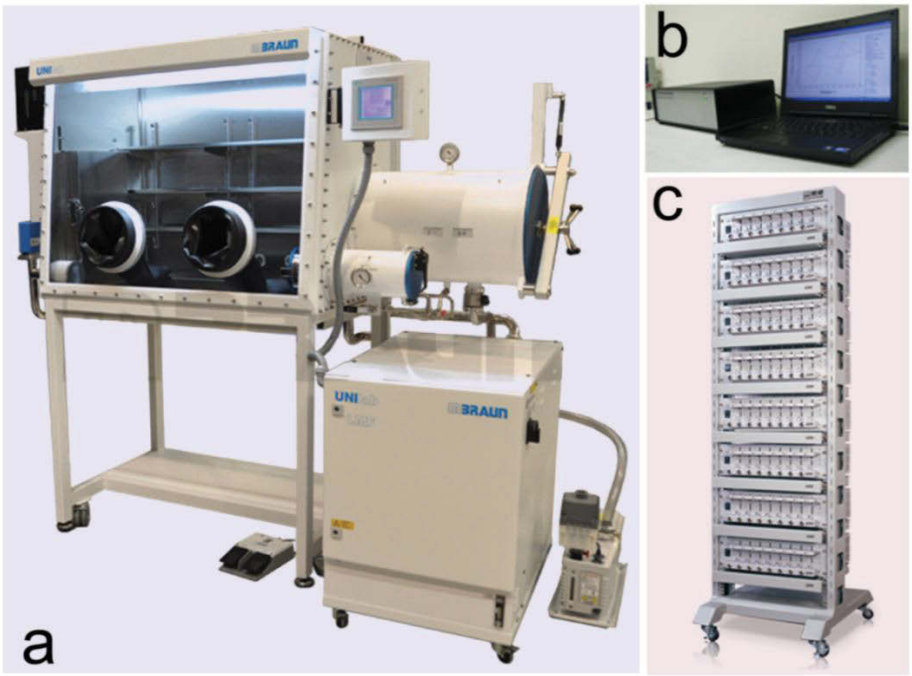

Figure 2-5 Photographs of (a) glove box, (b) CHI instrument, (c) Neware battery test system.

The cells were assembled in an argon filled glove box (Unilab, Mbraun, Germany) as shown in Figure 2-5 a, with O_2 and H_2O levels less than 0.1 ppm.

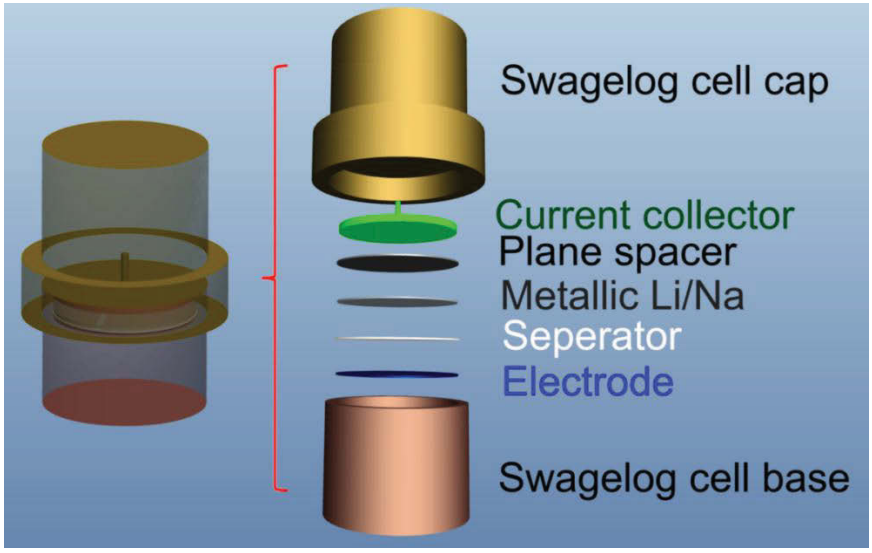

Figure 2-6 Schematic diagram of the Swagelog-type cell configuration.

In some cases, in order to investigate the structural and morphological changes of electrode crystals, Swagelog-type cells were assembled as shown in Figure 2-6. After cycling at required status, the cells were disassembled and the electrodes were soaked in DMC or PC in Glove-box for 24 h to remove the organic residues before used for *Ex-situ* SEM, TEM, or XRD analyses.

2.6 Electrochemical measurement

The electrochemical measurements for evaluating the electrochemical performance of Li-ion batteries and Na-ion batteries included cyclic voltammetry (CV), galvanostatic charge-discharge testing, and electrochemical impedance spectroscopy.

2.6.1 Cyclic Voltammetry

Cyclic voltammetry (CV) is a type of potentiodynamic electrochemical measurement and has been widely used to characterize the electrochemical performance of Li-ion batteries.[680]

In cyclic voltammetry, the electrode potential ramps linearly *vs.* time. This ramping is known as the experiment's scan rate (V s^{-1}). The potential is applied between the reference electrode and the working electrode and the current is measured between the working electrode and the counter electrode. These data are then plotted as current (i) *vs.* potential (E). There are forward scanning which will produce a current peak for any analytes that can be reduced (or oxidized depending on the initial scan direction) through the range of the potential scanned. The current increases as the potential reaches the reduction potential of the analyte, but then falls off as the concentration of the analyte is depleted close to the electrode surface. If the redox couple is reversible, reverse of application potential reaches a potential that will reoxidize the product formed in the first reduction reaction, and produce a current of reverse polarity from the forward scan. This oxidation peak will usually have a similar shape to the reduction peak. As a result, information about the redox potential and electrochemical reaction rates of the compounds is obtained.[680-682]

In this study, the CV measurements were conducted two electrode system, a lithium foil was used as both counter and reference electrode. While for the measurement of supercapacitance, a beaker-type three-electrode cell was fabricated using the as-prepared active materials as the electrode material. Platinum foil and a saturated calomel reference electrode (SCE) were used as the counter electrode and the reference electrode, respectively. CV measurements were conducted over the appropriate voltage range *vs.* SCE at various scanning rates. The specific capacitance C (F g^{-1}) was calculated based on the following equation:

$$C = Q / v \times m \times \Delta E \qquad (2\text{-}3)$$

Where Q is the voltammetric charge obtained by integrating the cyclic voltammogram curve; v is the scanning rate, m is the active mass of the electrode material; and ΔE is width of the potential window.

The CV measurements in this doctoral work were conducted via a CHI 660C or CHI 660D electrochemical workstation (CH Instrument, Cordova, TN) as shown in Figure 2-5 b.

2.6.2 Galvanostatic Charge and Discharge

The capacity is the most important criterion used to evaluate an electrode material. Generally, the capacity is the product of the current (A) multiplied by the time (h). In this study, the capacity of the electrode material was calculated by galvanostatic charge and discharge testing. The measurement was conducted under a constant current density. The charge/discharge capacities (Q) can be calculated using the following formula:

$$Q = I \times t \tag{2-4}$$

where I is current density and t is the charge/discharge time.

Different voltage cut-off ranges were chosen for different materials to evaluate their possible electrochemical performance. The test cells also were monitored at different charge/discharge currents, defined as the C-rate performance, which was used to evaluate the capacity of the electrode at different charge/discharge current densities. In units of current per mass of cell, as well as the C/n rate convention, n is the time (h) for complete charge or discharge at the nominal capacity.

The galvanostatic charge-discharge measurements in this doctoral work were collected on a computer-controlled Neware battery testing system as shown in Figure 2-5 c.

2.6.3 Electrochemical Impedance Spectroscopy (EIS)

Electrochemical impedance spectroscopy (EIS), measures the dielectric properties of a medium as a function of frequency.[683-685] Often, EIS reveals information about the reaction mechanism of an electrochemical process: different reaction steps will dominate at certain frequencies, and the frequency response shown by EIS can help identify the rate limiting step.

This technique measures the impedance of a system over a range of frequencies, and therefore the frequency response of the system, including the energy storage and dissipation properties, is revealed. Often, data obtained by EIS is expressed graphically in a Bode plot or a Nyquist plot.

Impedance is the opposition to the flow of alternating current (AC) in a complex system. A passive complex electrical system comprises both energy dissipater (resistor) and energy storage (capacitor) elements. If the system is purely resistive, then the opposition to AC or direct current (DC) is simply resistance.

In this thesis, the EIS data were collected from a CHI 660C or CHI 660D electrochemical workstation (CH Instrument, Cordova, TN). By monitoring the current response, the variation of resistance with frequency was examined. The obtained impedance Nyquist curve of battery system consists of a compressed semicircle in the medium-frequency region which was assigned to be the charge-transfer resistance (R_{ct}) and an inclined line in the low frequency range, which was assigned to be Warburg impedance.

2.7 Computational methods

2.7.1 The choice of theory

Basically, there are two methods to analyse the chemical and physical properties at an atoms scale: i): constructing a model containing free parameters and fitting it to experimental data, ii): one mounting a brute-force attack to determine the eigenfunctions and eigenvalues by solving the Schrödinger equation, or a similar relativistic equation. The later approach is mostly known as a first principle, or ab initio, calculation.

All theoretical calculations included in the thesis are based on density functional theory [686,687] - an approximate ab initio method. Semi-empirical and/or parametrized force-fields were not used here because the goal in many of the papers was to predict trends related to changes in chemical bonds (which is what one usually parametrizes, in order to predict e.g. structure and phase transitions).

Several ab initio methods can routinely be used for the simulation of big clusters, and doped supercells with > 100 atoms, including standard Hartree-Fock, 2nd order Møller-Plesset perturbation theory (MP2), and density functional theory (DFT). Coupled-cluster, higher-order perturbation theory, and quantum Monte Carlo are too computationally expensive. In this study, the DFT method was chosen because even the simplest local density approximation to the exchange-correlation energy gives better chemistry than Hartree-Fock. Additionally, predictions by generalized gradient approximations (GGA) such as PBE,[688] can surpass second order Møller-Plesset perturbation theory (MP2) wave functions.[689,690] Moreover, DFT is a well-developed quantum mechanical modelling method used in physics and chemistry to investigate the electronic structure (principally the ground state) of many-body systems, in particular atoms, molecules, and the condensed phases. With this theory, the properties of a many-

electron system can be determined by using functions, which is the spatially dependent electron density.

DFT has been very popular for calculations in solid-state physics since the 1970s. However, DFT was not considered accurate enough for calculations in quantum chemistry until the 1990s, when the approximations used in the theory were greatly refined to better model the exchange and correlation interactions. In many cases the results of DFT calculations for solid-state systems agree quite satisfactorily with experimental data.

There is a critical shortcoming of DFT, regarding the oxide state change of the transition metal produced by lithium deintercalation in the cathode materials in this work. The transition metals are bound to oxygen in tetrahedral or octahedral sites in the intercalation cathode material, such as the [FeO_4] tetrahedron in the Li_2FeSiO_4 crystal structure. The chemistry of Fe atoms cannot be treated accurately as normal DFT, due to the underestimation of intercalation voltages. The Li^+ ion binding in these materials is almost purely electrostatic and should be well represented by DFT, so the error is instead in the change of the transition metal's oxidation state. When the electron is extracted from a localized 3d orbital of e.g. Fe, and transferred to the metallic 2s orbital of the Li^+ ion in the crystal, it will experience much less self-interaction in the metallic state of lithium, producing an underestimation of the energy required for this redox process, and thus give an appearance of lower intercalation voltage. To tackle this problem, a GGA+U model was established to simulate the effect of localized electrons which can complement part of the missing voltage. However it must be pointed out that it still cannot accurately predict the properties of the material, because different model

parameters (U and J) are necessary to calculate the intercalation voltage over the cathode's complete lithium capacity range.

2.7.2 Methods and models of calculation

The calculations were performed based on the DFT + U approach[691] with the ABINIT.[692,693] The exchange-correlation energy function was represented by the local-density approximation (LDA) or the generalized gradient approximation (GGA) of Perdew, Burke and Ernzerhof (PBE),[688] employing ultra-soft pseudopotential (USPP) formalism.[694] This method allows a precise predication of the occupation state, which is a key factor for understanding the fundamental electronic properties of materials. The appropriate energy cutoff, and Monkhorst-Pack k-point were used to set up the calculation parameters. The effective values for on-site Coulomb repulsion (Hubbard U), which were derived by fitting to experimental oxidation enthalpies (it will gave better estimates for band gaps),[695] were applied for transition metal d states. The maximum self-consistent field convergent tolerance was chosen for calculating step converging. All calculations were performed in reciprocal space.

The activation barriers of Li^+ ion vacancy are estimated using the Nudged Elastic Band (NEB) method.[696] Calculated activation energies converged typically within 0.02 eV. The effects of cation exchange are also investigated based on the anti-site cation migration to adjacent vacant sites. Such cation mixing sites and Fe on Li sites may affect the Li ion migration and influence the electrochemical kinetics during Li extraction.

The structures and energies of the crystal surfaces were modelled using classical energy minimisation techniques. These atomistic simulation methods are based on the Born model of solids,[697] which assumes that ions in a crystal interact via short-range electrostatic forces and long-range van der Waals interactions between neighboring electron charged clouds. The electronic polarisability of the ions is included via the Bush shell model[698] which is especially for binary and ternary oxides. The Buckingham potential,φ_{ij} given in Eq. (2-5), is used to treat the short-range interactions:

$$\varphi_{ij} = Aexp\left(-\frac{r_{ij}}{\rho}\right) - \frac{C}{r_{ij}^6} \quad (2\text{-}5)$$

where r_{ij} is the separation of the ion centres and A, ρ, and C are ion-ion parameters. In order to model the long-range polarisation energy for defects, a massless shell,[699] on which all pair potentials act as coupled by a harmonic force to a core from which it is Coulombically screened:

$$E_{(core-shell)} = \frac{1}{2}k_{(core-shell)}r_{ij}^2 \quad (2\text{-}6)$$

yielding an ion polarisability α_i

$$a_i = \frac{q_{shell}^2}{k_{(core-shell)}+f_{shell}} \quad (2\text{-}7)$$

where $E_{(core\text{-}shell)}$ is the long-range polarisation energy, q_{shell} is the shell charge, $k_{(core\text{-}shell)}$ represents the restoring force between the core and the shell, and f_{shell} is the competing distorting forces due to the presence of the surrounding ions. Lattice energy calculations are combined with energy minimisation methods so that structural parameters are adjusted to obtain a minimum energy configuration.

According to the classification of Tasker,[700] there are three different types of surfaces: (1) an uncharged plane with cations and anions in stoichiometric ratio; (2) a stack of charged planes where the repeat unit perpendicular to the surface has no dipole moment; and finally (3) a stack of charged planes where the repeated unit has a dipole moment

perpendicular to the surface. In the last instance, the surface needs to be reconstructed to remove the dipole. This can be obtained by creating surface vacancies. The surface energy per unit area, $E_{surface}^{hkl}$, of a particular surface is calculated from the difference between the energy of the surface block, $E_{surface\ block}$, and the energy of the same number of bulk ions, E_{bulk}, per unit area, A, thus

$$E_{surface}^{hkl} = \frac{E_{surface\ block} - E_{bulk}}{A} \quad (2\text{-}8)$$

The attachment energy is defined as the energy per formula unit released when a new slice of depth d_{hkl} is attached to the crystal face, and assumed to be proportional to the growth rate by a layer-by-layer mechanism. Thus, surfaces with attachment energies smaller in magnitude have slower growth rates and can be morphologically important. The attachment energy can be expressed as

$$E_{attachment}^{hkl} = \frac{E_{crystal} - E_{slice}}{n} \quad (2\text{-}9)$$

where $E_{crystal}$ is the energy of the crystal, E_{slice} is the energy between all the ions within the slice hkl, and n is the number of formula units per slice.

For slab model construction, enough layers with large enough depths of the surface regions were chosen to ensure full relaxation of the surface ions and convergence of the surface energy. In each of case, surface structures were fully relaxed until the total energy difference was converged within 0.001 eV.

CHAPTER 3 AB INITIO CALCULATIONS ON STRUCTURAL AND ELECTROCHEMICAL PROPERTIES OF Li_2FeSiO_4 FOR LI-ION BATTERIES

3.1 Abstract

We have systematically investigated the crystal structure and electronic structure of Li_2FeSiO_4 and its delithiated products $LiFeSiO_4$ and $FeSiO_4$ based on a monoclinic supercell with the $P2_1$ symmetry. The expansion of the unit cell volume has been clearly identified for Li_2FeSiO_4 cathode material during the lithium extraction process. The calculations on the voltage profiles of Li_2FeSiO_4 suggest a two-step voltage plateau at 3.10 V and 4.16 V for $Fe^{+2/+3}$ and $Fe^{+3/+4}$ redox couples. Through calculations on density of states and partial density of states, we also confirmed that the electron transfer mainly occurs in Fe atoms during the lithium extraction and insertion process. Furthermore, we have studied the diffusion mechanism of Li ions in Li_2FeSiO_4 and its delithiated product $LiFeSiO_4$ with the $P2_1$ symmetry. The calculations on the energy barriers for possible spatial hopping pathways predicted that the activation barriers along the [101] direction and Li ion layer in the ac plane are relatively low, which can ensure the facile lithium diffusion along those directions. The migration through the voids in the Fe-Si layer along the body diagonal direction is unlikely, due to high barrier energy. The results indicate that Li_2FeSiO_4 with the $P2_1$ symmetry is an ionic conductor for Li ions with two-dimensional diffusion.

3.2 Introduction

Li-ion batteries are the most advanced power sources for portable electronic

devices. They are also currently being considered as the state-of-the-art candidate to power electric vehicles (EVs) and hybrid electric vehicles (HEVs).[701] However, conventional cathode materials, such as lithium cobalt oxide and lithium nickel cobalt oxide, cannot meet the requirements of large-scale and high-power applications due to the sizeable cost, safety and environmental concerns of cobalt. Lithium manganese oxides (either spinel or layered structure) have been explored as alternative cathode materials for large-size Li-ion batteries, but suffer from relatively low specific capacity and poor cyclability.[2-4] In recent years, lithium iron phosphate has emerged as a promising cathode material for power lithium batteries, particularly for high- power applications, which can be ascribed to its low cost and high thermal stability.[702,703] Within the same crystal structure family of $(XO_4)^{n-}$ polyanion compounds, orthosilicates Li_2MSiO_4 (where M is a transition metal) have also been considered as attractive cathode materials due to the virtue of their potential ability to extract more than one Li ion per formula.[270,704,705] Recently, lithium iron orthosilicate Li_2FeSiO_4 has been reported to exhibit reversible electrochemical activity with a specific capacity of 166 mA h g^{-1}.[276] Furthermore, this type of material generally allows a wide range of solid solutions with various compositions. Therefore, Li_2FeSiO_4 presents an exciting platform to explore new cathode materials for next generation high power Li-ion batteries.

The different crystal structure of Li_2FeSiO_4 has been successfully synthesized.[279,280,706,707] Through Rietveld refinements on a powder X-ray diffraction profile, it was proposed that the pristine Li_2FeSiO_4 has a β-Li_3PO_4-based structure ($Pmn2_1$ symmetry), in which, all the cations occupy half of the tetrahedral sites in a slightly distorted hcp oxygen array, forming a corner-sharing network of tetrahedron with an identical upward direction.[276] However, Shin-ichi Nishimura et al. recently

indicated three major problems associated with the $Pmn2_1$ structure for Li_2FeSiO_4. They proposed that Li_2FeSiO_4 more possibly adopt a monoclinic super cell ($P2_1$ symmetry). This assumption has been confirmed by the powder HR-XRD and SAED patterns along various zone axes.[708] Compared with $Pmn2_1$, the fully delithiated $MSiO_4$ with $P2_1$ structure has better stability. In Li_2FeSiO_4, the possibility of reversibly extracting more than one Li ion is enhanced because of the lower stability of the intermediate phase $LiFeSiO_4$, compared with the $Pmn2_1$ symmetry situation. Moreover, it was also found that Li_2FeSiO_4 based on the $P2_1$ symmetry structure are all stabilized in their ferromagnetic phase, while the delithiated compounds are all stabilized in the antiferromagnetic phase.[289] Examination of the intrinsic Li ion mobility in Li_2FeSiO_4 is of vital interest when considering its application as a cathode material in Li-ion batteries. However, to the best of our knowledge, there has been no report on the establishment of Li ion diffusion mechanisms in the Li_xFeSiO_4 (x = 1, 2) with the $P2_1$ symmetry structure so far. Similar calculations have been successfully applied to other cathode materials, including $LiCoO_2$ [709] and related layered and spinel systems.[710,711] One-dimensional Li ion transport has been proposed for $LiFePO_4$.[226,712,713] Recently, such calculations on the Li_3PO_4 have also been reported.[714] (Using atomistic simulation techniques it is possible to examine various diffusion paths by evaluating the activation energies at the atomic level for Li ion conduction, which are often difficult to probe on the atomic scale by experiment alone.)

This chapter presents a study on the crystal structure and electrochemical properties of Li_2FeSiO_4 cathode material based on the $P2_1$ symmetry with a monoclinic super cell. Model systems for Li_2FeSiO_4 and its delithiated phases $LiFeSiO_4$ and $FeSiO_4$ have been investigated using the density function theory (DFT) method. Through

this, the relationship between their electronic structure and electrochemical properties were established. In addition, we also computed the precise voltage profiles during lithium intercalation/de-intercalation in $Li_2FeSiO_4/LiFeSiO_4$ and $LiFeSiO_4/FeSiO_4$. We also investigated possible Li ion migration pathways and diffusion barriers for Li_xFeSiO_4 (x = 1, 2) cathode materials.

3.3 Methods and models of calculation

Ab initio calculations were carried out using the density functional theory (DFT) in the ultra-soft pseudopotential (USPP) formalism,[715] and implemented with the generalized gradient approximation (GGA) of Perdew, Burke and Ernzerhof (PBE) for the exchange correlation energy.[688] This method allows a precise predication of the occupation state, which is a key factor for understanding the fundamental electronic properties of materials.

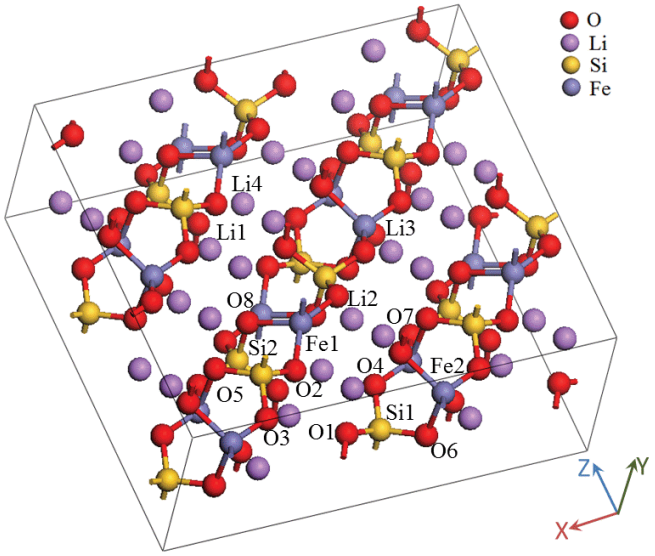

Figure 3-1 The structure of $P2_1$ symmetry with a monoclinic super cell.

Figure 3-1 shows the crystal structure of Li_2FeSiO_4 based on the $P2_1$ symmetry.[708] The intensities of the super cell reflection have been successfully illustrated by

considering the modified anion arrangement in the new set of monoclinic unit cells. The structural modulation leads to the variation in the orientation of trigonal pyramids, particularly those in the corner-shared one dimensional FeO_4 and SiO_4 chains along the $[\bar{1}01]$ direction.

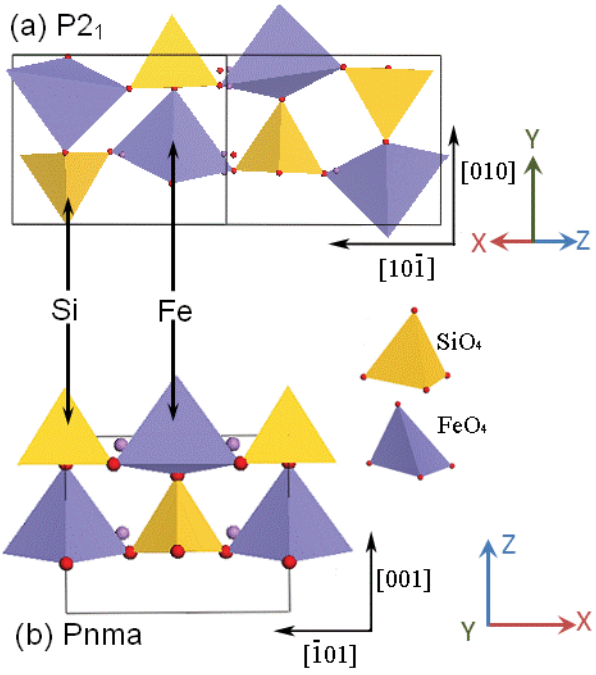

Figure 3-2 Corner-shared FeO_4 and SiO_4 in (a) the $P2_1$ structure model of Li_2FeSiO_4 and (b) the Pnma structure model.

Figure 3-2 further compares the structure of Li_2FeSiO_4 in the $P2_1$ and Pnma symmetry, respectively. In the $P2_1$ model, FeO_4 and SiO_4 trigonal pyramids periodically take opposite orientations, as shown in Figure 3-2 (a). It is strikingly contrasted to the previous orthorhombic Pnma model (as shown in Figure 3-2 (b)), where the orientations of all trigonal pyramids are identical. Atomic fractional coordinates and the crystallographic cell shape were relaxed at fixed volume. During the relaxation process, integrals were calculated over the Brillouin zone by the tetrahedral method of Blöchl with k-points based on a 2×4×2 Monkhorst and Pack

grid.[716] To address the on-site Coulomb energy interactions in the localized d electrons of the transition metal ions (Fe) in the silicates, an additional Hubbard-type U-term is taken into account with the GGA+U approach. This method was developed by Anisimov et al.[717] and has been widely used in DFT calculations.[718,719] With a larger value of U, the hybridization effect of the metal with its neighbors will be more reduced. The effective value U for Fe in this study was derived to be 5.0 eV by fitting to experimental oxidation enthalpies. It has given better estimations for band gaps,[720] which provides reasonably good approximations to the average U for Fe^{2+} and Fe^{3+} in the phosphate and silicate compounds.[721,722] For the calculations of partial density of states (PDOS) and density of states (DOS), the finer 3×5×3 grid in Brillouin Zone integration were approximated. Fe atoms were set in an antiferromagnetic spin-polarized arrangement in the ab-plane. The cut-off energy of plane wave was set at 380 eV. The maximum self-consistent field convergent tolerance was less than 2×10^{-6} eV $atom^{-1}$. All calculations were performed in the reciprocal space. For all cases, the 1 × 1 × 1 super-cell model consisting of four formula units (32 atoms in total) was used.

The starting crystal structures of $LiFeSiO_4$ and $FeSiO_4$ were obtained by removing Li(1) and Li(3) ions from the optimized Li_2FeSiO_4, and Li(2) and Li(4) ions from optimized $LiFeSiO_4$ structures, respectively, using the so called virtual crystal approximation (VCA).[282,723] The crystal structures were then relaxed in the same way as described above. Partial states of lithiation were also investigated at x = 0.25, 0.5, 0.75, 1.25, 1.5, and 1.75 in a supercell with four formula units.

The simulations of Li ion migration were carried out using the fixed volume supercells composed of 127 and 111 periodic atoms with 16 formula units in the

dimension a×2b×2c. The charged supercells are compensated with a uniform background charge for the purpose of calculating the Coulomb interaction. The distance between the created vacancy and its periodic image is >10 Å for the chosen cell-size. Several different pathways are probed, leading to effective Li-vacancy migration. The activation barriers of Li ion vacancy are estimated for $Li_{x-y}FeSiO_4$ (x = 1, 2, y≈0.06) using the Nudged Elastic Band (NEB) method.[696] Calculated activation energies converged typically within 0.02 eV. The effects of Li and Fe cation exchange are also investigated based on the anti-site cation migration of both Li_{Fe} and Fe_{Li} to adjacent vacant Li sites. Such cation mixing with Li on Fe sites and Fe on Li sites may affect the Li ion migration and influence the electrochemical kinetics during Li extraction.

3.4 Results and discussion

3.4.1 Structural characteristics of Li_2FeSiO_4, $LiFeSiO_4$ and $FeSiO_4$

Table 3-1 Optimized lattice parameters of Li_2FeSiO_4, $LiFeSiO_4$ and $FeSiO_4$.

Lattice parameters	Li_2FeSiO_4	$LiFeSiO_4$	$FeSiO_4$
a (Å)	8.21902 [8.22898(18)][a]	8.60728	8.99635
b (Å)	5.02380 [5.02002(4)][a]	5.20601	5.36468
c (Å)	8.22164 [8.23335(18)][a]	8.29366	8.43740
β (deg)	101.2698 [99.2027(5)][a]	92.8961	84.4178
Cell volume ($Å^3$)	332.931 [335.740(11)][a]	371.161	405.280

[a] Values in brackets are experimental values (Ref. [708]), standard deviations given in parentheses.

We calculated the lattice parameters of Li_2FeSiO_4 and its delithiated products: $LiFeSiO_4$ and $FeSiO_4$, based on the $P2_1$ symmetry. The results are shown in Table 3-1. For $LiFeSiO_4$, the calculated lattice parameters *a* and *c* are smaller than that of the experimental data, while *b* is almost the same as the experimental data. The calculated angle *β* is 2 degrees larger than that of the experimental one. The calculated cell volume of Li_2FeSiO_4 is 0.8 % smaller than that of the experimental value. The differences between calculated lattice parameters and the experimental data are less than 0.5 %, indicating good accuracy of the GGA method.

It should be noted that the lattice parameters *a*, *b*, and *c* increase with the extraction of Li ions. In contrast, the *β* angle decreases and becomes an acute angle (84.4178º) after the extraction of Li ions. From Li_2FeSiO_4 to $LiFeSiO_4$, the volume of the unit

cell expands by 11.5 % and further increases by 9.2 % when fully delithiated to $FeSiO_4$. This represents a significant expansion in volume of the unit cells with the de-intercalation of Li ions. The atomic fractional coordinates of Li_2FeSiO_4 were also computed based on the $P2_1$ symmetry, and the results are presented and compared with the experimental data[708] in Table 3-2.

Table 3-2 Optimized calculated and experimental (Ref. [708]) atomic fractional coordinates for Li_2FeSiO_4.

Atom	Experimental data			Calculated data		
	x	y	Z	x	y	z
Li(1)	0.670	0.903	0.670	0.6574	0.9175	0.6693
Fe(1)	0.2883	0.916	0.5371	0.2808	0.9172	0.5304
Si(1)	0.0438	0.805	0.7939	0.0518	0.8166	0.8026
O(1)	0.8583	0.920	0.8264	0.8696	0.9108	0.8368
O(2)	0.3742	0.835	0.3310	0.3689	0.8202	0.3359
O(3)	0.4293	0.325	0.8980	0.4221	0.3007	0.8777

Table 3-3 Calculated bond length (Å) and angle (deg) within the SiO_4 and FeO_4 tetrahedron for Li_2FeSiO_4, $LiFeSiO_4$ and $FeSiO_4$.

Bond length and angle		Li_2FeSiO_4	$LiFeSiO_4$	$FeSiO_4$
Fe(1)	-O(2)	1.942 [1.97(2)] [a]	1.846	1.785
	-O(4)	1.958 [1.999(11)] [a]	1.994	1.788
	-O(5)	1.965 [2.06(3)] [a]	1.773	1.750
	-O(8)	1.945 [2.06(7)] [a]	1.820	1.750
Mean		1.953[2.025] [a]	1.858	1.768
Fe(2)	-O(1)	1.941 [2.03(2)] [a]	1.894	1.785
	-O(3)	1.960 [1.960(13)] [a]	1.780	1.792
	-O(6)	1.964 [2.12(7)]	1.843	1.750
	-O(7)	1.944 [2.01(3)] [a]	1.896	1.748
Mean		1.952 [2.030] [a]	1.854	1.769
Si(1)	-O(1)	1.646 [1.64(3)] [a]	1.656	1.639
	-O(4)	1.642 [1.56(3)] [a]	1.666	1.642
	-O(6)	1.645 [1.59(3)] [a]	1.654	1.654
	-O(7)	1.647 [1.68(7)] [a]	1.662	1.629
Mean		1.645 [1.618] [a]	1.660	1.641
Si(2)	-O(2)	1.645 [1.58(3)] [a]	1.653	1.641
	-O(3)	1.642 [1.70(3)] [a]	1.649	1.641
	-O(5)	1.645 [1.63(3)] [a]	1.651	1.654
	-O(8)	1.646 [1.57(7)] [a]	1.624	1.630
Mean		1.645 [1.621] [a]	1.647	1.6414
Fe(1)-O(5)-Si(2)		114.646	132.717	135.731
Fe(2)-O(6)-Si(1)		114.702	121.897	136.067
Fe(2)-O(7)-Si(1)		117.412	127.452	150.461
Fe(1)-O(8)-Si(2)		117.395	138.052	148.911
Mean		116.039	130.030	142.793

[a]Reference values for Li_2FeSiO_4 are also given for comparison as shown in brackets (Ref. [708]), standard deviations given in parentheses (Å).

Table 3-3 shows the calculated bond length for fully lithiated Li_2FeSiO_4, delithiated $LiFeSiO_4$ and $FeSiO_4$, respectively. We noticed that the lengths of the Fe-O bond gradually become shorter as the oxidation of Fe^{2+} to its trivalent state and tetravalent state occurred; while the lengths of the Si-O bond remain virtually unchanged with the extraction of Li ions from the Li_2FeSiO_4 crystal structure. Nevertheless, the most important structural re-arrangement is the degree of corrugation, which depends on the angles of the Fe-O-Si bond formed by SiO_4 and FeO_4 tetrahedrons sharing an oxygen atom. These tetrahedrons form chains running along the b-axis. From the calculated angles of the Fe-O-Si bond within FeO_4 and SiO_4 tetrahedrons, it can be seen that as Li ions are extracted from Li_2FeSiO_4, these layers become less corrugated because the Fe-O-Si angles become larger. As a result, the b value increases.

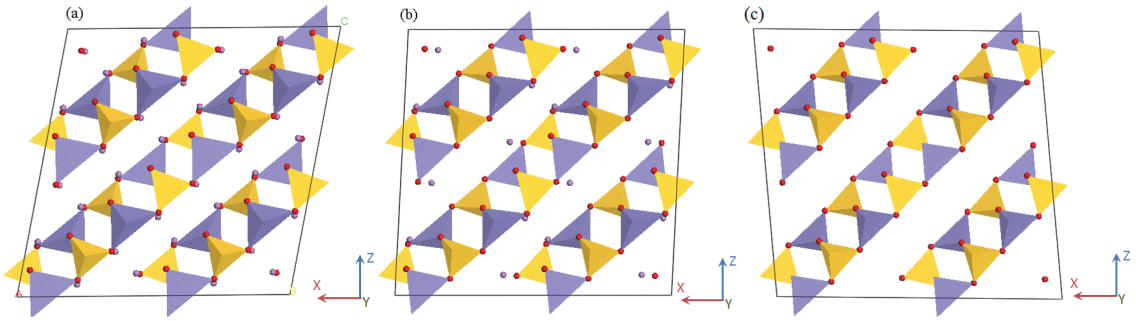

Figure 3-3 Optimized crystal structures of (a) $P2_1$ Li_2FeSiO_4, its derivative (b) $LiFeSiO_4$ and (c) $FeSiO_4$.

In addition, there are strong attractions between lithium anions and negative [$FeSiO_4$] layers. Therefore, Li ions link the FeO_4 and SiO_4 tetrahedrons together. As Li ions are extracted from Li_2FeSiO_4, these linkages will be weakened. The fully delithiated $FeSiO_4$ structure seems to be unstable because of the weak attraction or even the disappearance of the attraction. It might, therefore, become

thermodynamically metastable with respect to other structures. This results in an expansion of the unit cell along both a axis and c axis. Figure 3-3 shows the optimised crystal structures of Li_2FeSiO_4, delithiated $LiFeSiO_4$ and $FeSiO_4$ along a and c directions. Some rearrangements of the crystal structure occurred during the process of lithium extraction. The values of a and c increase by 4.7 %, 0.9 % for $LiFeSiO_4$, and 4.5 %, 1.7 % for $FeSiO_4$. Furthermore, Table 3-4 lists the calculated distances of Li-Si, Fe-Si, Fe-Fe and Si-Si bonds for Li_2FeSiO_4, $LiFeSiO_4$ and $FeSiO_4$. Based on these values, it is suggested that all Li ions are located near the centre of distorted $LiSi_4$ tetrahedra, which can minimize the lattice energy with respect to minimum electrostatic repulsion. The Fe-Si distances also increase by about 1.4 % for $LiFeSiO_4$ and by 9 % for $FeSiO_4$, respectively (as shown in Table 3-4). The Fe-Fe distances and Si-Si distances increase significantly with the extraction of lithium, corresponding to the weakening of the attraction between lithium anions and negative [$FeSiO_4$] layers.

Table 3-4 Calculated Li-Si, Fe-Si, Fe-Fe and Si-Si distance (Å) for Li_2FeSiO_4, $LiFeSiO_4$ and $FeSiO_4$.

Atom(1)-Atom(2)	Li_2FeSiO_4	$LiFeSiO_4$	$FeSiO_4$
Li(1)-Si(2)	3.083 [3.137(11)][a]	-	-
Li(1)-Si(2)	2.970 [3.00(4)][a]	-	-
Li(1)-Si(2)	3.092 [3.18(4)][a]	-	-
Li(1)-Si(1)	3.252 [3.120(12)][a]	-	-
Li(2)-Si(2)	3.252 [3.077(13)][a]	3.292	-
Li(2)-Si(1)	3.090 [3.049(12)][a]	3.365	-
Li(2)-Si(1)	3.065 [3.21(4)][a]	3.222	-
Li(2)-Si(1)	2.964 [3.06(4)][a]	3.728	-
Li(3)-Si(1)	3.048 [3.113(12)][a]	-	-
Li(3)-Si(2)	3.102 [2.96(4)]a	-	-
Li(3)-Si(2)	3.192 [3.126(11)][a]	-	-
Li(3)-Si(2)	3.080 [3.18(4)][a]	-	-
Li(4)-Si(1)	3.103 [3.11(4)][a]	3.331	-
Li(4)-Si(2)	3.051 [3.142(13)][a]	3.083	-
Li(4)-Si(1)	3.190 [2.99(4)][a]	3.269	-
Li(4)-Si(1)	3.081 [3.189(12)][a]	3.146	-
Fe(1)-Si(1)	6.315	6.225	6.855
Fe(1)-Si(2)	6.304	6.309	7.129
Fe(2)-Si(1)	6.304	6.659	7.066
Fe(2)-Si(2)	6.313	6.395	6.847
Mean	6.309	6.397	6.974
Fe(1)- Fe(2)	5.240	5.592	6.461
Si(1)-Si(2)	5.235	5.672	6.459

[a]Reference values for Li_2FeSiO_4 are also given for comparison as shown in brackets (Ref.[708]), standard deviations given in parentheses (Å).

A good example of such structural phase transformation upon lithium removal is provided by the transformation of a layered structure to a spinel structure, which occurs in $LiMnO_2$.[143,148] The shape of a voltage-composition curve reported for the full lithium extraction from Li_2MnSiO_4 suggests that an irreversible phase transformation may indeed occur at the end of the first charge. Ideally, changes in cell parameters should be minimised to avoid phase separation during charge and discharge cycling. The change in unit cell volume (11.5 %) on the extraction/re-insertion of 50 % Li ions (between Li_2FeSiO_4 and $LiFeSiO_4$) is relatively large, which could induce inferior reversibility and cyclability.

A powder X-ray diffraction pattern is usually generated by the collection of individual crystallites with random distribution of orientations. The diffraction intensity observed at diffraction angle 2θ can be calculated as:

$$I(\theta) = \sum_{hkl} p_{hkl}(2\theta - 2\theta_{hkl}) I_{hkl} \quad (3\text{-}1)$$

where the Integrated Bragg Intensity I_{hkl} is related to the structure factors F_{hkl}:

$$I_{hkl} = M_{hkl} P_{hkl} L_{hkl} |F_{hkl}|^2 \quad (3\text{-}2)$$

Here, M_{hkl} is the multiplicity of reflection $h\ k\ l$, P_{hkl} is the preferred orientation correction for the reflection $h\ k\ l$, and L_{hkl} is the Lorentz and polarization correction for the reflection $h\ k\ l$. $P_{hkl}(2\theta - 2\theta_{hkl})$ is an appropriate profile function.

In the case of a monoclinic phase with unit cell parameters a, b, and c, and interaxial angles α, β, and γ, we can write:

$$\frac{1}{d^2} = \frac{1}{a^2 b^2 c^2 (1 - cos^2\beta)} \times (b^2 c^2 h^2 + a^2 c^2 sin^2\beta k^2 + a^2 b^2 l^2) \quad (3\text{-}3)$$

For the orthorhombic phase:

$$\frac{1}{d^2} = \frac{1}{a^2b^2c^2}(b^2c^2h^2 + a^2c^2k^2 + a^2b^2l^2) \quad (3\text{-}4)$$

Using the Cu K_α with a radiation wavelength of 1.540562 Å, we calculated the diffraction pattern of $P2_1$ and Pnma symmetry of Li_2FeSiO_4 and indexed the peaks using the indexing algorithms, TREOR.[724] The calculated diffraction patterns are shown in Figure 3-4.

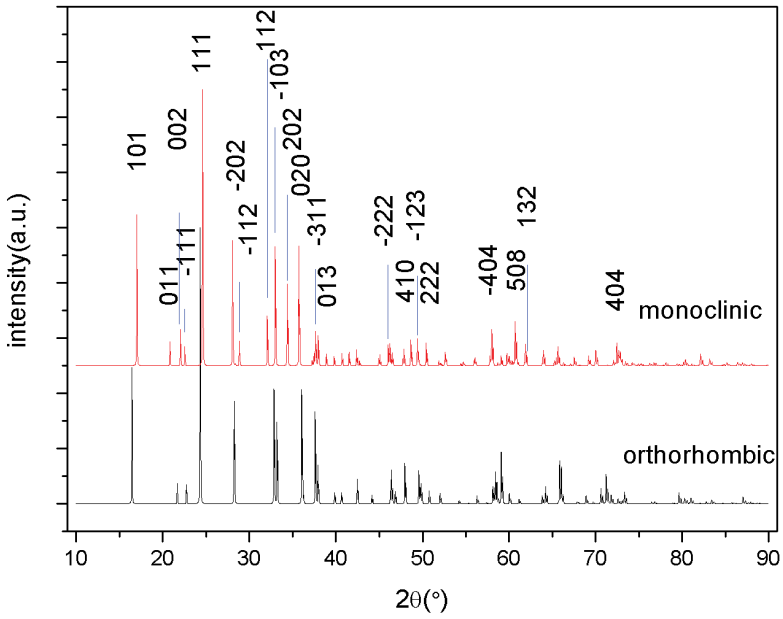

Figure 3-4 Simulated powder diffraction pattern of $P2_1$ (upper red line) and Pnma (bottom black line) structure Li_2FeSiO_4.

Compared with the experimental pattern that was obtained from high-resolution synchrotron XRD (HR-XRD),[708] it can be seen that the calculated pattern of Li_2FeSiO_4 based on the $P2_1$ structure matches the experimental result completely. In addition, several extra reflections that have been previously assigned to unidentified impurity phases[276] can be clearly indexed as (112) and (508) crystal planes, respectively. Therefore, these two diffraction lines should not be excluded for the

determination of the accurate structure.

3.4.2 Electrochemical properties

3.4.2.1 Average intercalation voltage

In order to study the charge/discharge process, it is important to examine both the lithiated and delithiated phases of the compounds. As pointed out by McKinnon,[725] any separation of the intercalation energy into an electronic and ionic part is arbitrary due to the strong interaction between the intercalated Li ions and the extra electrons. More rigorously, the equilibrium intercalation voltage depends on the chemical potential difference for lithium in the anode and cathode materials,[726] which is the partial derivative of the free energy (ΔG) of the cathode material *vs.* lithium composition. As Li ions are inserted into the cathode, the chemical potential increases, leading to a decrease of the intercalation voltage. It is possible to obtain the average intercalation voltage, $\overline{V}$, for perfectly ordered structures if the volume effects and entropic effects are negligible: $\Delta G = \Delta E$ (change in internal energy at 0 K).[727] So, for the reaction:

$$\mathrm{Li}_x\mathrm{FeSiO}_4 + \Delta x\mathrm{Li}^+ + \Delta x\mathrm{e}^- \leftrightarrow \mathrm{Li}_{x+\Delta x}\mathrm{FeSiO}_4 \qquad (3\text{-}5)$$

The average intercalation voltage:

$$\overline{V} = -\frac{E(\mathrm{Li}_x\mathrm{FeSiO}_4)+E(\mathrm{Li})-E(\mathrm{Li}_{x+\Delta x}\mathrm{FeSiO}_4)}{\Delta x} \qquad (3\text{-}6)$$

The energy density (U) and specific energy (E_s) of the battery reaction are given by:[723]

$$U = -\frac{\Delta E}{v} \qquad (3\text{-}7)$$

$$E_s = -\frac{\Delta E}{m} \tag{3-8}$$

where v denotes the average volume of one formula unit of the reactant and one formula unit of the product of the reaction (3-5). The quantity m denotes the mass of one molecular formula unit of either the reactant or the product of the reaction (3-5).

In principle, it is possible to fully extract all Li ions from Li_2MSiO_4, providing two electrons per formula unit (Fe^{+2}/Fe^{+3} and Fe^{+3}/Fe^{+4} couples). The reaction can be divided into the first Li ion extraction (reaction (3-9)) and the second Li ion extraction (reaction (3-10)):

$$LiFe^{3+}SiO_4 + Li^+ \leftrightarrow Li_2Fe^{2+}SiO_4 \tag{3-9}$$

$$Fe^{4+}SiO_4 + Li^+ \leftrightarrow LiFe^{3+}SiO_4 \tag{3-10}$$

To determine the average intercalation voltage, the total energy of all three structures in each reaction is required. Therefore, metallic lithium was assumed to have a body centred cubic structure with a lattice constant of 3.509 Å. It was relaxed using a 6 × 6 × 6 Monkhorst and Pack grid for k-point sampling. The properties of $\overline{V}$, U, E_s capacity for the cathode compounds in their lithiated, half and fully delithiated states were calculated and shown in Table 3-5.

Table 3-5 Calculated average intercalation voltage, energy density, specific energy and specific capacity for the first Li ion extraction (Fe^{+2}/Fe^{+3}couples) and the second Li ion extraction (Fe^{+3}/Fe^{+4} couples).

	$\overline{V}$ (V)	U (W h l^{-1})	E_s (W h kg^{-1})	Capacity (mA h g^{-1})
Fe^{+2}/Fe^{+3}	3.10	1259.41	405.92	165.58
Fe^{+3}/Fe^{+4}	4.16	1672.39	621.81	172.96
Fe^{+2}/Fe^{+4}	3.75	1458.18	500.60	338.54

The calculated average voltage of Fe^{+2}/Fe^{+4} redox couple is 3.75 V, which is slightly higher than that of the experimental one[276] and the calculated value (2.88 V) reported previously, based on Pnma symmetry.[283] This corresponds to an energy density of 1458.18 Wh l^{-1} and a specific energy of 500.60 Wh kg^{-1}. Lithium extraction from Li_2FeSiO_4 will proceed in marked two-step voltage plateaus: The first Li ion extraction occurs at 3.10 V, and is in good agreement with the available experimental data.[276, 270] The second Li ion extraction occurs at 4.16 V. There is voltage step of 1.06 V at lithium extraction from Li_2FeSiO_4 with the $P2_1$ symmetry structure, which is less than that with the $Pmn2_1$ symmetry (1.6 V).[282] It indicates that the reversibility and the cycling performance are improved in Li_2FeSiO_4 with the $P2_1$ symmetry. The voltage step is due to the fact that one moves from a d^6 ion (Fe^{+2}) to a closed-shell d^5 ion (Fe^{+3}), which requires a small ionization energy as compared to the other M^{2+} to M^{3+} oxidations.[289]

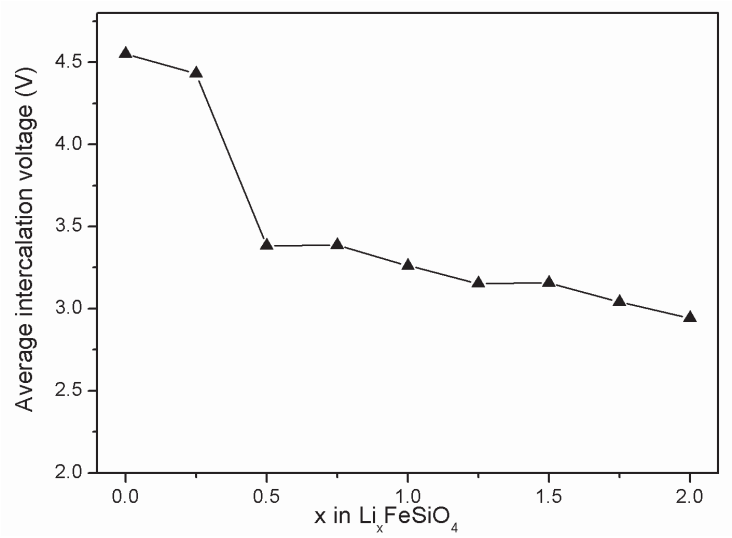

Figure 3-5 Calculated average intercalation voltage in Li_xFeSiO_4 for intervals $0 \leq x \leq 2$.

We also calculated the average voltage profile of lithium intercalation as a function of Li content in Li_xFeSiO_4 ($0 \leq x \leq 2$). During the approximation process, the starting crystal structures of Li_xFeSiO_4 ($0.25 \leq x \leq 1.75$) were obtained by removing Li ions from the former optimized $Li_{x+0.25}FeSiO_4$ structures and then relaxed in the same way as above. The result is shown in Figure 3-5. The voltage profile is a gently sloping curve in the range of $0.5 \leq x \leq 1.25$. At $x = 1.50$ the voltage slightly increases to 3.16 V and then decreases again to 3.04 V at $x = 1.75$. This curve shows a potential plateau in the voltage range of between 3.5 V and 3.0 V, which is inconsistant with the experimental results.[290]

3.4.2.2 Density of states

An analysis of the electronic structure can clearly identify the characteristics of the cathode materials in the discharged/charged states. We calculated the electronic densities of states (DOS) of Li_2FeSiO_4, $LiFeSiO_4$ and $FeSiO_4$ (shown in Figure 3-6).

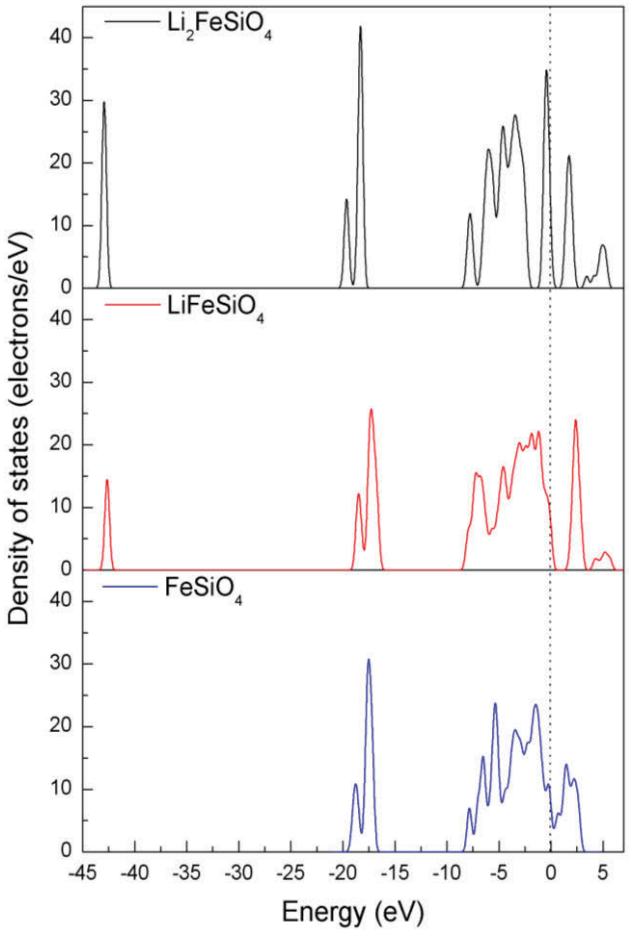

Figure 3-6 Density of states (DOS) for Li_2FeSiO_4 $LiFeSiO_4$ and FeSiO. The Fermi level is indicated by a vertical dot line.

The bandgap of Li_2FeSiO_4 was calculated to be 1.337 eV, indicating the insulating nature of the compound. The poor electronic conductivity induces high impedance for battery charge and discharge. With the extraction of Li ions from Li_2FeSiO_4, the valence band shifts to the right, and the conduction bands also slightly shift to the right with respect to the Fermi level. The DOS for $LiFeSiO_4$ corresponds to an insulator feature with a bandgap of 2.166 eV. When Li ions are completely extracted, the fully delithiated product of $FeSiO_4$ has a bandgap of 1.676 eV (as shown in Figure 3-6). We notice that the valence band and conduction band are connected in $FeSO_4$.

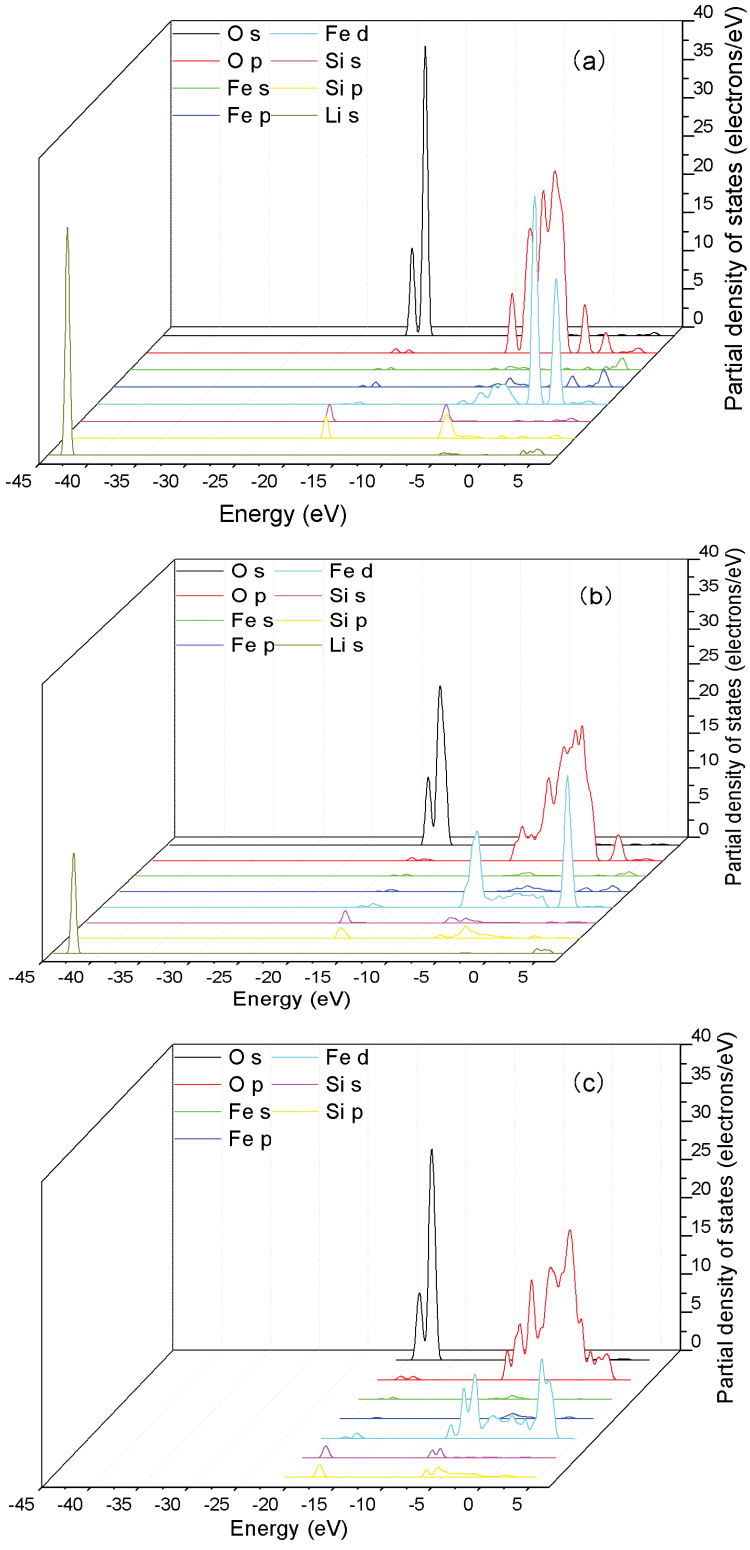

Figure 3-7 Partial density of states (PDOS) for (a) Li_2FeSiO_4, (b) $LiFeSiO_4$ and (c) $FeSiO_4$.

Calculated partial density of states (PDOS) for oxygen (s and p) orbits, iron (s, p,

and d) orbits, and silicon (s and p) orbits of Li_2FeSiO_4 are shown in Figure 3-7 (a). It reveals that the valence band of Li_2FeSiO_4 is formed by hybridised oxygen p-states, iron d-states and silicon p-states. The conduction bands are mainly made up of hybridized iron s-states, p-states, d-states and oxygen p-states. For $LiFeSiO_4$, the conduction band is formed by the hybridisation between the oxygen p-states, iron d-states, and silicon s-states and p-states (as shown in Figure 3-7 (b)). The formation of a conduction band is the same as $LiFeSiO_4$. However, it should be noted that the connected valence band and conduction band of pure $FeSiO_4$ is formed by hybridisation of oxygen p-states, iron d-states, silicon s-states and p-states showing in Figure 3-7 (c). The similar transition has been reported in the cathode material $LiCoPO_4$ and $CoPO_4$.[720]

By comparing the PDOS of the lithiated/delithiated phases, we found that the d-states of iron change significantly during the lithium intercalation and de-intercalation process. This corresponds to the electron transfer in Fe when Li ions are extracted and inserted in a Li_2FeSiO_4 compound. In contrast, the electron transfer between silicon and oxygen is negligible. Therefore, the calculations on the density of states have confirmed the valence change of Fe in Li_2FeSiO_4 during the lithium insertion and extraction process.

3.4.3 Li ion migration via vacancy diffusion

As shown in Figure 3-8, if a single Li ion is removed from the crystal there are several neighboring Li ions which can hop into the vacancy site and contribute to a three-dimensional diffusion. We considered several possible diffusion paths along the three lattice directions. For Li_2FeSiO_4 with the $P2_1$ symmetry, we have identified four main migration pathways (illustrated in Figure 3-8 (a)): (1) pathway A –

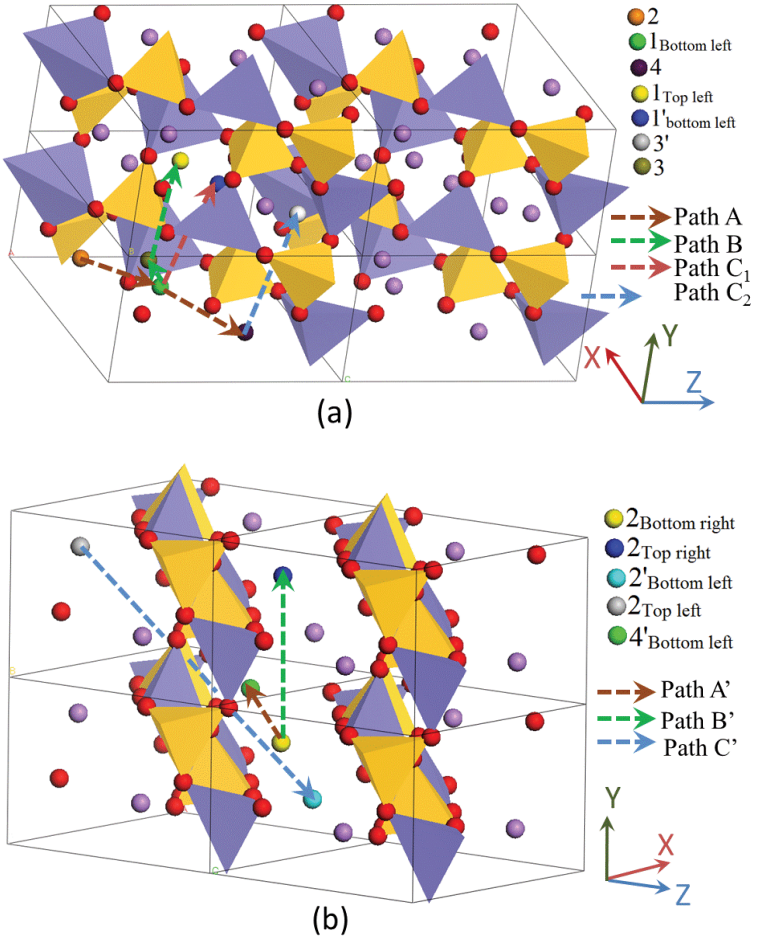

Figure 3-8 Li-vacancy migration pathways in the (a) Li_2FeSiO_4 and (b) $LiFeSiO_4$ structure. Different Li ion marked by number and position.

migration proceeds across channels along the [101] direction; (2) pathway B - migration proceeds in a zigzag trajectory in the ac plane $(10\bar{1})$ crystal plane; (3) pathway C_1 - migration proceeds through a small void in the Fe-Si layer along the [111] direction, which involves simultaneous edge-sharing with the two Fe and two Si tetrahedra; and (4) pathway C_2 – migration proceeds across a small void but in the Si-Fe layer, which also involves simultaneous edge-sharing with the two Si and two Fe tetrahedra. For the $LiFeSiO_4$ structure, three possible migration pathways have been considered (illustrated in Figure 3-8 (b)): (1) pathway A' - migration proceeds across channels along the [101] direction with a long jumping distance of about 8.72

Å; (2) pathway B' - migration proceeds between the adjacent M1 sites along the [010] direction (parallel to the b axis); and (3) pathway C' - migration proceeds through the void in the Fe-Si layer but with a long jumping distance of 10.67 Å. All migration pathways are summarized in Table 3-6, in which the labels described in Figure 3-8 are used to indicate the vacancy positions. For each step in the path, it lists the distance as measured from the corresponding perfect crystal sites and the maximal migration energy barrier (E_m) calculated from NEB formalism for that step.

Table 3-6 Pathways and energies of Li ion migration in Li_2FeSiO_4 and $LiFeSiO_4$.

Structure	Path	Step[a]	Net distance[b] (Å)	Activation barrier (eV)
Li_2FeSiO_4	A:[101]	$2\leftrightarrow 1_{\text{Bottom left}}$	3.017	0.71
		$1_{\text{Bottom left}}\leftrightarrow 4$	3.373	0.87
		$2\leftrightarrow 1_{\text{Bottom left}}\leftrightarrow 4$	3.370	0.87
	B: in $(10\bar{1})$ plane	$3\leftrightarrow 1_{\text{Top left}}$	3.537	0.54
		$1_{\text{Bottom left}}\leftrightarrow 3$	2.695	0.83
		$1_{\text{Bottom left}}\leftrightarrow 3\leftrightarrow 1_{\text{Top left}}$	5.024	0.83
	C_1:[111]	$1\leftrightarrow 1'_{\text{Bottom left}}$	4.236	1.99
	C_2:[111]	$4\leftrightarrow 3'$	4.582	2.51
$LiFeSiO_4$	A':[101]	$2_{\text{Bottom right}}\leftrightarrow 4'_{\text{Bottom left}}$	8.72	0.84
	B':[010]	$2_{\text{Bottom right}}\leftrightarrow 2_{\text{Top right}}$	5.206	0.79
	C':[111]	$2_{\text{Top left}}\leftrightarrow 2'_{\text{Bottom left}}$	10.67	3.06

[a]Labels defined in Figure 3-8.

[b]Equivalent perfect crystal distances.

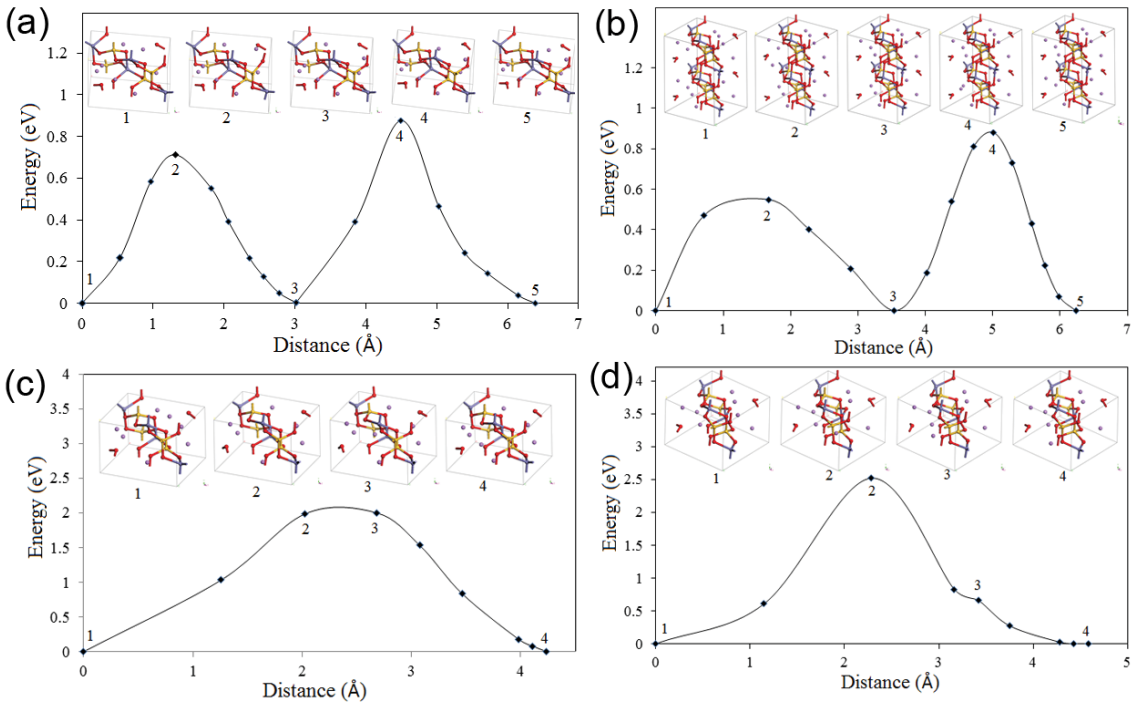

Figure 3-9 Calculated migration energies for Li-vacancy migration in the lithiated Li_2FeSiO_4 system along different pathways: (a) pathway A, (b) pathway B, (c) pathway C_1 and (d) pathway C_2, the insets are corresponding local structures marked in the curved trajectory between Li sites.

Figure 3-9 shows the calculated migration energies for Li-vacancy migration in the lithiated Li_2FeSiO_4 system along different pathways and the corresponding local structures marked in the curved trajectory between Li sites. For clarity, the Li ion is followed as it migrates along a path opposite to the route taken by the vacancy. As evident from Figure 3-8, vacancy diffusion generally involves zigzag motions such as the $2 \leftrightarrow 1_{\text{Bottom left}} \leftrightarrow 4$ path for diffusion along the [101] direction (pathway A). Figure 3-9 (a) plots the results of this case, showing a smaller energy barrier (0.71 eV) for the first step and a 0.87 eV barrier for the overall process.

Along pathway B, migration proceeds in the ac plane with a zigzag trajectory and in two distinct steps: first, Li ion in the 3 site (Figure 3-8) jumps 3.537Å upward along

the b-direction to the $1_{\text{Top left}}$ site (Figure 3-8). This can be seen as a transformation of the LiO_4 tetrahedron configuration (as shown from the inset 1 to 3 in Figure 3-9 (b)). This step costs only 0.54 eV of the migration energy. The Li ion in the down tetrahedron $1_{\text{Bottom left}}$ site then jumps 1.47 Å upward across the transition state (energy: 0.83 eV) (the inset 4 in Figure 3-9 (b)), and then 1.22 Å to the next site across the plane of the Li-layer (inset 5 in Figure 3-9 (b)). The availability of these low energy sites clearly enhances the Li ion migration as a result of the effectively lower activation barriers (0.83 eV).

For Li-vacancy migration along the [111] direction, the two possible pathways C_1 and C_2 are shown in Table 3-6 and Figure 3-9 (c) and (d). Here, the Li ions have to migrate through a small void in the Si-Fe layer, which involves simultaneous edge-sharing with the two Si and two Fe tetrahedra (the process is illustrated in the insets in Figure 3-9 (c), (b) and (d)). The distance between the two neighboring sites (as listed in Table 3-6) are 4.236 Å and 4.582 Å, which are longer than that of the inter-site distances of 3.37 Å in pathway A. Such configurations lead to direct diffusion between the adjacent sites, but with substantially higher activation barriers of 1.99 eV and 2.51 eV than that of pathways A and B.

Figure 3-10 shows the calculated migration energies for Li-vacancy migration in the delithiated $LiFeSiO_4$ system along different pathways and the corresponding local structures. Again, the Li ion is followed as it migrates along a path opposite the route of the vacancy.

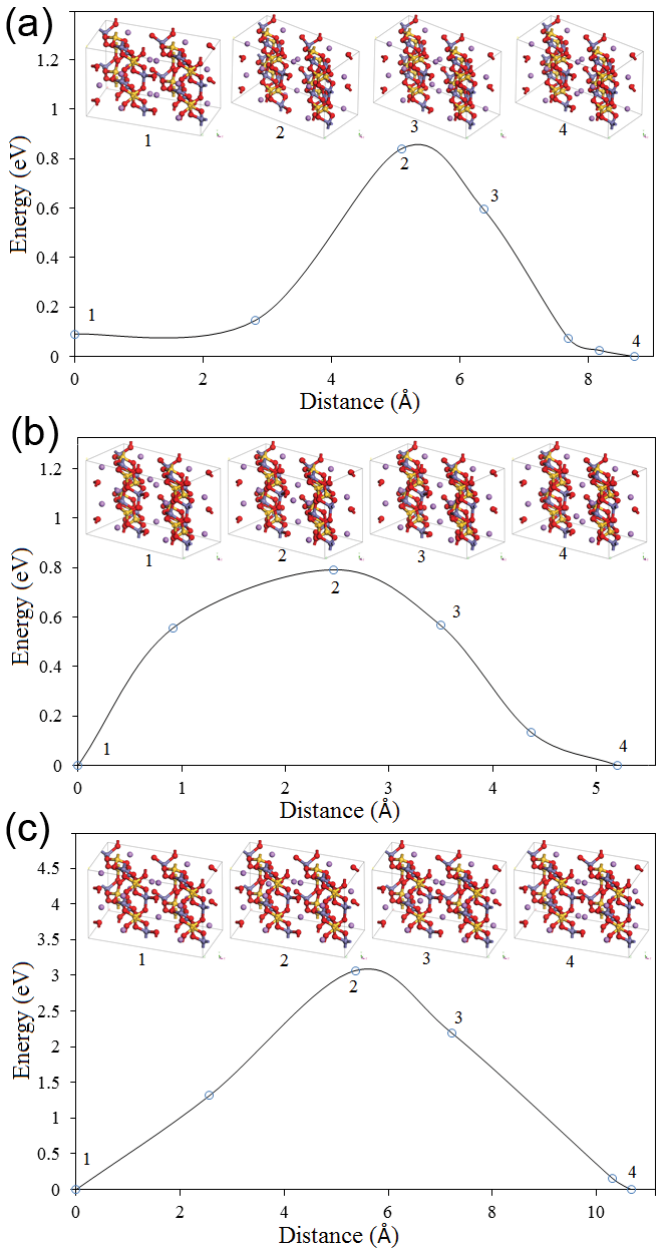

Figure 3-10 Calculated migration energies for Li-vacancy migration in the delithiated $LiFeSiO_4$ system along different pathways: (a) pathway A', (b) pathway B' and (c) pathway C', the insets are corresponding local structures marked in the curved trajectory between Li sites.

In the delithiated state, the activation barrier decreases to 0.87 eV and 0.79 eV for pathway A' and pathway B'. Another interesting feature for pathway A' is that 0.1 eV energy is needed for the formation of Li–Li dimer configurations (inset 1 in

Figure 3-10 (a)). The activation barrier between this dimer configuration and the Li-vacancy-Li configuration is only 0.77 eV (insets 1 and 2 in Figure 3-10 (a)). It is mainly caused by a significant expansion in volume of the unit cells with the de-intercalation of Li ions from Li_2FeSiO_4 to $LiFeSiO_4$. As Li ions are extracted from Li_2FeSiO_4, the linkages between Li ions and FeO_4 and SiO_4 tetrahedrons will be weakened. The weakening or even disappearance of the attraction between them lowers the Li ion migration energy. Meanwhile, the new Li ion fractional coordinates of $LiFeSiO_4$ also contribute to the easier migration because of the broadened channel. It can be seen from the optimized crystal structures of Li_2FeSiO_4 and $LiFeSiO_4$ (as shown in Figure 3-3). Furthermore, for both pathways A' and B' there is no zigzag trajectory between Li sites. The diffusion can proceed directly along the [101] and [010] directions with hops between the adjacent minimum energy sites. While for pathway C', the activation barrier increases to 3.06 eV (Figure 3-10 (c)), probably due to the presence of more positive Fe^{3+} ions and the extraction of electrons. This leads to less efficient charge screening. The migration distance through the Fe–Si layer in the pathway increases to 10.67 Å, which will need more energy to diffuse.

Because low energy migration proceeds along pathways A, B, A' and B' for Li_2FeSiO_4 and $LiFeSiO_4$, respectively, it would suggest that the Li ion migration in Li_2FeSiO_4 is determined by the percolation of corner-sharing tetrahedral sites throughout the structure. Meanwhile, the two-dimensional transportation mechanism of Li ions in the $P2_1$ symmetry structure Li_2FeSiO_4 can be established. Compared with the one-dimensional transport of Li ion in the olivine $LiFePO_4$,[226] Li_2FeSiO_4 has an obvious advantage over the Li ions diffusion as cathode material. With such two-dimensional transport, the block of long-range Li conduction can be avoided—

which occurs easily in one-dimension transport cathode materials. For instance, as reported by Islam et al,[728] the Li-Fe anti-site defects are intrinsic to $LiFePO_4$. It may be difficult to avoid Fe on Li sites blocking the diffusion pathways down [010] channels, unless the anti-site defect itself is highly mobile. This would obviously inhibit long-range Li migration and influence the electrochemical kinetics during Li extraction.

Table 3-7 Calculated activation barriers and estimation of diffusion coefficients for Li ion or vacancy migration in various cathode materials.

System	Space group	E_m (lithiated) (eV)	E_m (delithiated) (eV)	Li ion migration dimensions	D ($cm^2\ s^{-1}$)
Li_2FeSiO_4[729]	$Pmn2_1$	0.83[a]/0.75[c]	0.9[a]/1.0[c]	2	$10^{-14}/10^{-13}$
Li_2FeSiO_4[729]	$Pbn2_1$	0.82[b]/0.72[c]	-	>2	$10^{-14}/10^{-12}$
Li_2FeSiO_4	$P2_1$	0.87/0.83	0.84/0.79	2	$10^{-13}/10^{-11}$
Li_2MnSiO_4[288]	$P2_1/n$	0.60/0.54	-	2	-
Li_2MnSiO_4[288]	$Pmn2_1$	0.95	-	1	-
Li_xCoO_2[709]	$R\bar{3}m$	0.23	0.6	1	10^{-8}
$LiFePO_4$[226]	Pnma	0.27	0.2	1	10^{-7}
γ-Li_3PO_4[730]	Pnma	0.69[a]/0.67[b]/0.63[c]	-	3	-
β-Li_3PO_4[714]	$Pmn2_1$	0.72[a]/0.55[b]/0.71[c]	-	3	-
I-Li_2NiO_2[711]	Immm	0.45[b]/0.45	-	2	10^{-10}

[a, b, c]Crystallographic axis directions.

Calculated activation barriers and estimated diffusion coefficients of various materials are compared in Table 3-7. Diffusion coefficients are calculated based on

the Eq. (3-11)[711,731]

$$D = d^2 \cdot r \cdot exp(-E_m/K_B T) \quad (3\text{-}11)$$

Where d is the hopping distance along different pathways, r is the attempted frequency and E_m is the activation barrier for the hop. r is about 10^{13} Hz, which is in the range of phonon frequencies and consistent with typical values.[732] Therefore, diffusion coefficients of Li_2FeSiO_4 for the pathways A and B can be approximated to be 10^{-13} and 10^{-11} cm^2 s^{-1} at a temperature of 300 K. Considering D for the commercially used Li_xCoO_2 has been found to be within the range of 10^{-13} to 10^{-7} cm^2 s^{-1} at room temperature,[226] the pathways A and B in Li_2FeSiO_4 can be acceptable for cathode material in lithium ion cells. The activation barriers for Li_2FeSiO_4 with the $P2_1$ symmetry structure are slightly larger than those with the $Pmn2_1$ and $Pbn2_1$ symmetry structures.[729] They are significantly higher than those found in other common cathode materials such as Li_xCoO_2,[226] $LiFePO_4$[226] and Li_2NiO_2,[711] while activation barriers for the delithiated $LiFeSiO_4$ with the $P2_1$ symmetry structure are lower than that of the $Pmn2_1$ symmetry structure. Such differences in Li mobility would influence the ability to extract lithium from polymorphs with two different symmetries and hence lead to differences in rate capability and general electrochemical behavior as rechargeable electrodes.

From electrochemical studies on the related Li_2FeSiO_4 system, Nyten et al.[290] observed a shift in the potential plateau between the first and second cycles. They suggested that this is related to structural rearrangement involving the interchange of some of the Li and Fe ions. There is the experimental evidence of a low concentration of Li/Mn cation exchange in Li_2MnSiO_4.[733] Therefore, it is worth investigating the cation exchange effect.[734] Such cation mixing with Li on Fe sites

and Fe on Li sites may either facilitate or block the diffusion pathways. We examined the anti-site cation migration of both Li_{Fe} and Fe_{Li} to the adjacent vacant Li sites, while considering the process described by N. Kuganathan and M. S. Islam[288] on Li_2MnSiO_4. This process can be viewed as an exchange of an anti-site cation with a neighboring lithium vacancy. The lithium vacancy would then continue to migrate in the opposite direction. Very similar simulations were reported by C. A. J. Fisher et al. on anti-site migration in the olivine-type materials $LiMPO_4$ (M = Mn, Fe, Co, Ni).[735] The calculated lowest barrier energy of the Li_{Fe} anti-site cation is 0.86 eV. It is suggested that if there was a significant population of Li on Fe sites, it could facilitate long-range Li diffusion. In contrast, migration barrier energies of the Fe_{Li} anti-site cation has been calculated to be 1.32 eV, suggesting that Fe on Li sites would impede Li diffusion.

3.5 Summary and conclusion

By using the ab initio method, we have systematically calculated both the crystal and electronic structures of Li_2FeSiO_4 and its delithiated phases $LiFeSiO_4$ and $FeSiO_4$ based on a monoclinic super cell with $P2_1$ symmetry. Significant expansions of the unit cell volume occur during the delithiation process (11.5 % for the first lithium extraction and 9.2 % for the second lithium extraction). It is caused by the increase of a Fe-O-Si bond angle and a weakened attraction between Li ions and the FeO_4 and SiO_4 tetrahedrons during the lithium extraction process. This suggests possible structural instability and inferior cyclability of Li_2FeSiO_4 cathode materials. We also successfully calculated the lithium intercalation voltage and voltage profile for Li_2FeSiO_4 cathode material. The average intercalation voltages are 3.10 V and 4.16 V for Fe^{+2}/Fe^{+3} and Fe^{+3}/Fe^{+4} redox couples, respectively. Through the

calculations on density of states (DOS) and partial density of states (PDOS), the changes of electronic structures of Li_2FeSiO_4 cathode material have been illustrated. Furthermore, we have identified the Li ion diffusion mechanisms in all main crystallographic directions in Li_2FeSiO_4 and $LiFeSiO_4$ with the $P2_1$ symmetry. The diffusion process is slightly anisotropic, with the lowest migration energy occurring for pathways along the [101] direction and a zigzag trajectory in the ac plane determined. Reasonably good Li ionic conducting can be maintained in the $P2_1$ symmetry upon lithiation or delithaion with two-dimensional diffusion. Through the investigation on the effect of Li and Fe cation exchange, it is suggested that Li on Fe site defects could facilitate long-range Li diffusion. However, Fe on Li sites would impede Li diffusion due to the high migration barrier energies (1.32 eV) of the Fe_{Li} anti-site cation.

CHAPTER 4 SYNTHESIS OF TUNEABLE POROUS HEMATITE (α-Fe_2O_3) FOR LITHIUM STORAGE IN LI-ION BATTERIES

4.1 Abstract

Tuneable porous α-Fe_2O_3 materials were prepared by using a selective etching method. The structure and morphology of the as-prepared porous hematit have been systematically characterised by X-ray diffraction, field emission scanning electron microscope, and transmission electron microscope. We found that the pore size and pore volume can be controlled by adjusting the etching time during the synthesis process. The porous hematit have been applied for lithium storage in lithium ion cells, which demonstrated a reversible lithium storage capacity of 1269 mA h g^{-1}.

4.2 Introduction

Hematite (α-Fe_2O_3) is the most stable iron oxide under ambient conditions with the characteristics of non-toxicity, and high resistance to corrosion, and is low cost. It has been intensively investigated for applications in gas sensors,[736,737] rechargeable Li-ion batteries,[738] catalysts,[739] magnetic devices,[740] and bio-medical fields.[741,742] The performance of α-Fe_2O_3 strongly depends on the particle size, morphology, and structure. Various α-Fe_2O_3 nanostructures, like one-dimensional nanowire/nanotubes,[743] two-dimensional flake/film structures,[744] and three-dimensional hollow/porous structures,[745] have been synthesised by different methods, such as the sol-gel method,[746] electrostatic spray deposition,[747] hydrothermal treatment,[395] and the template method.[748] As anode materials in Li-ion batteries, a porous nanostructure can achieve a high rate specific capacity and good cycling stability. Porous α-Fe_2O_3 nanostructures can be

prepared by nanocasting using either hard templates, such as porous alumina embranes,[749] carbon nanotubes,[750] and porous silica,[751] or soft templates (surfactants).[752] Suslick et al[753] produced an iron/carbon composite by using ultrasound to irradiate a mixture of carbon nano-particles and iron pentacarbonyl in hexadecane, and then obtained hollow hematite particles by elaborately controlling the oxidation of the resulting composite. Xu et al. [400] prepared α-Fe_2O_3 hollow nanospheres by a controlled precipitation of Fe^{3+} with urea in the presence of carbonaceous saccharide nanospheres as hard templates. However, the template-directed synthesis suffers from the disadvantages of low yield and high cost. As an alternative, template-free solution-based synthetic methods have also been reported for the preparation of porous α-Fe_2O_3 nanostructures, such as nanotubes,[754] nanorings,[755] and porous nanorods,[756] in which the presence of some inorganic salts ($NH_4H_2PO_4$, Na_2SO_4, Na_2SO_3, NH_4Cl, KCl) are a prerequisite. In addition, the additives and experimental parameters must be carefully selected and controlled. Recently, an inorganic acid etching strategy has been used for the efficient synthesis of 2D transition-metal oxides.[404,405,757] However, it is still a challenge to develop a facile approach to synthesis α-Fe_2O_3 with porous or hollow nanostructures.

Herein, we report the synthesis of porous α-Fe_2O_3 via a controlled $H_2C_2O_4$ etching process. The as-prepared porous α-Fe_2O_3 nanostructures demonstrated a significantly improved lithium storage capacity and cycling stability in lithium ion cells. This is consistent with a generally recognised strategy of using hollow/porous structures to enhance the cycling stability of metal oxide anodes for Li-ion batteries.[758]

4.3 Experimental Section

4.3.1 Synthesis of porous α-Fe_2O_3

The porous α-Fe_2O_3 materials with a peanut-like shape were synthesised by a hydrothermal method. In a typical synthesis process, 9 ml 6 M NaOH (Sigma-Aldrich, ≥ 98 %) solution was added to 10 ml 2 M $FeCl_3$ (Sigma-Aldrich, ≥ 97 %) solution under vigorous stirring. A dark-red precipitate formed immediately. Then 1 ml 0.6 M Na_2SO_4 (Sigma-Aldrich, ≥ 98 %) solution was added. The mixture was then transferred into a Teflon-lined autoclave and heated at 102 °C for four days in an air-flow electric oven. After cooling to room temperature, the red product was collected by centrifugation and washed thoroughly with distilled water several times. The final products were obtained after drying for 12 h at 60 °C in the vacuum oven. For the preparation of porous α-Fe_2O_3 materials, 200 mg as-prepared α-Fe_2O_3 crystals were dispersed in a solution containing 20 ml of 0.5 M oxalic acid (Sigma-Aldrich, ≥ 99 %) and 0.0225 M KH_2PO_4 (Sigma-Aldrich, ≥ 99 %). The etching reaction proceeded at room temperature for 0-7.5 h to generate the uniform porous α-Fe_2O_3. As a comparison, the commercial α-Fe_2O_3 powders (Sigma-Aldrich, < 5 μm, ≥ 99 %) were also used for all testing.

4.3.2 Structural and physical characterisation

The crystal structure and phase of the as-prepared porous α-Fe_2O_3 were characterised by X-ray diffraction (XRD, Siemens D5000) using a Cu K_α radiation with 2θ ranging from 20° to 90° and a scanning step of 0.02° sec^{-1}. The morphology and microstructures were analysed by high resolution field emission scanning electron microscopes (FESEM, Zeiss Supra 55VP), transmission electron microscopy (TEM) and high-resolution TEM (HRTEM, JEOL 2011). The band gap energy of the as-prepared porous α-Fe_2O_3 was determined by ultraviolet-visible (UV-Vis) spectroscopy using a Shimadzu UV-1700 spectrophotometer.

4.3.3 Electrochemical testing

The electrodes were prepared by dispersing the as-prepared porous α-Fe_2O_3 powder (50 wt %), acetylene carbon black (40 wt %), and poly (vinylidene fluoride) binder (PVDF, 10 wt %) in N-methyl-2-pyrrolidone (NMP) to form a slurry. The resultant slurry was pasted onto copper foil using a doctor blade and dried at 100 °C for 12 h under vacuum conditions, followed by pressing at 200 kg cm^{-2}. Electrochemical measurements were carried out using two-electrode coin cells with lithium metal as the counter electrode. The CR2032-type coin cells were assembled in an argon-filled glove box (UniLab, Mbraun, Germany). The electrolyte solution was 1 M $LiPF_6$ dissolved in a mixture of ethylene carbonate (EC) and dimethyl carbonate (DMC) with a volume ratio of 1:1. Cyclic voltammetry (CV) was carried out on a CHI 660C electrochemistry workstation with a scan rate of 0.1 mV s^{-1} from 0.005 to 3.0 V in a two-electrode system. The charge-discharge measurements were performed at ambient temperature at different current densities in the voltage range from 0.05 to 3.0 V.

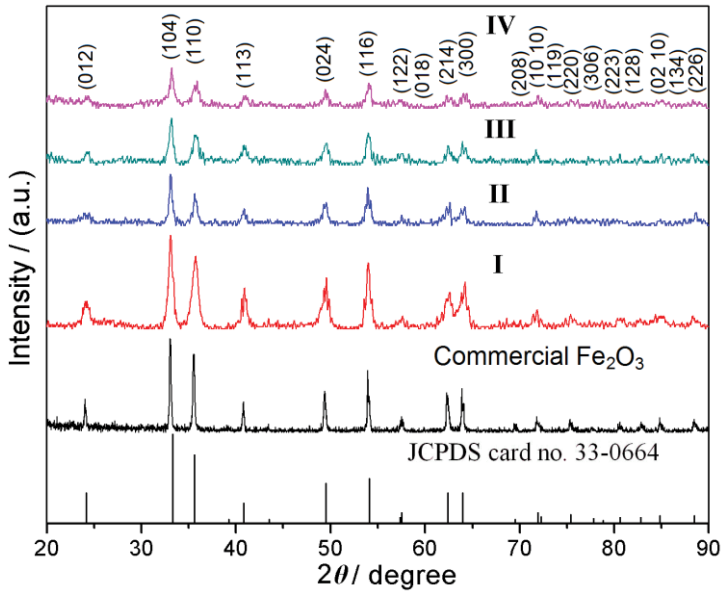

Figure 4-1 X-ray diffraction patterns of the as-prepared α-Fe_2O_3 powders before(I) and after being etched for different time durations: 3.5 h (II), 4.5 h (III), 5.5 h (IV) and the commercial Fe_2O_3 together with the standard pattern (JCPDS card no. 33-0664).

4.4 Results and discussion

4.4.1 Structural and morphological analysis

Figure 4-1 shows the powder X-ray diffraction pattern (XRD) of the as-prepared α-Fe_2O_3 before and after being etched for different time durations. All diffraction peaks can be indexed to the standard hematite (α-Fe_2O_3) crystal structure (JCPDS card number 33-0664), indicating that a pure and high crystalline product has been obtained. The average crystal size of pristine porous α-Fe_2O_3 was calculated to be about 10.2 nm based on the broadening of the (104) diffraction peak using the Scherrer formula. After being etched for different time durations, the average crystal size decreases with the increase of etching time. The average crystal sizes are 10.0 nm, 9.3 nm and 7.6 nm for the samples etched for 3.5 h, 4.5 h and 5.5 h, respectively. Furthermore, XRD analysis clearly shows that the chemical etching process did not change the crystal phase of α-Fe_2O_3 material.

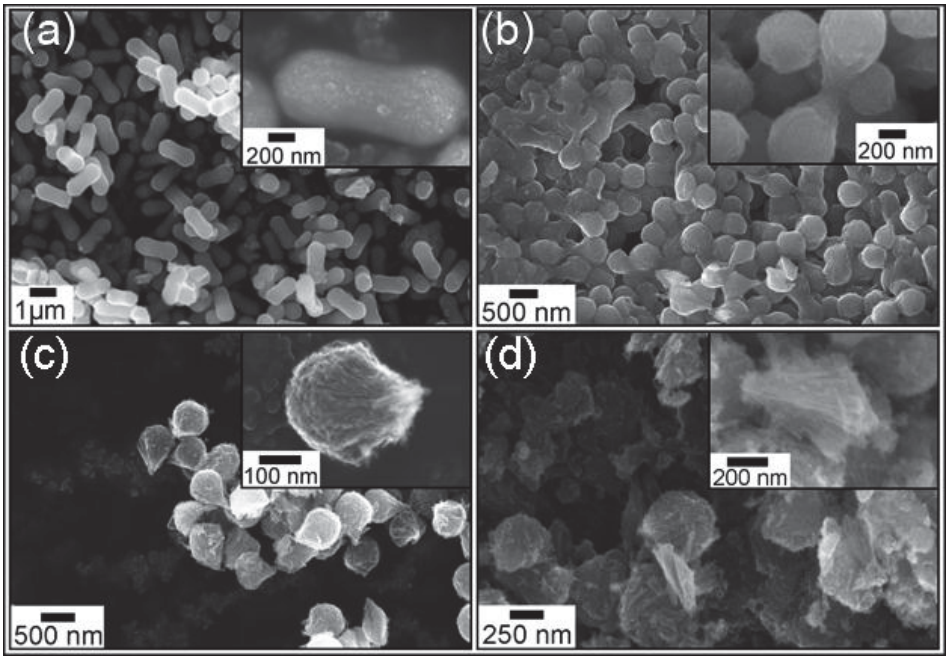

Figure 4-2 FESEM images of the porous α-Fe_2O_3 particles before (a) and after being etched for different time durations: (b) 3.5 h, (c) 4.5 h, and (d) 5.5 h. The insets are the magnified images of the corresponding sample.

The general morphology of the as-prepared α-Fe_2O_3 products was observed by field emission scanning electron microscopy (FESEM) shown in Figure 4-2. As compare, the commercial Fe_2O_3 particles are shown as Figure 4-2 (f). The as-prepared pristine hematite product is entirely composed of uniformly dispersed peanut-like[759-761] micro-particles with a length of ~1.2 μm and a diameter of ~ 400 nm (as shown in Figure 4-2 (a)). The magnified individual peanut-like particle is shown as the inset in Figure 4-2 (a). It can be seen that the individual peanut-like pristine α-Fe_2O_3 micro-particles is composed of tiny nanoparticles, illustrating the porous nature of the pristine α-Fe_2O_3 particles. For the porous structures, it is formed via assembly way. Sulfate ions are the most strongly adsorbed to hematite faces parallel to the c-axis of the hexagonal crystal system through bridging-bidentate adsorption, leading to the retarded growth in the direction normal to the c-axis, which forms the ellipsoidal or peanut-like shape.[761] A similar assembly porous structure had been reported.[762] For the etching reaction, oxalic acid ($H_2C_2O_4$) is considered as the most effective agent to dissolve the iron oxide contaminant in minerals.[763,764] Generally, the dissolution process proceeds as follow:

$$Fe_2O_3 + 6H_2C_2O_4 \rightarrow 2Fe(C_2O_4)_3^{3-} + 6H^+ + 3H_2O \quad (4\text{-}1)$$

$$Fe(C_2O_4)_3^{3-} + 6H^+ + 4H_2O \rightarrow 2FeC_2O_4 \cdot 2H_2O + 3H_2C_2O_4 + 6CO_2 \quad (4\text{-}2)$$

The overall reaction can be expressed as:

$$Fe_2O_3 + 3H_2C_2O_4 + H_2O \rightarrow 2FeC_2O_4 \cdot 2H_2O + 2CO_2 \quad (4\text{-}3)$$

The reactions between α-Fe_2O_3 particles and oxalic acid involve in both complexing and reducing Fe(III) to Fe(II).[764] After etching for 3.5 h, the morphology of the particles changes dramatically into a dumbbell-like structure (Figure 4-2(b) and the inset). It is apparent that the middle portion of the particles becomes much narrower. When the

etching is prolonged to 4.5 h, the connection parts of the dumbbell-like particles are ruptured and the two ends are etched, to a greater extent, into a pear-shape, with the presence of a large amount of porosity as shown in Figure 4-2 (c). The individual pear-shape particle can be clearly observed in the inset in Figure 4-2 (c). The surface of these micro-particles becomes noticeably rougher. Along with the increase of the etching time to 5.5 h, the pear-shape disappeared and porous nanostructure appeared. Keep increasing the etched time to 7.5 h the tears-like particle comes back which suggests the nano-particles are corroded totally (as shown in Figure 4-2 (e)). From the morphology comparison, the etching process could be described as follows: initially, phosphate ions, as an effective capping agent, will favourably attach to the two ends of the peanut-like particles. Hence the etching reaction main takes place at the middle regions on the peanut-like particles. As the etching proceeds, the middle regions are completely ruptured. Meanwhile, the generated Fe^{2+} ions will also enhance the etching kinetics due to an autocatalytic effect on Fe^{3+} detachment.[764] Finally, the etching will spread to the two ends of the particles. This leads to the dramatic morphological change and significant increase in porosity of the nano-particles.

The detailed crystal structures of porous α-Fe_2O_3 before and after etch, were further analysed by TEM, HRTEM and selected area electron diffraction (SAED). Figure 4-3 (a) shows a bright-field TEM image of a peanut-shaped particle prior to etching. The insets in Figure 4-3(a) further show the magnified view of the portion marked by the square, illustrating the porous nature of the pristine α-Fe_2O_3 particles. After etching for 3.5 h, the surfaces of α-Fe_2O_3 particles become noticeably rougher (as shown in Figure 4-3 (b) and the inset). A large amount of nanorod-like structures was presented, along with the increase of the etching time. By increasing the etching time to 4.5 h, it can be observed that some large pores have been created in the middle regions of the particles (Figure 4-

3 (c)), and individual α-Fe_2O_3 nanocrystals, with an average crystal size of 8-10 nm, also can be identified in the inset of Figure 4-3(c). An ordered porous structure with different shapes of pores exhibits in the sample etched for 5.5 h (Figure 4-3 (d)). The corresponding SAED pattern is shown as the inset in the right corner in Figure 4-3 (d). All diffraction rings can be readily indexed to the hexagonal crystal structure, confirming the α-Fe_2O_3 hematite phase. The inset in the left corner of Figure 4-3 (d) shows the lattice resolved HRTEM image of the α-Fe_2O_3 nanocrystal, in which two d spacings (110) and (012) crystal planes are indexed, further confirming the crystal structure of the as-prepared hematite.

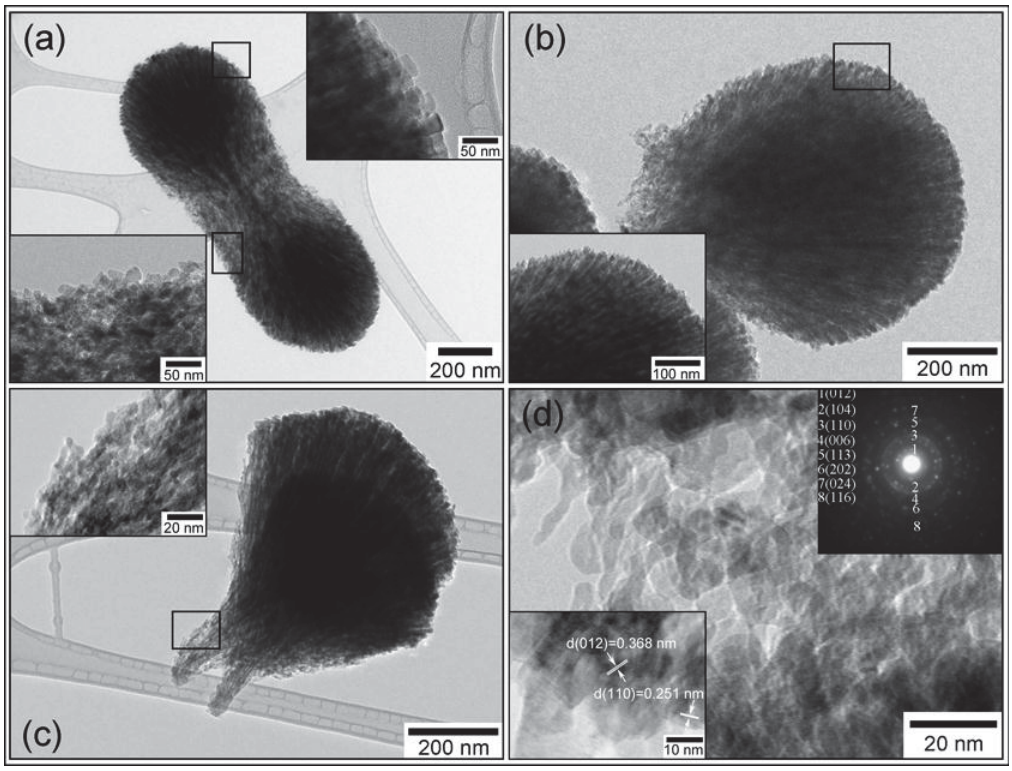

Figure 4-3 TEM and HRTEM images of the porous α-Fe_2O_3 particles before (a) and after being etched for different time durations: (b) 3.5 h, (c) 4.5 h, (d) 5.5 h. The insets in (a), (b), and (c) are the magnified images of the corresponding area marked by

rectangles. The right and left corner insets in (d) are corresponding selected area diffraction pattern and the lattice resolved HRTEM image respectively.

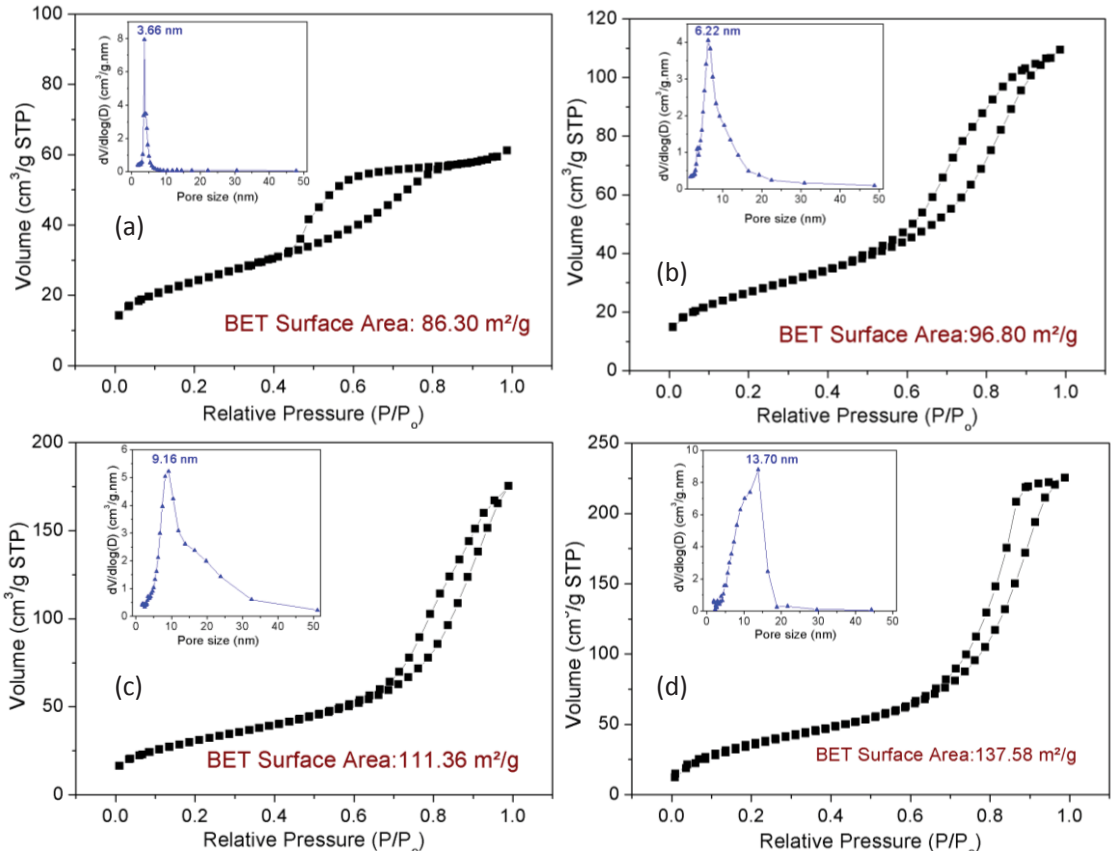

Figure 4-4 N_2 sorption isotherms of porous α-Fe_2O_3 after etched (a) 0h, (b) 3.5 h, (c) 4.5 h and (d) 5.5 h. The insets show the corresponding respective pore size distributions and the BET surface area values are all listed in the figures.

To examine the specific surface area and pore size distribution, N_2 adsorption-desorption isotherm measurements were performed on porous α-Fe_2O_3 samples. Figure 4-4 shows a typical H_2-type hysteresis loops.[746] The pore size distributions obtained from the Barrett-Joyner-Halenda (BJH) method are shown as insets in Figure 4-4. The average pore size increases with the extension of the etching time. The specific surface areas estimated from the Brunauer-Emmett-Teller (BET) method are 86.30, 96.30, 111.36 and 137.58 $m^2\ g^{-1}$ for samples etched for 0, 3.5, 4.5 and 5.5 hours.

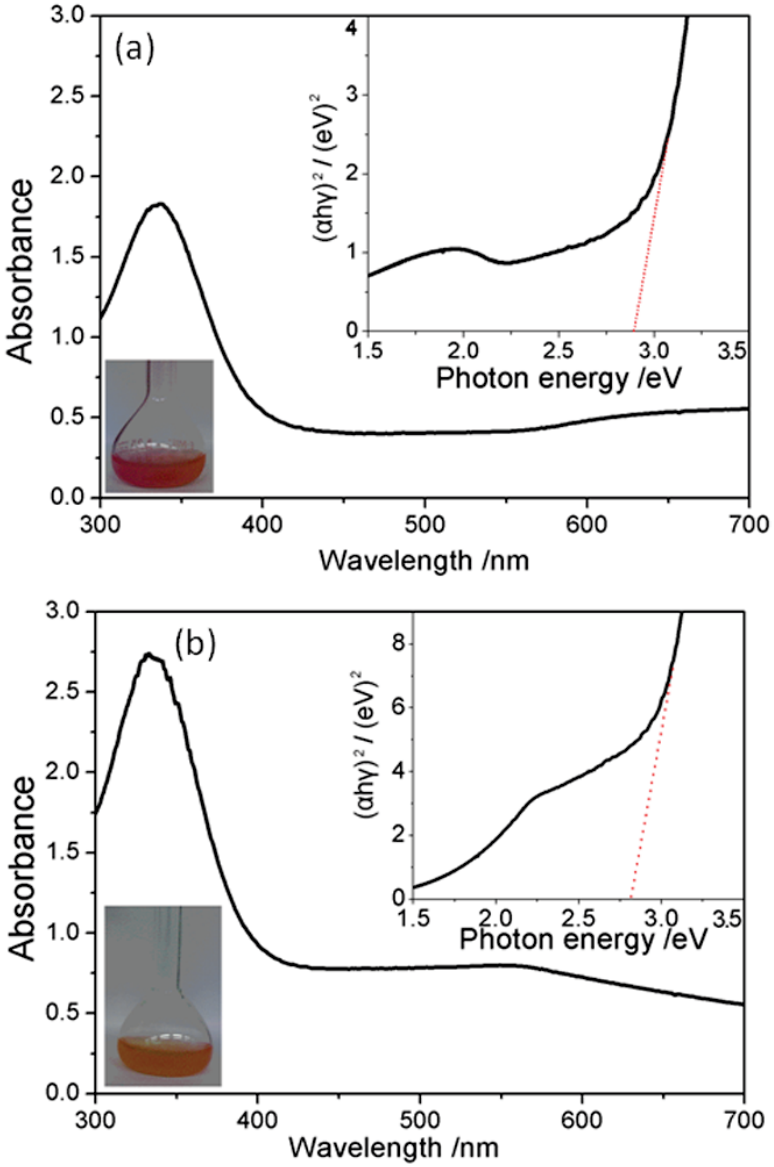

Figure 4-5 UV-visible absorption spectra of (a) as-prepared α-Fe_2O_3 nanoparticles and (b) the porous α-Fe_2O_3 material etched for 5.5 h. The insets in the upper right and lower left corners are the plot of transformed Kubelka-Munk function vs the energy of light and digital photos of sample solutions (10^{-3} mol L^{-1}), respectively.

Figure 4-5 shows the UV-visible absorption spectra of the as-prepared α-Fe_2O_3 particles and the porous α-Fe_2O_3 material etched for 5.5 h. Compared with the porous α-Fe_2O_3 sample, an additional visible light absorption band appears from 570 nm to 700 nm in the spectrum of the as-prepared α-Fe_2O_3 nanoparticles solution, which is consistent with

the deep red colour. The band gap of hematite varies in the range of 1.9-2.2 eV,[765] depending on the crystal size and preparation technique. The band gap E_g can be calculated by the Kubelka-Munk function:

$$(\alpha h\gamma)^2 = B \times (h\gamma - E_g) \quad (4\text{-}4)$$

where hν is the photon energy, α is the absorption coefficient, B is a constant. The band-gap can be derived from the plot of the Kubelka-Munk function *vs.* the absorption energy (as shown in the insets in Figure 4-4). The as-prepared α-Fe_2O_3 nanoparticles and the porous α-Fe_2O_3 (after 5.5 h etching) have a band-gap of 2.80 eV and 2.88 eV, respectively. This indicates a blue shift of 0.68-0.96 eV. Such a substantial increase of the band-gap energy may be ascribed to the quantum confinement due to the small crystal size of the as-prepared α-Fe_2O_3.[765]

4.4.2 Electrochemical performance of porous α-Fe_2O_3 for lithium storage in Li-ion battery

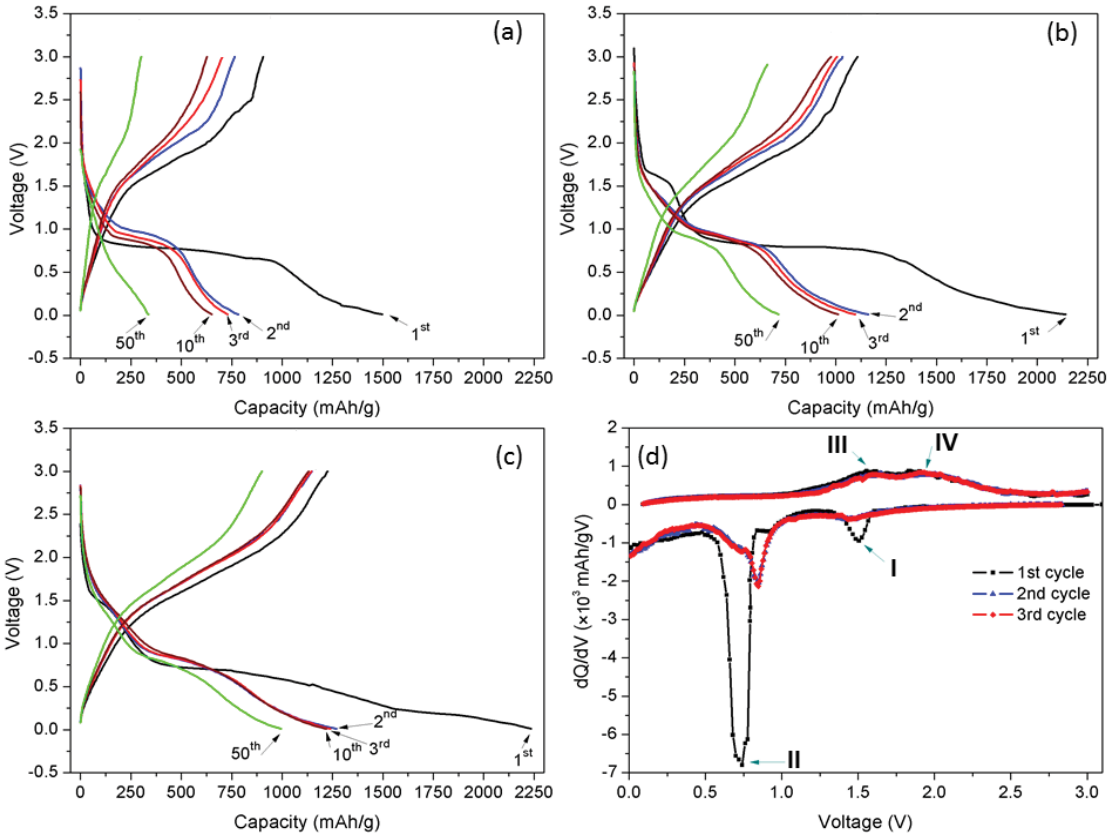

Figure 4-6 Voltage-capacity profiles of (a) commercial α-Fe_2O_3, (b) pristine porous α-Fe_2O_3, (c) 5.5 h etched porous α-Fe_2O_3 and its corresponding differential capacity *vs.* voltage plot (d).

The electrochemical performance of porous α-Fe_2O_3 for lithium storage in lithium ion cells was evaluated by galvanostatic charge/discharge testing. Figure 4-6 shows the voltage profiles of porous α-Fe_2O_3 electrodes. As a comparison, the performances of commercial porous α-Fe_2O_3 and α-Fe_2O_3 nanoparticles are also presented. All samples show the similar charge-discharge voltage profiles in the first cycle, which are consistent with the previous report.[766] For the discharge curve in the first cycle, the voltage initially decreased quickly to approximately 1.6 V, followed by a slope (1.6-

0.75 V) and a plateau at 0.75 V. The first slope can be ascribed to the formation of cubic $Li_2Fe_2O_3$ from Fe_2O_3, and the plateau could be attributed to the reduction from Fe^{2+} to Fe^0 and the formation of amorphous Li_2O.[767] This electrochemical behaviour is consistent with the results of two reduction peaks (~1.6 and 0.7 V) identified in the differential capacity *vs.* voltage plot as shown in Figure 4-6 (d), which are indexed by the peak I and the spiky peak II, respectively. These correspond to the following lithiation steps:[768]

$$\alpha\text{-}Fe_2O_3 + 2Li^+ + 2e^- \rightarrow Li_2Fe_2O_3(\text{cubic}) \quad (4\text{-}5)$$

$$Li_2Fe_2O_3(\text{cubic}) + 4Li^+ + 4e^- \rightarrow 2Fe + 3Li_2O \quad (4\text{-}6)$$

At the initial stage of lithium intercalation (peak I), a small amount of lithium was inserted into the crystal structure of α-Fe_2O_3, followed by the transformation to cubic $Li_2Fe_2O_3$. The spiky peak (peak II) corresponds to the complete reduction of iron from Fe^{2+} to Fe^{0+} and the decomposition of electrolyte. In the anodic polarisation process, two broad overlapping peaks were recorded at about 1.7 and 1.85 V (peak III and IV), corresponding to the oxidation of Fe^0 to Fe^{2+} and further oxidisation to Fe^{3+}.[768] The curves of the subsequent cycles are significantly different from that of the first cycle, as only one cathodic peak appears at about 0.8 V with decreased peak intensity, while the anodic polarisation only showed two weaker broad peaks with a little decrease in peak intensity. The difference between the first and the second cathodic curves is due to an irreversible phase transformation during the process of lithium insertion and extraction in the initial cycle. After the first discharge process, α-Fe_2O_3 was completely reduced to iron nano-particles and was dispersed in a Li_2O matrix.[766] The disappearance of the peaks at 1.6 and 0.7 V from the second cathodic process indicates that the lithium

insertion reaction and phase transformation from hexagonal α-$Li_xFe_2O_3$ to cubic $Li_2Fe_2O_3$ are irreversible.[768]

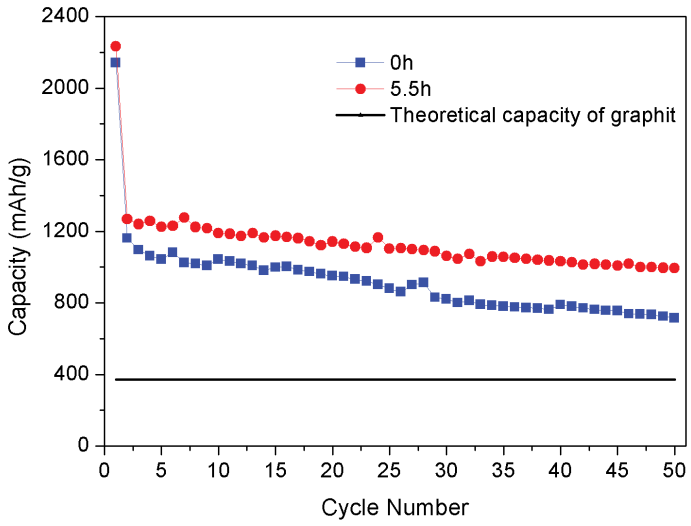

Figure 4-7 Cycling performance at the 50 mA g^{-1} current density for (a) as prepared pristine porous α-Fe_2O_3 and (b) 5.5 h etched porous α-Fe_2O_3.

In the first cycle, the capacity of the porous α-Fe_2O_3 electrode is 2234 mA h g^{-1} after discharging the voltage to 0.01 V. The large capacity could be ascribed to the decomposition of the electrolyte at low voltage (generally below 0.6 V *vs.* Li^+/Li) to form a solid electrolyte inter phase layer and further lithium storage via interfacial charging at the metal/Li_2O interface.[767] It has been demonstrated in previous reports that the morphology plays a significant role in the discharge performance.[767] The materials that have small particles with a high surface area always yield high discharge capacities, indicating that a high surface area can enhance the interfacial charge storage. During the second cycle, the discharge curve only shows a slope at 1.0-0.8 V, and the capacity is reduced to 1269 mA h g^{-1}. Usually, the slope behaviour during the discharge process of metal oxide anode materials is considered to be related to the irreversible formation of a nano-composite of crystalline grains of metals and amorphous Li_2O matrix.[768] For the charge curves of the first and second cycles, no obvious plateau can be observed, and

the charge capacities are 1225 mA h g^{-1} and 1147 mA h g^{-1}, respectively. This corresponds to the oxidation of Fe^{0} to Fe^{2+}, with part of Fe further oxidised to Fe^{3+}, along with some contribution from the reversible surface layer formed during discharge process. The difference of the capacity between as-prepared pristine porous α-Fe_2O_3 and after the 5.5 h etched porous α-Fe_2O_3, compared with theoretical capacity of graphite, has been shown in Figure 4-7. Both of the as-prepared α-Fe_2O_3 electrodes show a stable cycle life and a higher capacity than graphite. After 50 cycles, the electrode maintained a high capacity of 1094 mA h g^{-1} for 5.5 h etched porous α-Fe_2O_3. The porous space can offer better electrolyte accessibility and buffers the volume change during the charge-discharge processes, which can effectively accommodate a larger degree of structural deformation during Li insertion/extraction.[767] Furthermore, the high porosity provides larger material-electrolyte contact areas, rendering an increased number of electrochemically active surface preventing the active materials from falling off the current collector.[769]

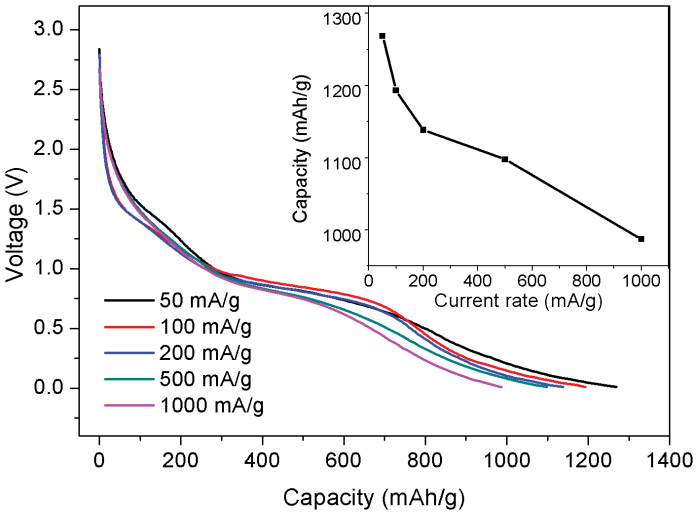

Figure 4-8 The second discharge voltage profiles of the electrode made of 5.5 h etched porous α-Fe_2O_3 at different current densities. The insert is the discharge capacity at different current densities.

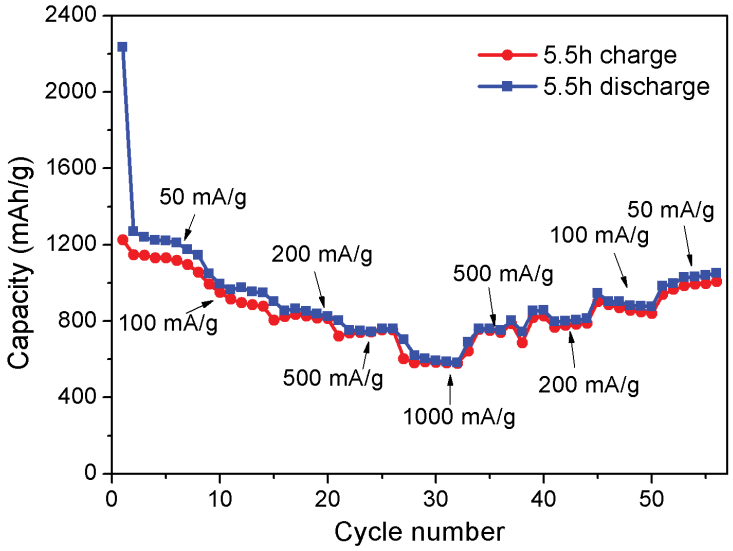

Figure 4-9 Cycling stability of porous α-Fe_2O_3 (etched for 5.5 h) electrode at various current densities.

We also investigated the electrochemical performance of the porous α-Fe_2O_3 electrode at different current densities (as shown in Figure 4-8). Even at the high current density 1000 mA g^{-1}, the electrode achieved a lithium storage capacity of 987 mA h g^{-1} at the second cycle. The porous structure with the high surface area provides high surface contact with the electrolyte and decreases the current density per unit area. This is the best performance achieved, compared with the previously reported electrochemical performance for α-Fe_2O_3 material. The excellent cycling stability and high rate specific capacity of the as-prepared porous α-Fe_2O_3 indicate its attractive potential for use as an anode material in Li-ion batteries. For a better understanding of the advantage of etched porous α-Fe_2O_3 in lithium energy storage, the cycling response at continuously variable current density (50, 100, 200, 500 and 1000 mA g^{-1}) was evaluated (as shown in Figure 4-9). When the current density is increased stepwise to as high as 1000 mA g^{-1}, it can retain a capacity of~650 mA h g^{-1}. Subsequently, the current density is decreased stepwise to 50 mA g^{-1}, it shows a pronounced increase in capacity. As long as the

current density reverses back to a low current density, the cell capacity can recover to the original value, indicating that the integrity of the porous anode material has been maintained even after a high current density charge and discharge. This clearly demonstrates that our porous material architecture is tolerant to varied charge and discharge currents, which is a desirable characteristic required for high power application.

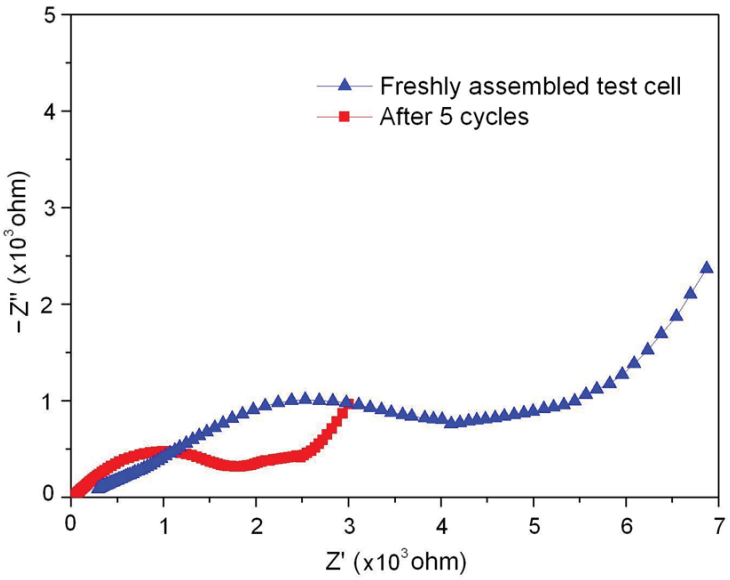

Figure 4-10 A.c impedance spectra of 5.5 h etched porous α-Fe_2O_3 in freshly assembled test cell and after 5 cycles. All cells were discharged to 0.01 V and measured in frequency range from 0.01 Hz to 100 kHz.

In order to find out how the impedance changes with cycling, A.C. impedance measurement has been conducted on the porous α-Fe_2O_3 working electrode. Figure 4-10 shows the A.C impedance spectra of the freshly assembled cell and the cell after five cycles. The A.C. impedance spectrum consists of two semicircles in the high and medium frequency ranges and a straight line in the low-frequency range. The two semicircles can be ascribed to the charge-transfer processes on the interfaces between

the electrolyte and the electrode or the metallic lithium counter electrode. The straight line is due to the lithium-ion diffusion and accumulation process in the working electrodes. This capacitive behaviour should be related to lithium storage in the porosities. It should be noticed that the cell impedance decreases substantially after cycling. After five cycles, the total charge transfer resistance of the cell decreases from 4078 Ω to 1666 Ω. This decrease of the resistance may be related to the wetting process between the electrode and the liquid electrolyte.

In general, the lower activation energy of porous α-Fe_2O_3 will be generated because of the higher surface area along with the increase of the etching time. It indicates the higher reactivity and intercalation kinetics in porous α-Fe_2O_3. This improvement is related to the instinct properties of porous α-Fe_2O_3 material for gas sensing property and Li-ion battery, such as intimate contact between media (for the sensing interaction the media is the various gas, while for the Li-ion intercalation the media is the electrolyte) and α-Fe_2O_3 nanoparticle materials, and short path for diffusion.

4.5 Conclusion

In summary, we have successfully prepared uniform porous α-Fe_2O_3 nanostructures through a controlled oxalic acid etching process at room temperature. The total pore volume and average pore size of the micro-particles can be readily tuned by varying the etching time. For the application as anode materials in Li-ion batteries, the porous α-Fe_2O_3 demonstrated a high lithium storage capacity and significantly improved capacity retention, compared to the non-porous α-Fe_2O_3. The porous α-Fe_2O_3 electrode also showed a high rate capacity and tolerance towards the varied charge/discharge current density.

CHAPTER 5 SYNTHESIS, STRUCTURE MODELLING, MAGNETIC PROPERTY AND ELECTROCHEMICAL APPLICATION OF POLYHEDRAL FACET MAGNETITE

5.1 Abstract

Polyhedral magnetite nanocrystals with multiple facets were synthesised by a low temperature hydrothermal method. Atomistic simulation and calculations on surface attachment energy successfully predicted the polyhedral structure of magnetite nanocrystals with multiple facets. X-ray diffraction, field emission scanning electron microscopy, and high resolution transmission microscopy confirmed the crystal structure of magnetite, which is consistent with the theoretical modelling. The magnetic property measurements show the superspin glass state of the polyhedral nanocrystals, which could originate from the nanometer size of individual single crystals. When applied as an anode material in lithium ion cells, magnetite nanocrystals demonstrated an outstanding electrochemical performance with a high lithium storage capacity, a satisfactory cyclability, and an excellent high rate capacity.

5.2 Introduction

In recent years, magnetite nanoparticles (Fe_3O_4) have been widely utilised in various fields, such as information storage, magnetic separation[770] and magnetic resonance imaging,[771] due to their ability to rapidly respond to an applied magnetic field, accompanied with negligible remanence and coercivity.[772-774] Magnetite nanoparticles can also rapidly separate the target molecules from the samples by simply applying an appropriate magnetic field. They have broad applications in biology and biomedicine areas, including drug delivery and targeting,[775] immunoassays,[776] hyperthermia,[777]

magnetic resonance imaging contrast enhancements,[778] biosensing,[779] and the separation, purification or detection of proteins, DNA, viruses, and cells etc.[780-782] For biological applications, many researchers have prepared Fe_3O_4 magnetic nanoparticles with various structures, or loaded them with silica,[782] polymer,[783] and lipid vesicles,[784] etc. Furthermore, magnetite nanoparticles have been applied as electrode materials in supercapacitors,[785,786] and Li-ion batteries.[787,788] Magnetite has a higher theoretical lithium ion storage capacity (926 mA h g^{-1}) than that of commercial graphite (372 mA h g^{-1}).[789,790] Theoretically, one Fe_3O_4 can react with eight Li ions, therefore it can be considered a promising electrode material for Li-ion batteries.[296,791] However, Fe_3O_4 anode materials have poor cyclic performance owing to agglomerations and huge volume change during lithium insertion/extraction. Several strategies have been pursued to resolve this problem, including preparation of nano-architectured materials and core-shell structured materials.[792-794] To the best of our knowledge, there has been no report on the synthesis of polyhedral Fe_3O_4 nanocrystals with multiple facets through a simple low temperature hydrothermal method.

The control of nanocrystalline materials plays an important role in tuning their physical and chemical properties. In this study, we have synthesised uniform nano-size polyhedral single crystal magnetite with multiple facets by a low temperature hydrothermal method. We have carried out a computer simulation study to determine the kinetically and thermodynamically stable surfaces and examined surface structures and crystal morphology of Fe_3O_4. Similar calculations have been successfully performed for TiO_2,[795,796] gibbsite (γ-$Al(OH)_3$),[797] γ-Fe_2O_3,[798] $Ca_{10}(PO_4)_6F_2$,[799] $LiFePO_4$,[800] and many other inorganic solids.[801] When applied as an electrode material in lithium ion cells, magnetite nanocrystals can tolerate the volume change during the charge/discharge process, which maintains the integrity of the electrode. Our results

show that magnetite nanocrystals outperform the previously reported Fe_3O_4 thin-films and carbon-coated Fe_3O_4.[793,794,802-804]

5.3 Experimental Section

Materials preparation: Magnetite (Fe_3O_4) nanocrystals were synthesised by a low temperature hydrothermal method. In a typical synthesis process, iron (II) sulfate heptahydrate ($FeSO_4 \cdot 7H_2O$, Sigma-Aldrich, 0.7 g), iron (III) nitrate nonahydrate ($Fe(NO_3)_3 \cdot 9H_2O$, Sigma-Aldrich, 2.02 g) and lithium hydroxide monohydrate ($LiOH \cdot H_2O$, Sigma-Aldrich, 0.31 g) were first dissolved in 20 ml distilled water and stirred for ten minutes. The solution was then de-oxygenated by bubbling with N_2 gas for half an hour to form an aqueous solution containing Fe(III) and Fe(II) ions at a molar ratio of Fe(III)/Fe(II) = 2. The solution was then sealed in a Teflon-lined stainless steel autoclave (25 ml capacity). The autoclave was heated and maintained at 180 ºC for 2 h. After then, the autoclave was cooled down to room temperature, leading to the conversion of the precipitate into a black solid product. The precipitates were retrieved by washing with ethanol and water for several times and dried in a vacuum oven at 70 °C for 12 hours.

Structural, optical and magnetic characterisation: The crystal structure and phase of the as-prepared Fe_3O_4 nanocrystals were characterised by X-ray diffraction (XRD, Siemens D5000) using a Cu K_α radiation with 2θ ranging from 20° to 90° at a scanning step of 0.02° sec^{-1}. The morphology was analysed by high resolution field emission scanning electron microscopes (FESEM, Zeiss Supra 55VP). The microscope was operated at a working distance of 2 mm with an acceleration voltage of 20 kV and an in-lens detector was used for the imaging. The structure of Fe_3O_4 nanocrystals was further characterised by transmission electron microscopy (TEM) and high-resolution

transmission electron microscopy (HRTEM, JEOL JEM-2011). Selected area electron diffraction (SAED) patterns were recorded by a Gatan CCD camera in a digital format. The band gap energy of the as-prepared Fe_3O_4 nanocrystals has been determined by ultraviolet-visible (UV-Vis) spectroscopy using a Shimadzu UV-1700 spectrophotometer.

Magnetic measurements were performed using the Quantum Design MPMS-5 SQUID magnetometer. The magnetic moment was measured as a function of temperature under three different protocols: zero-field-cooled (ZFC), field-cooled upon cooling the sample (FCC), and field-cooled upon warming the sample (FCW). In the ZFC measurements, the sample was cooled in a zero magnetic field to 10 K. A magnetic field was then applied and the magnetic moment was measured upon warming the sample to 300 K in a constant field with a constant sweep rate of temperature. The FCC measurement was then performed by measuring the magnetic moment as the temperature was decreased from 300 K to 10 K without changing the field. The FCW measurement was followed by measuring the moment upon warming from 10 K to 300 K in the same magnetic field.

Electrochemical testing: Electrochemical measurements were carried out using two-electrode coin cells (CR2032) with lithium metal as the counter electrode. To prepare the working electrode, the as prepared Fe_3O_4 powder (50 wt. %), acetylene black (40 wt. %), and poly (vinylidene fluoride) (PVDF, 10 wt. %) were mixed in N-methyl-2-pyrrolidone (NMP) to form a slurry. The resultant slurry was pasted onto copper foil with a blade and was dried at 100 °C for 12 h under the vacuum condition and followed by pressing at 200 kg cm^{-2}. The coin-cells were assembled in an argon-filled glove box. The electrolyte was 1 M $LiPF_6$ dissolved in a mixture of ethylene carbonate (EC) and dimethyl carbonate (DMC) with a volume ratio of 1:1. The charge-discharge

measurements were carried out on a NEWARE 660 battery testing system at different current densities in the voltage range of 0.05 to 3.0 V. The AC impedance spectra were measured on a CHI660C electrochemical workstation in the frequency range of 0.01 Hz to 100 kHz.

Computational methods: The structures and energies of the magnetite surfaces were modelled using classical energy minimisation techniques. These atomistic simulation methods are based on the Born model of solids,[697] which assumes that ions in a crystal interact via short-range electrostatic forces and long-range van der Waals interactions between neighboring electron charged clouds. The electronic polarisability of the ions is included via the Bush shell model[698] which is especially for binary and ternary oxides. The Buckingham potential, φ_{ij} given in Eq. (5-1), is used to treat the short-range interactions:

$$\varphi_{ij} = Aexp\left(-\frac{r_{ij}}{\rho}\right) - \frac{C}{r_{ij}^6} \quad (5\text{-}1)$$

where r_{ij} is the separation of the ion centers and A, ρ, and C are ion-ion parameters. In order to model the long-range polarisation energy for defects, a massless shell,[699] on which all pair potentials act as coupled by a harmonic force to a core from which it is Coulombically screened:

$$E_{(core-shell)} = \frac{1}{2}k_{(core-shell)}r_{ij}^2 \quad (5\text{-}2)$$

yielding an ion polarisability α_i

$$a_i = \frac{q_{shell}^2}{k_{(core-shell)}+f_{shell}} \quad (5\text{-}3)$$

where $E_{(core\text{-}shell)}$is the long-range polarisation energy, q_{shell} is the shell charge, $k_{(core\text{-}shell)}$ represents the restoring force between the core, and the shell and f_{shell} the competing distorting forces due to the presence of the surrounding ions. Lattice energy calculations

are combined with energy minimisation methods so that structural parameters are adjusted to obtain a minimum energy configuration.

According to the classification of Tasker,[700] there are three different types of surfaces: (1) an uncharged plane with cations and anions in stoichiometric ratio; (2) a stack of charged planes where the repeat unit perpendicular to the surface has no dipole moment; and finally (3) a stack of charged planes where the repeated unit has a dipole moment perpendicular to the surface. In the last instance, the surface needs to be reconstructed to remove the dipole. This can be obtained by creating surface vacancies. The surface energy per unit area, $E_{surface}^{hkl}$, of a particular surface is calculated from the difference between the energy of the surface block, $E_{surface\ block}$, and the energy of the same number of bulk ions, E_{bulk}, per unit area, A, thus

$$E_{surface}^{hkl} = \frac{E_{surface\ block} - E_{bulk}}{A} \quad (5\text{-}4)$$

The attachment energy is defined as the energy per formula unit released when a new slice of depth d_{hkl} is attached to the crystal face, and assumed to be proportional to the growth rate by a layer-by-layer mechanism. Thus, surfaces with attachment energies smaller in magnitude have slower growth rates and can be morphologically important. The attachment energy can be expressed as

$$E_{attachment}^{hkl} = \frac{E_{crystal} - E_{slice}}{n} \quad (5\text{-}5)$$

where $E_{crystal}$ is the energy of the crystal, E_{slice}, the energy between all the ions within the slice hkl, and n, the number of formula units per slice.

5.4 Results and Discussion

5.4.1 Structure and morphological analysis

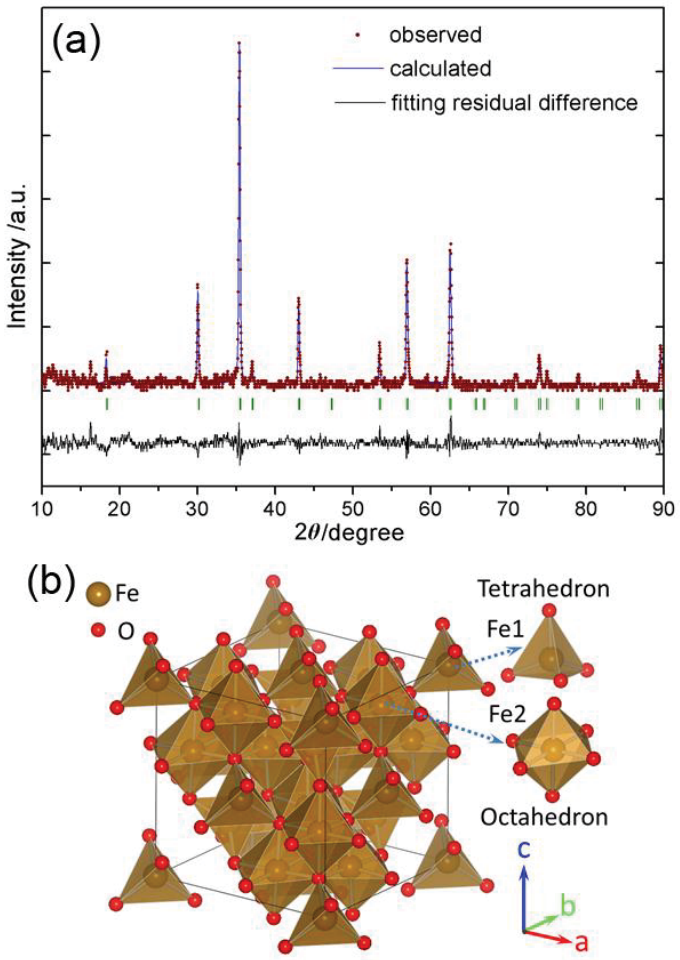

Figure 5-1 (a) X-ray diffraction pattern of the magnetite nanocrystals. The calculated pattern and the fitting residual difference of the Rietveld refinement are also represented (b) Crystal structure of the unit cell of Fe_3O_4, showing the tetrahedral iron (corresponding Fe1), octahedral iron (corresponding Fe2) and oxygen (red) ions.

Figure 5-1(a) shows the x-ray diffraction pattern of the as-prepared Fe_3O_4 nanocrystals. The results of the Rietveld refinement are also presented in Figure 5-1(a). The fitting is quite satisfactory (R_{wp} = 8.12 %, R_p = 9.23 %, R_{Bragg} = 3.03). No other trace impurities can be identified and all the Bragg deflection lines can be successfully indexed to the cubic symmetry phase with the space group: $Fd\bar{3}m$. The lattice parameters were

calculated as a = b = c = 8.391 Å and α = β = γ = 90 º. The schematic crystal structure of Fe_3O_4 nanocrystals is shown in Figure 5-1(b), which has a spinel structure. The oxygen anions (O^{2-}) form a close-packed face-centred cubic (fcc) sublattice with Fe^{2+} and Fe^{3+} cations located in the interstitial site. Two different types of cation sites exist in the magnetite crystal, which are tetrahedrally coordinated 8a sites occupied by Fe1 (typically assigned with a charge state 3+), and octahedrally coordinated 16d sites occupied by Fe2 (typically assigned to the charge states of 2+ and 3+ in equal numbers). All 32 oxygen sites fully occupy the e sites. Fe1 forms the regular FeO_4 tetrahedron and Fe2 forms octahedron as illustrated in Figure 5-1(b).

Table 5-1 Inter-atomic potential and shell model parameters used in this paper.

Ion pair	Buckingham		
	A / eV	ρ / Å	C / eV Å^6
Fe1-O	3219.335	0.2641	0
Fe2-O	3334.382	0.2641	0
O-O	25.410	0.6937	32.32
	Shell Model Parameters		
Ion	Spring constant k / eV Å^{-2}	Shell Charge q_{shell}/ e	
Fe1	20.53	1.029	
Fe2	17.11	1.029	
O	179.58	-2.513	

Table 5-2 Calculated and experimental crystallographic coordinates of the constituent atoms for Fe_3O_4.

Properties	Experimental			Calculated			Δ / %
a, b, c / Å	8.391			8.183			2.4
α, β, γ / º	90			90			0
Cell volume / $Å^3$	590.801			547.865			7.2
Density / gcm^{-3}	5.206			5.614			7.3
	X	y	z	x	Y	z	
Fe1	0	0	0	0	0	0	0
Fe2	0.625	0.625	0.625	0.625	0.625	0.625	0
O	0.385	0.385	0.385	0.3832	0.3832	0.3832	0.5
Fe1-O distance / Å	2.017			1.981			1.7
Fe2-O distance / Å	1.962			1.888			3.7

The inter-atomic potential and the shell model parameters used in this work to model magnetite Fe_3O_4 are listed in Table 5-1. Upon energy minimisation of the bulk crystal, the lattice parameters were calculated as a = b = c = 8.183 Å, and α = β = γ = 90 º (as shown in Table 5-2). The calculated results are within 3 % deviation of the experimental values. Table 5-2 also lists the calculated and experimental crystallographic coordinates of the constituent atoms, from which we can see the good agreement between calculated structure and experimental crystal structure. In particular, there is no difference for the coordinate of iron ions between calculated and experimental results. The experimental coordinate value of oxygen differs from the calculated one, resulting in the shortening of Fe1-O and Fe2-O bond distances. This contributes to the expansion of cell volume and the decrease of the density for the calculated bulk magnetite nanocrystals.

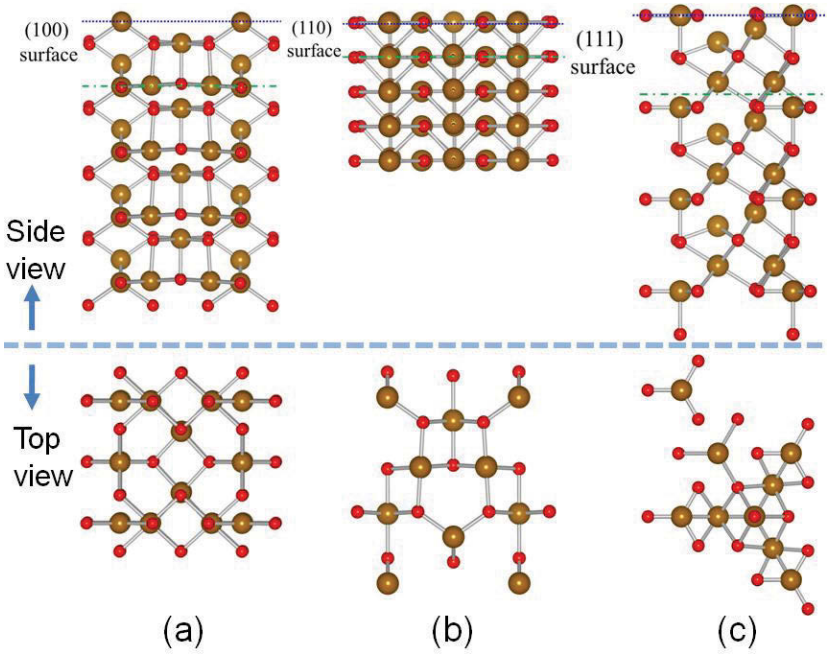

Figure 5-2 Side and top views of the relaxed (a) (100), (b) (101), and (c) (111) surfaces of Fe_3O_4 nanocrystals. The growth slices are demarcated by dotted-dashed lines.

To predict the morphology of magnetite, the surface and attachment energies must be obtained. The surface region in our calculation is composed of a finite number of two-dimensional infinite planes formed by cutting the crystal along a particular Miller index (hkl) plane. In each plane, a two-dimensional cell represents each site in the plane. Following the approach of Tasker,[700] several cells in successive planes comprise the basic repeated unit of Fe_3O_4 that contains the composition of the bulk crystal unit cell. We considered low index surfaces containing planes with the largest inter-planar spacing (d_{hkl}), which are usually the most stable surfaces. These are the most important planes morphologically predicted by the Bravais-Friedel-Donnay-Harker theory.[805] This approach assumes that the morphologically dominant faces (slowest growing) are those with thicker growth slices. We considered the (100), (010), (001), (110), (101), (011) and (111) facets of Fe_3O_4 nanocrystals. According to the previous report,[806] the relaxed surface energy is lower than the unrelaxed surface energy, which indicates the

importance of modelling the surface relaxation. Herein, the ion coordinates in each cell are calculated by using relaxed crystal coordinates. Low energy (100), (110) and (111) facets of Fe_3O_4 nanocrystals are presented in Figure 5-2. Growth slices are demarcated by dotted-dashed lines. In each case, the terminating layer contains all three moieties (Fe1, Fe2 and O).

Table 5-3 Relaxed surface and the attachment energies of magnetite nanocrystals.

Surface	Tasker surface type	Surface energy / J m^{-2}	Attachment energy / J m^{-2}
(100)	3	1.07	-3.78
(010)	3	1.15	-3.85
(001)	3	1.15	-3.85
(011)	2	0.49	-4.77
(110)	2	0.47	-4.77
(101)	2	0.49	-5.00
(111)	3	0.66	-11.85

The most stable surface and attachment energies of the relaxed surface facets are listed in Table 5-3. It shows that the (100) surface has a low energy of 1.07 Jm^{-2}, signifying its stability. The (010) and (001) facets have the same surface energy, which is less than 2 Jm^{-2}, indicating their structural similarities. The most stable surfaces are (011), (110), (101) and (111), which give almost similar low surface energy facets. The facets with the lowest attachment energies were found to be (111), (101), (110) and (011). In this approach, the facets with the smallest surface energies have proportionally the greatest area. These calculated low index facets have similar surface energies, which reveal the equilibrium habit of these surfaces. These results indicate that it is possible to achieve

polyhedral magnetite single crystals with multiple facets including (100), (010), (001), (110), (101), (011) and (111).

The general morphology of the as-prepared Fe_3O_4 nanocrystals was observed by FESEM and shown in Figure 5-3. The individual nanocrystals have a polyhedral shape with multiple facets. The average crystal size of nanocrystals was estimated to be 120 to 150 nm. The simulated model of these Fe_3O_4 nanocrystals is shown in Figure 5-3(c) and (d), which further confirms the well-defined polyhedral structure with multiple facets. The results of the FESEM observation are in good agreement with the theoretical predication.

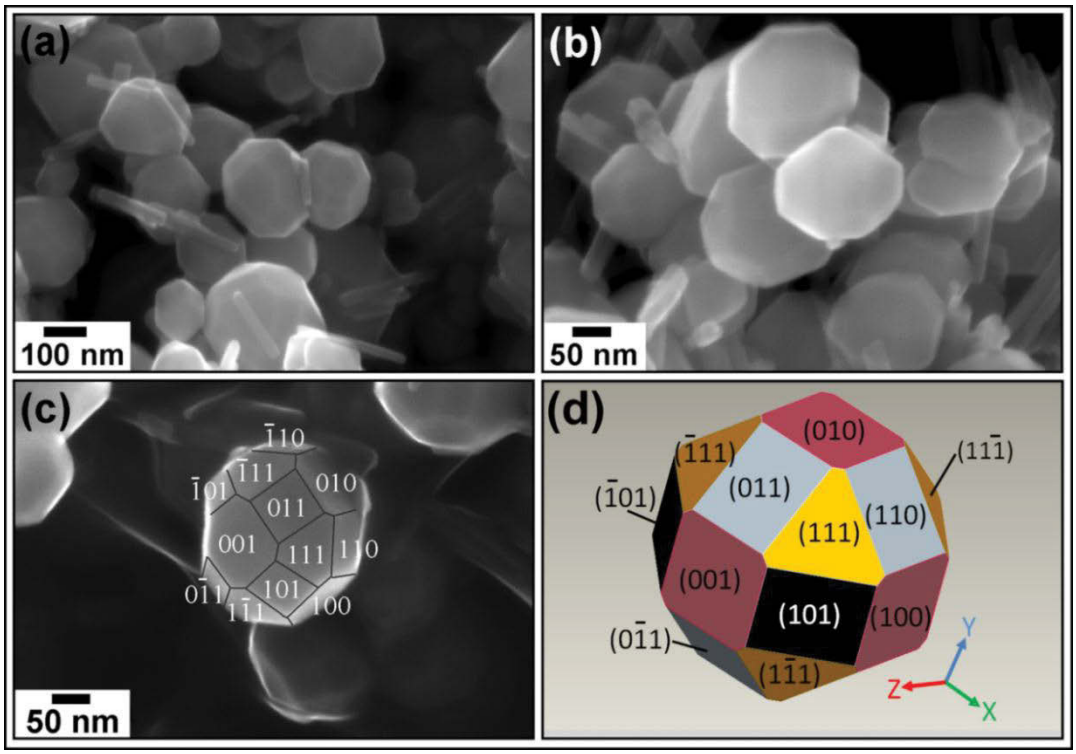

Figure 5-3 FESEM images of the as-prepared Fe_3O_4 nanocrystals: (a) low magnification and (b) high magnification SEM images, showing multifacet morphology of the Fe_3O_4 nanocrystals. (c) A SEM view of a single magnetite crystal, in which the visible facets have been labelled. (d) Simulated polyhedral crystal with multiple facets.

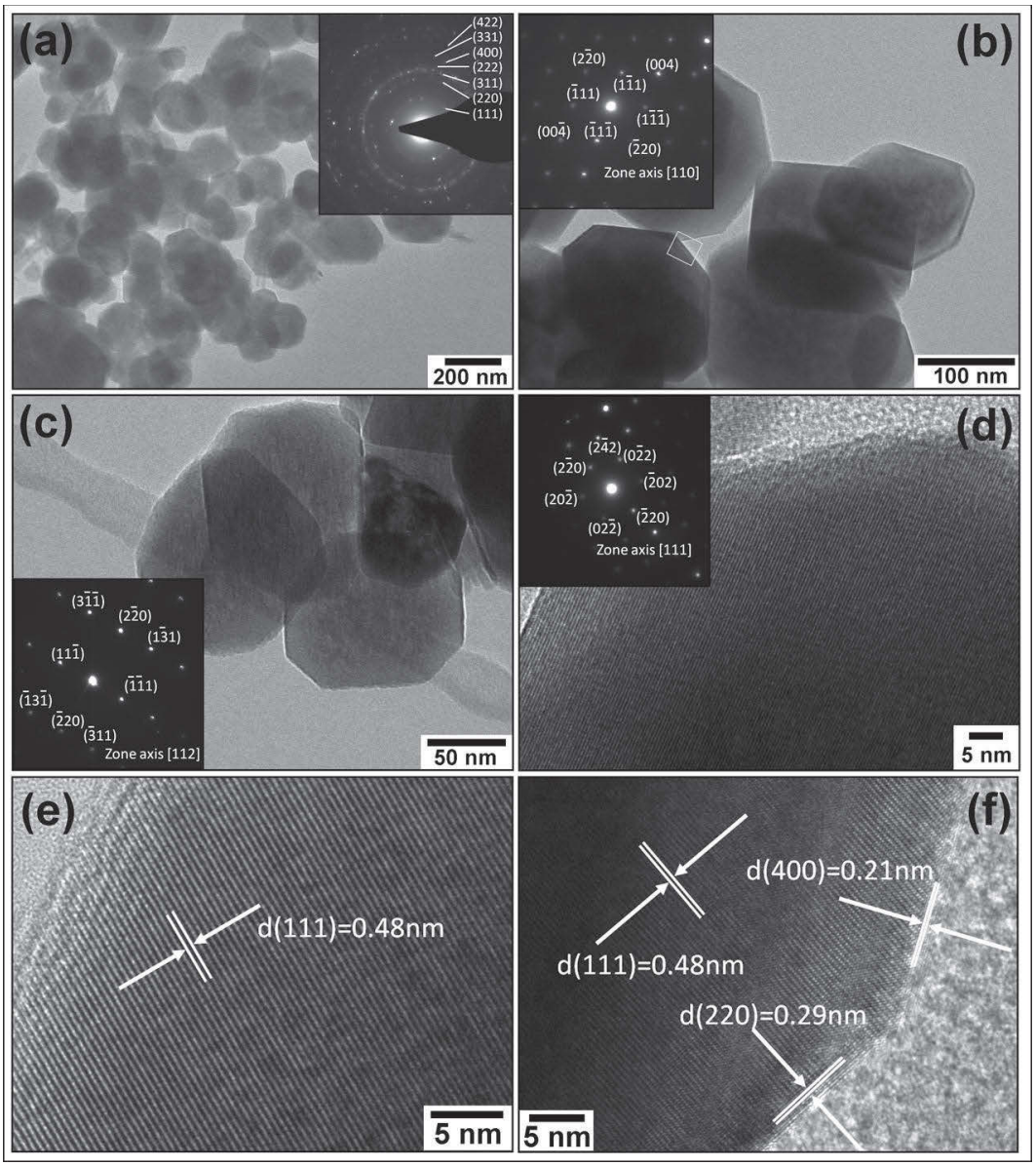

Figure 5-4 (a) – (c): TEM images of Fe_3O_4 nanocrystals at different magnifications. (d) – (f): Lattice resolved high resolution TEM images of Fe_3O_4 nanocrystals. The inset in (a) is a selected area electron diffraction ring pattern taken from many nanocrystals. The insets in (b), (c) and (d) are SAED patterns taken on individual nanosryctals along different zone axis.

The crystal structure of Fe_3O_4 nanocrystals was further analysed by TEM, HRTEM and selected area electron diffraction (SAED). Figure 5-4(a) shows a low magnification TEM image of Fe_3O_4 nanocrystals and the corresponding SAED pattern is shown as the

inset. All diffraction rings can be readily indexed to the Fe_3O_4 magnetite phase. In addition, the zone axis SAED patterns taken from individual Fe_3O_4 nanocrystals show perfect regular diffraction spots along the [110] (the inset of Figure 5-4(b), [112] (the inset of Figure 5-4(c) and [111] (the inset of Figure 5-4(d) zone axes. These SAED patterns along different zone axis clearly confirm the cubic crystal structure of Fe_3O_4 nanocrystals. Therefore, we can conclude that each free-standing nanocrystal shows single crystal characteristic with perfectly oriented aggregation. The lattice resolved HRTEM images of Fe_3O_4 single crystal presented in Figure 5-4(e) and 4(f) illustrate the inter-planar distance of (111), (220) and (400) crystal planes (0.48 nm, 0.29 nm and 0.21 nm, respectively). The clear lattice fringes of (220) and (400) crystal planes shown in Figure 5-4(f) indicate that these two crystal planes have the equilibrium growth habit. This further proved that the Fe_3O_4 nanocrystals consist of well-defined polyhedral structures with multiple facets.

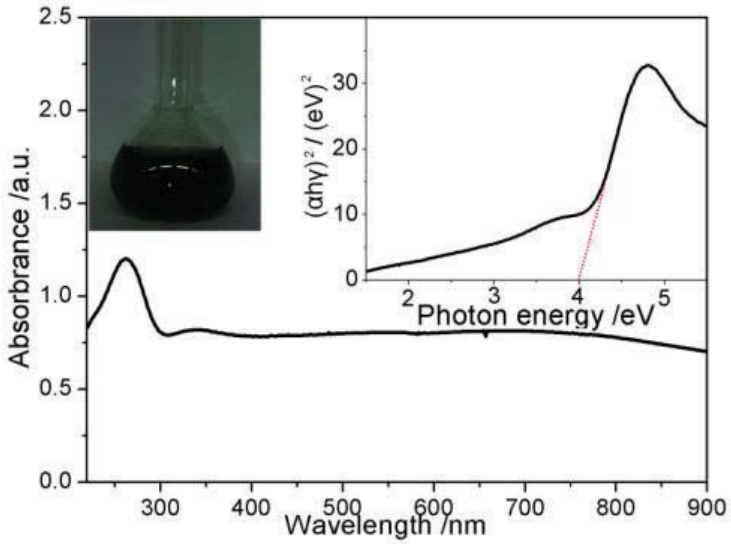

Figure 5-5 UV-Vis absorption spectrum of the as-prepared Fe_3O_4 nanocrystals. The insets in the top right and left corners are the plots of transformed Kubelka-Munk function *vs.* the energy of light and optical photo of sample solution (10^{-3} mol L^{-1}), respectively.

5.4.2 Optical and magnetic properties

Figure 5-5 shows the UV-Vis absorption spectrum of the as-prepared Fe_3O_4 nanocrystals. An additional visible light absorption band appears from 300 nm to 900 nm, which is consistent with the black color (top left inset in Figure 5-5). The band gap E_g can be calculated by the Kubelka-Munk function:

$$(\alpha h\gamma)^2 = B \times (h\gamma - E_g) \quad (5\text{-}6)$$

where hν is the photon energy, α the absorption coefficient, and B a constant. The top right inset in Figure 5-5 shows a plot of the Kubelka-Munk function *vs.* the energy of the light absorbed. The band gap of magnetite Fe_3O_4 can be derived to be 4.0 eV, which depends on its crystal size and preparation technique. Such a big band gap may be ascribed to the quantum confinement due to the small crystal size of Fe_3O_4. [807]

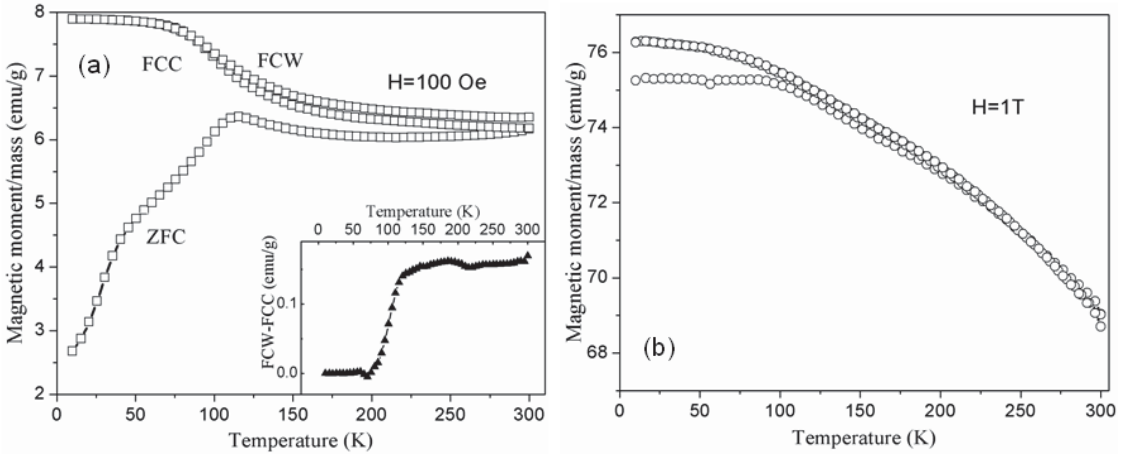

Figure 5-6 Zero-field cooled (ZFC), field-cooled upon cooling (FCC) and field-cooled upon warming (FCW) magnetic moment for nano-size Fe_3O_4 single crystals. Constant magnetic field was 100 Oe (a) and 1 T (b). Inset of (a): FCC moment subtracted from FCW moment for the two samples, showing that the difference between FCW and FCC moments builds up almost entirely at the temperatures of spin freezing.

Figure 5-6 shows the zero-field cooled (ZFC), field-cooled upon cooling (FCC), and field-cooled upon warming (FCW) measurements for the nano-size Fe_3O_4 single crystal with the constant field of 100 Oe (a) and 1T (b). The temperature was changed at a rate of 2 K min^{-1}. A common feature for the sample is that the magnetic moment has the lowest values for ZFC measurements. For H = 100 Oe, the ZFC moment rises sharply with the increase of temperature up to 50 K, followed by a slightly weaker increase between 50 K and 115 K. There is a peak at 115 K. Between 115 and 220 K, the magnetic moment decreases with temperature. There is a slight increase of the moment with temperatures between 200 and 300 K. The value of the FCC moment gradually increases as the sample cooled from 300 K to 115 K. This is followed by a much faster increase with further cooling from 115 K to 70 K. Finally, the magnetic moment changes little with further cooling below 70 K, staying at 7.9 emu g^{-1}. The value of the FCC moment is always larger than that of the ZFC one. The value of the FCW moment is the same as for the FCC moment between 10 and 75 K. For higher temperatures, the FCW moment is larger than the FCC moment. The difference between the FCW and FCC moments builds up in the temperature range between 75 and 115 K, where a magnetic transition is evident for all three measuring sequences (the inset in Figure 5-6(a). Figure 5-6(b) shows the temperature dependence of ZFC, FCC and FCW magnetic moments under the same conditions as in Figure 5-6a, but at a higher constant field of 1 T. Similar features are obtained, with a notable difference being the ZFC moment is constant below 100 K. Above that, the difference between the FCC and FCW magnetic moments is negligibly small. The curvatures in this plot are all positive above 125 K, whilst they were negative for the field of 100 Oe.

Because of nanometre size of Fe_3O_4 nanocrystals, the net spin of each nanocrystal is small enough to be perturbed by thermal excitations. These spins are called superspins,

because they are still much larger than the spins of individual iron atoms. If these superspins do not interact with each other, or only weakly interacted, they are called superparamagnets. At high temperatures, their orientation is completely randomised by thermal excitations, similar to paramagnetism of atomic spins. An external magnetic field provides some degree of alignment against thermal disorder. By cooling the superparamagnets down to low enough temperatures in the magnetic field, the magnetic moment of a superparamagnet gradually freezes-in.

However, if the nanocrystals have a large enough magnetic moment and anisotropy, and are packed densely enough, they will strongly interact with each other. This interaction causes different dynamics of the superspins than in the case of superparamagnets, resulting in different relaxation characteristics and different spin alignment upon cooling or warming in the magnetic field. The strongly interacting superspins will also freeze-in as the temperature decreases; however, their exact alignment also depends on the interaction between them. The samples consisting of strongly interacting superspins are called superspin glasses.

An experimental procedure that would allow a distinction between superparamagnets and spin glasses was put forward,[808] relying on the difference in superspin dynamics for superparamagnets and spin glasses. Memory effects occurring when the cooling was paused in FCC measurements for a few hours were ascribed to superspin glass behaviour. This interpretation was later refuted by Sasaki et al.,[809] showing experimentally that both superspin glasses and superparamagnets can exhibit such behaviour. They showed both theoretically and experimentally that the superspin glasses and paramagnets can be distinguished by the temperature dependence of the FCC moment below freezing temperature. For superparamagnets, the FCC moment is

expected to continuously increase as the sample is cooled through its freezing temperature. This is simply because the superspins are gradually frozen in the direction of the external field upon cooling. However, the FCC moment for superspin glasses will remain constant, or even decrease, upon cooling through the freezing temperature. This could be ascribed to the strong interactions between superspins.

Our measurements show clearly that FCC moments saturate during the cooling of samples across the freezing temperatures (Figure 5-6). This indicates that the as-prepared nano-size Fe_3O_4 single crystals are superspin glasses, with freezing temperatures of 115 K. The spin relaxation of strongly interacting nanocrystals is still significant above the freezing temperature, and it causes the difference between ZFC and FCC moments at high temperatures. An increased relaxation rate upon unfreezing the spins in FCW measurements is responsible for the difference between FCC and FCW moments at high temperatures.

Sasaki et al. also considered the memory effects associated with pausing the initial cooling for a few hours at a particular temperature, T_{stop}, for ZFC and FCC measurements.[809] They ascertained that there will be a difference between ZFC magnetic moments for superspin glasses with and without the pause at T_{stop}. A small magnetic field had to be used to obtain these effects. The difference in thus obtained ZFC moments was predicted to be the largest at T_{stop}. No difference in so measured ZFC moments should be obtained in superparamagnets. Their experiments on Fe_3N nanoparticles (superspin glass)[810] and ferritin (superparamagnet)[811] confirmed those theoretical predictions, using the field of 2 Oe.

To prove the superspin glass state of Fe_3O_4 nanocrystals, we performed magnetic memory measurements suggested by Sasaki et al.[45]. Samples were first cooled down

from 200 K (well above the freezing temperatures of our samples) to 10 K at a rate of 10 K min^{-1}. A field of 100 Oe was applied and the ZFC moment measured as the temperature was increased at the rate of 1.5 K min^{-1}. Our superconducting magnet has a remanent field of a few Oe. A field of 100 Oe was chosen to minimise the effects of the remanent fields of the magnet. In the second set of ZFC measurements, the initial cooling down from 200 K at the rate of 10 K min^{-1} was stopped for 7200 seconds at T_{stop}. We chose T_{stop} = 30 K. Samples were then further cooled to 10 K at the rate of 10 K min^{-1}. The field of 100 Oe was applied and the ZFC moment again measured from 10 K to 200 K with a sweep rate of 1.5 K min^{-1}.

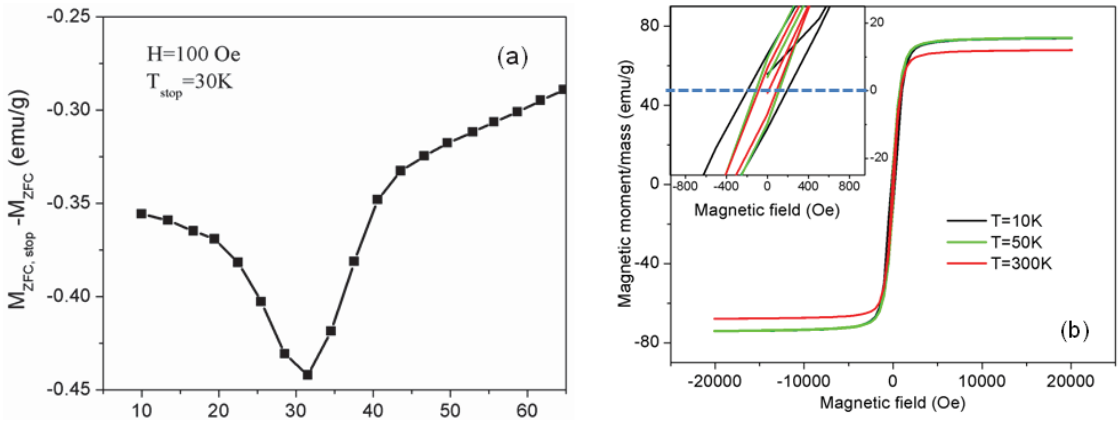

Figure 5-7 (a) Temperature dependence of the difference between the ZFC moment measured after a pause of the initial cooling of the sample at T_{stop} for 7200 s and the reference ZFC moment, measured without the pause in the initial cooling; and (b) magnetic hysteresis loops measured at 10, 50 and 300 K.

The ZFC moments measured without stopping the temperature sweep at T_{stop} were subtracted from the ZFC measurements with a two hour pause at T_{stop}, as shown in Figure 5-7(a). A dip occurs at 30 K, which is the value of T_{stop} used for the samples, exactly as predicted by the theory. Thus, we obtained definite proof that our samples are superspin glasses. We note that the dips at T_{stop} were obtained at a relatively large field

of 100 Oe. The same measurements with the 1T field did not show any difference in the two ZFC measurements. Our results with the field of 100 Oe are consistent with the equivalent measurements performed on Fe_3O_4 nanoparticles using a 5 Oe field.[812]

Magnetic hysteresis loops for nano-size Fe_3O_4 single crystals are shown in Figure 5-7(b). The magnetic moment gets almost fully saturated at 4000 Oe. The saturation moment at 2 T was 73.99, 74.12 and 67.89 $emug^{-1}$ at temperatures of 10, 50 and 300 K, respectively. There was a small coercive field of 195, 114 and 90 Oe, for temperature of 10, 50 and 300 K, respectively. The shape of our hysteresis loops and the value of the saturation moment are comparable to other Fe_3O_4 nanoparticles.[813,814] The shape of the hysteresis loops is characteristic for samples consisting of superspins, which confirms our arguments based on temperature dependence of the magnetic moment.

The magnetic properties of our nanoparticles are affected by their shape. The strongest magnetic interaction in bulk Fe_3O_4 is the superexchange interaction between Fe ions in tetrahedral sites and octahedral sites, via an O ion. This interaction gives an antiferromagnetic-type ordering of Fe ions with different spins, resulting in a ferrimagnetic system with ordering temperature of 858 K. This interaction and ionic states of Fe and O will be disrupted at surfaces. Each of different surfaces in our nanoparticles will contain different terminating layers, resulting in different magnetic properties. Due to the shape of nanoparticles, they can be packed closely together, which could be responsible for the observed strong interaction between them and formation of superspin glass state (Figure 5-7). We note that the spin ordering temperature for our samples is close to Verwey temperature for Fe_3O_4 (T_V = 122K), which is associated with ordering of Fe^{2+} and Fe^{3+} in octahedral sites and lattice distortion. It is unclear if the Verwey transition would affect the observed magnetic

properties of our samples, because its contribution to net magnetic moment of Fe_3O_4 is not significant and the exact mechanism of this transition is still unclear.

The only phases other than the polyhedral Fe_3O_4 detected by XRD and SEM in our samples are Fe_3O_4 nanorods (Figure 5-3). They are not likely to be responsible for the distinguishing magnetic features of our samples.

5.4.3 Electrochemical performance of Fe_3O_4 nanocrystals for lithium storage in lithium ion cells

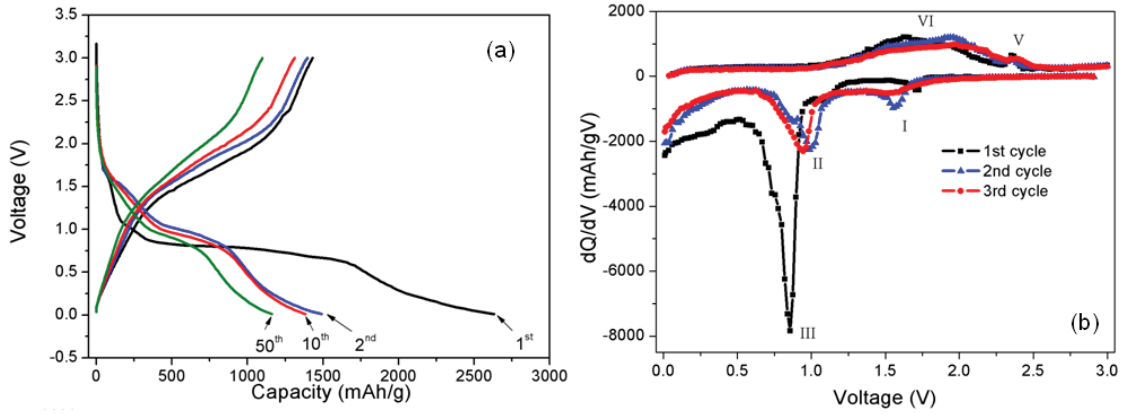

Figure 5-8 (a) Voltage-capacity profiles of as-prepared nano-size Fe_3O_4 nanocrystal electrode cycled at the current density of 50 mA g^{-1}. (b) The corresponding differential capacity *vs.* voltage.

We tested the lithium storage capacity of the as-prepared Fe_3O_4 nanocrystals as potential anode materials for Li-ion batteries. Figure 5-8 shows the charge/discharge profiles of Fe_3O_4 nanocrystal electrodes cycled at 50 mA g^{-1} current density. The voltage profiles of Fe_3O_4 nanocrystals are similar to those reported previously.[766,815] As shown in Figure 5-8(a), the voltage initially quickly drops to approximately 1.75 V, followed by a slope to 0.85 V, and a plateau between 0.8 V and 0.75 V. To identify all electrochemical reactions, the differential charge-discharge capacity *vs.* voltage is presented in Figure 5-

8(b). In the first cycle, the reduction peak is observed at 1.75 V (peak I), which can be attributed to the irreversible reaction with the electrolyte. The reduction peaks at 1.25 and 0.8 V (peak II and peak III) can be assigned the lithiation of Fe_3O_4:[793]

$$Fe_3O_4 + xLi \rightarrow Li_xFe_3O_4 \quad (5\text{-}6)$$

$$Li^+ + Li_xFe_3O_4 \rightarrow Fe^0 + Li_2O \quad (5\text{-}7)$$

The conversion of Fe_3O_4 to Fe and the formation of amorphous Li_2O lead to the irreversible capacity during the first discharge step. Meanwhile, two oxidation peaks at about 1.5 V and 2.4 V (peak IV and peak V) in the anodic process are corresponding to the oxidation of Fe^0 to Fe^{2+} and Fe^{3+}. During the subsequent cycles, both cathodic and anodic peaks are positively shifted, which is caused by polarisation of electrode materials. The cells show different voltage profiles with a long plateau at about 1.0 V in the discharge (lithiation) process and a short plateau at about 1.6 V in the charge process. The voltage plateaus measured here reveals the presence of Fe_3O_4 and the heterogeneous reaction between lithium and metal oxide:[816]

$$8Li + Fe_3O_4 \leftrightarrow 3Fe + 4Li_2O \quad (5\text{-}8)$$

In fact, the discharge profiles above 0.8 V can be divided into two segments, i.e. a decreasing trend from about 3.0 V to 0.8 V, which can be attributed to the reaction: $Fe_3O_4 + xLi \rightarrow Li_xFe_3O_4$, and a plateau at 0.8 V, which can be attributed to the conversion reaction $Li_xFe_3O_4 + (8\text{-}x)Li \rightarrow 3Fe + 4Li_2O$.[785]

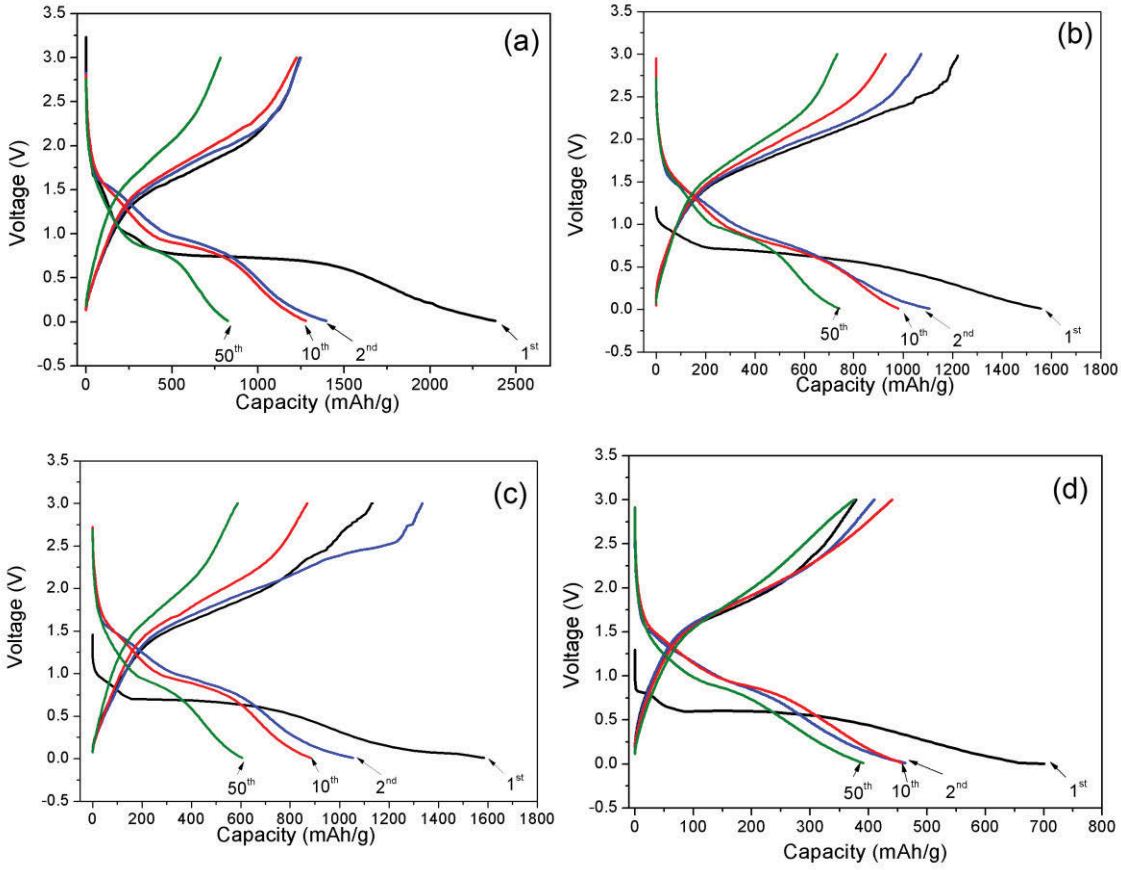

Figure 5-9 Voltage-capacity profiles of the as-prepared Fe_3O_4 nanocrystals at different current densities: (a) 100 mA g^{-1}, (b) 200 mA g^{-1}, (c) 400 mA g^{-1}, (d) 1000 mA g^{-1}.

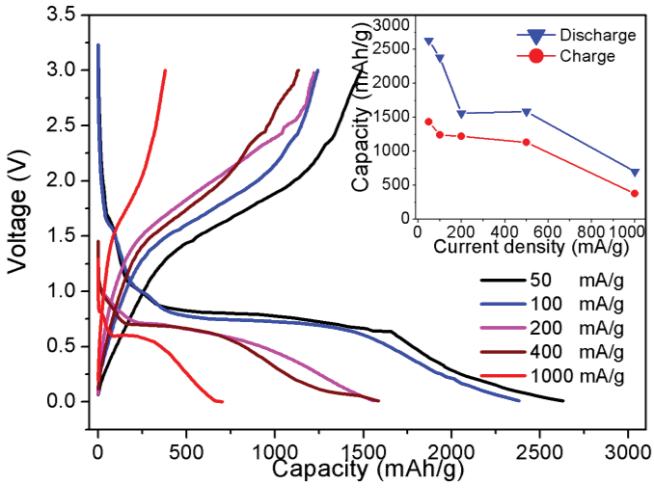

Figure 5-10 Comparison of charge and discharge voltage profiles in the 1st cycle of at different current densities. The inset is the specific capacity at different current densities.

After discharging the voltage to 0.01 V, the capacity of Fe_3O_4 is 2632 mA h g^{-1}, corresponding to 22 mole Li per mole of Fe_3O_4, which is much higher than the theoretical capacity of Fe_3O_4 (8 mole of Li per mole of Fe_3O_4). The large excess capacity can be ascribed to the decomposition of the electrolyte at low voltage to form a solid electrolyte inter phase (SEI) layer and further lithium storage via interfacial charging at metal/Li_2O interface.[315,817] It has been demonstrated in previous reports that the morphology and particle size play significant roles in the discharge performance.[817] The materials that have small particles with high surface area always provide high discharge capacities, indicating that high surface area can enhance the interfacial charge storage. Such large irreversible capacity observed in the first cycle could be attributed to the conversion of Fe_3O_4 to Fe nanoparticles and the formation of amorphous Li_2O, trapped Li^+ in the inner holes. During the second cycle, the discharge capacity is reduced to 1489 mA h g^{-1}. Unusually, the reducing trend during the discharge process of metal oxide anode materials is related to the irreversible formation of a nano-composite of crystalline grains of metals and amorphous Li_2O matrix.[818] The voltage profiles of Fe_3O_4 nanocrystals at different current densities are further shown in Figure 5-9. We also compared the 1st cycle charge and discharge voltage profiles of the electrode at different current densities as shown in Figure 5-10.

Figure 5-11 shows the cycling performance of the as-prepared Fe_3O_4 nanocrystals at different current densities. Fe_3O_4 nanocrystals demonstrated a good rate capacity. Even at the high current of 1000 mA g^{-1}, the electrode can still deliver a specific capacity of 700 mA h g^{-1} in the first cycle. From the second cycle, Fe_3O_4 nanocrystal electrodes have maintained satisfactory capacity retention on cycling. Further, Fe_3O_4 nanocrystals delivered a higher lithium storage capacity than that of graphite at all current densities.

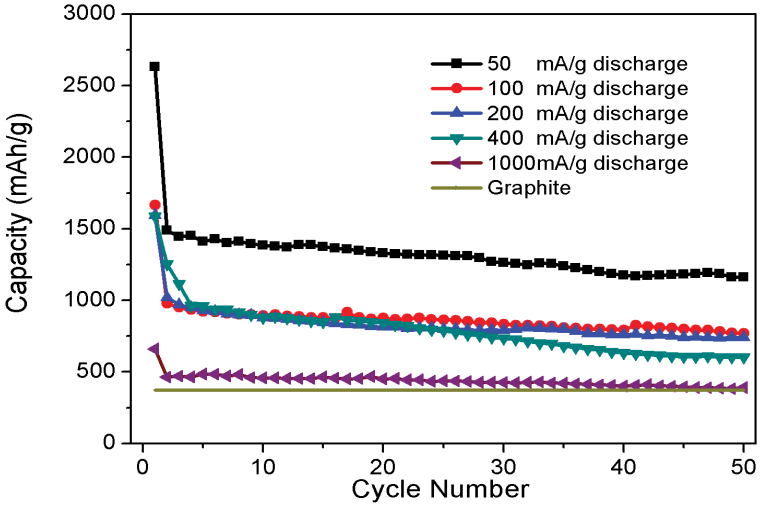

Figure 5-11 Cycling performance of the as-prepared Fe_3O_4 nanocrystals at different current densities.

Nano-size crystals offer much high surface area for the interaction between lithium ions and active material. Nanocrystals can also accommodate a larger degree of structural deformation during Li insertion/extraction. Furthermore, large material-electrolyte contact areas render an increase of electrochemically-active surface sites and prevent the active materials from falling off the current collector.[429,819,820]

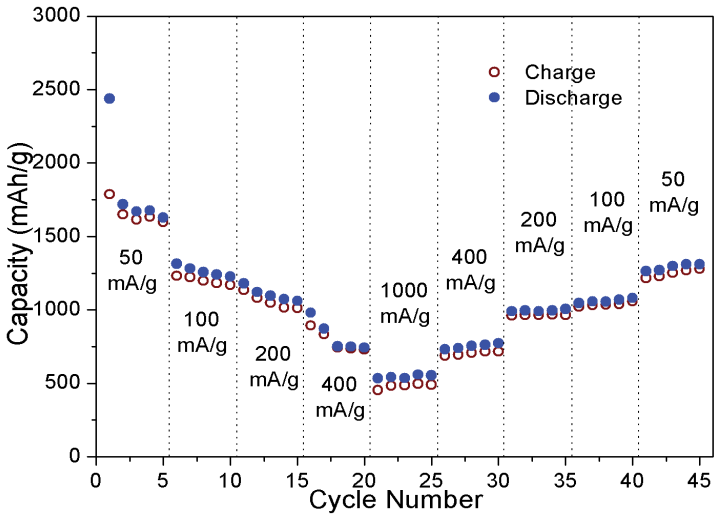

Figure 5-12 Cycling stability of the as-prepared Fe_3O_4 nanocrystal electrode at varied current densities.

For a better understanding of the advantage of the as-prepared Fe_3O_4 nanocrystals in lithium energy storage, the cycling performance at continuously variable current densities was evaluated (as shown in Figure 5-12). When the current densities increase, the lithium storage capacity decreases. As long as the current density reverses back to low current density, the cell capacity can recover almost to the original value, indicating that Fe_3O_4 nanocrystals can tolerate high current charge/discharge cycling.

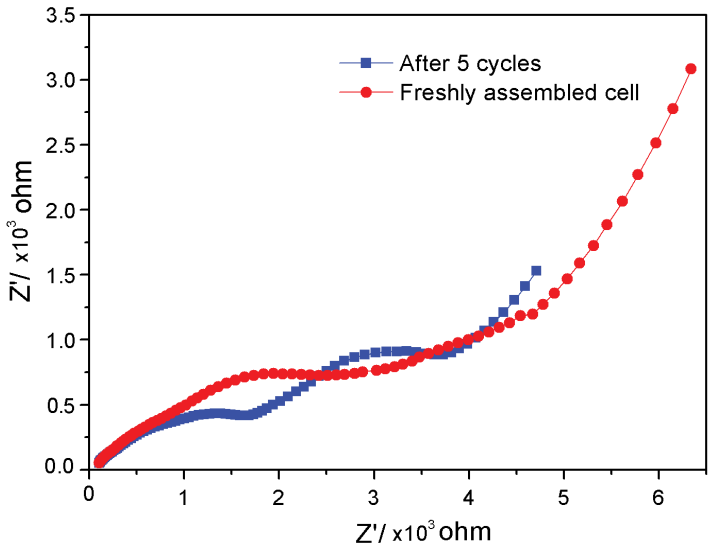

Figure 5-13 A. C. impedance spectra of as-prepared Fe_3O_4 in freshly assembled test cell and after 5 cycles test cell. All cells were discharged to 0.01 V and measured in frequency range from 0.01 Hz to 100 kHz.

A.C. impedance measurements were conducted on the Fe_3O_4 nanocrystals electrodes for both the freshly assembled cell and the cycled cell. Figure 5-13 shows the A. C. impedance spectra, which consist of semicircles in high frequency range and a straight line in the low-frequency range. The semicircles can be ascribed to the charge-transfer processes on the interfaces between the electrolyte and the electrode. The straight line is due to the lithium-ion diffusion and accumulation process in working electrodes. This capacitive behaviour should be related to lithium storage in the large surface area. It

should be noted that the cell impedance decreases substantially with cycling. After five cycles, the total charge transfer resistance decreased from 2789 Ω to 1521 Ω. This reduced resistance could be related to the generation of iron during the electrochemical reaction.

5.5 Conclusion

Polyhedral magnetite nanocrystals with multiple facets have been prepared by a simple low temperature, hydrothermal method. Theoretical calculations on the attachment energy indicate that it is possible to synthesize magnetite Fe_3O_4 nanocrystals with multiple facets, including (100), (010), (001), (110), (101), (011) and (111). The morphology and crystal structure of Fe_3O_4 nanocrystals have been systematically characterised by XRD, FESEM, TEM and HRTEM analysis, which confirmed a polyhedral crystal shape with multiple facets. The magnetic relaxation measurements show the superspin glass behaviour of the polyhedral Fe_3O_4 nanocrystals, which has been confirmed by the measurement of magnetic hysteresis loops further. When applied as anode material in lithium ion cells, Fe_3O_4 nanocrystals demonstrated a high lithium storage capacity and a satisfactory cycling performance. In particular, Fe_3O_4 nanocrystals show the tolerance towards charge and discharge at high current densities.

CHAPTER 6 PROPERTY OF 1-D Fe_3O_4 NANOWIRES AS ELECTRODE MATERIALS FOR LI-ION BATTERIES AND SUPERCAPACITORS

6.1 Abstract

One-dimensional magnetite (Fe_3O_4) nanowires were synthesized by the low temperature hydrothermal method. The as-prepared Fe_3O_4 nanowires were systematically characterized by X-ray diffraction, field emission scanning electron microscopy and transmission electron microscopy. X-ray diffraction and transmission electron microscopy have confirmed the cubic structure of Fe_3O_4 nanowires with a space group of $Fd\bar{3}m$. Electrochemical properties of Fe_3O_4 nanowires were tested as anodes in lithium-ion cells by cyclic voltammetry and galvanostatic charge/discharge. Fe_3O_4 nanowires exhibited an excellent reversible lithium storage capacity and a satisfactory cycling performance.

6.2 Introduction

Li-ion batteries are expected to be the choice of power sources for the future electric vehicles (EVs).[821] The demand to enhance the performance and safety of Li-ion batteries has stimulated the search for new electrode materials. A number of transition metal oxides have been reported to have much high specific capacity than that of graphite. Among them, magnetite (Fe_3O_4) can store up to 8 Li per formula with a theoretical specific capacity of 926 mA h g^{-1} at a relative low potential.[377,822] Moreover, it is highly favored as anode materials because of their lower toxicity, natural abundance, and superior safety compared with those based on V, Co, or Fe.[823] Its density, 5.17 g cm^{-3}, is much higher than that of graphite, 2.268 g cm^{-3}, which results in volumetric

energy density as several times as graphite. Although magnetite is very attractive for its high specific capacity, low-cost and availability, agglomerations and volume changes during lithium insertion/extraction induce poor cyclability. Several strategies have been employed to overcome this problem, including the preparation of nano-architectured materials, mixing the particles with various carbon additives, and the synthesis of core-shell nanostructured materials.[824-827] The controlled synthesis of low dimensional nanostructures transition metal oxides has also been elaborated to improve the electrochemical performance.[755,828,829] In particular, one-dimensional nanostructures including nanowires, nanorods, nanotubes and nanoribbons, have been extensively explored for energy storage and conversion.[830-832] For examples, V_2O_5 nanotubes, $LiCoO_2$ nanowires and $Li(Ni_{1/2}Mn_{1/2})O_2$ nanowires have exhibited improved electrochemical performance.[833-835] Cobalt oxide (Co_3O_4) nanowires and gold–cobalt oxide hybrid nanowires were synthesized by using a virus-enabled synthesis process, which demonstrated a stable capacity of 800–1200 mA h g^{-1}.[836] Porous Co_3O_4 nanotubes were prepared using carbon nanotubes (CNTs) as templates and demonstrated a high capacity of 1200 mA h g^{-1} and good cycle life.[837] Tin oxide (SnO_2) nanowires were prepared through a self-catalysis grown process via thermal evaporation. They showed better electrochemical performance than that of microcrystalline SnO_2 powders due to the increased charge-transfer properties along the radial direction of the nanowire.[838] The use of nanowire architectures will offer high capacity and improved cyclic stability because of their high interfacial contact area with the electrolyte and better accommodation of strain and volume change without any structural change or fracture.[839,840] Moreover, the one-dimensional nanowire morphology is beneficial for achieving high rate performance since it facilitates better electron and lithium ion transport than electrodes comprising small nanoparticles in which the electrons and

lithium-ions have to move through particles and are limited by the inter-particle contacts. The morphological control of nanocrystalline materials is becoming increasingly important because their properties are highly shape and size dependent.[841] In this chapter, we report the one step hydrothermal synthesis of magnetite nanowires as an anode material for Li-ion batteries at low temperature (220 C°) compared with the traditional high temperature (around 450-550 C°) synthesis method.[842,843] The as-prepared Fe_3O_4 nanowires exhibited a higher reversible capacity and better cycling performance than that of previously reported Fe_3O_4 thin-film and carbon coated Fe_3O_4 powders.

6.3 Experimental

6.3.1 Materials preparation

Fe_3O_4 nanowires were synthesized through a hydrothermal route. In a typical synthesis process: Iron (II) sulfate heptahydrate ($FeSO_4 \cdot 7H_2O$, Sigma-Aldrich, 0.875 g), iron (III) nitrate nonahydrate ($Fe(NO_3)_3 \cdot 9H_2O$, Sigma-Aldrich, 2.525 g) and lithium hydroxide monohydrate ($LiOH \cdot H_2O$, Sigma-Aldrich, 0.3875 g) were first dissolved in 25 ml distilled water and stirred for 10 minutes. Then the solution was de-oxygenated by bubbling N_2 gas for 30 minutes to form an aqueous solution containing Fe(III) and Fe(II) ions at a molar ratio of Fe(III)/Fe(II) = 2. The solution was sealed and then transferred into a Teflon-lined stainless steel autoclave. The whole procedure was carried out in a glove-box filled with Ar gas to prevent oxidation of Fe(II). The autoclave was heated to and maintained at 220 $^{\circ}$C for 28 h. The reaction product was retrieved by washing with ethanol and water several times and dried in a vacuum oven at 70 °C for 12 hours.

6.3.2 Structural and magnetic characterization

The crystal structure and phase purity of the as-prepared Fe_3O_4 nanowires were characterized by X-ray diffraction (XRD, Siemens D5000) using Cu K_α radiation. The morphology was analysed by high resolution field emission scanning electron microscopes (FESEM, Zeiss Supra 55VP), transmission electron microscopy (TEM) and high-resolution transmission electron microscopy (HRTEM, JEOL JEM-2011).

6.3.3 Electrochemical testing

Electrochemical testing was carried out using two-electrode coin cells with lithium metal as the counter electrode. To prepare the working electrode, the as-prepared Fe_3O_4 nanowires (60 wt. %), acetylene black (30 wt. %), and poly (vinylidene fluoride) (PVDF, 10 wt. %) were mixed in N-methyl-2-pyrrolidone (NMP) solvent to form a slurry. The resultant slurry was pasted onto copper foil and was dried at 100 °C for 12 h under vacuum conditions followed by pressing at 200 kg cm^{-2}. The CR2032-type cells were assembled in an argon-filled glove box. The electrolyte solution was 1 M $LiPF_6$ dissolved in a mixture of ethylene carbonate (EC) and dimethyl carbonate (DMC) with a volume ratio of 1:1. The charge-discharge measurements were carried out on a NEWARE 660 battery testing system at ambient temperature in the voltage range from 0.01 to 3.0 V.

6.4 Results and discussion

6.4.1 Structure and morphological analysis

Figure 6-1 shows the X-ray diffraction pattern and the Rietveld refinement of the as-prepared Fe_3O_4 nanowires. The sharp diffraction peaks indicate the high crystallinity of as-prepared products. No any trace impurity phase was identified. All diffraction lines

were successfully indexed to the space group of $Fd\bar{3}m$, having a cubic symmetry unit cell with lattice parameters a, b, c = 8.3945 Å, α, β, γ = 90 º. When performing the Rietveld refinement, the fitting was satisfactory (R_{wp} = 9.82 %, R_p = 9.37 %, R_{Bragg} = 5.58). The refined crystal structure of Fe_3O_4 has a spinel type crystal structure, in which oxygen anions O^{2-} form a close-packed face centred cubic (fcc) sublattice with Fe^{2+} and Fe^{3+} cations located in interstitial site.[844] Two different kinds of cation sites exist in the magnetite crystal: tetrahedrally coordinated 8a sites occupied by Fe1 (typically assigned with a charge state 3+), and octahedrally coordinated 16d sites occupied by Fe2 (typically assigned with charge states 2+ and 3+ in equal numbers). All 32 oxygen sites are fully occupied e sites. Fe1 is coordinated as the regular FeO_4 tetrahedron, and Fe2 is coordinated as the FeO_6 octahedron.

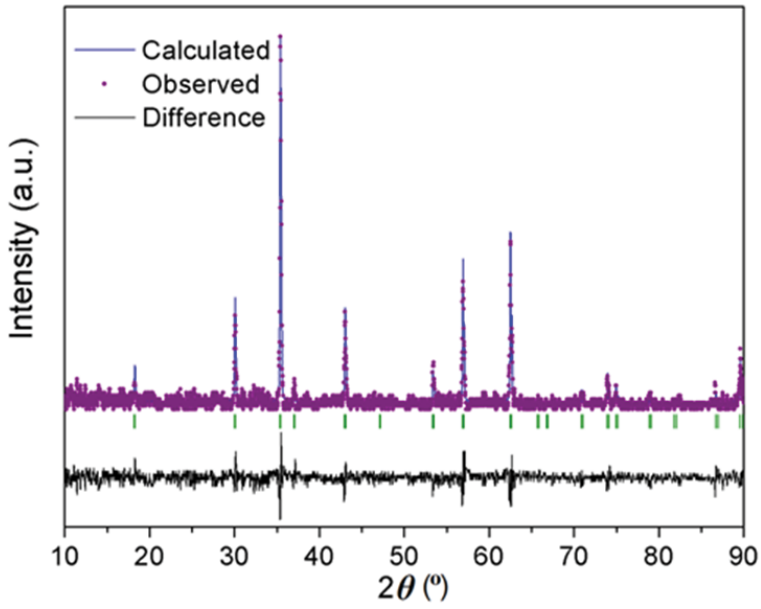

Figure 6-1 Rietveld refinement pattern of X-ray diffraction data for the Fe_3O_4 nanowires; the observed and calculated intensity are represented by purple solid circle markers and blue solid lines respectively. The bottom black line shows the fitting residual difference. Bragg positions for Fe_3O_4 are represented as light green tick marks.

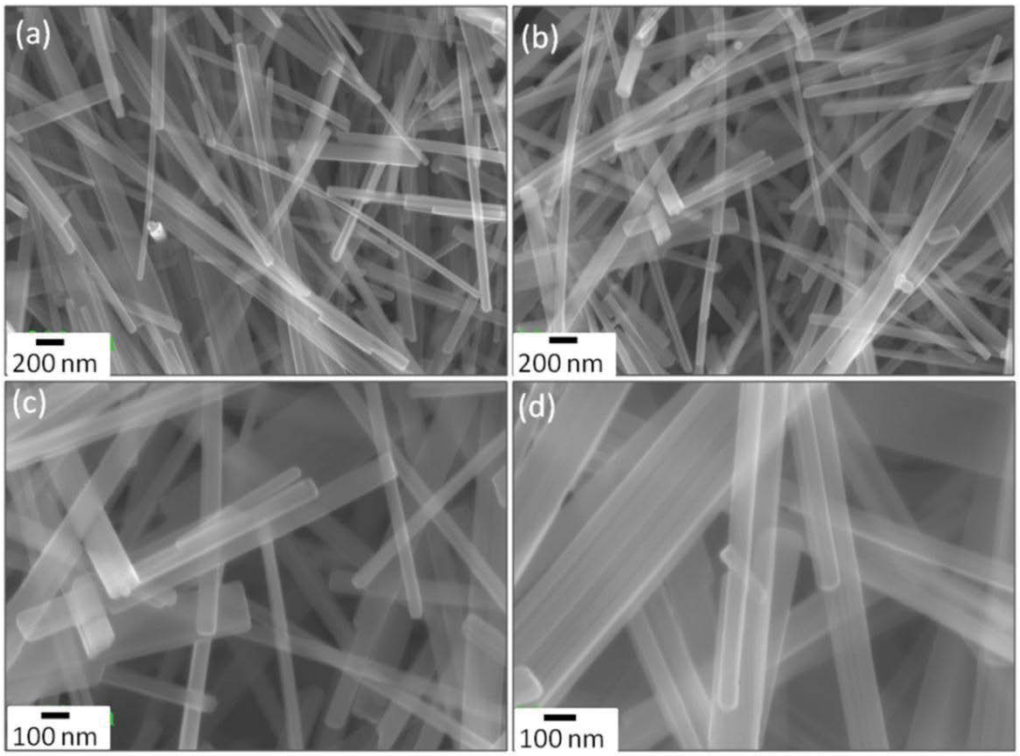

Figure 6-2 FESEM images of the as-prepared Fe_3O_4: (a), (b) low magnification, (c) and (b) high magnification.

The general morphology of as-prepared Fe_3O_4 nanowires was observed by FESEM (as shown in Figure 6-2). Typical FESEM images reveal that as-prepared Fe_3O_4 nanowires consists of long and straight nanowires with a diameter of about 50 nm and a length extending from several micrometers to a few tens of micrometers. Figure 6-2 (c) and (d) further shows a magnified view of the Fe_3O_4 nanowires, clearly illustrating that the nanowires have a smooth surface and a homogeneous distribution of diameters. TEM analysis combined with selected area electron diffraction (SAED) and high resolution TEM observation (Figure 6-3) further characterised the nanowire morphology and the crystal structure of the Fe_3O_4 sample. Figure 6-3(a) and (b) shows low magnification TEM images of Fe_3O_4 nanowires. The diameter of nanowires is determined to be about 50 nm and the length-to-diameter aspect ratio is more than 100. It is in consistent with the results of FESEM analysis. Figure 6-3(c) shows a magnified TEM view of an

individual Fe_3O_4 nanowire with smooth surface. The SAED pattern shown as the inset in Figure 6-3 (c) has been indexed to $(1\bar{1}1)$ and (220) crystal planes along the $[1\bar{1}2]$ zone axis, respectively. The dot SAED pattern clearly indicates that the Fe_3O_4 nanowire is a single crystalline and has a preferred growth direction of [531]. The corresponding HRTEM image (Figure 6-3 (d)) illustrates the inter-planar distance of (111) crystal planes.

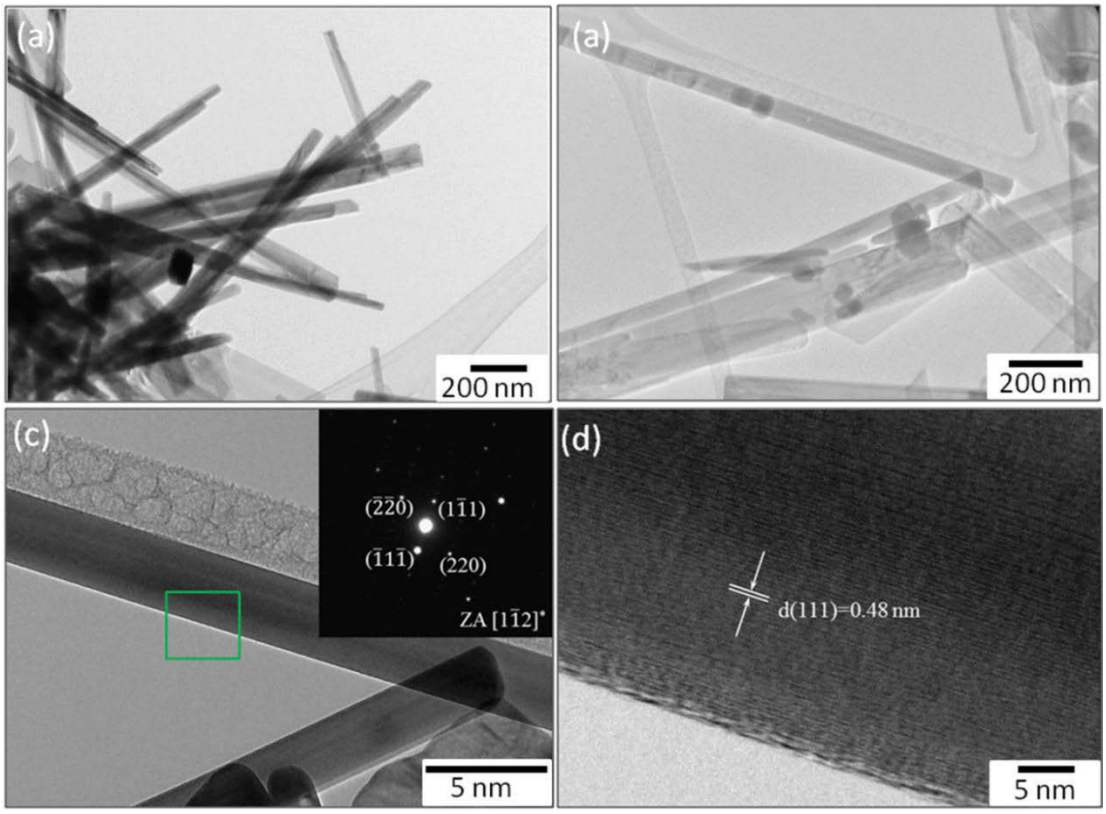

Figure 6-3 TEM images of Fe_3O_4 nanowires at different magnifications. (a), (b) low magnification, (c) high magnification and (d) Lattice resolved high resolution TEM images of Fe_3O_4 nanowires. The inset in (c) is a selected area electron diffraction patterns taken from marked area.

6.4.2 Electrochemical performance

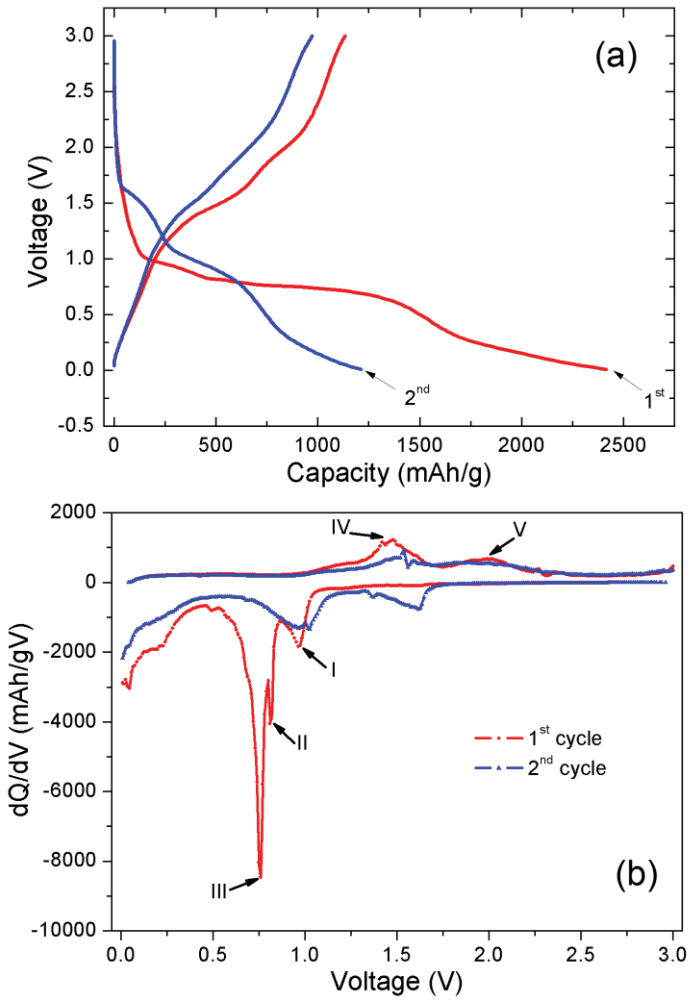

Figure 6-4 (a) Voltage-capacity profiles of as-prepared nano-size Fe_3O_4 nanowires electrode cycled at the current density of 50 mA g^{-1}. (b) The corresponding differential capacity *vs.* voltage.

The lithium storage capacity of the as-prepared Fe_3O_4 nanowires was evaluated by electrochemical testing. Figure 6-4 shows the charge/discharge profiles. The charge-discharge curves are consistent with the previous report.[815,845] As shown in Figure 6-4 (a) the voltage decreases quickly to 1.6 V, then declines to 1.0 V, followed by a slope from 1.0 to 0.82 V and a plateau between 0.82 and 0.75 V. From the second cycle, the discharge curve shows two plateaus: one is from 1.6 to 1.3 V and the other one is

between 1.3 and 1.0 V. The differential charge-discharge capacity is presented in Figure 6-4 (b). In the first cycle, the cathodic peak at 1.0 V (peak I) is attributed to the irreversible reaction with the electrolyte In the first cycle, the cathodic peak at 1.0 V (peak I) is attributed to the irreversible reaction with the electrolyte which turns out to be linked to the growth of the solid electrolyte interphase (SEI) contains both an inorganic and an organic layer around the particles. Li_2CO_3 and alkyl carbonates were the main constituents of the inorganic layer, while the poly(ethylene oxide) oligomers mainly presented within the organic layer.[846] The peak II (0.82 V) and peak III (0.75 V) correspond to the lithiation reactions of Fe_3O_4 to $Li_xFe_3O_4$ and $Li_xFe_3O_4 \rightarrow Fe^0 + Li_2O$.[793] Meanwhile, two peaks are recorded at about 1.5 and 2.0 V (peak IV and peak V) in the anodic process, corresponding to the oxidation of Fe^0 to Fe^{2+} and Fe^{3+}during the anodic process. During the subsequent cycles, both cathodic peaks are positively shifted. That might be caused by the small size of resultant Fe particles (with several nanometer sizes) decomposed from the Fe_3O_4 after the initial lithiation process.[847,848]

After discharging the voltage to 0.01 V, the discharge capacity of Fe_3O_4 is 2416 mA h g^{-1}, corresponding to 15 mole Li per mole of Fe_3O_4, which is much higher than the theoretical capacity of Fe_3O_4 (8 mole of Li per mole of Fe_3O_4). The large excess capacity can be ascribed to the decomposition of the electrolyte at low voltage to form a solid electrolyte inter phase layer and further lithium storage via interfacial charging at metal/Li_2O interface.[817,848,849] It has been demonstrated in previous reports that the morphology plays a significant role in the discharge performance.[817] The charge capacity is 1135 mA h g^{-1} in the first cycle at 50 mA g^{-1} current density. During the second cycle, the discharge capacity is reduced to 1214 mA h g^{-1}. Unusually, the slope behaviour during the discharge process of metal oxide anode materials is considered to

be related to the irreversible formation of a nano-composite of crystalline grains of metals and amorphous Li_2O matrix.[818]

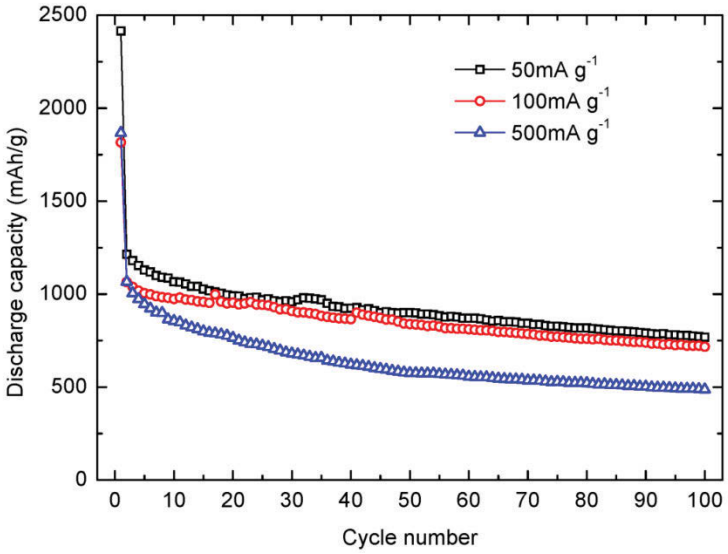

Figure 6-5 Cycling performance at the current density of 50, 100, and 500 mA g^{-1}.

The as-prepared Fe_3O_4 nanowires show a good cyclability as shown in Figure 6-5. After 50 cycles, the electrode still maintained a discharge capacity of 900 mA h g^{-1} at the current density of 50 mA g^{-1}. When increasing the current density to 100 mA g^{-1}, there is no obvious decrease of the discharge capacity. Even increasing the current density to 500 mA g^{-1}, a high initial discharge capacity of 1868 mA h g^{-1} was still obtained. Apparently, the as-prepared Fe_3O_4 nanowires also exhibit good capacity retention at high current density.

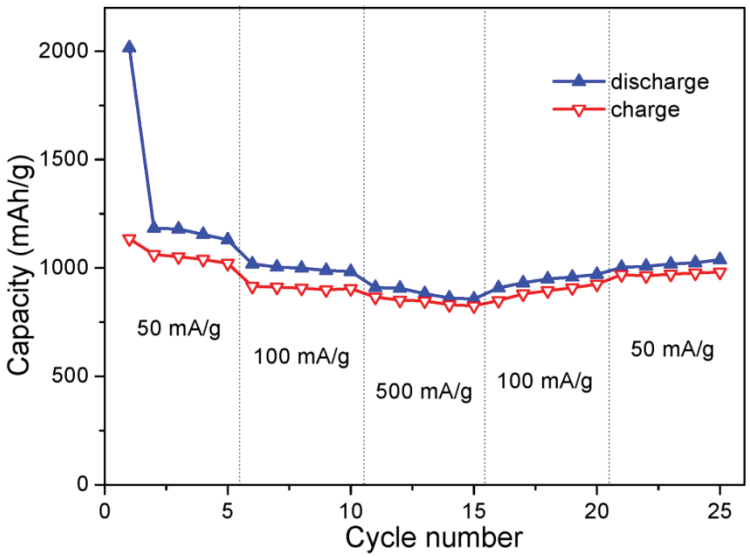

Figure 6-6 Cycling stability at various current density for as-prepared Fe_3O_4 nanowires.

For a better understanding of the advantage of as-prepared nano-size Fe_3O_4 single crystal in lithium energy storage, the cycling response at continuously variable current density was evaluated (Figure 6-6). When the current density is increased stepwise from 50 to 500 mA g^{-1}, it can retain a discharge capacity of 906 mA h g^{-1}. Subsequently, the current density is decreased stepwise to 50 mA g^{-1}, it shows a stable increase in capacity. As long as the current density reverses back low current density, the cell capacity can recover almost to the original value, indicating that the integrity of as-prepared Fe_3O_4 nanowires anode material has been maintained even after high current density charge and discharge. The improved electrochemical performance of the 1D nanostructure as anode materials in lithium-ion cells could be ascribed to the facile lithium diffusion and high electrochemical reactivity.

6.5 Conclusions

One-dimensional magnetite (Fe_3O_4) nanowires were synthesized by a hydrothermal method. The morphology and crystal structure of Fe_3O_4 nanowires have been

systematically characterised by XRD, FESEM, TEM and HRTEM analysis, which confirmed the uniform preferred growth direction and single crystal characteristics. When as-prepared Fe_3O_4 nanowires were applied as anodes in Li-ion cells, they demonstrated a high lithium storage capacity and a satisfactory cycling performance.

CHAPTER 7 NiO NANOWIRES AS ELECTRODE MATERIALS FOR LI-ION BATTERIES AND SUPERCAPACITORS

7.1 Abstract

Mesoporous nickel oxide nanowires were synthesized by a hydrothermal reaction and subsequent annealing at 400 ºC. The porous one-dimensional nanostructures have been analysed by field emission scanning electron microscope, high resolution transmission microscope and N_2 adsorption–desorption isotherm measurement. When applied as the anode material in Li-ion batteries, the as-prepared mesoporous nickel oxide nanowires demonstrated an outstanding electrochemical performance with a high lithium storage capacity, a satisfactory cyclability, and an excellent rate capacity. Mesoporous nickel oxide nanowires also exhibited a high specific capacitance of 348 F g^{-1} as electrodes in supercapacitors.

7.2 Introduction

Li-ion batteries and supercapacitors are important electrochemical energy storage and conversion devices. Currently, Li-ion batteries are the most advanced power sources for portable electronic devices.[850-852] The combination of Li-ion batteries and supercapacitors are being considered as the state-of-the-art energy sources to power electric vehicles (EVs) and hybrid electric vehicles (HEVs).[32] The intrinsic diffusivity of the lithium ions in the solid state electrodes limits the rate of lithium intercalation/de-intercalation. The high energy applications urgently require the development of new electrode materials with high capacity (in particular, high rate capacity) and high energy density. Therefore, extensive studies have been devoted to improve the high

intercalation rate performance of electrode materials for high energy Li-ion batteries.[25,819,853-861]

Transition metal oxides have been widely investigated as anode materials for Li-ion batteries because they have higher specific capacity and volumetric energy density than that of commercial graphite anode materials.[487,854,862,863] The electrochemical performance of metal oxide anodes depends on the composition, morphology and crystal structure of materials. During the lithiation and de-lithiation process, it is usually associated with significant variations for transition metal oxide anode materials, which induces the pulverization of the electrode.

The porous structure can provide voids to cushion electrode materials from pulverization in Li-ion batteries.[864-867] Recently, many mesoporous structured materials have been developed as electrode materials for Li-ion batteries, including cathode materials such as $LiCoO_2$, $LiMn_2O_4$, MnO_2, $LiFePO_4$, and $LiTiO_2$[868-872] and anode materials like Co_3O_4, SnO_2, MoO_2 and TiO_2 based materials.[435,873-877] Porous structured materials can provide high surface area, large surface-to-volume ratio, and favourable structural stability against volume expansion/contraction. These characteristics improve electrochemical performance because they can lead to fast ion/electron transfer and sufficient contact interface between active materials and electrolyte.

In this chapter, a facile synthesis of mesoporous NiO nanowires by a hydrothermal method was reported. High quality polycrystalline NiO nanowires have been obtained. The as-prepared mesoporous NiO nanowires exhibited a superior electrochemical performance for reversible lithium storage in Li-ion batteries and a high charge storage supercapacitance in supercapacitors.

7.3 Experimental Section

7.3.1 Materials preparation

Mesoporous NiO nanowires were synthesized by the combination of a hydrothermal method and the annealing treatment. In a typical synthesis process: 0.5 mmol $NiCl_2 \cdot 6H_2O$ (Sigma-Aldrich, ≥ 97 %)) was dissolved in 20 ml distilled water. Then 0.03 g of $K_2C_2O_4$ (Sigma-Aldrich, 98 %) and 8.0 ml of ethylene glycol (Sigma-Aldrich, 99 %) were added under vigorous stirring. A clear transparent solution was formed gradually. The mixture was then transferred into a Teflon lined stainless steel autoclave and heated to 220 °C for 12 h. After cooling to room temperature, the product was collected by centrifugation and washed thoroughly with distilled water and absolute ethanol several times, respectively, then dried at 80 °C for12 h in a vacuum oven. Finally, the as-prepared precursor materials were annealed at 400 ºC for 2 h.

7.3.2 Structural, optical and magnetic characterisation

The crystal structure and phase purity of the as-prepared products were characterized by X-ray diffraction (XRD, Siemens D5000) using Cu K_α radiation. The morphology and crystal structure were analysed by high resolution field emission scanning electron microscopes (FESEM, Zeiss Supra 55VP) and transmission electron microscopy (TEM) and high-resolution TEM (HRTEM, JEOL JEM-2011). FTIR spectra of the samples were recorded on a Bruker Tensor 27 IR spectrometer by using KBr as the dispersant. Thermogravimetric and differential thermal analysis (TGA–DTA) was performed at a heating rate of 5 °C/min in air using a 2960 SDT system. N_2 adsorption–desorption isotherms were measured using a Quadrasorb SI analyzer at 77 K. BET surface area was

calculated using the experimental points at a relative pressure of P/P_0 = 0.05–0.25. The pore size distribution was calculated by the Barret–Joyner–Halenda (BJH) method.

7.3.3 Electrochemical testing

For electrochemical testing, the electrodes were prepared by dispersing the as-prepared NiO nanowires (70 wt %), acetylene carbon black (20 wt %), and poly (vinylidene fluoride) binder (PVDF, 10 wt %) in N-methyl-2-pyrrolidone (NMP) solvent to form a slurry. The resultant slurry was pasted onto copper foil and dried at 100 °C for 12 h in a vacuum oven. Electrochemical measurements were carried out using two-electrode coin cells with lithium foil as the counter electrode. The CR2032-type coin cells were assembled in an argon-filled glove box (UniLab, Mbraun, Germany). The electrolyte solution was 1 M $LiPF_6$ dissolved in a mixture of ethylene carbonate (EC) and dimethyl carbonate (DMC) with a volume ratio of 1:1. Cyclic voltammetry (CV) was carried out on a CHI 660C electrochemistry workstation with a scan rate of 0.1 mV s^{-1} from 0.01 to 3.0 V in a two-electrode system. The charge-discharge measurements were performed at different current densities in the voltage range from 0.01 to 3.0 V. For the measurement of supercapacitance, a beaker-type three-electrode cell was fabricated using the as-prepared NiO nanowires as the electrode material. The electrochemical properties were evaluated in 2M KOH electrolyte at room temperature by the cyclic voltammetry (CV) method. Platinum foil and a saturated calomel reference electrode (SCE) were used as the counter electrode and the reference electrode, respectively. CV measurements were conducted over the voltage range from -0.2 to 0.6 V vs. SCE at various scanning rates (5, 10, 20, 50, and 100 mV s^{-1}). The specific capacitance C (F g^{-1}) was calculated based on the following equation:

$$C = Q / v \times m \times \Delta E \qquad (7\text{-}1)$$

Where Q is the voltammetric charge obtained by integrating the cyclic voltammogram curve; v is the scanning rate, m is the active mass of the electrode material; and ΔE is width of the potential window.

7.4 Results and Discussion

7.4.1 Structure and morphological analysis

The morphologies of the $NiC_2O_4 \cdot 2H_2O$ precursor nanowires and the annealed products were analysed by FESEM observation. Figure 7-1(a) and (b) show the FESEM images of $NiC_2O_4 \cdot 2H_2O$ nanowires (precursor) and NiO nanowires (final product), respectively. As shown in Figure 7-1(a), the precursors consist entirely of $NiC_2O_4 \cdot 2H_2O$ nanowires with lengths extending to a few tens micrometers. After annealing treatment, the precursor $NiC_2O_4 \cdot 2H_2O$ nanowires were successfully converted to NiO nanowires without any by-products such as nanoparticles and broken fragments (as shown in Figure 7-1(b)). A high magnification FESEM image of a NiO nanowire is shown in Figure 7-2.

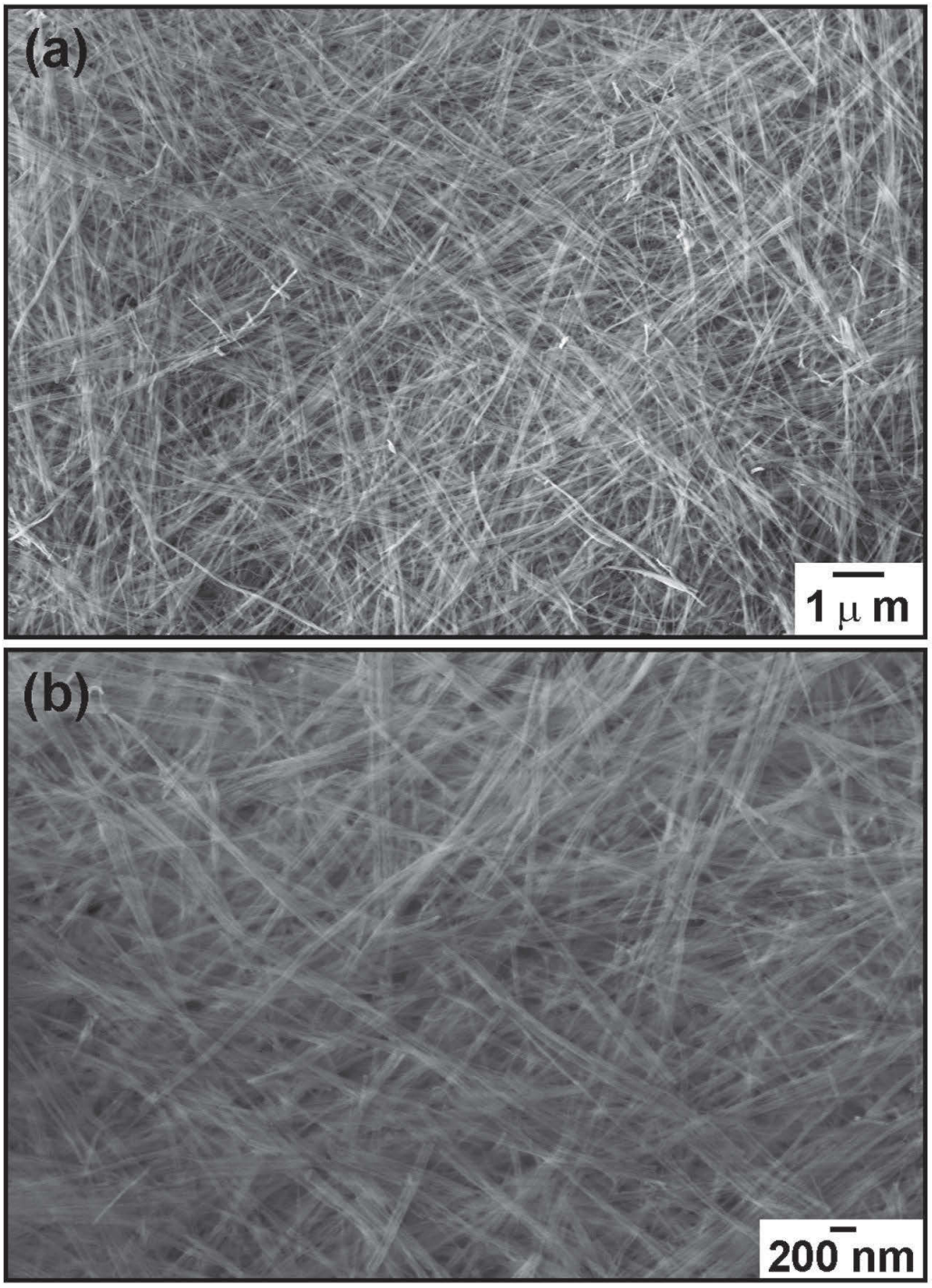

Figure 7-1 FESEM images of (a) the as-prepared $NiC_2O_4 \cdot 2H_2O$ precursor nanowires, and (b) NiO nanowires.

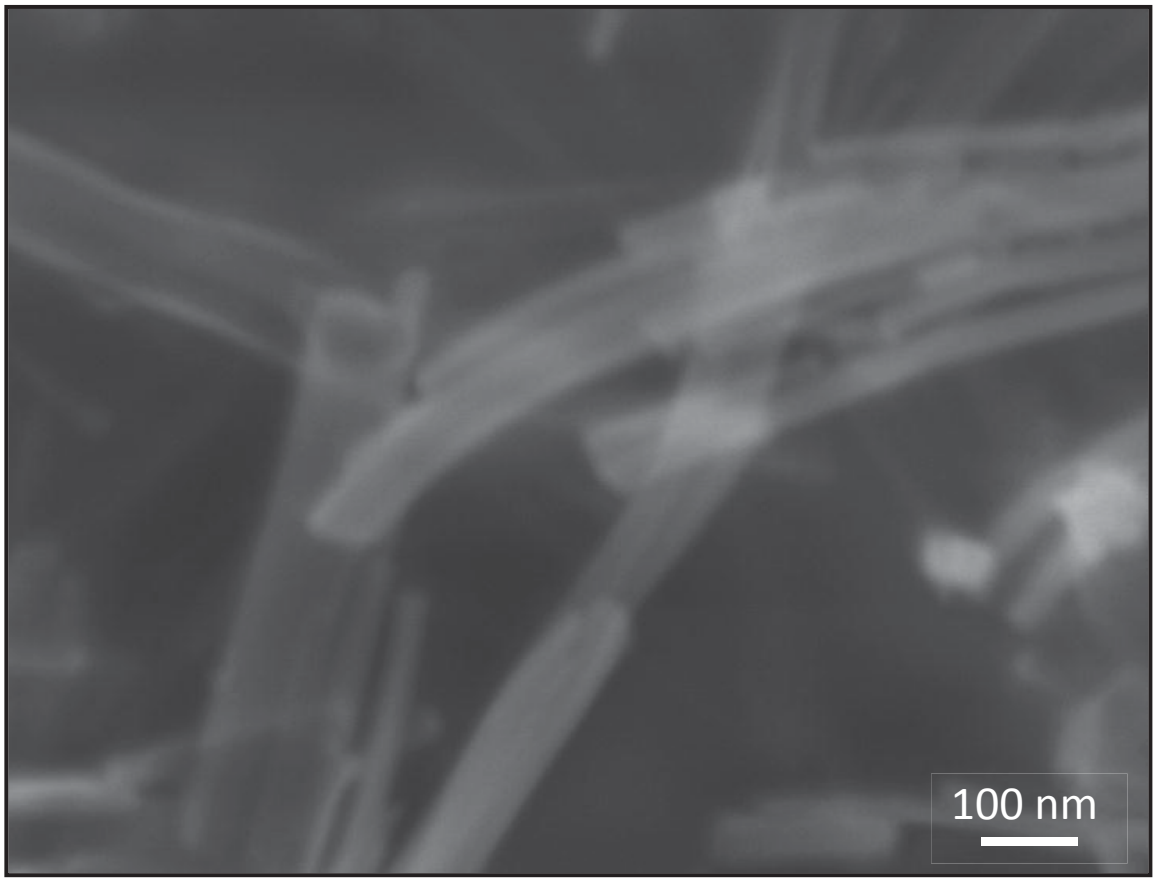

Figure 7-2 High magnification FESEM images of the as-prepared $NiC_2O_4 \cdot 2H_2O$ precursor nanowires.

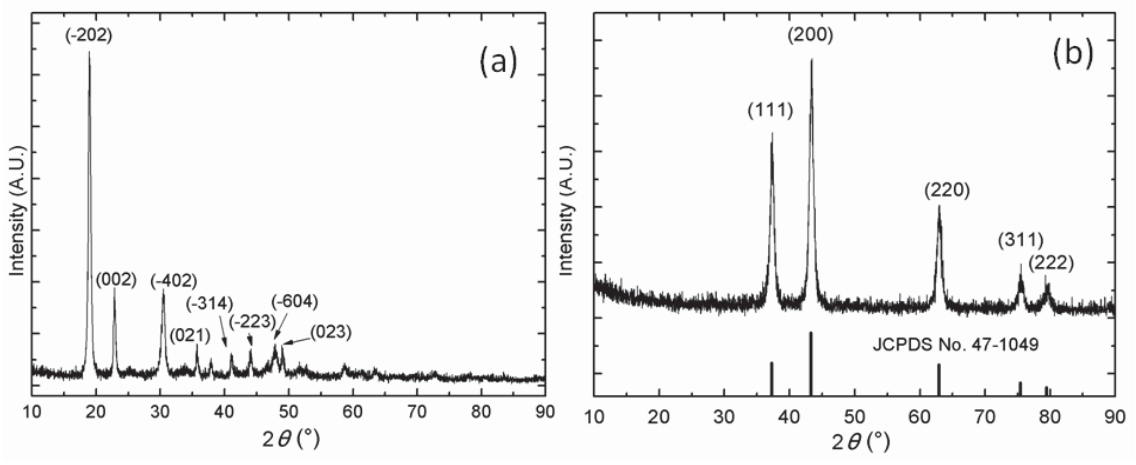

Figure 7-3 XRD patterns of (a) the $NiC_2O_4 \cdot 2H_2O$ precursor nanowires, and (b) NiO nanowires obtained by annealing treatment.

Figure 7-3 (a) and (b) show the powder X-ray diffraction patterns of the hydrothermal reaction and annealed products, respectively. In Figure 7-3 (a), the diffraction peaks at 18.8°, 22.7°, 30.4°, 35.5° and 37.6° can be assigned to ($\bar{2}$ 0 2), (0 0 2), ($\bar{4}$ 0 2), and (0 2 1) diffraction lines of monoclinic $NiC_2O_4 \cdot 2H_2O$ (JCPDS 25–0581). Figure 7-3 (b) shows a well-crystalline cubic NiO phase (JCPDS 47-1049). All diffraction peaks can be indexed to the cubic symmetry unit cell with the space group of $Fm\bar{3}m$. The lattice parameter (a) was calculated to be 4.1667 Å. There is no any impurity phase presenting in Figure 7-3 (b), confirming that $NiC_2O_4 \cdot 2H_2O$ precursors had been completely converted to NiO after annealing treatment.

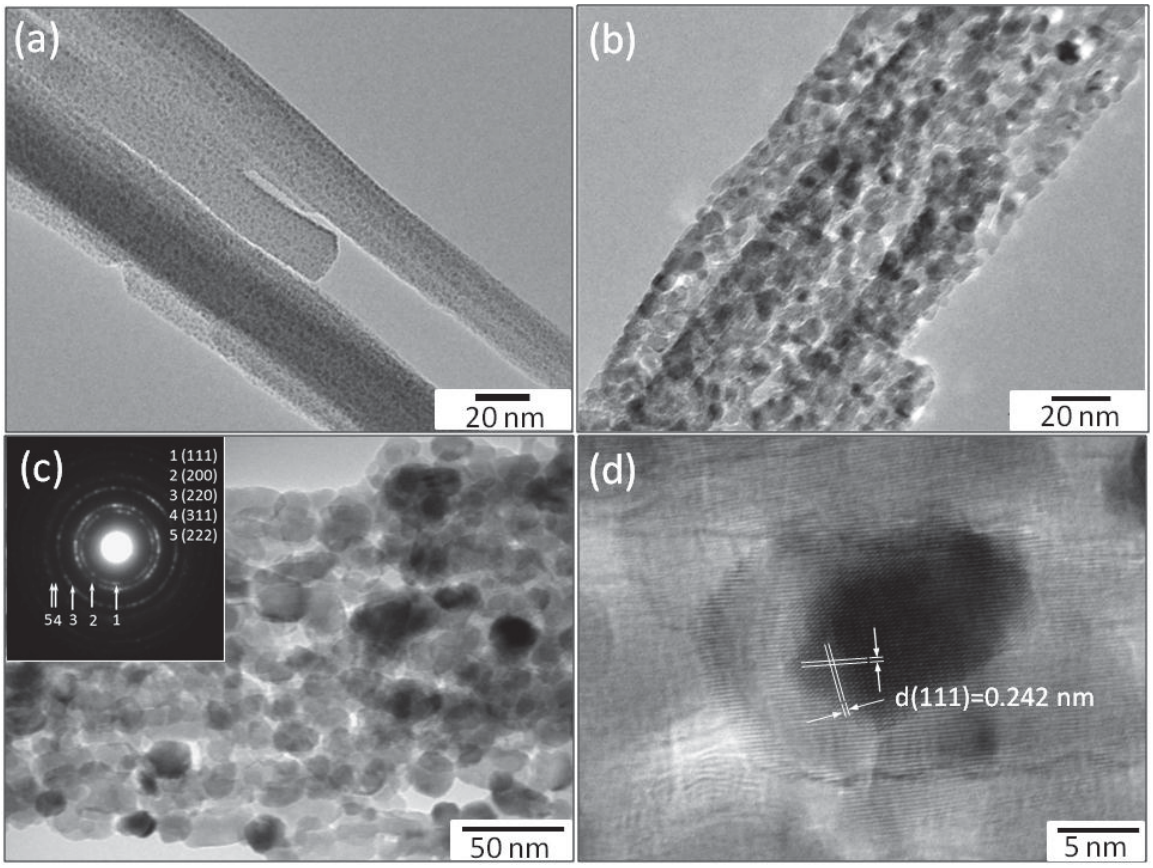

Figure 7-4 (a) Low magnification TEM image of $NiC_2O_4 \cdot 2H_2O$ precursor nanowires. (b) A NiO nanowire, (c) High magnification TEM image of a NiO nanowire, The inset is the SAED pattern. and (d) Lattice resolved HRTEM image of NiO nanocrystals.

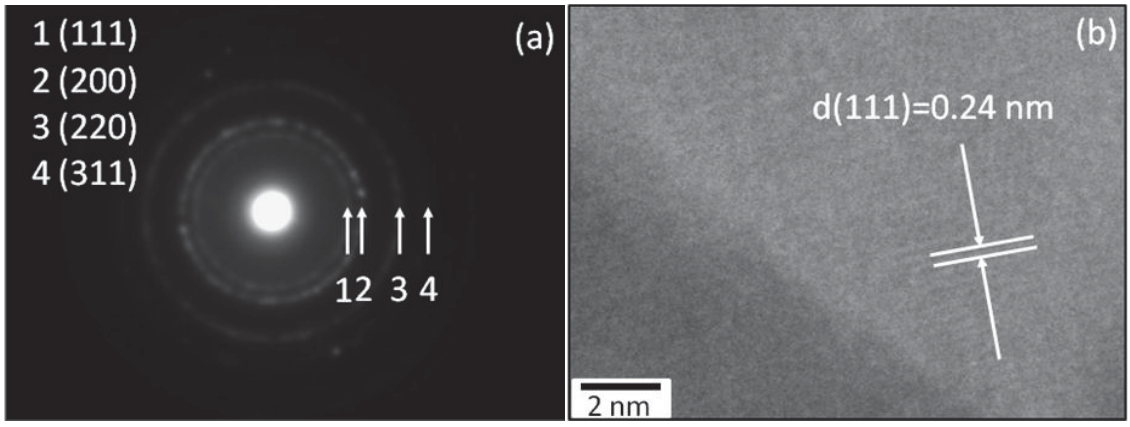

Figure 7-5 Selected area electron diffraction patterns on the $NiC_2O_4 \cdot 2H_2O$ nanowires and (b) Lattice resolved HRTEM image on the individural $NiC_2O_4 \cdot 2H_2O$ nanowire.

The crystal structure of the precursor $NiC_2O_4 \cdot 2H_2O$ nanowires and NiO nanowires were further characterised by TEM and HRTEM analysis. Figure 7-4(a) shows a TEM image of the precursor nanowires, from which the diameters of individual nanowires can be determined to be around 30 – 50 nm. The surfaces of the precursor $NiC_2O_4 \cdot 2H_2O$ nanowires are very smooth. During the TEM observation, we found that the precursor nanowires were unstable and very sensitive to the electron beam irradiation, which is associated with the decomposition of $NiC_2O_4 \cdot 2H_2O$ to NiO. A HRTEM image and the corresponding selected area electron diffraction pattern (SAED) are shown in Figure 7-5, which further confirms the crystal structure of $NiC_2O_4 \cdot 2H_2O$ precursor nanowires. Figure 7-4(b) is a TEM image of a NiO nanowire obtained from the annealing treatment. The diameters of NiO nanowires expanded to 40 – 60 nm. NiO nanowires are polycrystalline and consist of small nanoparticles. Figure 7-4(c) shows a high magnification TEM image of a NiO nanowire. It is clear that individual NiO nanocrystals (a few nanometers) aggregated together to form the nanowire shape. It should be noted that mesopores exist between NiO nanocrystals, reflecting the mesoporous nature of the as-prepared NiO nanowires. The inset in Figure 7-4(c) is a

SAED pattern, in which the diffraction rings can be indexed to the cubic NiO phase. The lattice resolved HRTEM image of a NiO nanowire is presented in Figure 7-4(d). The interplanar distance of the (111) crystal plane was measured to be 0.242 nm.

In general, NiO nanowires were formed via two steps. In the first step, nickel chloride salts reacted with $K_2C_2O_4$ and H_2O to form $NiC_2O_4 \cdot 2H_2O$ nanowires under the influence of ethylene glycol in the hydrothermal condition. In the second step, the $NiC_2O_4 \cdot 2H_2O$ precursors were converted to NiO nanowires through the heat treatment. During this process, NiC_2O_4 decomposed to NiO, accompanied with the evaporation H_2O and the release of CO_2. Simutaneously, mesopores also formed during this process. The reactions are formulated as follows:

$$NiCl_2 + K_2C_2O_4 + 2H_2O \rightarrow NiC_2O_4 \cdot 2H_2O + 2KCl \quad (7\text{-}2)$$

$$NiC_2O_4 \cdot 2H_2O \rightarrow NiC_2O_4 + 2H_2O \quad (7\text{-}3)$$

$$2NiC_2O_4 + O_2 \rightarrow 2NiO + 4CO_2\uparrow \quad (7\text{-}4)$$

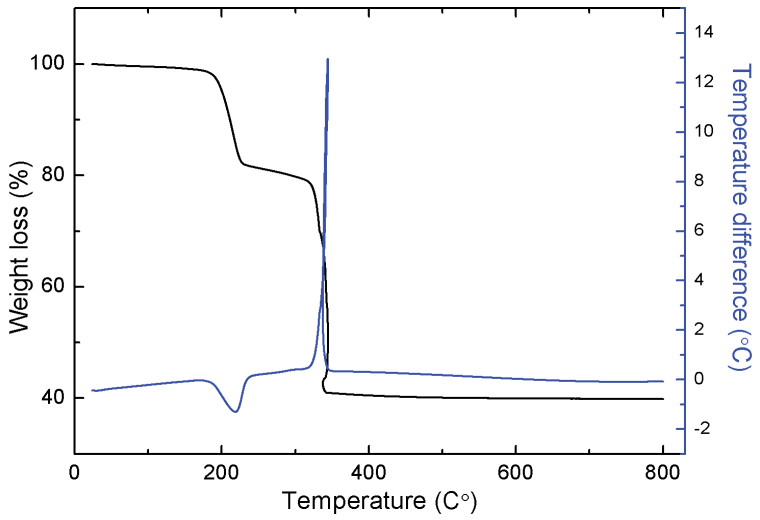

Figure 7-6 TG/DTA curves of the $NiC_2O_4 \cdot 2H_2O$ precursor nanowires.

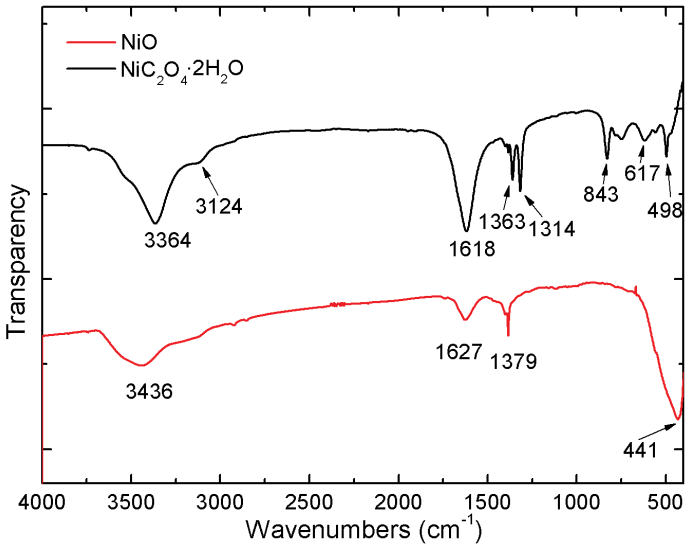

Figure 7-7 FTIR spectrums of the $NiC_2O_4 \cdot 2H_2O$ and NiO nanowires.

In order to inspect the conversion process, TG/DTA mesurement was performed on the as-prepared $NiC_2O_4 \cdot 2H_2O$ nanowire precursor. As shown in Figure 7-6, a two-step weight-loss process was observed from the TG and DTA curves. The first measured weight loss is about 17.7 wt % from 182 to 227 °C with the feature of an endothermic peak at 217 °C, corresponding to the dehydration of $NiC_2O_4 \cdot 2H_2O$. The second weight loss is about 40.0 % from 325 to 345 °C, which is associated with the decomposition of NiC_2O_4 to NiO. The measurement of FTIR spectra further confirmed the conversion from $NiC_2O_4 \cdot 2H_2O$ precursor nanowires to NiO nanowires (Figure 7-7). The broad peak at 3364 cm^{-1} is the characteristic of O-H asymmetrical stretching vibration, which comes from H_2O in $NiC_2O_4 \cdot 2H_2O$. The vibration band at 3124 cm^{-1} is attributed to the asymmetrical stretching vibrations of the $–CH_2$. The peak at 1616 cm^{-1} is ascribed to the asymmetrical stretching vibration of the C = O. The bands at 1363, 1314 and 843 cm−1 are originated from C–O symmetrical stretching vibration and O–C = O bending vibration, respectively. The peaks in the range of 400 - 850 cm^{-1} can be assigned to metal oxygen vibrations and metal-OH bending vibrations. After annealing treatment,

two strong peaks centered at 3436 and 441 cm^{-1} are the characteristic of Ni–O vibration band.

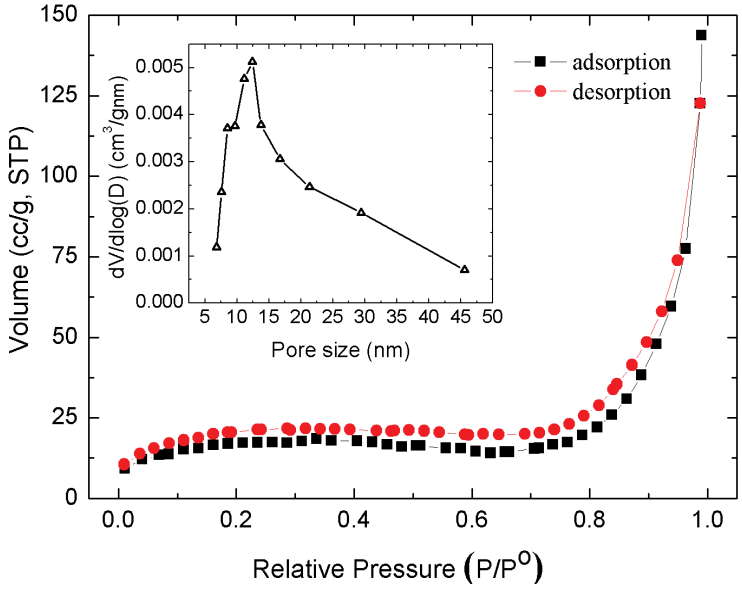

Figure 7-8 N_2 sorption isotherms of mesoporous NiO nanowires. The inset shows the corresponding respective pore size distributions.

The mesoporous nanostructures of NiO nanowires were investigated by measuring nitrogen adsorption/desorption isotherms at 77 K as shown in Figure 7-8, which is a typical type-IV isotherm with an H_1-type loop hysteresis. From the pore size distribution curves (inset in Figure 7-8), it can be found that the as-prepared NiO nanowires have mesopore distribution from 5 to 40 nm with an mean pore size of 12.5 nm. The specific surface area of NiO nanowires was calculated to be 85.18 $m^2\ g^{-1}$ and the total pore volume is 0.18 $cm^3\ g^{-1}$.

7.4.2 Electrochemical performance of mesoporous NiO nanowires

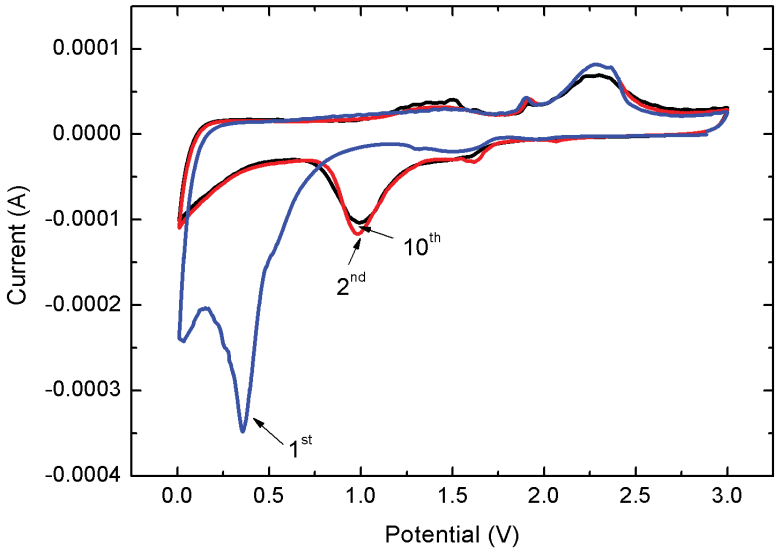

Figure 7-9 The CV curves of the as-prepared NiO nanowires as anode for lithium ion cell.

The electrochemical reactivity of porous NiO nanowires for lithium storage was evaluated by cyclic voltammetry (CV) measurement. Figure 7-9 shows the CV curves of NiO nanowire electrode in the first, second and tenth scanning cycles, which revealed the electrochemical reaction mechanism. In the first scanning cycle, the major cathodic peak is located at 0.375 V *vs.* Li^+/Li, which can be ascribed to the reduction process of Ni^{2+} to Ni^0. This cathodic process could also be associated with the electrolyte decomposition and lithiation reaction to form Li_2O. In the first scanning cycle, the major cathodic peak is located at 0.375 V vs. Li/Li^+; While in the subsequent scanning cycles, the major cathodic peak shifted to 1.0 V. This indicates different lithium reaction mechanisms between the first cycle and the subsequent cycles. In the first cycle, lithium ions react with NiO nanowires and form Ni^0 and Li_2O:[854]

$$2\ Li^+ + NiO \rightarrow Li_2O + Ni^0 \qquad (7\text{-}5)$$

During the anodic scanning process, the generated Ni^0 was oxidised, corresponding to the anodic peak at 2.25 V. After the first cycle, the positions of the cathodic peak and anodic peak remain unchanged. This result is consistent with our recent report on the *Ex-situ* XRD analysis for mesoporous NiO, which has clearly confirmed the above mechanism.[878]

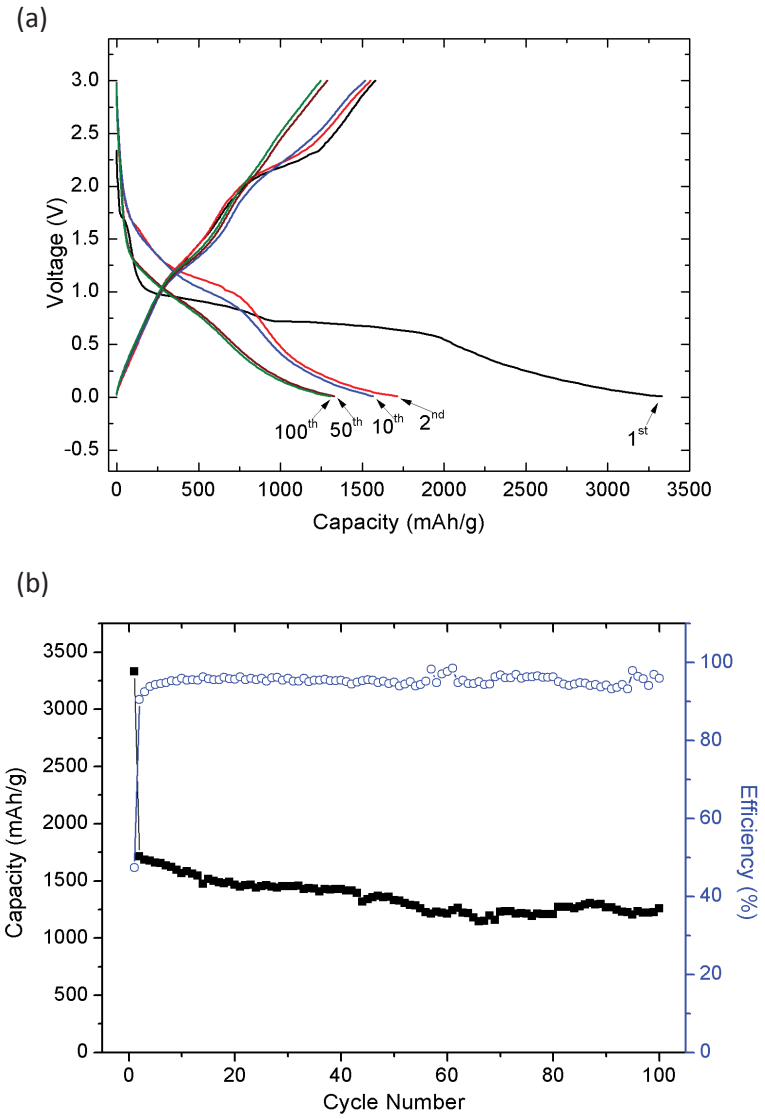

Figure 7-10 (a) Discharge and charge profiles of NiO nanowire electrodes. (b) Cycling performance and coulombic efficiency at 100 mA g^{-1} current density.

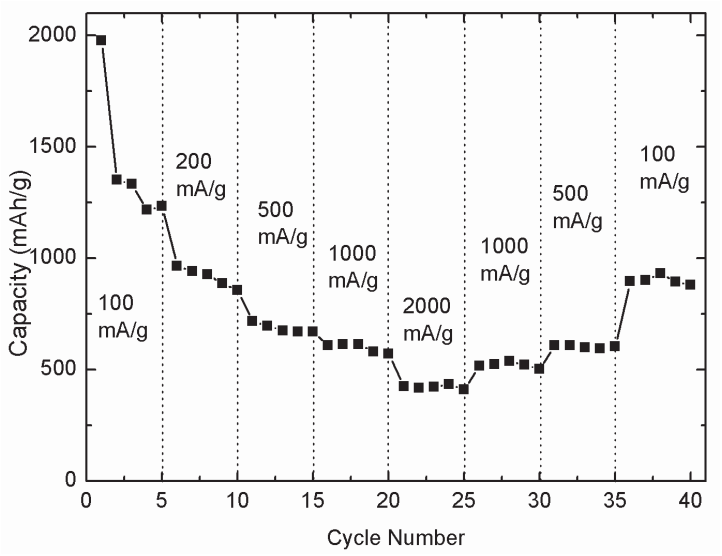

Figure 7-11 Rate performance of the NiO nanowire electrode at different current densities.

The lithium storage capacity of NiO nanowires was tested by constant current charge/discharge cycling. Figure 7-10(a) shows the discharge and charge profiles of the NiO nanowire electrode at a current density of 100 mA g^{-1}. In the first discharge, the NiO nanowire electrode delivered a high specific capacity of 3200 mA h g^{-1}. The extra capacity could be attributed to the formation of the solid electrolyte interface (SEI) layer. The formation of the SEI layer can effectively protect the electrode from the intercalation of solvent during the subsequent cycles. From the second cycle, the NiO nanowire electrode maintained a stable capacity (as show in Figure 7-10 (b)). After 100 cycles, the electrode still delivered a lithium storage capacity of 1280 mA h g^{-1}, which is much higher than the previously reported result.[879] The excess discharge capacity could be ascribed to the interfacial charging at the metal/Li_2O interface.[880,881] The materials that have high surface area can yield high discharge capacities, indicating that high surface area enhances the interfacial charge storage. In order to investigate the high rate capability of mesoporous NiO nanowires, the electrodes were cycled at different current

densities. The results are shown in Figure 7-11. When the current density was increased to 2000 mA h g^{-1}, the electrode still delivered a capacity of 435 mA h g^{-1}. As long as the current density reverses back to low current density, the cell capacity can recover to the high value, indicating that as-prepared NiO nanowires can tolerate high current charge/discharge cycling. The high lithium storage capacity of NiO nanowires should be credited to the unique nanostructure of the as-prepared mesoporous nanowires. As identified by TEM and HRTEM analysis, NiO nanowires are polycrystalline and consist of small nanocrystals with a size less than 10 nm, in which nano/mesopores exist between individual nanocrystals. During the BET measurement, some nano/mesopores and nanocrystal boundaries may be not accessible for gas adsorption, inducing a lower value of the BET area. However, Li^+ ions would be able to diffuse and form a monolayer of Li^+ per boundary on the surfaces of all individual NiO nanocrystals, leading to extra lithium storage capacity.[766]

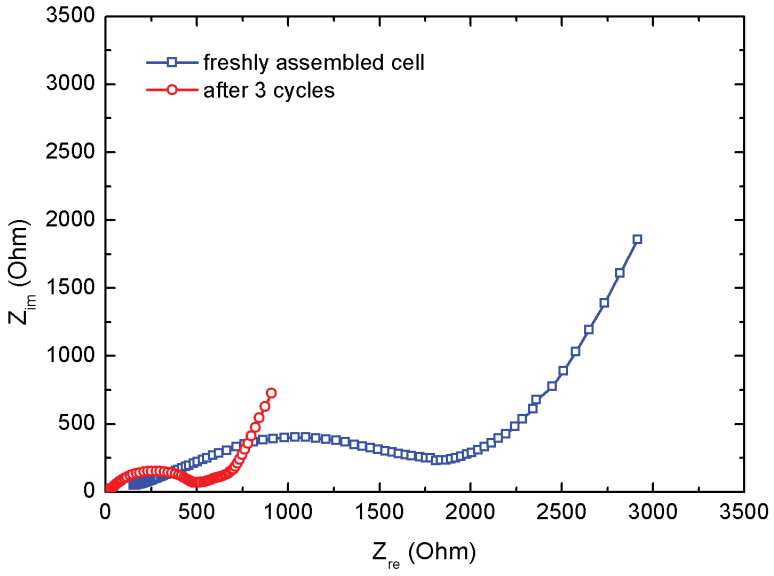

Figure 7-12 A.C. impedance spectra of the as-prepared mesoporous NiO nanowire electrode before cycling and after 3 cycles. The a.c. impedance spectra were measured at the discharged state of 0.01 V in frequency range from 0.01 Hz to 100 kHz.

Figure 7-12 shows the Nyquist plots of the a.c. impedance spectra of the as-prepared porous NiO nanowire electrode before cycling and after 3 cycles. The a.c. impedance spectra exhibit a semicircle in the high frequency region and a straight line in the low frequency region. The straight line in the low frequency region represents typical Warburg behaviour, which is related to the diffusion of lithium ions in the active anode materials. The depressed semicircle in the medium frequency region is attributed to the charge transfer process. The numerical value of the diameter of the semicircle on Z_{re} axis gives an approximate indication of the charge transfer resistance (R_{ct}). It is noted that the R_{ct} decreases substantially after 3 cycles. This suggested that a few cycles are necessary for the electrolyte to diffuse into the mesopores in NiO nanowires, which facilitate the facile charge transfer at the nano-scale particles /electrolyte interface. The electrochemical enhancement of the as-prepared one-dimensional NiO nanowires as an anode material might be ascribed to the high surface area and high reactivity of mesoporous nanostructures, which maximises contact areas between electrolyte and active electrode materials. Consequently, the high contact area of electrolyte/electrode can provide more reaction sites for lithium ions intercalation/de-intercalation.[882]

Since the as-prepared NiO materials have a large specific surface area, it is an ideal electrode material for supercapacitors. The capacitances of as-prepared NiO nanowires were evaluated by cyclic voltammetry measurements. Figure 7-13 (a) shows the CV curves obtained at 5, 10, 20, 50 and 100 mV s^{-1} scanning rates. All CV curves exhibited a broad oxidation peak and a sharp reduction peak rather than the ideally rectangular shape. This characteristic indicates that the supercapacitance was not double layer capacitance, but originated from faradaic pseudocapacitance. Figure 7-13 (b) shows the relationship between the specific capacitance and the scanning rates. A maximum specific capacitance of 348 F g^{-1} was achieved at a 10 mV s^{-1} scan rate. The as-prepared

mesoporous NiO nanowires exhibited a much higher capacitance than that of previously reported nanoporous NiO nanorods.[883,884] This improvement is related to the intrinsic properties of the as-synthesised mesoporous NiO nanowires, NiO nanowires are polycrystalline and consist of small nanocrystals with sizes less than 10 nm. Furthermore, nano/mesopores exist between individual nanocrystals, leading to extra charge storage on the boundaries of NiO nanocrystals.

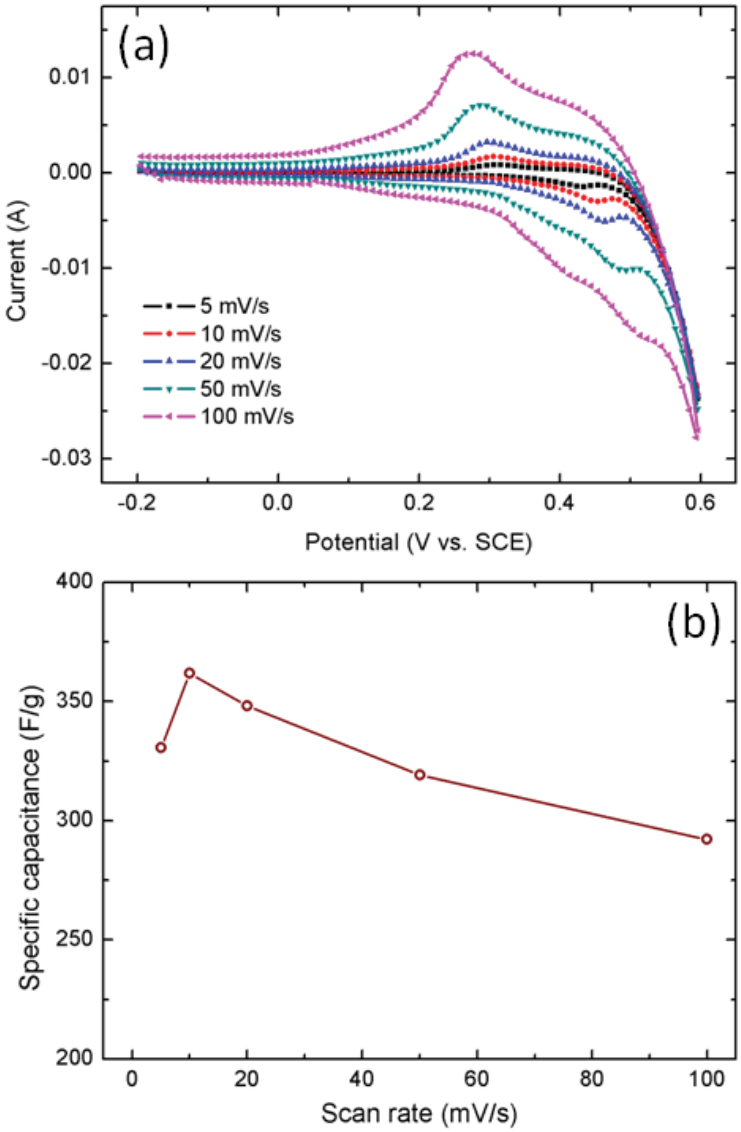

Figure 7-13 (a) Cyclic voltammetry of the as-prepared mesoporous NiO nanowires as electrodes in supercapacitors at different scanning rates, (b) Specific capacitance of NiO electrodes at different scanning rate.

7.5 Conclusion

In summary, one-dimensional mesoporous nickel oxide nanowires were successfully synthesised by a hydrothermal reaction and subsequent annealing at 400 °C in air. FESEM, HRTEM and N_2 adsorption analysis revealed that the as-prepared individual NiO nanowire consisted of aggregated nanocrystals with a mesoporous structure. This induced a high specific surface area, allowing mesoporous NiO nanowires in lithium ion cells to deliver a high lithium storage capacity, high rate capacity and good cycle life as anodes in lithium ion cells. Mesoporous NiO nanowires also demonstrated a high specific capacitance of 348 F g^{-1} as electrode materials in supercapacitors.

CHAPTER 8 MESOPOROUS NiO CRYSTALS AS ANODE MATERIALS FOR LITHIUM STORAGE

8.1 Abstract

Faceted crystals with exposed highly reactive planes have attracted intensive investigations for applications such as hydrogen production, enhanced catalytic activity, and electrochemical energy storage and conversion. Herein, we report the synthesis of mesoporous NiO crystals with dominantly exposed {110} reactive facets by the thermal conversion of hexagonal $Ni(OH)_2$ nanoplatelets. When applied as anode materials in Li-ion batteries, mesoporous NiO crystals exhibit a high reversible lithium storage capacity of 700 mA h g^{-1} at 1 C rate in 100 cycles and an excellent cyclability. In particular, the dominantly exposed {110} reactive facets and mesoporous nanostructure of NiO crystals lead to ultrafast lithium storage, which mimics the high power delivery of supercapacitors.

8.2 Introduction

Faceted crystals with exposed highly reactive crystal plane have great potentials for many applications such as photocatalytic water splitting, new catalysts, and electrochemical energy conversion. However, highly reactive facets usually have high surface energy, and are therefore difficult to synthesise in the equilibrium state. A breakthrough in the synthesis of TiO_2 crystals with 46 % high energy {001} facets has recently been achieved by Lu's group,[406] which demonstrated excellent photocatalytic activities.[405] Further improvements have also been reported increasing the percentage of the {001} reactive facets of TiO_2 crystals up to 100 %.[885] Following studies on TiO_2 facet crystals, Co_3O_4 crystals with exposed high energy planes ({110} and {112}) were

also successfully synthesized and applied as catalysts for low temperature oxidation of CO and trace ethylene, and methane combustion.[886,887]

Li-ion batteries are regarded as the choice of power source for vehicle electrification. However, energy and power densities of current generation Li-ion batteries are limited by electrode material. Transition metal oxides have been proposed as high capacity anode materials based on a "conversion" reaction, which is different from the classical insertion/de-insertion.[5] The theoretical capacity of NiO anode is 718 mA h g^{-1}, based on the conversion reaction: $NiO + 2Li^+ + 2e^- \leftrightarrow Li_2O + Ni$. This is almost double the capacity of the graphite anode. NiO is highly favoured as anode materials because of its low cost, low toxicity, and superior safety, compared with other transition metal oxides. Moreover, the density of NiO is 6.67 g cm^{-3}, resulting in high volumetric energy density (about 5.8 times over graphite).[847] However, the rate performance and cyclability of NiO anode are poor, owing to slow kinetics of the conversion reaction and large volume change of NiO electrode (95.69 %). To circumvent these disadvantages, many approaches have been investigated, including the use of carbon materials as a conductive matrix, synthesis of nanostructured nickel oxides (nanocone,[6] nanotubes,[7] nanofilm,[8] and nanowires[9] *etc.*), and preparation of nickel oxide with porous architecture.[9-13] So far, it has achieved 1031 mA h g^{-1} at 0.1 C (1C = 718 mA g^{-1}) rate,[461] 550 mA h g^{-1} at 0.7 C rate,[456] 400 mA h g^{-1} at 2 C rate,[446] 375 mA h g^{-1} at 10 C rate[888] capacities. It still remains a challenge to attain high rate performance for NiO anode.

Recently, anatase (TiO_2) nanosheets with nearly 100 % exposed {001} facets have exhibited a property of fast lithium diffusion in lithium ion cells, but with a low specific capacity less than 200 mA h g^{-1}.[885] It was also reported that the Co_3O_4 nanomesh with

exposed {112} high energy facets delivered a good rate capacity above 380 mA h g^{-1} at a discharge rate of 1000 mA g^{-1}.[889]

Herein, we report the facile synthesis of mesoporous NiO single crystals with dominantly exposed {110} reactive planes. When applied as anode materials in lithium ion cells, mesoporous NiO crystals exhibited a high and stable average lithium storage capacity of 700 mA h g^{-1} at 1 C rate and an outstanding capability for ultrafast reversible lithium storage, mimicing supercapacitors.

8.3 Methods

8.3.1 Synthesis of facet $Ni(OH)_2$ crystals and mesoporous faceted NiO crystals

The faceted $Ni(OH)_2$ single crystalline crystals were synthesized by a hydrothermal method. In a typical synthesis process, 0.02 mol $NiCl_2$ (Sigma-Aldrich, ≥ 97 %) was dissolved in 10 ml distilled water. Then 10 ml 6 M NaOH (Sigma-Aldrich, ≥ 98 %) solution was added under vigorous stirring. After a pink transparent solution formed gradually, 0.6 mmol Na_2SO_4 (Sigma-Aldrich, ≥ 98 %) was added into the solution. The mixture was then transferred into a Teflon-lined autoclave and heated at 170 °C for 24 hours in an air-flow electric oven. After cooling to room temperature, the pink product was collected by centrifugation and washed thoroughly with distilled water several times. The $Ni(OH)_2$ crystals were obtained after drying for 12 h at 60 °C in the vacuum oven. The final mesoporous faceted NiO crystals were prepared by annealing the $Ni(OH)_2$ precursor at 500 °C for 5 h.

8.3.2 Structural and physical characterization

The crystal structure and phase of the as-prepared materials were characterized by X-ray diffraction (XRD, Siemens D5000) using a Cu Kα radiation at a scanning step of

0.02°/min. The morphology was analyzed by field emission scanning electron microscopes (FESEM, Zeiss Supra 55VP). The structure details were further characterized by transmission electron microscopy (TEM) and high-resolution transmission electron microscopy (HRTEM, JEOL JEM-2011). Selected area electron diffraction (SAED) patterns were recorded by a Gatan CCD camera in a digital format.

8.3.3 Electrochemical testing

The electrodes were prepared by dispersing the as-prepared NiO crystals (70 wt %), acetylene carbon black (20 wt %), and poly (Vinylidene fluoride) binder (PVDF, 10 wt %) in N-methyl-2-pyrrolidone (NMP) to form a slurry. The resultant slurry was pasted onto copper foil using a doctor blade and dried at 100 °C for 12 h under vacuum, followed by pressing at 200 kg cm^{-2}. Electrochemical measurements were carried out using two-electrode coin cells with lithium metal as the counter electrode. The CR2032-type coin cells were assembled in an argon-filled glove box (UniLab, Mbraun, Germany). The electrolyte solution was 1 M $LiPF_6$ dissolved in a mixture of ethylene carbonate (EC) and dimethyl carbonate (DMC) with a volume ratio of 1:1. Cyclic voltammetry (CV) was carried out on a CHI 660C electrochemistry workstation with a scan rate of 0.1 mV s^{-1} from 0.01 to 3.0 V in a two-electrode system. The charge-discharge measurements were performed at ambient temperature at different current densities in the voltage range from 0.01 to 3.0 V. In order to investigate the lithium-driven structural and morphological changes of mesoporous faceted NiO crystals during the lithium insertion and extraction processes, Swagelog-type cells were assembled. The cells were discharged or charged to the required voltages and then opened in the Glove-box. The partially lithiated or de-lithiated materials were removed from the electrodes

and washed with dimethyl carbonate (DMC) before being placed onto a copper grid mounted on the TEM sample holder.

8.3.4 Computational methods

The calculations were performed based on the density-functional theory (DFT) +U approach[691] with the ABINIT.[692,693] The exchange-correlation energy function was represented by the local-density approximation (LDA) employing ultra-soft pseudopotential (USPP) formalism.[694] We used an energy cutoff of 350 eV. Monkhorst-Pack k-point sets of 6×6×6 were used. The on-site Coulomb repulsion (Hubbard U) was applied for Ni d states. The effective values for U of 8.0 eV for Ni had been derived by fitting to experimental oxidation enthalpies and it will gave better estimates for band gaps.[695] The maximum self-consistent field convergent tolerance was less than 2×10^{-6} eV $atom^{-1}$. All calculations were performed in reciprocal space. To predict the morphology and surface energy of $Ni(OH)_2$ and NiO, a set of suitable faces were used. The surface region in our calculation is composed of a finite number of two-dimensional infinite planes formed by cutting the crystal along a particular Miller index (hkl) plane. In each plane, a two-dimensional cell represents every site in the plane. Following the approach of Tasker,[890] several of these cells in successive planes comprise the basic repeat unit that contains the composition of the bulk crystal unit cell. The surface energy per unit area, $E_{surface}^{h\,k\,l}$, of a particular surface is calculated from the difference between the energy of the surface block, $E_{surface\ block}$, and the energy of the same number of bulk ions, E_{bulk}, per unit area, A (cross-sectional), thus

$$E_{surface}^{h\,k\,l} = \frac{E_{surface\ block} - E_{bulk}}{A} \tag{8-1}$$

For slab model construction, 8 layers were used and the depths of the surface regions were chosen to be large enough to ensure full relaxation of the surface ions and convergence of the surface energy. In each of case, surface structures were fully relaxed until the total energy difference was converged within 0.001 eV.

8.4 Results

8.4.1 Characterization of $Ni(OH)_2$ crystals and mesoporous faceted NiO crystals

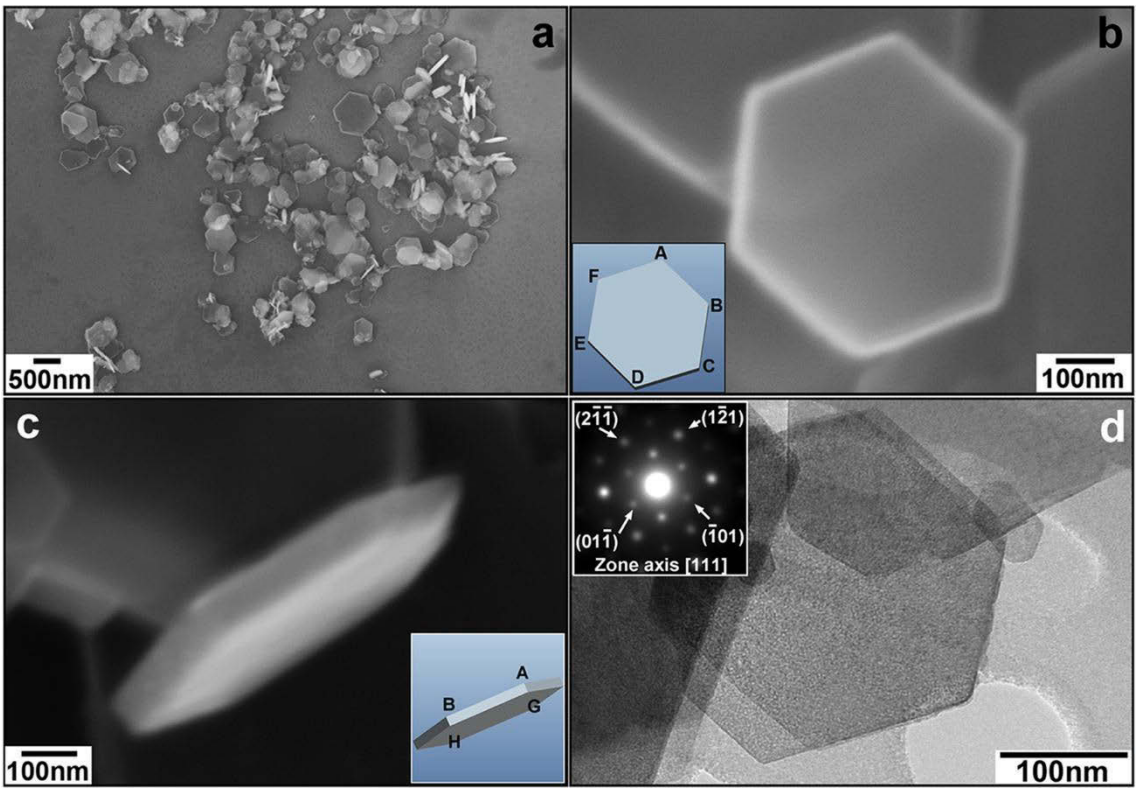

Figure 8-1 $Ni(OH)_2$ crystals. (a) A low magnification FESEM image of $Ni(OH)_2$ faceted crystals. (b) A high magnification FESEM image of $Ni(OH)_2$ faceted crystals, showing hexagonal platelet shape. (c) The side view of a $Ni(OH)_2$ crystal, from which the thickness can be determined. (d) TEM image of faceted $Ni(OH)_2$ crystal. The insets of (b) and (c) are the corresponding simulated model of the faceted crystals. The inset in (d) shows the SAED pattern along the [111] zone axis.

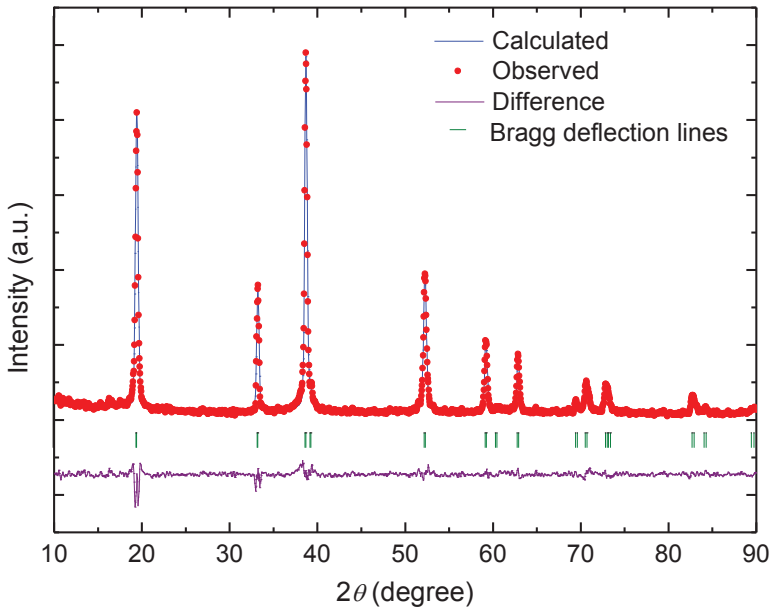

Figure 8-2 Rietveld refinement pattern of X-ray diffraction data for $Ni(OH)_2$ crystals. The observed and calculated intensity are represented by red solid circle and blue solid line, respectively. The bottom purple line shows the fitting residual difference. Bragg positions are represented as light green tick.

In the first step of the preparation, faceted $Ni(OH)_2$ crystals were synthesised by a hydrothermal method using SO_4^{2-} ions as the morphology directing agent. Figure 8-1 shows the field emission scanning electron microscope (FESEM) images, transmission electron microscope (TEM) image and selected area electron diffraction pattern (SAED) of $Ni(OH)_2$ precursor crystals. The hydrothermal product consists of single crystals with a size in the range of 200 – 400 nm (Figure 8-1a). As shown in Figure 8-1b, the as-obtained $Ni(OH)_2$ crystals have well-defined facets with a truncated symmetric hexagonal pyramid shape. Figure 8-1c shows a side view of a $Ni(OH)_2$ crystal, from which the thickness can be determined to be about 80 nm. A free-standing $Ni(OH)_2$ crystal is thin enough to be transparent under the electron beam (TEM image of Figure 8-1d). The SAED pattern (the inset of Figure 8-1d) shows perfect rhombus diffraction

spots along the [111] zone axis, indicating the single crystalline feature of $Ni(OH)_2$ crystals. The (110), (101), (011), and (211) atomic planes can be fully indexed. This confirms that the faceted $Ni(OH)_2$ single crystal has the dominantly exposed planes of {111}, which is the only crystal plane normal to all the above indexed crystal planes. The X-ray diffraction pattern (XRD) also confirmed the pure hexagonal phase of $Ni(OH)_2$ crystals with the space group of $P\bar{3}m1$ (Figure 8-2).

The ratio of the exposed {111} facets to total surface area for $Ni(OH)_2$ crystals can be calculated from the following equation:

$$S_{\{111\}}\% = \frac{S_{\{111\}}}{S_{\{111\}}+S_{\{110\}}+S_{\{011\}}+S_{\{101\}}} \approx \frac{6AB^2 \sin 60^\circ}{6AB^2 \sin 60^\circ + 6AB \cdot AG} = \frac{1}{1+\frac{\frac{AG}{AB}}{\sin 60^\circ}} = 95.64\ \% \quad (8\text{-}2)$$

Where the {111}, {110}, {011}, and {101} facets and the length of AB, AG can be seen in Figure 8-1 b and c and Figure 8-3

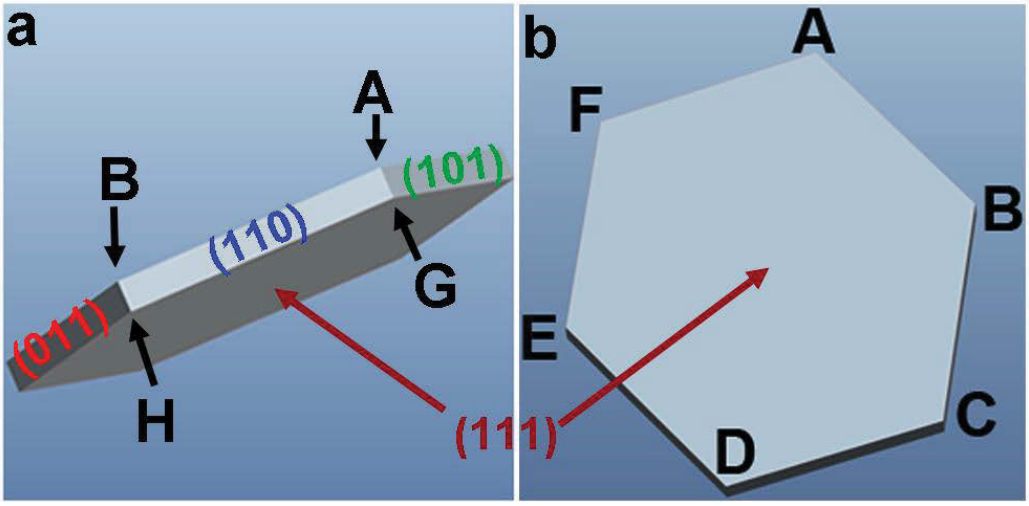

Figure 8-3 The simulated geometrical model of the facet $Ni(OH)_2$ nanoplatelet indexed with the different enclosed facets.

According to the symmetries of $Ni(OH)_2$, the two hexagonal surfaces are the {111} facets and the six isosceles trapezoidal surfaces are the {110}, {011}, and {101} facets.

The ratio of the dominantly exposed {111} facets to the total surfaces were estimated to be 95.64 %.

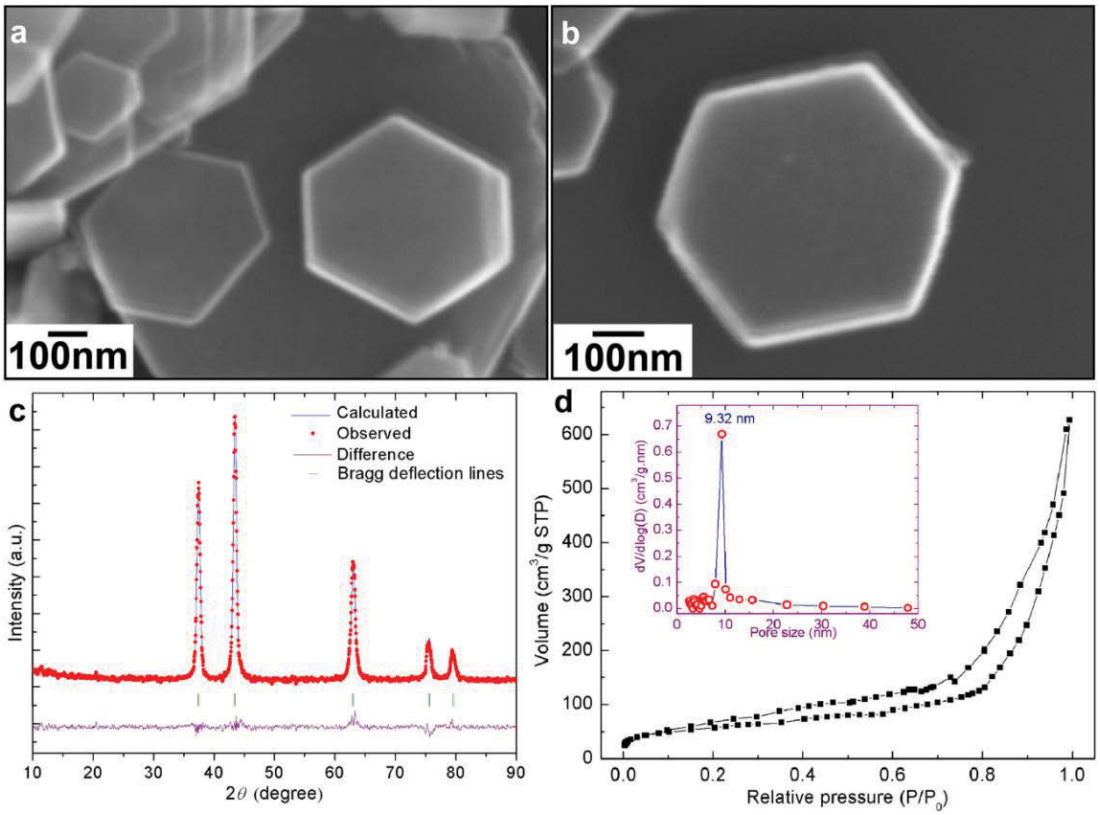

Figure 8-4 Morphology and Phase analysis of NiO mesoporous crystals. (a) and (b) FESEM images of NiO faceted crystals. (c) Rietveld refinement pattern of X-ray diffraction data of NiO crystals, the observed and calculated intensity are represented by red solid circle and blue solid line, respectively. The bottom purple line shows the fitting residual difference. Bragg positions are represented as light green tick. (d) N_2 sorption isotherms of mesoporous faceted NiO crystals. The inset shows the pore size distributions.

Figure 8-4a and b show the FESEM images of NiO faceted crystals, which reveal that the hexagonal platelet shape of precursor $Ni(OH)_2$ crystals has been preserved after sintering. X-ray diffraction was performed to determine the phase of NiO crystals (Figure 8-4c), in which all diffraction peaks can be indexed to the cubic symmetry with

the space group of $Fm\bar{3}m$. The BET surface area and porosity of NiO crystals were investigated by nitrogen adsorption/desorption isotherms at 77 K. As shown in Figure 8-2d, the hysteresis feature of the NiO crystals can be classified as the typical-IV isotherm with an H_1-type loop, reflecting the mesoporous nature of the NiO crystals. The pore size distribution curve is shown as the inset of Figure 8-4d, which exhibits a monomodal pore size distribution with a mean pore size of 9.32 nm (calculated by the Barrett-Joyner-Halenda (BJH) method). The specific BET surface area and total pore volume were determined to be 197.5 $m^2 g^{-1}$ and 1.22 $cm^3 g^{-1}$, respectively.

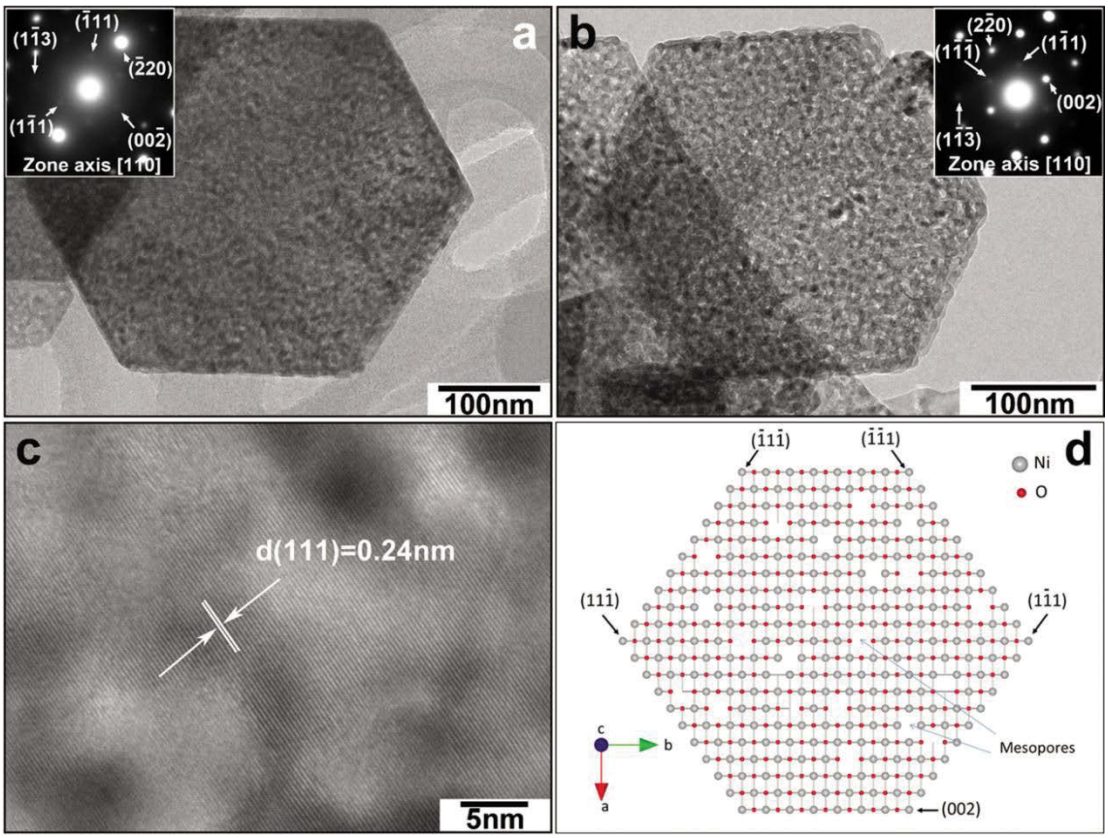

Figure 8-5 Structure analysis of NiO mesoporous crystals. (a) and (b) are TEM images of individual NiO faceted crystals. (c) Lattice resolved HRTEM image of NiO crystals. (d) Schematic diagram of crystal structure of as-prepared NiO faceted crystals. Insets in (a) and (b) are SAED along the [110] zone axis.

The morphology and crystal structure of the mesoporous faceted NiO crystals were further characterised by TEM and HRTEM. It is evidenced from the bright-field TEM images of mesoporous NiO crystals in Figure 8-5a and b, from which we can see that NiO crystals maintain the faceted nanoplatelet shape with a porous architecture. The insets in Figure 8-5a and b present the corresponding SAED patterns along the [110] zone axis. The dot SAED patterns imply the single crystalline nature of the mesoporous NiO crystals, from which the (111), (002), and (220) planes can be indexed. The normal direction to the dominantly exposed crystal planes (hexagon surface) is the [110] axis, which is coincident with the direction of the electron beam. Figure 8-5c shows a lattice resolved HRTEM image of a NiO crystal, in which the lattice can be determined to be the (111) crystal plane with a d spacing of 0.24 nm. As illustrated in Figure 8-5d, the mesoporous NiO crystals have the dominantly exposed {110} planes on both hexagon surfaces together with [647] and {111} facet planes, forming a close-packed hexagonal nanoplatelet. Indeed, there are very dense mesopores dispersed in NiO nanoplatelets. However, the total pore area was calculated to be 61.26 $m^2 g^{-1}$ from the integrated Barret–Joyner–Halenda (BJH) adsorption measurement. It should be noted that the specific surface area of NiO nanocrystals is 197.5 $m^2 g^{-1}$. If subtracting the pore area from the total surface area, 68.98 % surface area is contributed by the enclosed facets of the nanoplatelets, in which 95.64 % is {110} facets (deduced from the ratio of exposed {111} facets to total surface area in $Ni(OH)_2$ precursor). Therefore, the {110} crystal planes occupy about 66 % of the total surface area even counting the pore area. The {110} crystal plane is a dominant fact in the as-prepared mesoporous NiO nanoplatelets.

8.4.2 Crystal growth mechanism

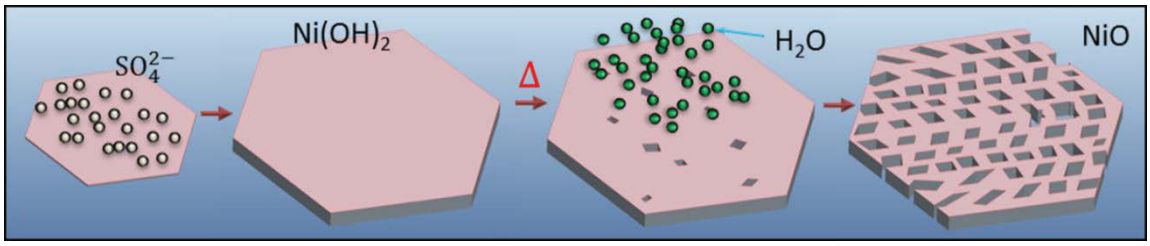

Figure 8-6 Schematic illustration of the formation mechanism of facet $Ni(OH)_2$ single crystal and mesoporous facet NiO crystals.

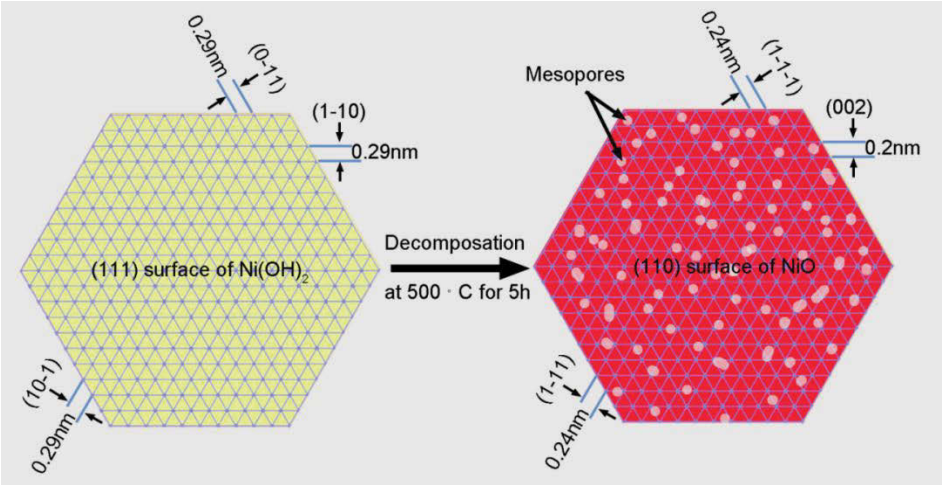

Figure 8-7 Schematics to introduce the mechanism through which the hexagonal $Ni(OH)_2$ nanoplatelets is converted into NiO nanoplatelets while maintaining the single crystal feature. The crystal mismatch between $Ni(OH)_2$ and NiO is small from the calculation based on the crystal planes of $(10\bar{1})$, $(0\bar{1}1)$, and $(1\bar{1}0)$ in $Ni(OH)_2$ and $(1\bar{1}1)$, $(1\bar{1}\bar{1})$, and (002) in NiO. And the interfacial angles between each other of these crystal planes of these two crystals are similar. Formation of mesopores in NiO nanoplatelets can compensate the gas emission after $Ni(OH)_2$ nanoplatelets is calcined at 500 °C, and is favorable for maintaining single crystallinity throughout the chemical conversion process.

In the alkaline solution under hydrothermal condition, Ni^{2+} ions react with OH^- to form $Ni(OH)_2$ crystals. The previous study has shown that sulphate ions (SO_4^{2-}) are most strongly adsorbed to the surfaces perpendicular to the c-axis of the hexagonal crystal system through bridging-bidentate adsorption, leading to retarded growth in the direction along the c-axis.[891] As a result, the faceted hexagon nanoplate shape was formed. $Ni(OH)_2$ decomposed to NiO crystals in the sintering process, during which the mesoporous structure was generated simultaneously. The crystal growth and conversion processes are illustrated in Figure 8-6. NiO crystals preserved the single crystalline feature and hexagonal shape of the precursor $Ni(OH)_2$ nanoplatelets, which could be attributed to the low crystal mismatch between $Ni(OH)_2$ and NiO crystals.[889] Because the {111} crystal planes of $Ni(OH)_2$ and {110} crystal planes of NiO have low crystal mismatch as illustrated in the Figure 8-7. For example, the $(1\bar{1}0)$ lattice planes of $Ni(OH)_2$ crystals has a d-spacing of 0.29 nm, which is very close to d-spacing of the $(\bar{1}11)$ planes of NiO crystals (0.24 nm). The control of the crystal mismatch within a low range is highly favourable for monocrystallization.[892] Therefore, the monocrystallization and conversion from $Ni(OH)_2$ to NiO can be considered as a thermodynamically favoured recrystallization process, during which the single crystalline was maintained throughout the whole transformation. The partial collapse of the porous structure upon template-removal or thermal annealing is always inevitable in the preparation of amorphous or polycrystalline mesoporous structures through the conventional template route.[893] The reported solid-state crystal re-construction is a facile approach to obtain uniform mesoporous structures with 3D single crystal framework.

8.4.3 Electrochemical properties of mesoporous NiO crystals for lithium storage in Li-ion batteries

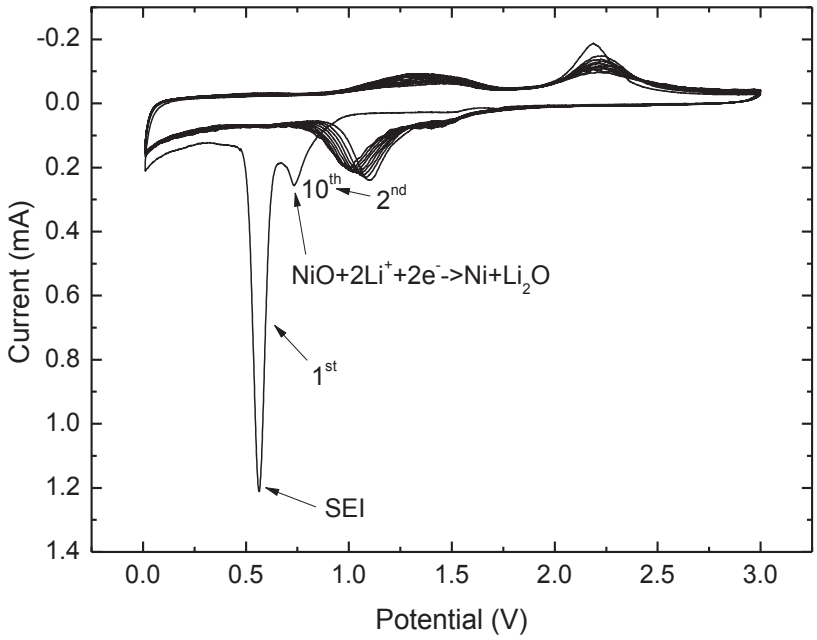

Figure 8-8 The first ten cycles CV curves of the mesoporous NiO crystals as anode for lithium ion cell.

The electrochemical properties of mesoporous NiO crystals were tested by cyclic voltammetry (CV) and galvanostatical charge and discharge cycling. The CV curves were shown in Figure 8-8, reflecting reversible lithium storage of NiO crystals.

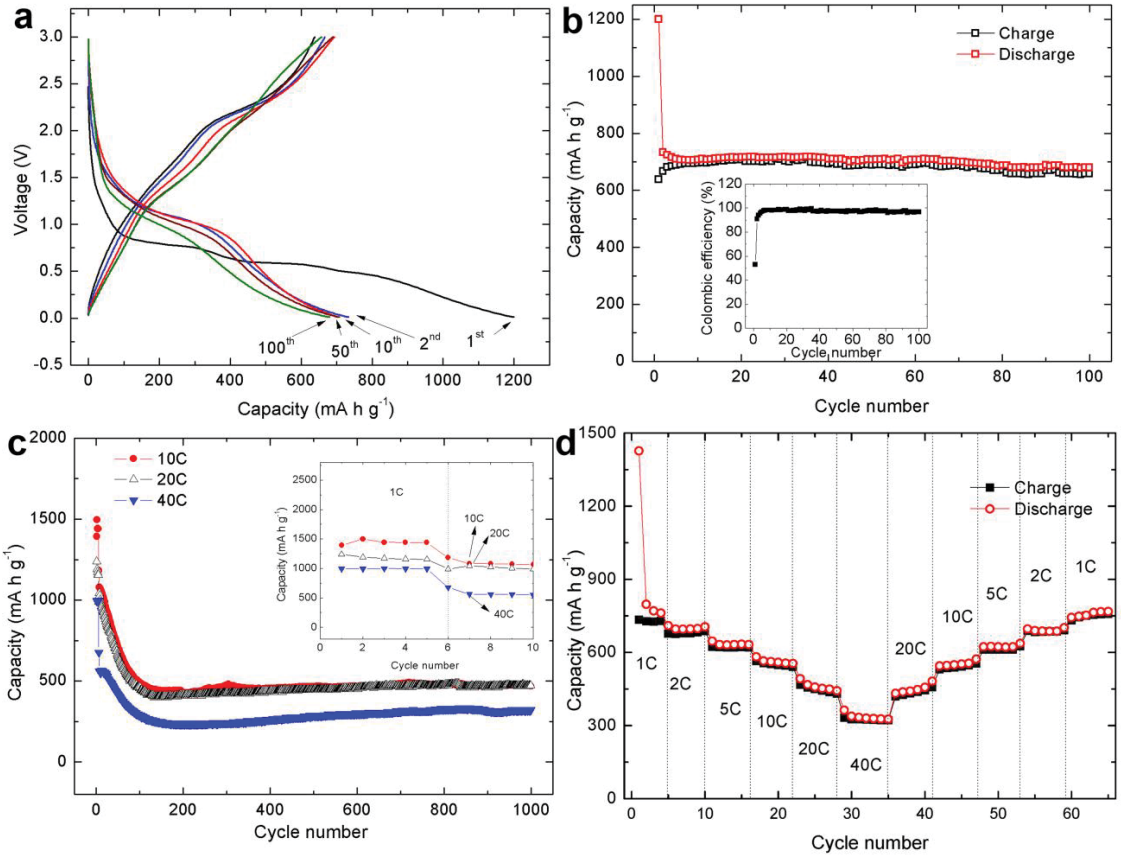

Figure 8-9 Electrochemical characterizations. (a) Discharge and charge profiles of mesoporous NiO crystals at 1 C current rate. (b) Cycling performance of mesoporous NiO crystals at 1 C current rate. The inset of (b) shows the Coulombic efficiency. (c) Discharge capacity vs. cycle number of mesoporous NiO crystals at high current rates of 10 C, 20 C, and 40 C. The inset shows discharge capacity in the initial 10 cycles. (d) The rate performance of mesoporous NiO crystals at varied current rates.

Figure 8-9a shows the charge and discharge profiles in the 1st, 2nd, 10th, 50th and 100th cycles at 1 C rate. In the first cycle, the electrode delivered a capacity of 1200 mA h g^{-1}, in which partial capacity could be consumed for the formation of solid electrolyte interface (SEI).[766,894] From the second cycle, the electrode maintained high reversibility.

The cycling performance of mesoporous NiO crystal at 1 C is presented in Figure 8-7b. After 100 cycles, the electrode still retained a capacity of 682 mA h g^{-1}. The

corresponding Coulombic efficiency is shown as the inset in Figure 8-9b. The mesoporous NiO crystal electrodes were cycled at high rates of 10 C, 20 C, and 40 C for 1000 cycles. The electrodes exhibited almost the same capacity and cycling performance at 10 C and 20 C. After 1000 cycles, mesoporous NiO crystals retained lithium storage capacity of 468 mA h g^{-1} at 10 C and 20 C rate, and 322 mA h g^{-1} at 40 C rate, respectively (Figure 8-9c). This performance is much better than that of carbon based anode materials.[895,896] We also tested the cycling performance at varied current rates: 1 C, 2 C, 5 C, 10 C, 20 C, and 40 C. The results are presented in Figure 8-9d. It should be noticed that as long as the current rate reversed back low current rate, the cell capacity recovered to the original values, indicating that the integrity of mesoporous NiO crystals has been preserved even after high rate cycling. This implies that mesoporous NiO crystals are tolerant to varied charge and discharge currents, which is preferred for high power applications. Mesoporous NiO crystals exhibited a much higher capacity than the previously reported NiO anode materials,[10,847,897] mesoporous NiO synthesized by the hard template method[13], and NiO/graphene hybrid anode materials.[898,899]

8.5 Discussion

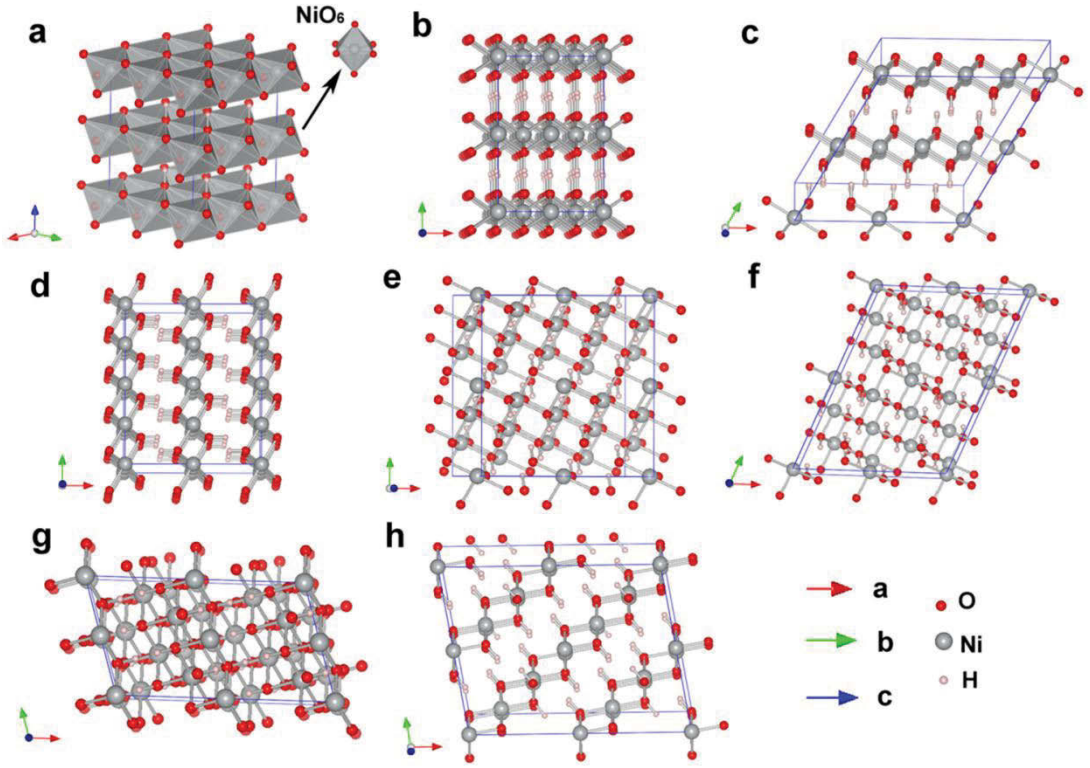

Figure 8-10 (a) The unit cell of $Ni(OH)_2$ crystal, and side views of relaxed (b) {100}, (c) {111}, (d) {110}, (e) {112}, (f) {113}, (g) {101}, and (h) {121} crystal planes of $Ni(OH)_2$.

Table 8-1 The calculated surface energies of $Ni(OH)_2$.

surface	d-spacing, d_{hkl}/Å	Surface energy / J m^{-2}
100	3.088	1.674
110	5.863	1.176
111	4.894	0.952
112	5.349	0.955
113	5.036	1.279
121	7.336	1.253
101	6.444	1.072
211	7.336	1.421

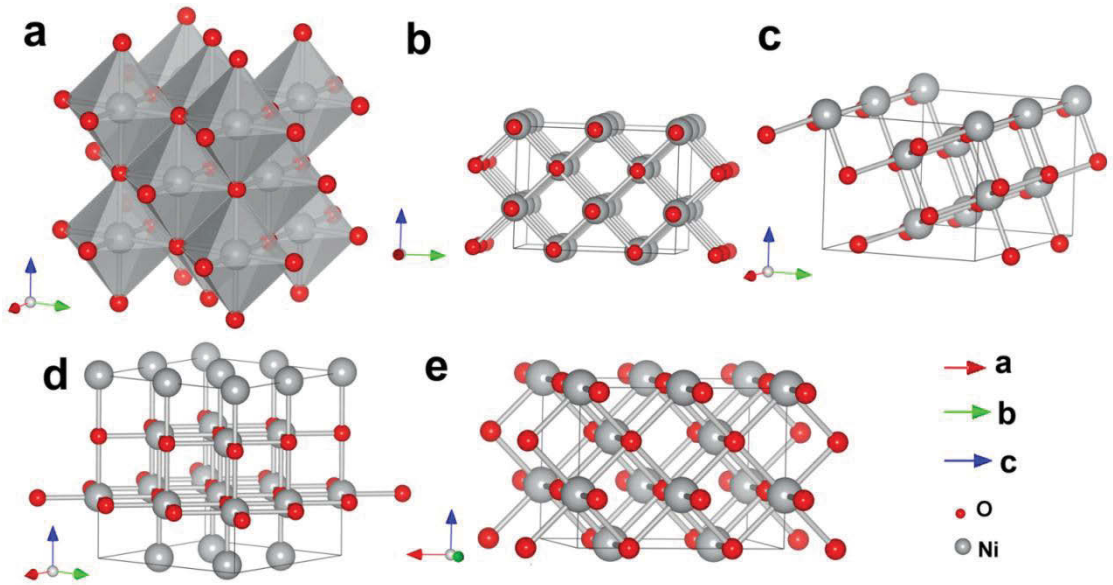

Figure 8-11 (a) The unit cell of NiO crystal, and side views of relaxed (b) {113}, (c) {100}, (d) {110}, and (e) {101} crystal planes of NiO.

Table 8-2 The calculated surface energies of NiO.

Surface	d-spacing, d_{hkl}/Å	Surface energy / J m^{-2}
100	1.311	0.958
110	1.683	1.476
113	1.254	1.264
101	1.38	1.482

The refined crystal structure and relaxed side views of $Ni(OH)_2$ and NiO are shown in Figure 8-10 and Figure 8-11, respectively. $Ni(OH)_2$ has a tabular crystal structure, in which the NiO_6 octahedrons are compressed parallel to the threefold axis, inducing an enlargement of the distance between the oxygen atoms at positions (1/3, 2/3, z) and (2/3, 1/3, -z). The structure of NiO is commonly known as the rock salt structure in which octahedral Ni (II) and O^{2-} occupy the 4 a and 4 b sites, respectively. The calculated surface energies for $Ni(OH)_2$ and NiO crystals are listed in table 8-1 and 8-2,

respectively. The (111) plane of $Ni(OH)_2$ crystal has the lowest energy of 0.952 J m^{-2}, suggesting it is the most stable. The other crystal planes have higher surface energies, indicating these are meta-stable surfaces. Thus, it is possible to grow $Ni(OH)_2$ crystals with a high percentage of exposed {111} facets. This theoretical predication was confirmed in this investigation. The most stable crystal plane for NiO crystal is the {100} facet with the lowest surface energy of 0.958 J m^{-2}. The {113} plane has the second lowest surface energy (1.264 J m^{-2}). The {110} and {101} planes have relatively high value larger than 1.47 J m^{-2}. Therefore, it is not favourable to obtain highly exposed {110} facets for NiO crystals under the equilibrium condition. Since the $Ni(OH)_2$ crystals have a nanoplatelet shape, in which the two basal planes ({111} facets) are dominantly exposed crystal planes. After sintering, the nanoplatelet shape was preserved for NiO crystals, in which the two basal planes indexed as the {110} facets, are still dominantly exposed planes. Generally, high-energy surfaces have a large density of low-coordinated atoms situated on steps and kinks, with high reactivity.[900] This favours fast ion transfer between the surface and the interior.[901,902] Because the {110} facets have relatively high surface energy, the {110} crystal planes provide reactive sites for reaction with lithium ions, which can facilitate fast conversion reaction towards lithium during the charge and discharge process. On the other hand, the mesoporous architecture contributes to the excellent electrochemical performance of NiO crystals. In lithium-ion cells, liquid electrolyte can flood into mesopores, inducing high surface area contact with active NiO crystals. Thin nanoplate and mesoporous structure provide a short path for lithium transport and high surface area for interfacial lithium storage.[766,767]

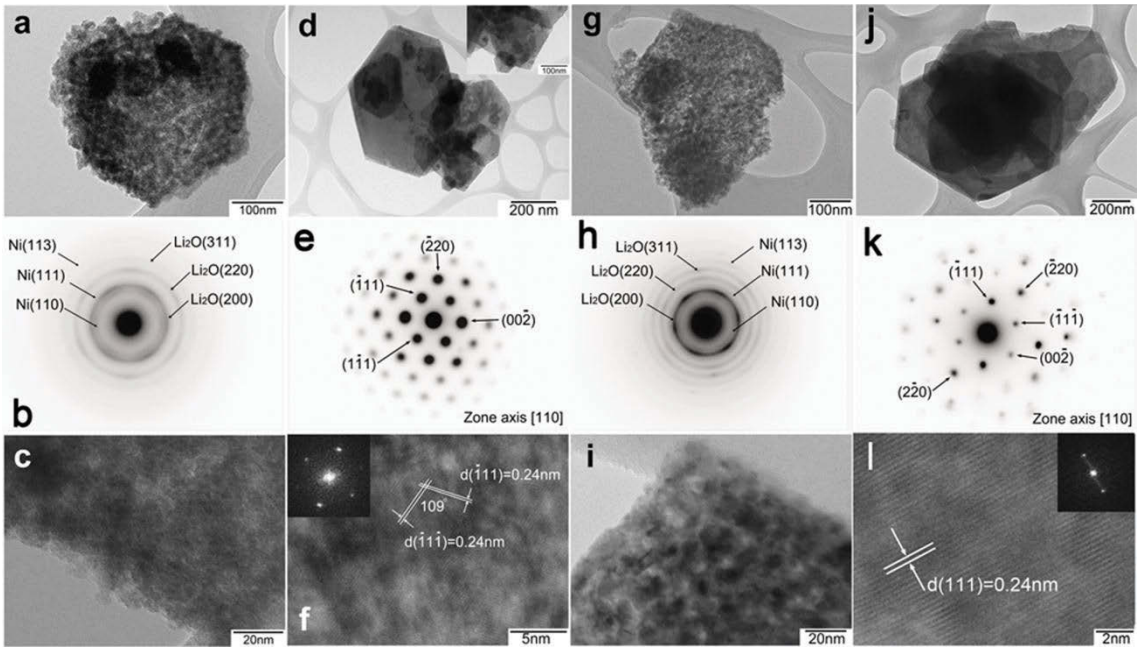

Figure 8-12 structural and morphological changes of mesoporous NiO facet crystals during the charge and discharge processes. TEM images and SAED patterns of NiO electrodes taken from fully discharged states (a)-(c) and fully charged states (d)-(f) in the first cycle, fully discharged (g)-(i) and fully charged (j)-(l) states after 100 cycles. (a), (d), (g), and (j) show bright-field TEM images of individual NiO crystals at different stages of the reduction and oxidation processes. (b), (e), (h), and (k) are the corresponding SAED patterns. (c), (f), (i), and (l) are the lattice resolved TEM images at various stages of the reduction and oxidation processes. The inset in (d) is the magnified TEM image of a NiO facet crystal. The insets in (f) and (l) are the corresponding FFT images.

In order to investigate the lithium-driven structural and morphological changes during the charge and discharge processes, we performed *Ex-situ* TEM and SAED analysis on mesoporous facet NiO crystals at the fully discharged (reduced) and charged (oxidized) states in the first cycle and the 100^{th} cycle at 1 C rate. The results are shown in Figure 8-10. At the fully discharged state in the first cycle, the crystal shape was preserved and

the surface of the crystal became rough as shown in the bright-field TEM image (Figure 8-12a). NiO was reduced to metallic Ni and dispersed in the lithia (Li_2O) matrix[5]. The corresponding SAED pattern presents the (200), (220) and (311) diffraction rings of Li_2O (Figure 8-12b). HRTEM (Figure 8-12c) reveals the pseudo-amorphous characteristic, suggesting the formation of the solid electrolyte interphase layer (SEI). After being fully charged in the first cycle, the NiO crystals recovered to the pristine state. As shown in Figure 8-12d, individual crystals have a clear hexagon appearance with smooth surface. When taking SAED from an individual crystal, spot SAED patterns were obtained (Figure 8-12e). The SAED pattern can be well indexed to NiO crystal along the [110] zone axis. This unambiguously confirmed the recovery of the single crystalline feature at the fully charge state for mesoporous NiO crystals in the first cycle. A lattice resolved HRTEM image (Figure 8-12f) shows the $(\bar{1}1\bar{1})$ and $(\bar{1}11)$ crystal planes with a d-spacing of 2.5 Å and 109 ° angle. The fast Fourier transform (FFT) spot pattern (the inset in Figure 8-12f) further confirms the single crystalline feature. Mesoporous structure can also be clearly observed in Figure 8-12f. Therefore, mesoporous faceted NiO crystals can fully recover to their original states after the first cycle.

To further illustrate the outstanding cycle performance of facet NiO crystals, we conducted *Ex-situ* TEM analysis on the electrode at the discharged and charged states in the 100^{th} cycle. When the electrode was fully discharged after 100 cycles, the crystals still maintained the original appearance (the bright-field TEM image, Figure 8-12g), which is similar to that after the initial cycle. The SAED ring pattern (Figure 8-12h) can be indexed to Li_2O. Figure 8-12i shows the HRTEM image of the NiO crystal at the discharged state in the 100^{th} cycle, from which the mesoporous architecture can be

easily distinguished. Figure 8-12j shows the bright-field TEM image of NiO crystals at the fully charged state in the 100th cycle. The hexagonal nanoplate shape was restored

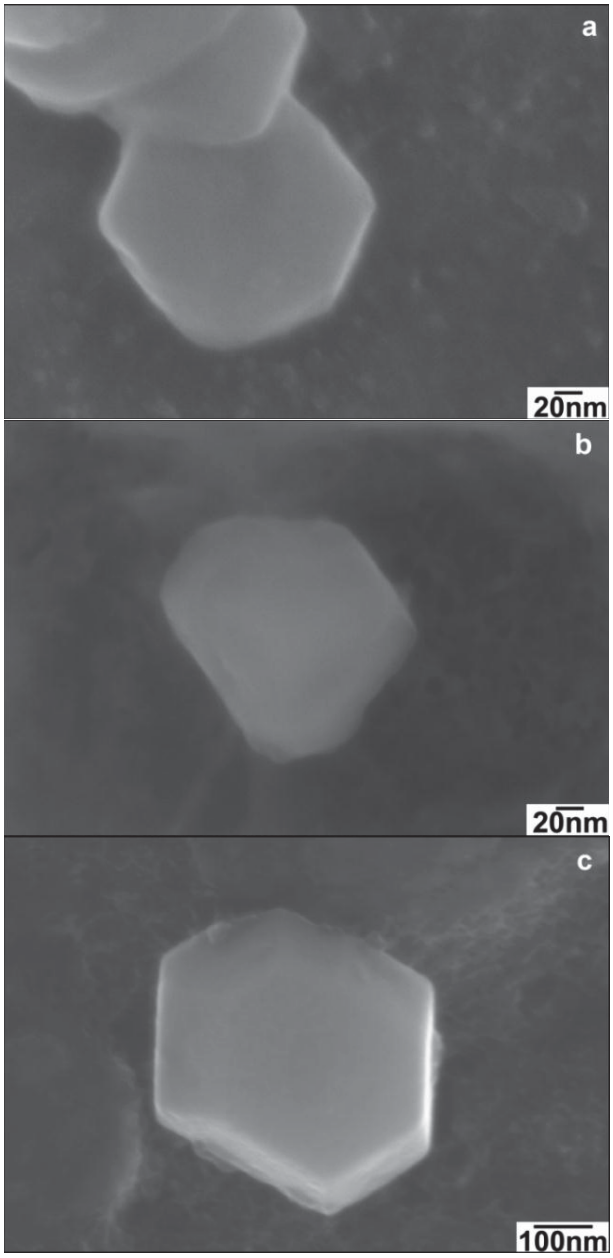

Figure 8-13 SEM images of NiO electrodes taken from fully charged state at (a) 0.5 C current rate after 100 cycles, (b) 10 C current rate after 1000 cycles, and (c) 40 C current rate after 1000 cycles.

even after 100 cycles. The SAED spot pattern (Figure 8-12k) taken from individual crystal can be fully indexed along the [110] zone axis of cubic NiO. This suggests the recovery of single crystalline NiO after long time cycling. The corresponding HRTEM image is presented in Figure 8-12l, from which the (111) crystal planes of NiO with a d-spacing of 0.24 nm can be indexed. The regular mesopores are also visible from the HRTEM image. The FFT pattern shows the spot feature, further illustrating the single crystalline of NiO crystals. We also performed the *Ex-situ* observation of mesoporous facet NiO crystals after 100 cycles at 0.5 C and after 1000 cycles at 10, and 40 C current rates by FESEM. Figure 8-13 shows the FESEM images of the individual mesoporous NiO crystals at the fully charged states. All crystals were restored to faceted crystal shape with good crystalinity even cycled at high current rate of 40 C.

Recently, J.-M tarascon *et al*. have identified a special mechanism for reversible lithium storage in mesoporous metal oxides (MO), which differs from bulk materials.[903] They found that mesoporous MO reacts with Li through a conversion reaction, leading to the formation of large metallic M nanoparticles (10 nm) upon discharge. These nanoparticles are embedded into a Li_2O matrix together with a copious amount of polymeric materials coming from electrolyte degradation, which surround the particles and fill the pores. During the following charge, re-oxidation of the nanoparticles occurs with the formation of MO. The main difference, when compared to bulk MO electrodes, is the preservation of the polymeric layer at the end of the charge. Therefore, the origin of this difference lies in the material mesoporosity, via capillary effects. Our mesoporous NiO crystals match this newly discovered mechanism. The mesoporous structure has been preserved during discharge and charge processes, owing to the formation of polymeric SEI layer. Mesoporous NiO crystals with exposed {110} facets were restored during charging, which has been confirmed by *Ex-situ* TEM analysis.

8.6 Conclusion

In summary, mesoporous faceted NiO crystals were synthesised by a hydrothermal method combined with annealing treatment. TEM analysis confirmed that NiO crystals had dominantly {110} exposed crystal planes and mesoporous architecture. When applied as anode materials in lithium-ion cells, mesoporous faceted NiO crystals delivered a high reversible lithium storage capacity of around 700 mA h g^{-1} in 100 cycles with high Coulombic efficiency at 1 C current rate. The materials also demonstrated an outstanding high rate performance, which mimics supercapacitors for high power delivery. *Ex-situ* TEM characterisation clearly illustrated that the mesporous and faceted crystal structure had been retained after long term discharge/charge cycling even at high current rates. The mesoporous and faceted crystal architecture may be extended to other electrode materials for energy storage applications with high performance.

CHAPTER 9 HYDROTHERMALLY SYNTHESIZED α- AND β-MnO_2 NANORODS AS CATHODE MATERIALS FOR NA-ION BATTERIES

9.1 Abstract

Two types of MnO_2 polymorphs, α-MnO_2, β-MnO_2 nanorods, have been synthesized by a hydrothermal method. Their crystallographic phases, morphologies, and crystal structures were characterized by XRD, FESEM and TEM analysis. Different exposed crystal planes have been identified by TEM. The electrochemical properties of α-MnO_2 and β-MnO_2 nanorods as cathode materials in Na-ion batteries were evaluated by galvanostatic charge/discharge testing. Both α-MnO_2 and β-MnO_2 nanorods achieved high initial sodium ion storage capacities of 278 mA h g^{-1} and 298 mA h g^{-1}, respectively. β-MnO_2 nanorods exhibited a better electrochemical performance such as a good rate capability and cyclability than that of α-MnO_2 nanorods, which could be ascribed to more compact tunnel structure of β-MnO_2 nanorods. Furthermore, the one-dimensional architecture of nanorods could also contribute to facile sodium ion diffusion in the charge and discharge process.

9.2 Introduction

Li-ion batteries are considered to be the most advanced power sources for portable electronic devices and electric vehicles.[18] However, the high cost of Li-ion batteries and limited Li reserves hampered their applications for large-scale energy storage such as for renewable energy and smart electric grids. In this regard, Na-ion batteries have emerged as an alternative due to the low cost,[18,19] abundant supply (4th

most abundant element in the earth crust) and widespread terrestrial reserves of sodium mineral salts. Na-ion batteries have similar features to Li-ion batteries: non-aqueous electrolytes, alkali insertion electrodes,[15] stable diffusion barrier of Na-ion.[20] However, the higher ionization potential[3] and larger ionic diameter of the Na ((1.02 Å) *vs.* Li (0.76 Å))[21] limit the structural variability and choice of Na insertion materials in crystalline materials. Therefore, finding and optimizing suitable electrode materials are crucial for the development of Na-ion batteries. So far, considerable progress has been achieved. Hard carbon materials with large interlayer distance and disordered structure, which facilitates Na ion insertion and extraction, have been studied as anode materials.[660,661,663] Alternative oxide anodes such as $Na_2Ti_3O_7$[666] and TiO_2-nanotubes[904] have also been recently investigated. For cathode materials, layered oxides: Na_xCoO_2,[610] $Na_{2/3}(Ni_{1/3}Fe_{1/3}Mn_{2/3})O_2$,[905] $NaCrO_2$,[906,907] Na_xVO_2[669] and new type of bi-layered $Na_xV_2O_5$,[908] have been investigated. However, they are all limited by either low capacity or poor cyclability. In addition, framework material based on the phosphate polyanion, olivine $NaFePO_4$, has also been reported by Zaghib et al.[909] It demonstrated a 147 mA h g^{-1} initial specific capacity, but its reversibility is poor (50.6 mA h g^{-1} in the second cycle). Fluoride-based cathode materials, $NaMF_3$ (M = Fe, Mn, V and Ni),[910,911] have been prepared with the aim to overcome the low theoretical specific capacity of polyanionic cathodes, but they still did not achieve the satisfactory specific capacities (ranging from 30 to 170 mA h g^{-1}). Manganese oxides have large-size tunnels which is potential host to accommodate Na ion insertion and extraction.[912] And lots of research was focus on sodium intercalated manganese oxide materials.[913-915] Recently, MnO_6 octahedra and MnO_5 square pyramids were found to form large, double ion channels in orthorhombic $Na_4Mn_9O_{18}$ ($Na_{0.44}MnO_2$) and offer ca. 130 mA

h g^{-1} capacity.[913-915] They show stable cycling performance because of their capability to tolerate some stress during structural changes. Morales et al. reported that layered P2-$Na_{0.6}MnO_2$ can deliver a 150 mA h g^{-1} first cycle capacity,[912,916,917] but this material exhibited a poor capacity retention capability with more than 50 % of capacity loss after only 10 cycles. So far it is still lack of appropriate active materials having sufficiently big interstitial space within their crystallographic structure to host Na ions.

Manganese dioxides have many different types of polymorphs, and all of them have large open tunnels, which can accommodate guest cations.[918] Therefore, they in self can be potentially used as cathode materials for Na-ion batteries. Herein, we report synthesis, structural characterisation and electrochemical performance of α-MnO_2 and β-MnO_2 nanorods. Both α-MnO_2 and β-MnO_2 nanorods exhibited the capability for reversible Na-ion storage as cathode materials in Na-ion batteries. In particular, β-MnO_2 nanorods demonstrated a high capacity, a good rate performance and a satisfactory cyclability. To the best of our knowledge, this is the first report on the MnO_2 as cathode for Na-ion battery.

9.3 Experiment

9.3.1 Materials Synthesis

α-MnO_2 and β-MnO_2 nanorods were synthesized by a hydrothermal method. For the synthesis of α-MnO_2 nanorods, 1.5 mmol $KMnO_4$ and 5 mmol concentrated HCl were added to 15 mL deionized water. The mixture was stirred vigorously for several minutes until a transparent purple solution was formed and then transferred into a Teflon-lined stainless steel autoclave (25 mL in capacity). The autoclave was

sealed and heated to 140 °C and maintained for 12 h. To produce β-MnO_2 nanorods, 1 mmol $(NH_4)_2S_2O_8$ and $MnSO_4 \cdot H_2O$ were dissolved in 20 mL deionized water. 0.2 g cationic surfactant cetyltrimethylammonium bromide (CTAB) as soft template was added into the solution and was heated to 140 °C in a Teflon-lined autoclave for 12 h. The precipitates were cooled down to room temperature, collected by centrifugation and washed with distilled water several times. After drying at 60 °C in a vacuum oven overnight, the final products were obtained.

9.3.2 Structural and physical characterization

The crystal structure and phase of the as-prepared materials were characterized by X-ray diffraction (XRD, Siemens D5000) using a Cu Kα radiation at a scanning step of 0.02°/min. The morphology was analyzed by field emission scanning electron microscopes (FESEM, Zeiss Supra 55VP). The crystal structure details were further characterized by transmission electron microscopy (TEM) and high-resolution transmission electron microscopy (HRTEM, JEOL JEM-2011). Selected area electron diffraction (SAED) patterns were recorded by a Gatan CCD camera in a digital format. The specific surface areas were measured by N_2 adsorption isotherm using a Quadrasorb SI analyzer at 77 K. Brunauer–Emmett–Teller (BET) surface areas were calculated using experimental points at a relative pressure of $P/P_0 = 0.05–0.25$.

9.3.3 Electrochemical testing

The electrodes were prepared by dispersing the as-prepared MnO_2 nanorods (70 wt %), acetylene carbon black (20 wt %), and poly (Vinylidene fluoride) binder (PVDF, 10 wt %) in N-methyl-2-pyrrolidone (NMP) to form a slurry. The resultant slurry was pasted onto aluminium foil (1 cm × 1 cm) using a doctor blade and dried in a

vacuum oven for 12 h, followed by pressing at 200 kg cm^{-2}. The mass of each electrode is around 1.4 mg. Electrochemical measurements were carried out using two-electrode coin cells with Na metal as counter and reference electrodes and the glass microfiber (Whatman) as the separator. The CR2032-type coin cells were assembled in an argon-filled glove box (UniLab, Mbraun, Germany). The electrolyte solution was 1 M $NaClO_4$ dissolved in a mixture of ethylene carbonate (EC) and propylene carbonate (PC) with a volume ratio of 1:1. Cyclic voltammetry (CV) was carried out on a CHI 660C electrochemistry workstation with a scan rate of 0.1 mV s^{-1} from 1 to 4.3 V in a two-electrode system. The charge-discharge measurements were performed at ambient temperature at different current densities in the voltage range from 1 to 4.3 V. The AC impedance was carried out on a CHI 660C electrochemistry workstation in the frequency range between 100k and 10m Hz. In order to investigate the sodium-driven structural and morphological changes after 100 cycles of the as-prepared α- and β-MnO_2 nanorods, Swagelok-type cells were assembled. The cells were opened in the Glove-box after 100 cycles test. The active materials were removed from the electrodes and washed with propylene carbonate (PC) before being used for *ex-situ* TEM analyses.

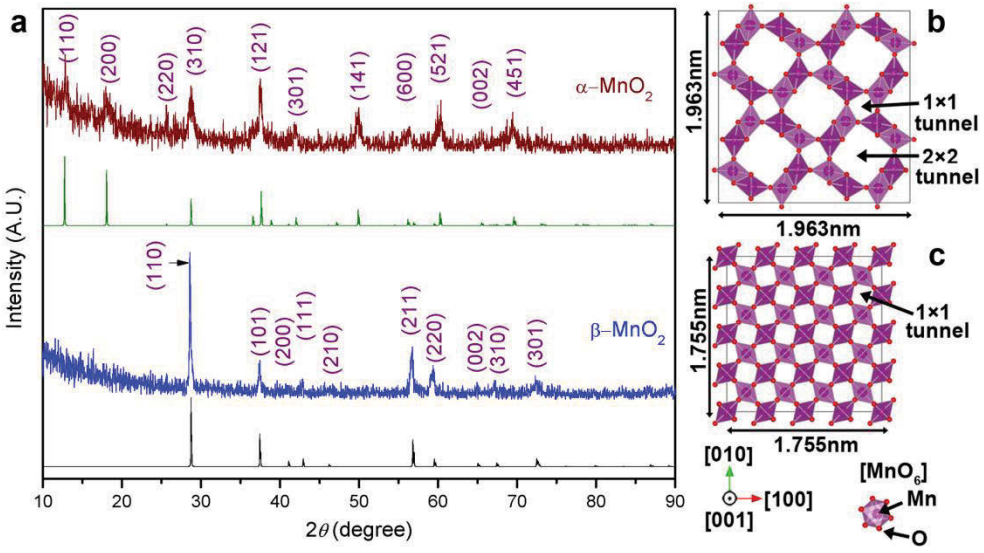

Figure 9-1 (a) X-ray diffraction patterns of α-MnO_2 nanorods (wine in color), β-MnO_2 nanorods (blue in color). The black and green solid lines are simulated diffraction patterns based on the refined crystal structure of α-MnO_2, (b) The crystal structure of α -MnO_2 along the [001] direction, (c) The crystal structure of β-MnO_2 along the [001] direction.

9.4 Results and discussion

Figure 9-1a shows the XRD patterns of α-MnO_2 and β-MnO_2 nanorods. The product prepared by $KMnO_4$ precursor solution was identified to be pure α-MnO_2 phase (JCPDS No. 44−0141, tetragonal, I4/m, a = b = 9.78 Å, c = 2.86 Å). While the product prepared by $MnSO_4 \cdot H_2O$ precursor solution can be identified to be pure β-MnO_2 phase (JCPDS No. 24−0735, tetragonal, P42/mnm, a = b = 4.39 Å, c = 2.87 Å). No impurity phases were observed, comparing to the simulated diffraction patterns of α- MnO_2 and β-MnO_2 (the black and green solid lines in Figure 9-1 a, respectively). In general, MnO_2 can form several polymorphs since the MnO_6 octahedral units can be linked in different ways.[368] α-MnO_2 is constructed from the double chains of edge-sharing MnO_6 octahedra that are linked at the corners to form

(2 × 2) + (1 × 1) tunnel structure. While β-MnO_2 shows 1D channel (1 × 1) structure composed of individual chains of the MnO_6 octahedral units as illustrated in Fig.1 b and c, respectively. Actually, β-MnO_2 is more stable phase compare with α-MnO_2. And the β-MnO_2 with compact (1 × 1) tunnel will be easily formed instead of the α-MnO_2 without the present of big guest cations. The K ions, coming from $KMnO_4$, can serve as the crucial guest cations to direct the precursor to form (2 × 2) tunnel structure of α-MnO_2.[919] There is no suitable guest cation in the $MnSO_4$ precursor, therefore, the small (1 × 1) tunnel of β-MnO_2 will be formed.[920] From the [001] projected direction of the simulated crystal structure, it can be seen that α-MnO_2 has 2 × (1 × 1) and 2 × (2 × 2) tunnels per formula unit with a tunnel density of 0.042 $Å^{-2}$, while β-MnO_2 has 2 × (1 × 1) tunnels per formula unit with a tunnel density of 0.104 $Å^{-2}$. Therefore, β-MnO_2 has more than twice tunnels per unit area than that of α-MnO_2. It suggests that β-MnO_2 can accommodate more Na ions.

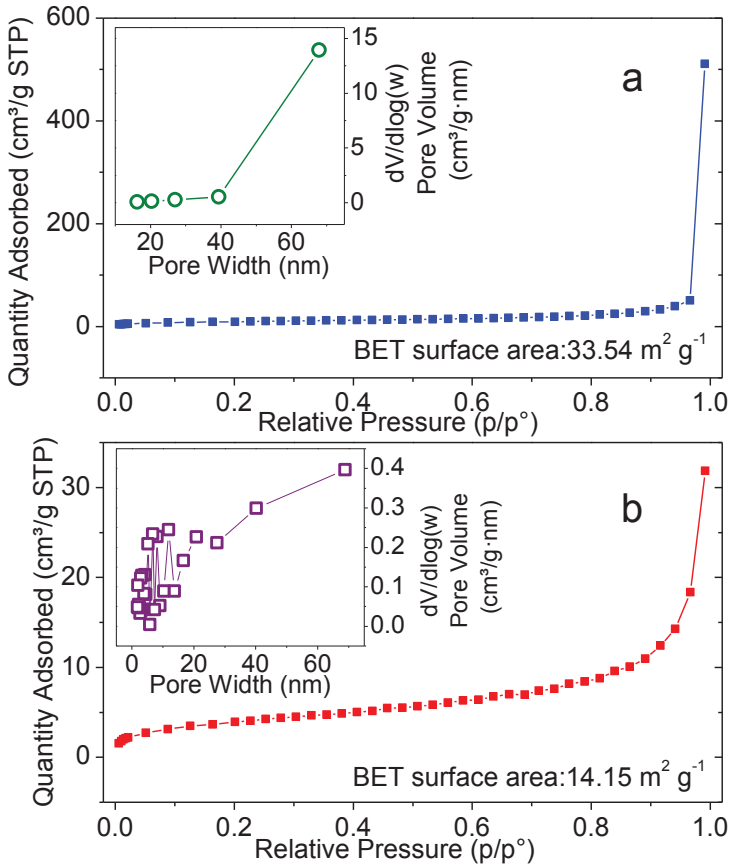

Figure 9-2 N_2 absorption isotherms of α-MnO_2 nanorods (a) and β-MnO_2 nanorods (b). Insets are their corresponding pore size distributions derived from absorption hysteresis of Brunauer-Emmett-Teller (BET) surface area measurement.

The BET specific surface areas were measured by nitrogen adsorption isotherm at 77 K as shown in Figure 9-2. α-MnO_2 nanorods have higher surface area (33.54 m^2 g^{-1}) than β-MnO_2 nanorods (14.15 m^2 g^{-1}).

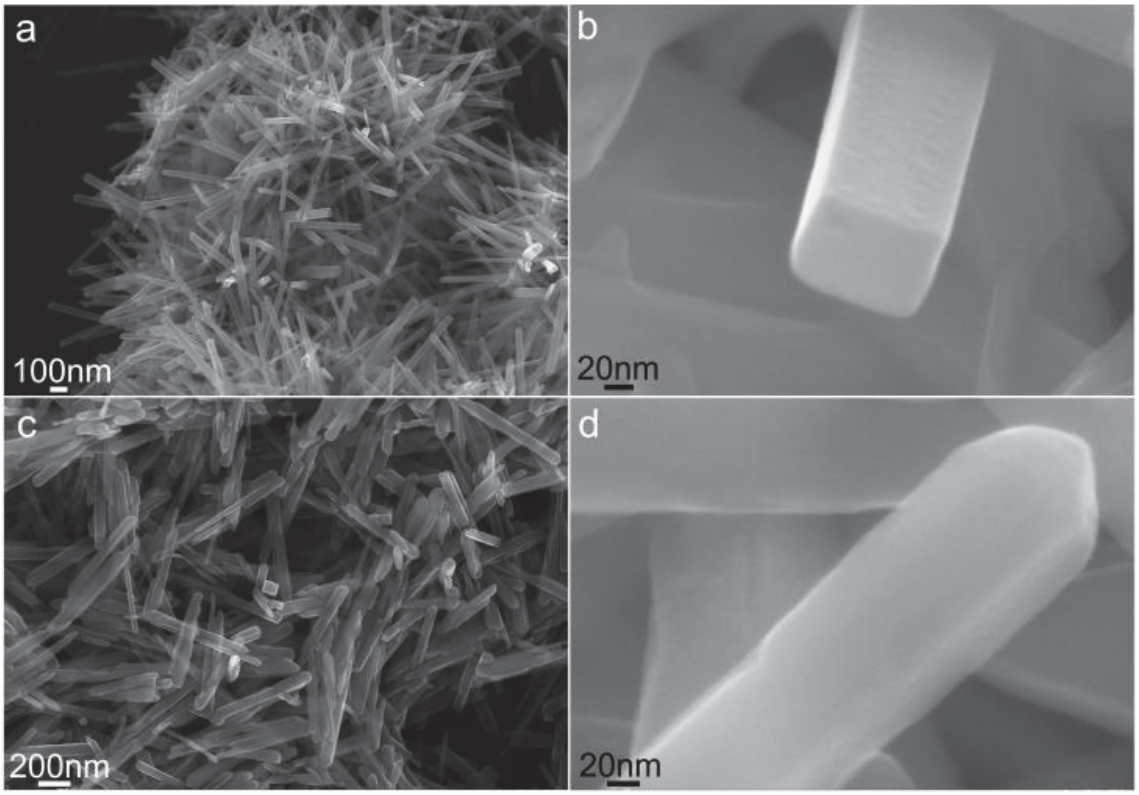

Figure 9-3 (a) and (c) are Low magnification FESEM images of α-MnO_2 nanorods, and β-MnO_2 nanorods, respectively. (b) and (d) are high magnification FESEM images of α-MnO_2 nanorods and β-MnO_2 nanorods, showing the cross section of nanorods.

Both α-MnO_2 and β-MnO_2 show typical nanorod morphology with uniform size distribution. As shown in Figure 9-3a and c, the low magnification FESEM images exhibit the lengths of nanorods extending to a few micrometers. Figure 9-3b and d show the cross sections of α-MnO_2 and β-MnO_2 nanorods, respectively. α-MnO_2 nanorods have a rectangle cross section, while β-MnO_2 nanorods have a rectangle pyramid tip.

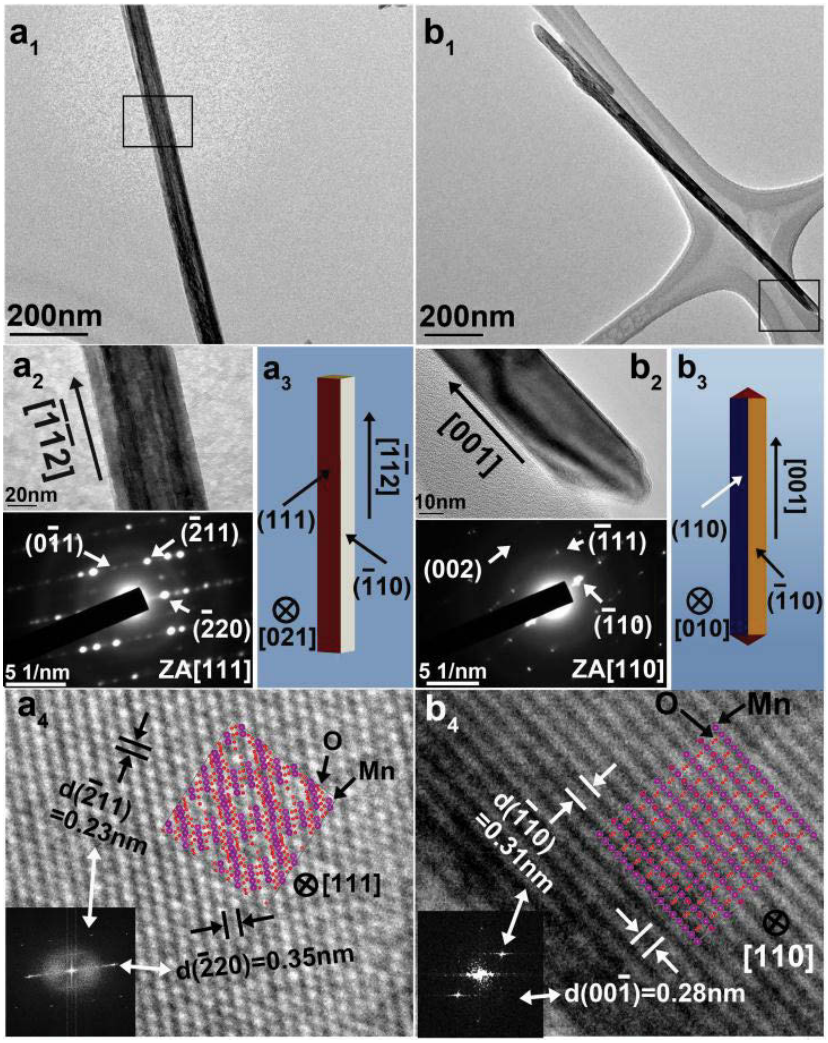

Figure 9-4 Low magnification TEM images of a free standing α-MnO_2 nanorod (a_1) and β-MnO_2 nanorod (b_1). (a_2) and (b_2) are high magnification TEM images taken from rectangular regions in (a_1) and (b_1) The inset images in (a_2) and (b_2) are their corresponding selected area electron diffraction spot patterns (SAED). (a_3) and (b_3) are geometrical models of α-MnO_2 and β-MnO_2 nanorods, in which different colours present different crystal planes. Lattice resolved HRTEM images of α-MnO_2 nanorod (a_4) and β-MnO_3 nanorod (b_4). Left bottom inset images in (a_4) and (b_4) are their corresponding Fast-Fourier-Transform (FFT) patterns. The middle insets in (a_4) and (b_4) simulate [111] projection of tetragonal α-MnO_2 crystal structure and [110] projection of tetragonal β-MnO_2 crystal structure, respectively (Mn and O marked as purple and red in colour).

Crystal structures of α-MnO_2 and β-MnO_2 nanorods were analysed by TEM, HRTEM and SAED characterisation (Figure 9-4). The individual nanorods are clearly distinguishable (as shown in Figure 9-4(a_1) and (b_1), respectively). Figure 9-4(a_2) and (b_2) show high magnification TEM images of a α-MnO_2 nanorod and a β-MnO_2 nanorod, respectively. Their corresponding SAED patterns are shown as insets. The dot style SAED patterns confirmed the single crystalline nature of α-MnO_2 and β-MnO_2 nanorods. For α-MnO_2 nanorod, the rhombic SAED spot pattern can be well indexed along the [111] zone axis, which indicates the facet vertical to the electron beam is the (111) crystal plane. The two side facets are the $(\bar{1}10)$ and $(1\bar{1}0)$ exposed crystal planes, respectively. α-MnO_2 nanorods were identified to grow along the $[\bar{1}\bar{1}2]$ direction.

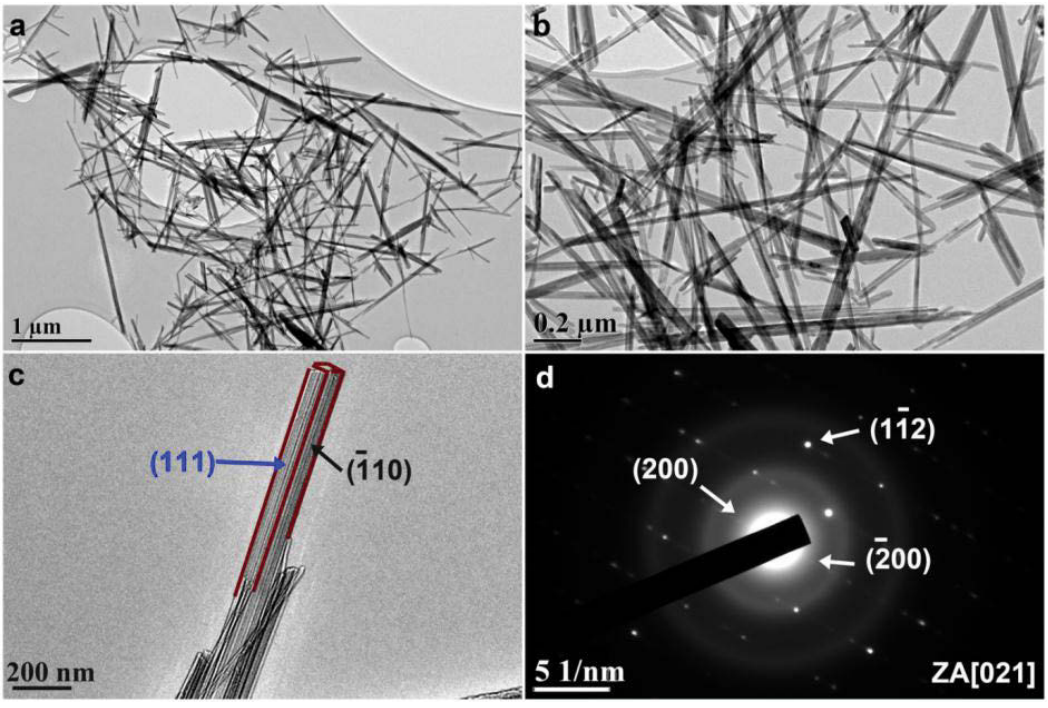

Figure 9-5 Low (a) and medial (b) magnification TEM images of α-MnO_2 nanorods. c. A single α-MnO_2 nanorod with the [021] projected direction, in which the (111) and $(\bar{1}10)$ crystal planes are marked. And d is its corresponding SAED patterns which can be indexed along the [021] zone axis of tetragonal α-MnO_2.

Additional TEM images and SAED pattern of α-MnO_2 nanorods presented in Figure 9-5, further identified the features of α-MnO_2 nanorods. Therefore, the (111) and (110) crystal planes are exposed facets along the longitudinal direction. Figure 9-4(a_3) shows the geometric model of the α-MnO_2 nanorod.

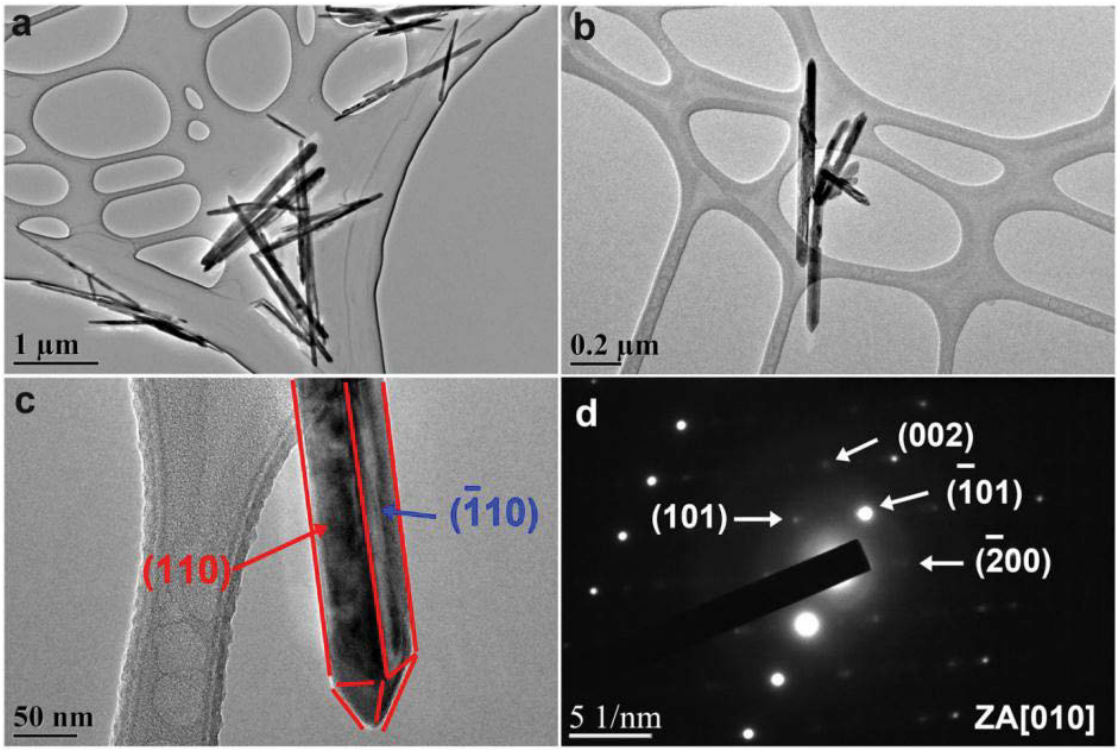

Figure 9-6 Low (a) and medial (b) magnification TEM images of β-MnO_2 nanorods. c. A single β-MnO_2 nanorod with the [010] projected direction in which the (110) and ($\bar{1}$10) crystal planes are marked. And d is its corresponding SAED patterns which can be indexed along the [010] zone axis of tetragonal β-MnO_2.

Similarly, the exposed facet of the β-MnO_2 nanorod (vertical to the electron beam) can be identified as the (110) crystal plane based on the rectangle SAED spot pattern (Figure 9-4(b_2)), along the [110] zone axis. β-MnO_2 nanorods grow along the (001) direction. If tilting 45 ° around [001] axis, the SAED spot pattern can be indexed along the [010] zone axis (Figure 9-6 c and d), indicating that the other two exposed

facets of the β-MnO_2 nanorod are $(\bar{1}10)$ and $(1\bar{1}0)$ crystal planes. The schematic model of β-MnO_2 nanorods is presented in Figure 9-4(b_3), from which it is evident that the β-MnO_2 nanorod is enclosed with the (110) and $(\bar{1}10)$ crystal planes along the longitudinal direction. The lattice resolved HRTEM images of α-MnO_2 and β-MnO_2 nanorods are shown in Figure 9-4(a_4) and (b_4), respectively. Their corresponding Fast-Fourier-Transform (FFT) patterns are shown as the insets in Figure 9-4(a_4) and (b_4). The FFT pattern of α-MnO_2 nanorod can be simulated by formula units of tetragonal crystal structure along the [111] projected direction (presented as the inset (middle) in Figure 4 (a_4)). When turned 42 ° along the $[1\bar{1}0]$ axis, the tunnels towards the (001) crystal plane can be observed. The $(\bar{2}11)$ and $(\bar{2}20)$ crystal planes with 0.23, 0.35 nm lattice spacings and 58.9° interfacial angle can be directly observed. For β-MnO_2 nanorod, two orthogonal crystal planes $(\bar{1}10)$ and $(00\bar{1})$ with 0.31 and 0.28 nm lattice spacings were identified. The (110) crystal plane presents a rectangle atom arrangement as simulated along [110] projected direction (middle inset in Figure 9-4 (b_4)).

Electrochemical properties of α-MnO_2 and β-MnO_2 nanorods as cathode materials in Na-ion batteries were investigated by constant charge and discharge cycling. Figure 9-7 shows the voltage profiles of α-MnO_2 and β-MnO_2 nanorods at a low current density of 20 mA g^{-1} in the first and second cycles. For α-MnO_2 nanorods, the initial specific discharge and charge capacities are 278 and 407 mA h g^{-1}, respectively. At second cycle, they dropped to 204 and 250 mA h g^{-1}. No obvious discharge potential plateau appeared during charge and discharge cycling. β-MnO_2 nanorods exhibited an initial discharge capacity of 298 mA h g^{-1} and then dropped to 240 mA h g^{-1} in the second cycle. Although the initial discharge potential plateau is not obvious, β-

MnO_2 nanorods evolved a discharge voltage plateau between 3.0 V and 2.0 V in the second cycle.

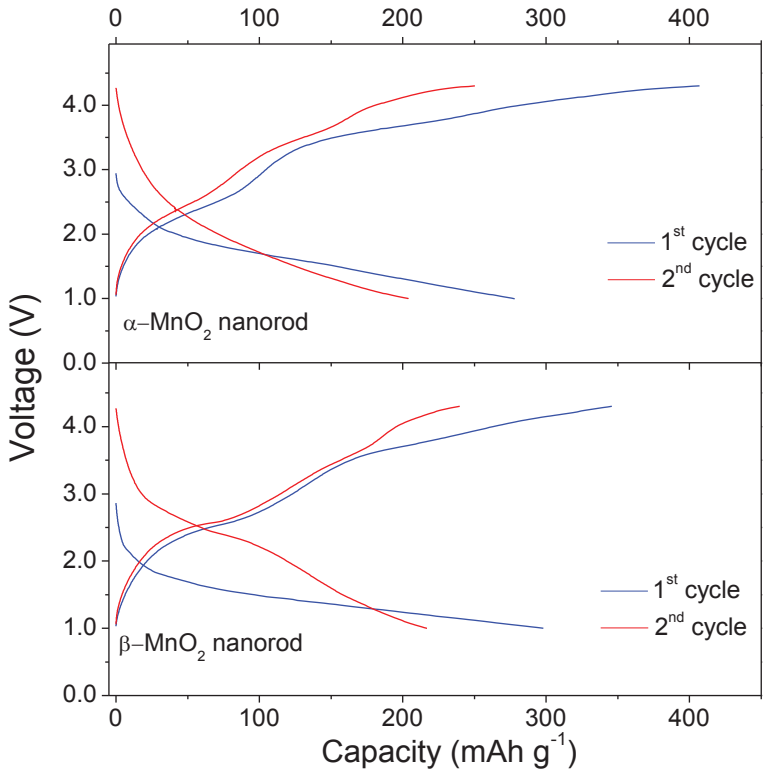

Figure 9-7 The discharge and charge profiles of α-MnO_2, and β-MnO_2 nanorods in 1st and 2nd cycles. Current density: 20 mA g^{-1}.

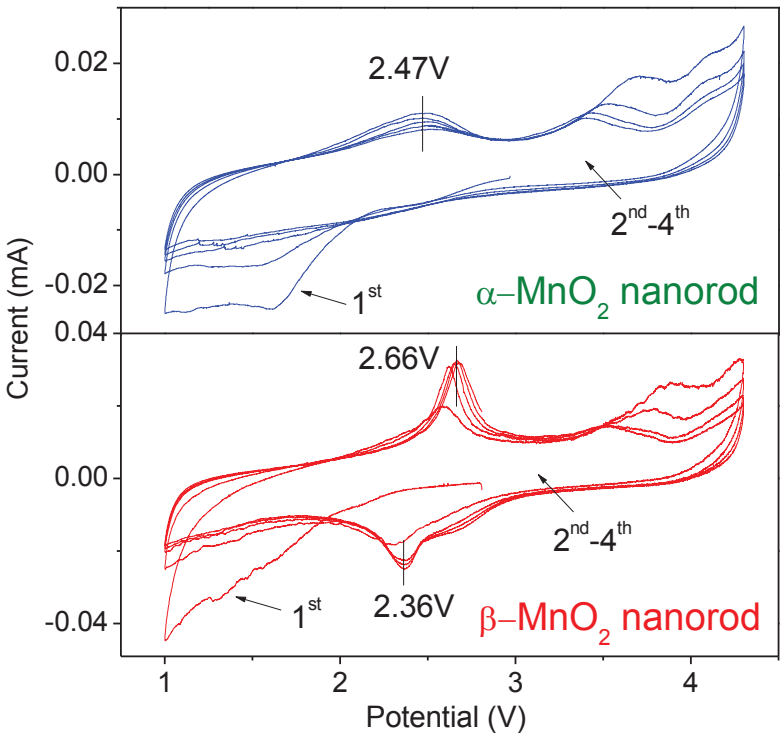

Figure 9-8 The 1-5 cycles CV curves of the α-MnO_2 nanorods and β-MnO_2 nanorods cathodes for sodium ion cells.

Their chemical reactions during the charge and discharge process were further studied by the cyclic voltammetry technique as shown in Figure 9-8, from which we can observe the cathodic and anodic peaks agree well with the charge-discharge voltage plateau. Hereinto, β-MnO_2 nanorods have the low over potential after first cycle. Two redox peaks at 2.36 and 2.66 V should correspond to the absorption/desorption of sodium ions at the electrode surface and Na^+ insertion/extraction process in the lattice framework of β-MnO_2, which is similar with the previous reports on Li-ion battery.[920,921]

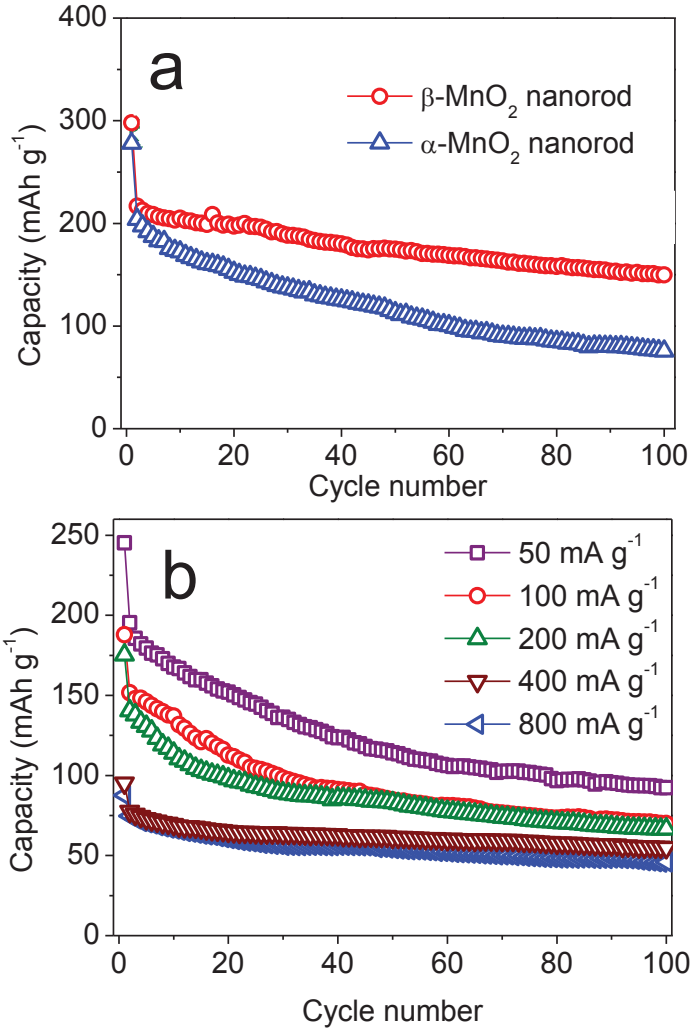

Figure 9-9 (a) Cycling performances of α-MnO_2 and β-MnO_2 nanorod electrodes at the current density of 20 mA g^{-1}. (b) Discharge capacity vs. cycle number of the β-MnO_2 nanorod electrode at high current densities of 50, 100, 200, 400, and 800 mA g^{-1}.

The cycling performances of α-MnO_2 and β-MnO_2 nanorods are shown in Figure 9-9. β-MnO_2 nanorods demonstrated a much better cyclability than that of α-MnO_2 nanorods. β-MnO_2 nanorods maintained 145 mA h g^{-1} discharge capacity after 100 cycles. However, α-MnO_2 nanorods only delivered a capacity of 75 mA h g^{-1} after 100 cycles. The rate capabilities of β-MnO_2 nanorods were also tested at different current densities (Figure 9-9(b)). β-MnO_2 nanorods delivered a discharge capacity of 246 mA h g^{-1} at 50 mA g^{-1}, 188 mA h g^{-1} at 100 mA g^{-1}, and 176 mA h g^{-1} at 200 mA g^{-1} current densities.

Although the specific capacity gradually decreases with increasing current density, a high initial discharge capacity (96 mA h g^{-1}) has been achieved at 400 mA g^{-1}. Even at 800 mA g^{-1}, 88 mA h g^{-1} discharge capacity was still obtained. After 100 cycles, they all stabled at acceptable values of 93 mA h g^{-1} at 50 mA g^{-1}, 70 mA h g^{-1} at 100 mA g^{-1}, 68 mA h g^{-1}, and 55 mA h g^{-1} at 400 mA g^{-1} and 800 mA g^{-1}, respectively. The rate performance of β-MnO_2 nanorods is much better than that of α-MnO_2 nanorods (Figure 9-10) and previous reported cathode materials for Na-ion batteries.[669,905-907,912,913,915,917]

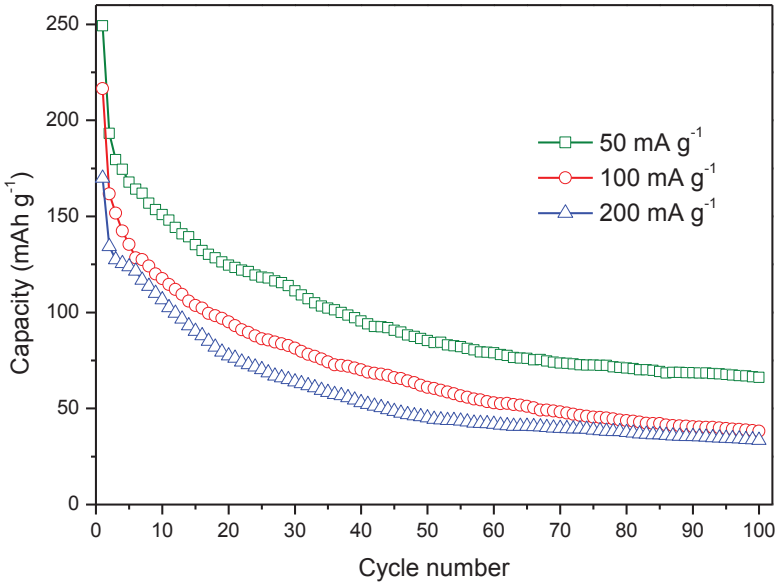

Figure 9-10 Discharge capacity vs. cycle number of α-MnO_2 nanorods at high current densities of 50, 100, and 200 mA g^{-1}.

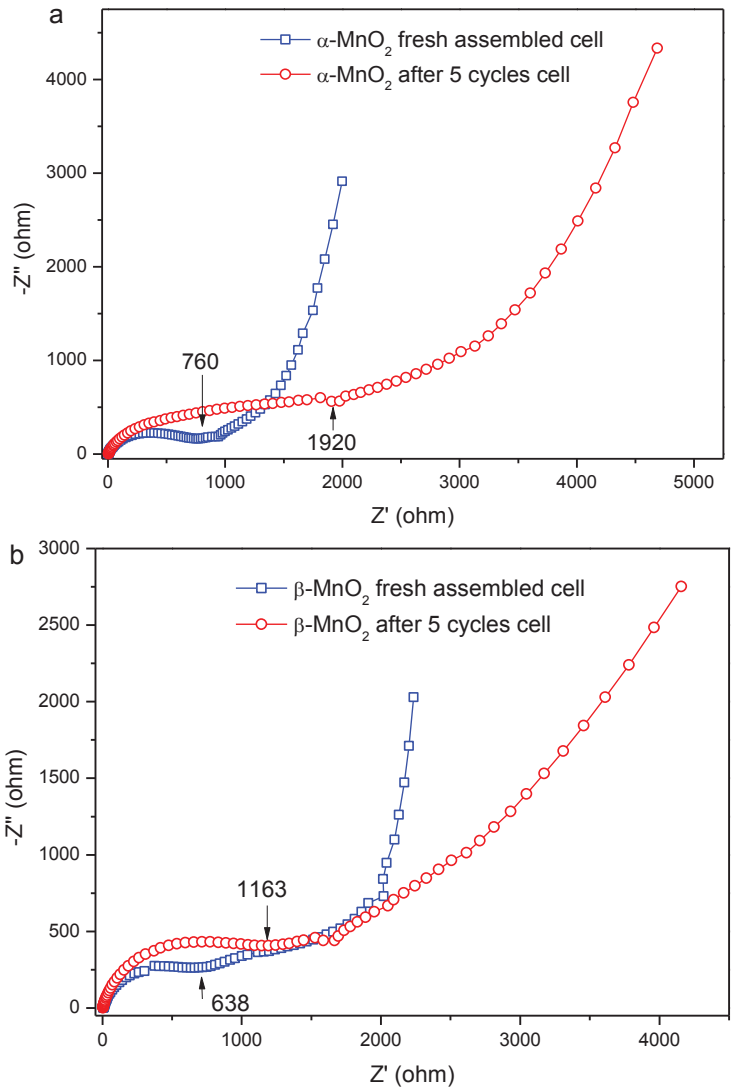

Figure 9-11 The Nyquist plots of α-MnO_2 nanorods (a) and β-MnO_2 nanorods (b) in freshly assembled test cell and after 5 cycles test cell in the frequency range between 100k and 10m Hz at room temperature.

From the Nyquist plots of the AC impedance (Figure 9-11), we can observe relative lower impedance of β-MnO_2 nanorods (both fresh cell and after 5 cycles cell). It is apparent that the charge transfer resistance of β-MnO_2 nanorods is much lower than that of the α-MnO_2 nanorods, which can enhance the electron kinetics in the electrode material, and hence, improve the electrochemical performance of β-MnO_2 nanorods electrode for sodium storage.

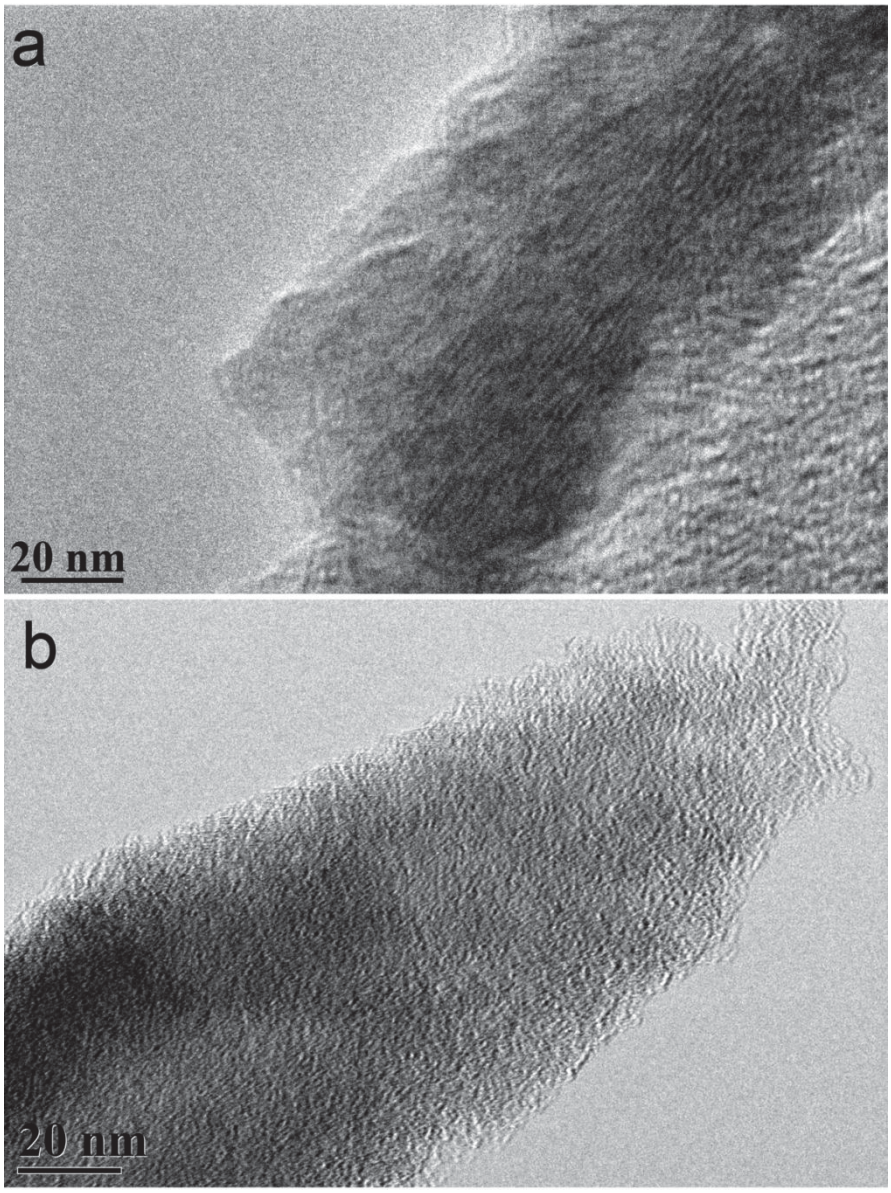

Figure 9-12 TEM images of α-MnO_2 (a) and β-MnO_2 (b) nanorods electrodes after 100 cycles testing.

In order to investigate the sodium-driven structural and morphological changes after 100 cycles of the as-prepared α- and β-MnO_2 nanorods, *ex-situ* TEM analysis was conducted as shown in Figure 9-12. It can be seen that the nanorods shape and structure were preserved after 100 cycles, but due to the volume expansion during the discharge process, their morphologies became rough.

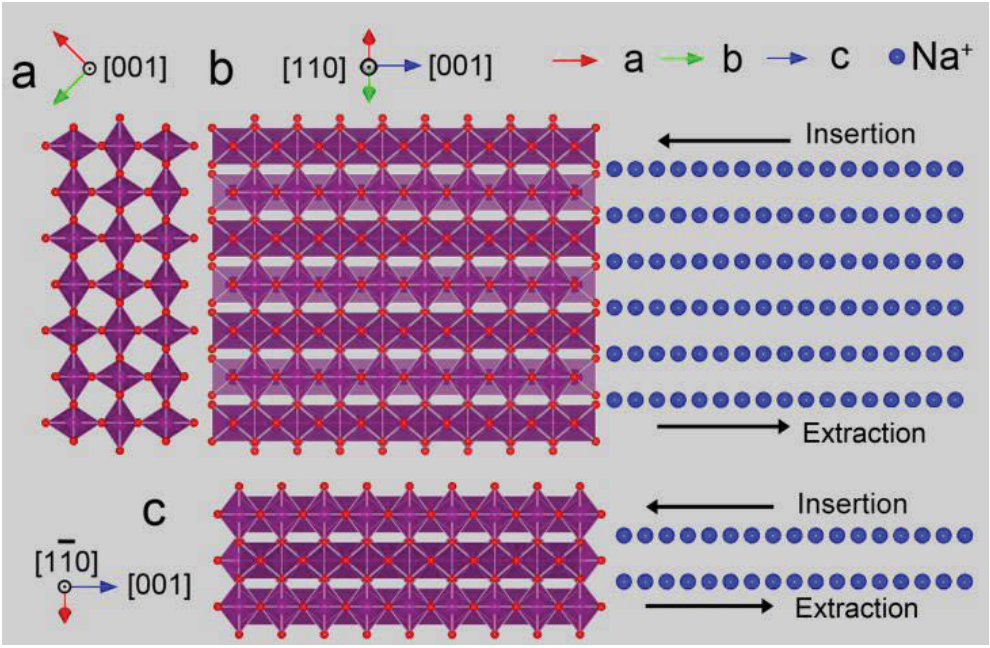

Figure 9-13 Schematic illustration of the crystal structure of β-MnO_2 nanorods (a) along the [001] direction, (b) along the [110] direction, (c) along the [1$\bar{1}$0] direction. (b) and (c) illustrate Na ions insert and extract in the tunnels of β-MnO_2 nanorods. The Mn, O, and Na were colored in purple, red and blue respectively.

The excellent electrochemical performance of β-MnO_2 nanorods could be ascribed to the compact and dense (1 × 1) tunnel-structure in β-MnO_2 crystals. The radius of Na ion (1.02 Å) is much smaller than the size of the (1 × 1) tunnel (2.3 Å × 2.3 Å).[921,922] Therefore, Na ions can facilely insert and extract along the (1 × 1) tunnels in β-MnO_2 nanorods. Figure 9-12 illustrates the Na ion transportation in β-MnO_2 nanorods. We can see that Na ions intercalate/de-intercalate in the compact (1 × 1) tunnels along the [001] direction, resulting a high Na storage capacity and a good cyclability. On contrary, the (2 × 2) + (1 × 1) two-tunnel structure in α-MnO_2 is not stable, inducing a low capacity and poor cyclability. [920]

9.5 Conclusions

α-MnO_2 and β-MnO_2 nanorods have been synthesized by a hydrothermal method. FESEM and TEM analyses confirmed the nanorod morphology and single crystalline nature of the as-prepared products. When applied as cathode materials in Na-ion batteries, β-MnO_2 nanorods exhibited a much better electrochemical performance than that of α-MnO_2 nanorods, which could be ascribed to the more compact tunnel-structure of β-MnO_2. β-MnO_2 nanorods also demonstrated a good high rate performance and durable cyclability. More specifically, β-MnO_2 nanorods delivered a high reversible Na ion capacity of 298 mA h g^{-1} at 20 mA g^{-1} current density. After 100 cycles, the electrode maintained a capacity of 145 mA h g^{-1}. β-MnO_2 nanorods could be a promising high capacity cathode material for Na-ion batteries.

CHAPTER 10 SnO_2@GRAPHENE NANOCOMPOSITES AS ANODE MATERIALS FOR NA-ION BATTERY

10.1 Abstract

An *In-situ* hydrothermal synthesis approach has been developed to prepare SnO_2@graphene nanocomposites (SnO_2@graphene does mean the SnO_2 particles distribute on the graphene layers). The nanocomposite exhibited a high reversible sodium storage capacity of above 700 mA h g^{-1} and excellent cyclability for Na-ion battery. In particular, it also demonstrated a good high rate capability for reversible sodium storage.

10.2 Introduction

Na-ion batteries are considered to be an alternative to Li-ion batteries owing to natural abundance of sodium.[580] They have emerged as an attractive electrochemical power source for large-scale electrical energy storage (EES).[923-926] Na ion has a larger ionic radius than that of Li ion, making it more difficult to identify suitable electrode materials for Na-ion batteries. Electrode materials with an open framework are required for facile Na ion insertion/extraction. Following this strategy, many breakthroughs on cathode materials have been achieved, such as layered transition metal oxide,[587,589,590,592] three-dimensional $Na_{0.44}MnO_2$ with S-shaped tunnel,[601,913] and prussian blue with a new framework[927]. However, the development of suitable anode materials for Na-ion batteries remains a considerable challenge. It was found that hard carbon is a suitable anode material for Na-ion batteries because it has large interlayer distance and disordered structure.[600] However, Dahn *et al.* reported that the Na-intercalated hard carbon (Na_xC) has high reactivity with the non-aqueous

electrolyte[928], raising new concerns about the stability of the electrolyte when used as a carbon based electrode. Alternative oxide anodes such as $Na_2Ti_3O_7$[929] and amorphous TiO_2-nanotubes[930] have been investigated, but they all show less than 300 mA h g^{-1} capacities, which is far from meeting the demand of high energy storage. Transition metal oxides also did not achieve satisfactory performance,[651] although they have demonstrated excellent electrochemical properties in Li-ion batteries. Recently, it was found that anodes based on Na alloying reaction can dramatically improve the capacity of sodium storage.[672,931] It was reported that SnSb/C nanocomposite achieved 544 mA h g^{-1} capacity, good rate capacity and cyclability for Na-ion storage.[672] And pure micrometric antimony can sustain a capacity close to 600 mA h g^{-1} at a high rate in Na-ion batteries.[20]

SnO_2 also can react with Na based on a reversible Na alloying reaction and generate Na-Sn alloy, which has potential as anode materials for Na-ion batteries. And base on the reaction of $4SnO_2 + 31Na^+ + 31e^- \rightarrow Na_{15}Sn_4 + 8Na_2O$,[18] SnO_2 can achieve as high as 1378 mA h g^{-1} theoretical sodium storage capacity. However, due to the reaction with Na, SnO_2 will be easily met large volume variation and aggregation problems during charging/discharging process. They will cause exfoliation of active materials from the current collector and increase of the ions transport distance in the active materials particles, which lead to electrochemical capacity loss. Therefore, to alleviate the volume expansion and particle aggregation are the critical issues for practical application of this material. Embedding SnO_2 in carbon matrix is no doubt an effective effort. Among various carbon matrixes, graphene has several superiorities: superior conductivity, large surface areas, and excellent mechanical strength. As anode material for Na-ion battery, graphene itself also demonstrated high theoretical sodium storage capacity (744 mA h g^{-1} base on the NaC_3). Still, to

date, there have been no experimental studies on SnO_2/graphene nanocomposites for reversible Na-ion battery. Herein, we report *In-situ* hydrothermal synthesis of SnO_2@graphene nanocomposites, in which SnO_2 nanocrystals are uniformly anchored on graphene nanosheets. The as-prepared SnO_2@Graphene nanocomposite demonstrated a high reversible capacity of over 700 mA h g^{-1} in Na-ion batteries and an excellent cyclability.

10.3 Experiment details

10.3.1 Synthesis

Graphene oxide nanosheets were synthesised from natural graphite powders by a modified Hummer's method.[932] To synthesize bare graphene, the obtained graphene oxide was dispersed in distilled water and then exfoliated to generate graphene oxide nanosheets by ultrasonication using a Brandson Digital Sonifer (S450D, 40 % amplitude). The brown graphene oxide nanosheet dispersion was poured into a round-bottomed flask, to which hydrazine monohydrate (as reducing agent) was added. The mixed solution was then refluxed at 130 °C for 3 h, during which the colour of the solution gradually changed to dark black as the graphene nanosheet dispersion was formed. The bare SnO_2 and SnO_2@graphene nanocomposites were produced via hydrothermal method. In a typical process, 2 mmol $SnCl_2 \cdot 5H_2O$ (Sigma-Aldrich, ≥ 98 %) were dissolved in 20 mL distilled water. Then 0.315 g poly vinyl pyrrolidone (PVP) as surfactant was added. After stirring for at least 20 mins, 0.4 ml 37.5 % H_2SO_4 was added. After stirring for another several minutes, the precursor solution was separated by two parts (10 ml each). One part was added with 10ml GO ethylene glycol (EG) solution (20 g L^{-1}) and was treated by ultrasonic for 30 mins. Then both two mixtures were heated up to 200 °C in the Teflon-lined autoclave (25 mL in capacity)

and maintained at that temperature for 12 h. The precipitates were cooled down to room temperature naturally, collected and washed with distilled water and ethanol several times. After drying at 60 °C in vacuum oven overnight, the final products were obtained.

10.3.2 Structural and physical characterization

The crystal structure and phases of as-prepared materials were characterized by X-ray diffraction (XRD, Siemens D5000) using a Cu Kα radiation at a scanning step of 0.02° sec^{-1}. The morphology was analysed by field emission scanning electron microscope (FESEM, Zeiss Supra 55VP). The crystal structure details were further characterized by transmission electron microscopy (TEM) and high-resolution transmission electron microscopy (HRTEM, JEOL JEM-2011). Selected area electron diffraction (SAED) patterns were recorded by a Gatan CCD camera in a digital format. TGA/DTA was performed to analyse the weight ratio of nanocomposite at a heating rate of 5 °C min^{-1} in air from room temperature to 900 ºC with a 2960 SDT system.

10.3.3 Electrochemical testing

The electrodes were prepared by dispersing the as-prepared material (80 wt %), acetylene carbon black (10 wt %), and poly (Vinylidene fluoride) binder (PVDF, 10 wt %) in N-methyl-2-pyrrolidone (NMP) to form a slurry. The resultant slurry was pasted onto copper foil using a doctor blade and dried in vacuum oven for 12 h, followed by pressing at 200 kg cm^{-2}. Electrochemical measurements were carried out using two-electrode coin cells with Na metal as counter and reference electrodes and the glass microfiber (Whatman) as the separator. The CR2032-type coin cells were assembled in an argon-filled glove box (UniLab, Mbraun, Germany). The electrolyte solution was 1 M $NaClO_4$ dissolved in a mixture of ethylene carbonate (EC) and

propylene carbonate (PC) with a volume ratio of 1:1. Cyclic voltammetry (CV) was conducted on a CHI 660C instrument between 0.01 and 3 V *vs.* Na/Na^+ at room temperature. The charge-discharge measurements were performed at ambient temperature at different current densities in the voltage range from 0.01 to 3 V *vs.* Na/Na^+.

10.4 Results and discussion

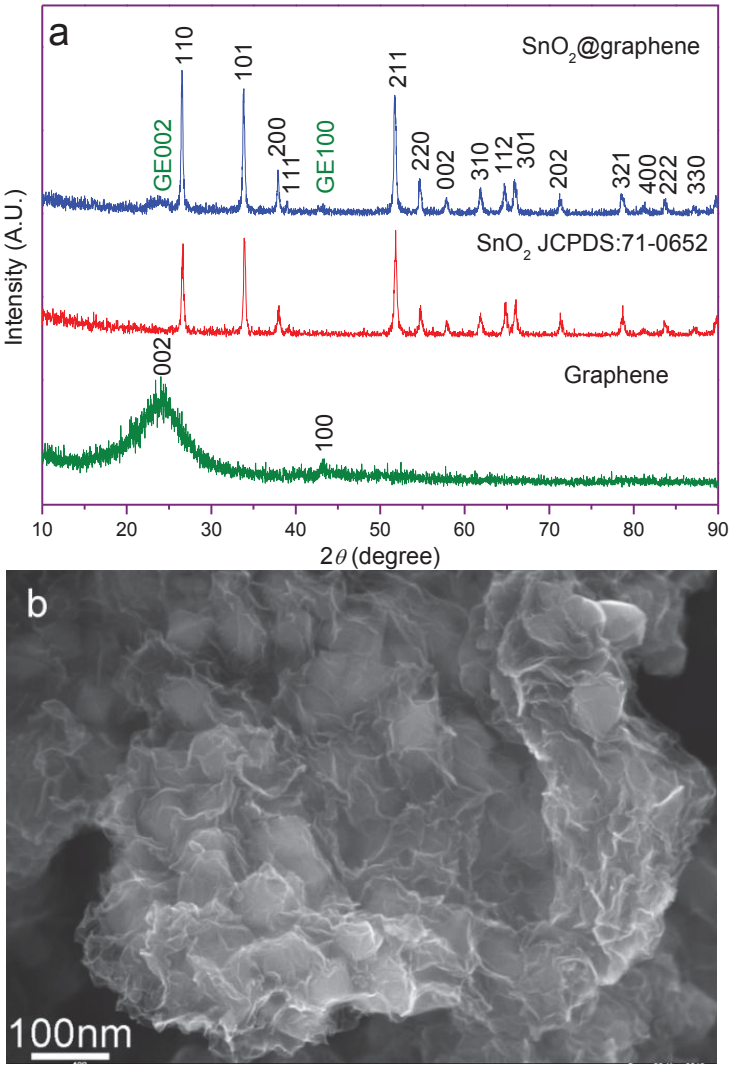

Figure 10-1 (a). XRD patterns of bare graphene, bare SnO_2, and SnO_2@graphene nanocomposite. (b). FESEM image of SnO_2@graphene nanocomposite.

SnO_2@graphene nanocomposites were synthesised by an *In-situ* hydrothermal method. For comparison, bare graphene and SnO_2 nanocrystals were also prepared. Graphene oxide nanosheets were used as the precursor to prepare SnO_2@graphene nanocomposites, which were synthesized from natural graphite powders by a modified Hummer's method.[932] The crystallographic phases of as-prepared materials were identified by XRD (as shown in Figure 10-1a). The bare SnO_2 can be well indexed as tetragonal symmetry unit cell (JCPDS: 71-0652), with the space group of P42/mnm. For SnO_2@graphene nanocomposites, the strong diffraction lines can be indexed to the tetragonal SnO_2 phase and the weak diffraction peaks correspond to graphene (002) and (100) crystal planes, which confirm the co-existence of SnO_2 nanocrystals and graphene nanosheets.

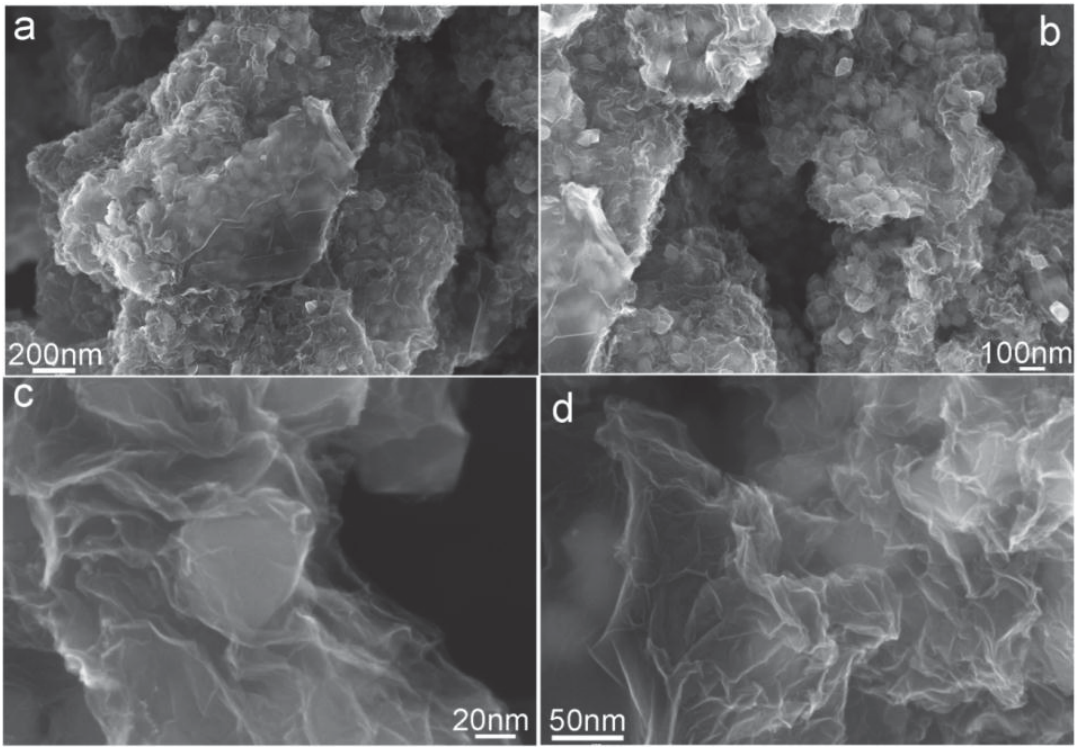

Figure 10-2 a and b are low magnification FESEM images of SnO_2@graphene nanocomposites. c and d are high magnification FESEM images of SnO_2@graphene nanocomposites.

The morphology of SnO_2@graphene nanocomposites was characterised by FESEM. As shown in Figure 10-1b, SnO_2 nanocrystals homogeneously distribute on graphene nanosheets. It should be noted that individual SnO_2 nanocrystals are wrapped with graphene nanosheets. The sizes of SnO_2 nanocrystals are estimated to be about 60 nm. More FESEM images are shown in Figure 10-2, which further depicts the morphological features of SnO_2@graphene nanocomposites.

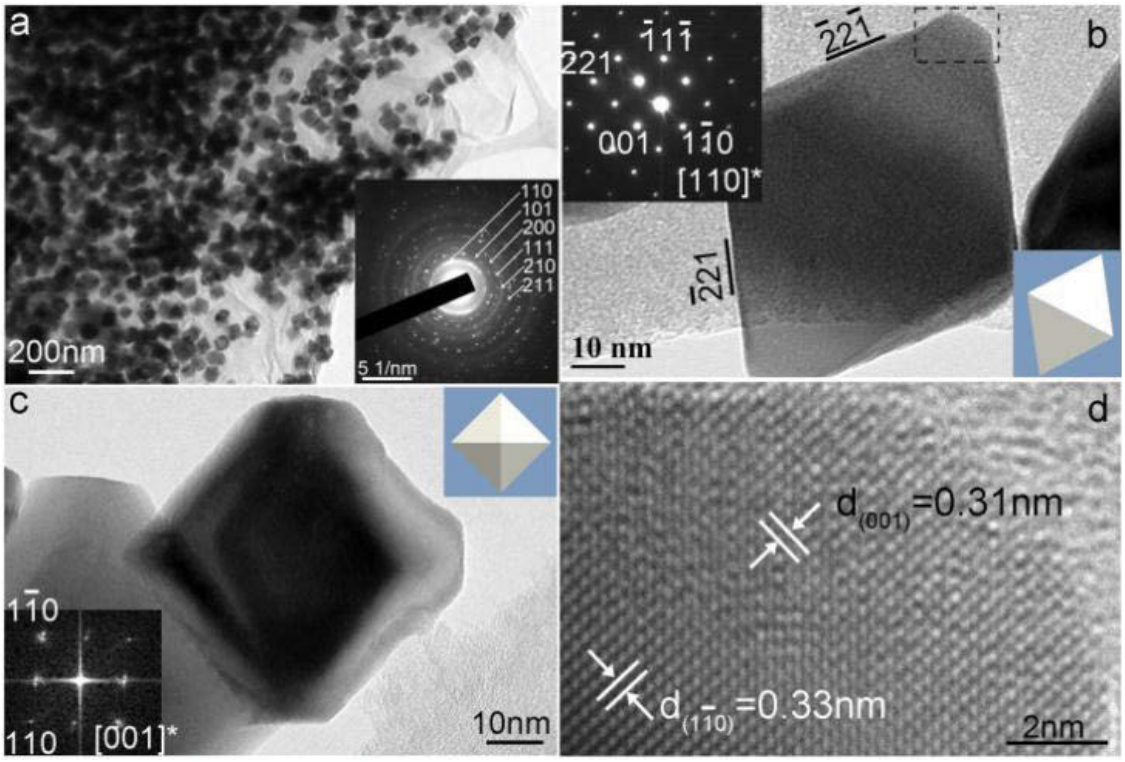

Figure 10-3 (a). Low magnification TEM image of SnO_2@graphene nanocomposites. (b) and (c) are typical TEM images of single octahedral SnO_2 nanocrystals projecting from [110] and [001] directions, respectively. (d) is lattice resolved HRTEM image taken from the rectangular area marked in (b). The inset in (a) is selected area electron diffraction (SAED) pattern. Right bottom inset in (b) and right top inset in (c) are the corresponding geometric models. The left top inset in (b) is the SAED pattern. The left bottom inset in (c) is the Fast-Fourier-Transform (FFT) pattern.

The crystal structure and architectural of SnO_2@graphene nanocomposites were analysed by TEM and HRTEM analysis (as shown in Figure 10-3). Figure 10-3a shows a low magnification TEM image illustrating SnO_2 nanocrystals uniformly anchored on graphene nanosheets. When we analysed individual SnO_2 nanocrystals, we found that SnO_2 nanocrystals have a well–defined octahedral shape with an apex-to-apex length of around 60 nm (Figure 10-3b). The inset (right bottom) in Figure 10-3b illustrates its geometric model, which depict its outline and projected direction. The selected area electron diffraction (SAED) of this nanocrystal is shown as the inset on the left-top corner in Figure 10-3b, which can be well indexed along the [110] zone axis of tetragonal SnO_2. The spot SAED pattern array confirmed the single crystalline nature of SnO_2 nanocrystals. Figure 10-3c shows another typical free-standing octahedral SnO_2 nanocrystal, which was observed from the top view. The corresponding FFT pattern along the [001] zone axis is shown as the inset in Figure 10-3c (left bottom corner), which confirmed the growth of octahedral SnO_2 along the [001] direction. A lattice resolved HRTEM image is shown in Figure 10-3d (recorded from rectangle area marked in Figure 10-3b). The regular arrangement of the (110) crystal planes is clearly visible. The orthogonal (001) and $(1\bar{1}0)$ crystal planes with 0.31 nm and 0.33 nm d-spacings, respectively, have been determined.

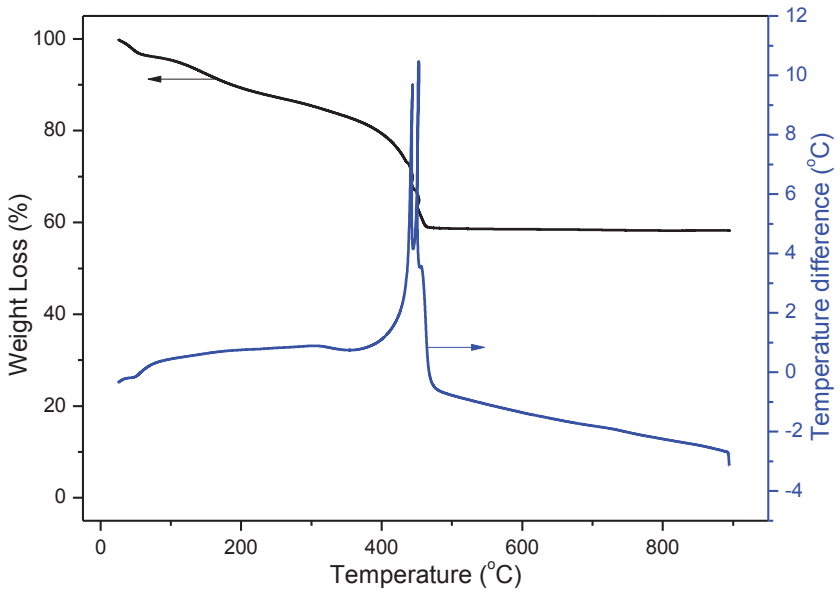

Figure 10-4 TG/DTA curves of SnO_2@graphene nanocomposites.

The weight ratio between SnO_2 nanocrystals and graphene nanosheets was determined to be 60: 40 by TG and DTA measurement (Figure 10-4). The 40 wt % weight loss occurred mainly from 400 to 500 °C with the feature of an endothermic peak at 447 °C, corresponding to the oxidation of carbon.

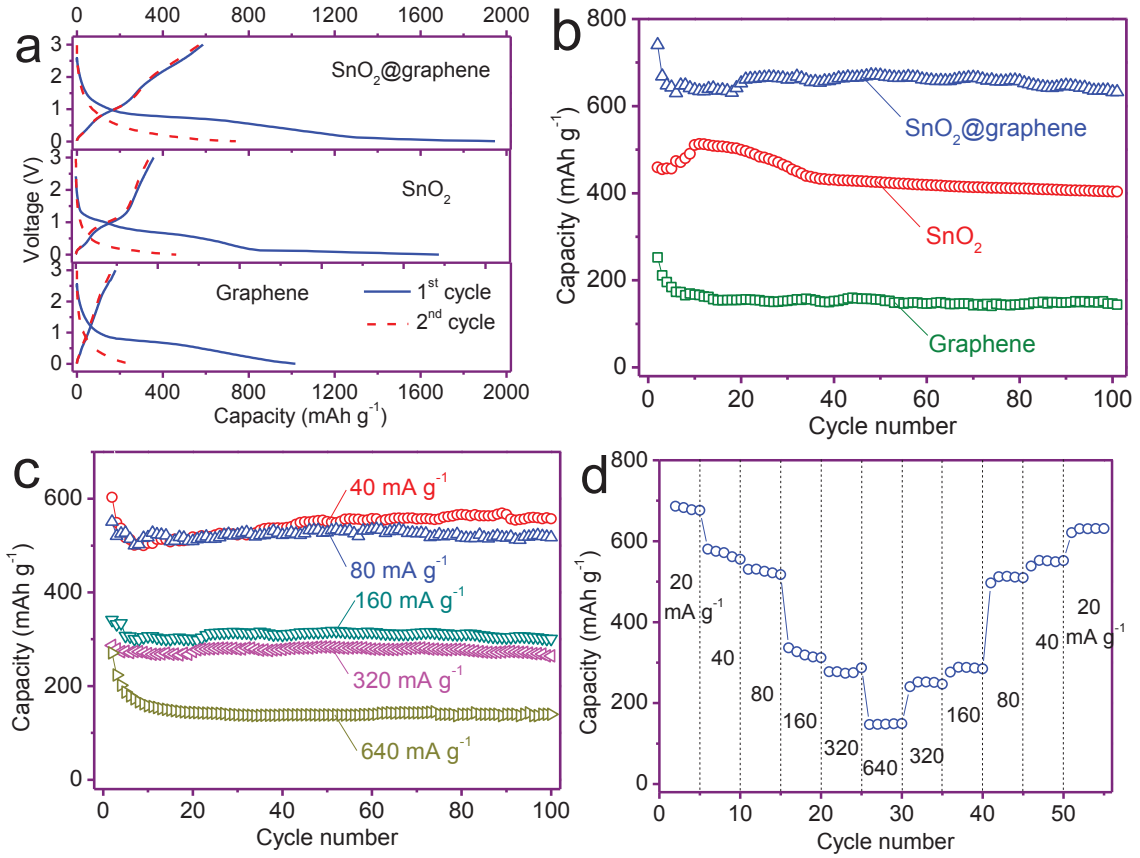

Figure 10-5 (a) 1st and 2nd cycles discharge and charge profiles of bare graphene, bare SnO_2, and SnO_2@graphene nanocomposites at 20 mA g^{-1} current density. (b) Cycling performance of bare graphene, bare SnO_2, and SnO_2@graphene nanocomposites at 20 mA g^{-1} current density. (c) Cycling performance of SnO_2@graphene nanocomposites at current densities of 40, 80, 160, 320, and 640 mA g^{-1}. (d) The rate performance of SnO_2@graphene nanocomposites at varied current densities. (b-d) are recorded from the 2nd cycle.

Applied as anode materials in Na-ion batteries, electrochemical performances of bare graphene, bare SnO_2, and SnO_2@graphene nanocomposites are shown in Figure 10-5. They exhibit different discharge/charge profiles in the first and second cycles (Figure 10-5a). For bare graphene nanosheets, the specific discharge capacity is 1009 mA h g^{-1} in the first cycle. It dramatically dropped to 237 mA h g^{-1} in the

second cycle. Bare SnO_2 nanocrystals delivered 1773 and 473 mA h g^{-1} discharge capacities in the first and the second cycles, respectively, while SnO_2@graphene nanocomposites demonstrate the highest initial discharge capacity of 1942 mA h g^{-1}. After the first cycle, a capacity of 741 mA h g^{-1} was maintained. Similar to Li-ion batteries, the irreversible capacity in the first cycle could be consumed to form the solid electrolyte interface (SEI) layer on the surface of the electrode. From the second cycle, Na storage capacities of all tested electrodes had stabilised (as shown in Figure 10-5b). SnO_2@graphene nanocomposites delivered an average of more than 700 mA h g^{-1} capacity in 100 cycles. The value is much higher than that of bare SnO_2 nanocrystals and bare graphene nanosheets. In particular, SnO_2@graphene nanocomposites demonstrated an excellent capacity retention capability with almost no capacity fading within 100 cycles. This evidenced in Na storage capacity reaching 638 mA h g^{-1} after 100 cycles for SnO_2@graphene nanocomposite anode. The discharge/charge profiles of SnO_2@graphene nanocomposites in the 5^{th}, 20^{th} and 100^{th} cycles test at 40 mA g^{-1} current density are shown in Figure 10-6. The overlapped curves indicate the stable nature and excellent cyclability of the electrode.

Figure 10-5c shows the cycling performance of SnO_2@graphene nanocomposite electrodes at different current densities (from the second cycle). The nanocomposite exhibited decent high rate performance. After 100 cycles, the discharge capacities were maintained at high values when cycled at different current densities: 569 mA h g^{-1} at 40 mA g^{-1}, 508 mA h g^{-1} at 80 mA g^{-1}, 302 mA h g^{-1} at 160 mA g^{-1} and 263 mA g^{-1} at 320 mA g^{-1}. Even cycled at 640 mA g^{-1}, a discharge capacity of 143 mA h g^{-1} was still obtained after 100 cycles.

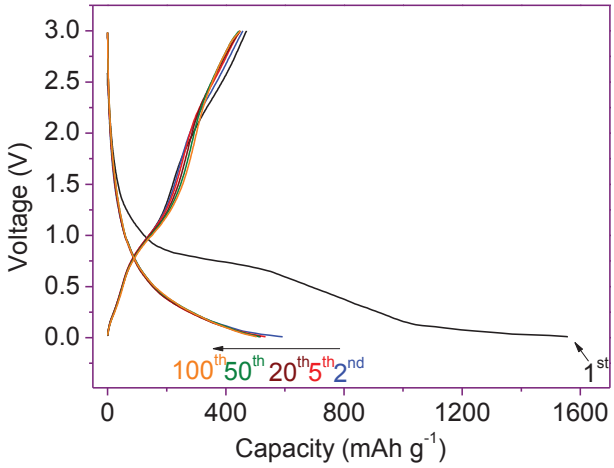

Figure 10-6 The 1st, 2nd 5th, 20th, 50th, and 100th cycles discharge and charge profiles of SnO_2@graphene nanocomposites at 40 mA g^{-1}.

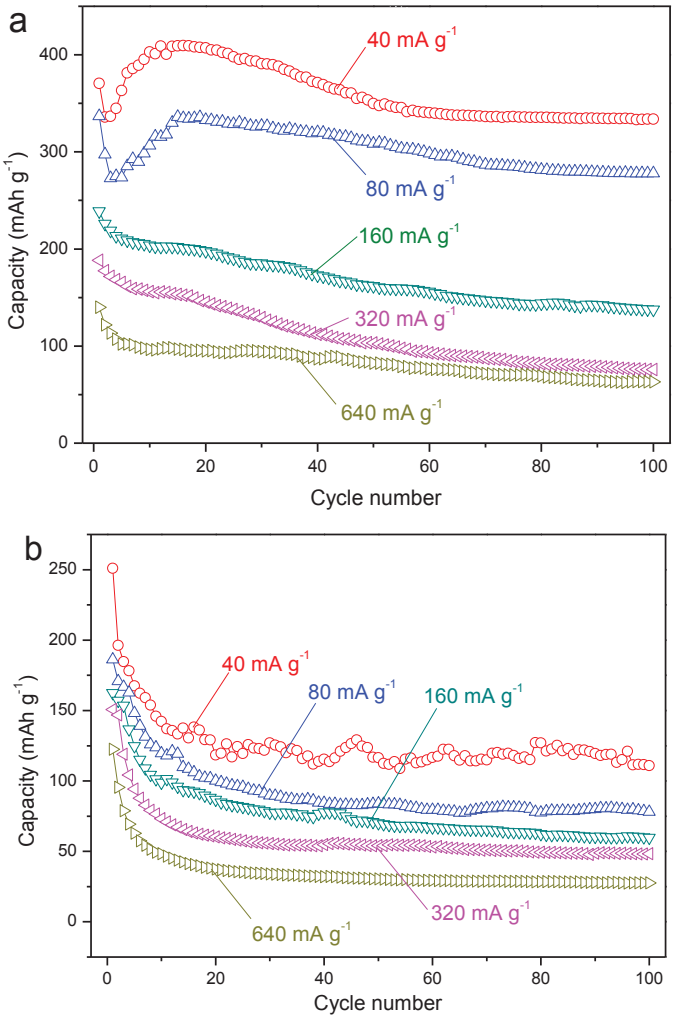

Figure 10-7 Cycling performance of bare SnO_2 (a) and graphene (b) at current densities of 40, 80, 160, 320, and 640 mA g^{-1},which are recorded from the 2nd cycle.

The high rate performance of SnO_2@graphene nanocomposites is much better than that of bare SnO_2, graphene electrodes (Figure 10-7) and previously reported anode materials for Na-ion batteries.[653,654,929,930] We also tested the cycling performance of SnO_2@graphene nanocomposites at varied current densities (Figure 10-5d). After cycling at high current densities, the cell capacity can recover to the original values as long as the current density reversed back to low current density. This confirmed that SnO_2@graphene nanocomposites are tolerant to high rate cycling.

The outstanding performance of SnO_2@graphene nanocomposites could be ascribed to the unique 3D architecture of the material. During the discharge and charge process, Na ions reversibly react with SnO_2 to form Na_xSn and Na_2O[672,933-936]:

$$(4+x)Na^+ + SnO_2 + (4+x)e^- \leftrightarrow Na_xSn + 2Na_2O \qquad (10\text{-}1)$$

This process usually accompanies large volume change. As illustrated by FESEM and TEM characterisation, individual SnO_2 nanocrystals are embedded and wrapped by flexible and conductive graphene nanosheets.

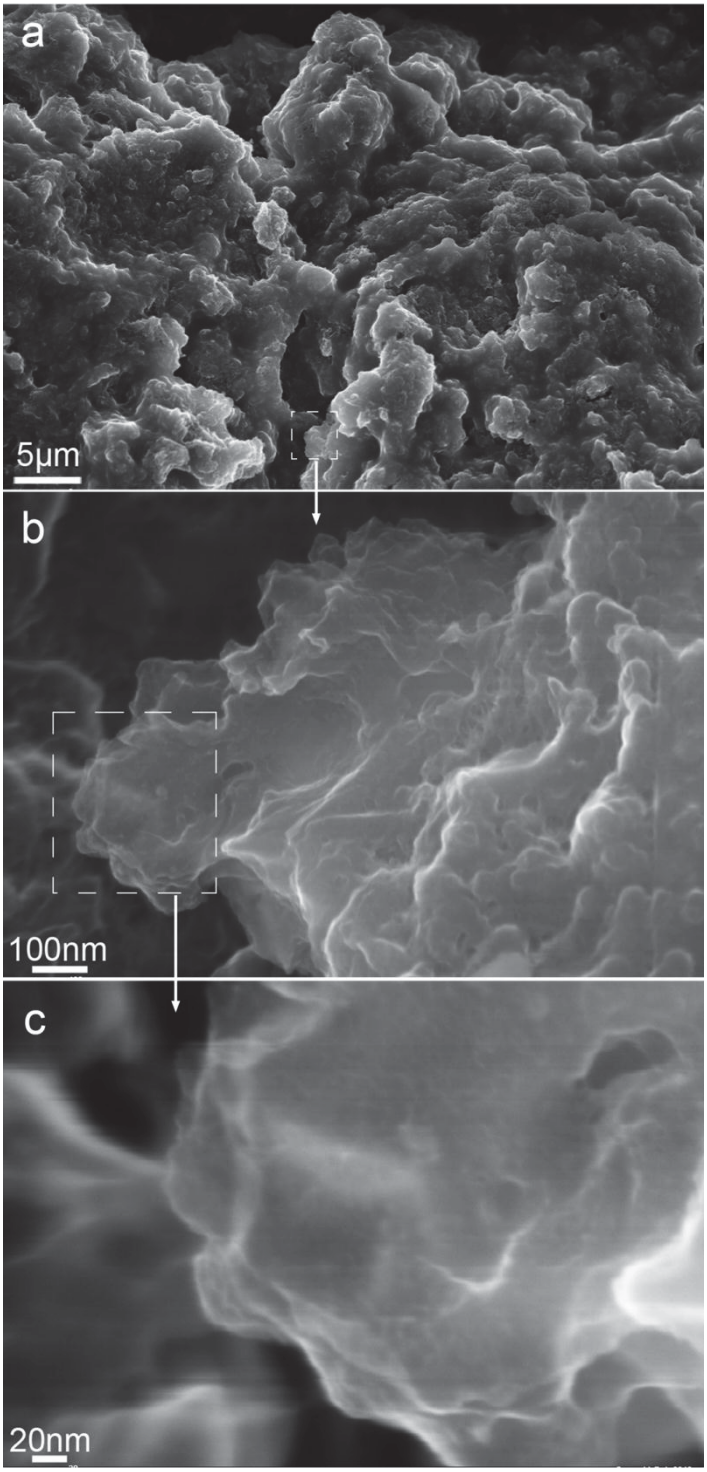

Figure 10-8 (a) Low magnification, (b) medium magnification, and (c) high magnification SEM images of SnO_2@graphene nanocomposites electrodes taken from fully charged state at 20 mA g^{-1} current rate after 100 cycles.

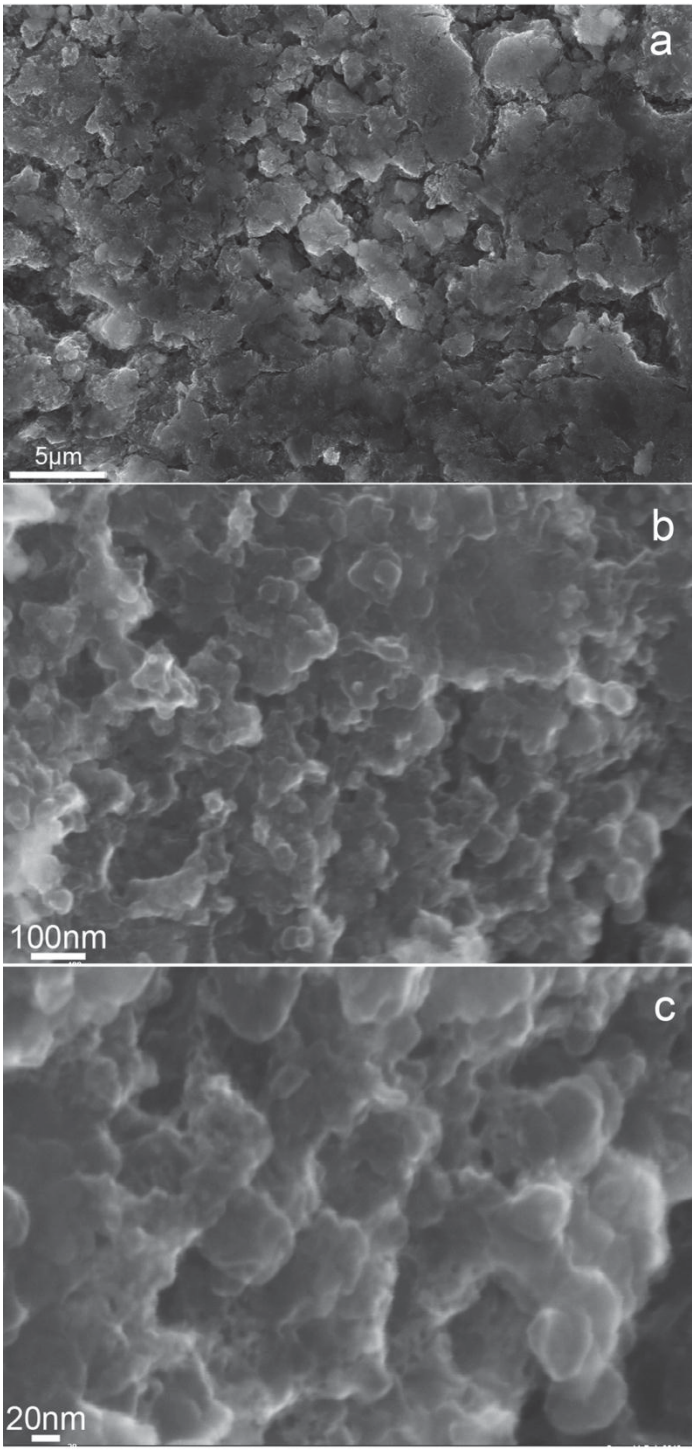

Figure 10-9 (a) Low magnification, (b) medium magnification, and (c) high magnification SEM images of bare SnO_2 nanoparticles electrodes taken from fully charged state at 20 mA g^{-1} current rate after 100 cycles.

The cycled SnO_2/graphene electrodes were further examined by *Ex-situ* SEM as

shown in Figure 10-8, from which we can observe that after 100 cycles, graphene still preserve their original morphology, while SnO_2 lost their octahedral architecture and disintegrated into less than 5 nm nanoparticles (Figure 10-8 c) due to the reaction with Na ions. In addition, the SnO_2 nanoparticles uniformly distribute in the graphene matrix. While along with cycling process, the bare SnO_2 electrodes were easily aggregated together inducing cracking and crumbling of the structure, and capacity loss (Figure 10-9). The graphene matrix can effectively buffer the volume variation during the Na insertion and extraction process. Furthermore, graphene nanosheets also serve as conductive media for electron transfer during the discharge and charge process. As a result, the integrity of the electrode can be maintained, leading to an enhanced performance for Na storage.

10.5 Conclusion

In conclusion, SnO_2@graphene nanocomposites with 3D architecture were synthesized by an *In-situ* hydrothermal method. Homogeneous distribution of SnO_2 nanocrystals on graphene nanosheets has been confirmed by FESEM and TEM characterisation. HRTEM analysis identified that SnO_2 nanocrystals (~ 60 nm in size) have an octahedral shape. Galvanostatic charge-discharge measurements show the highly reactive nature of SnO_2@graphene nanocomposites towards sodium storage in Na-ion cells. It demonstrated a high reversible specific capacity of above 700 mA h g^{-1}, excellent cyclability, and decent high rate performance, which could be ascribed to the unique 3D architecture of the nanocomposite. SnO_2@graphene nanocomposites could be a promising high performance anode material for Na-ion batteries.

CHAPTER 11 CONCLUSION AND OUTLOOK

11.1 General Conclusion

The aim of this doctoral work was to explore the relationship between designed nanostructure materials and their electrochemical performance for Li-ion batteries and Na-ion batteries, by means of theoretical calculation, structural, physical, and electrochemical characterization techniques. As-prepared nanocomposite materials show several of advantages as electrode materials for Li-ion battery and Na-ion battery, which benefit from the high surface area, improving the accessibility of electrolyte, shorting the diffusion length of ions (Li^+ or Na^+), or the high surface energy, enhancing the reactivity towards the conversion reaction between the as-prepared material and Li^+ ions.

The conductive composite materials (SnO_2@graphene) are improved with enhanced electron transport within the electrode, facilitating the achievement of high rate capability. In addition, the composite also buffers the volume change to improve the cycle life. Following are the summary of the outcomes.

11.1.1 Ab initio calculations on structural and electrochemical properties of Li_2FeSiO_4 cathode material for Li-ion batteries

The crystal and electronic structures of Li_2FeSiO_4 and its delithiated phases, $LiFeSiO_4$ and $FeSiO_4$, which are based on a monoclinic super cell with $P2_1$ symmetry, have been systematically researched according to the DFT calculation. It was found that 11.5 % expansions of the unit cell volume occur for the first lithium extraction and 9.2 % expansions happen for the second lithium extraction because of the increased Fe-O-Si bond angle and a weakened attraction between Li ions and the

FeO_4 and SiO_4 tetrahedrons during the delithiation process. This suggests possible structural instability and inferior cyclability of Li_2FeSiO_4 cathode materials. Based on the calculation of lithium intercalation voltage, 3.10 V and 4.16 V for Fe^{+2}/Fe^{+3} and Fe^{+3}/Fe^{+4} redox couples, respectively were successfully anticipated. Further density of states (DOS) and partial density of states (PDOS) calculation results indicate that the electron transfer mainly occurs in Fe atoms during the lithium extraction and insertion process. According to the activation barriers of Li ion vacancy using the Nudged Elastic Band (NEB) method, it was identified that the Li ion diffusion process in all main crystallographic directions in Li_2FeSiO_4 and $LiFeSiO_4$ is slightly anisotropic. The lowest migration energy was achieved along the [101] direction and a zigzag trajectory in the ac plane determined. Within these two diffusion pathways, well-defined Li ionic conduction can be maintained. Furthermore, differential cation exchange between Li and Fe will generate a contrast effect: Li on Fe site defects could facilitate long-range Li diffusion, while Fe on Li sites would impede Li diffusion due to the high migration barrier energies (1.32 eV). The results indicate that Li_2FeSiO_4 with the $P2_1$ symmetry is an good ionic conductor for Li ions with two-dimensional diffusion.

11.1.2 Nanostructure Iron oxide (hematite and magnetite) as Anode Materials for Li-ion batteries

Uniform peanuts shaped porous α-Fe_2O_3 was successfully synthesised by the hydrothermal method. Through further control of the oxalic acid etching process at room temperature, the total pore volume and average pore size of the as-prepared α-Fe_2O_3 were readily tuned. When worked as anode materials for Li-ion batteries, all etched or pristine porous α-Fe_2O_3 exhibited high lithium storage capacity and acceptable

capacity retention ability. In addition, etched α-Fe_2O_3 electrode presented a higher capacity, rate performance and tolerance towards the varied charge/discharge current density than the pristine peanut shaped porous α-Fe_2O_3. After 50 cycles, the electrode maintained a high capacity of 1094 mA h g^{-1} for 5.5 h etched porous α-Fe_2O_3 at 50 mA g^{-1} current density. The higher surface area of as-prepared α-Fe_2O_3 can provide high surface contact with the electrolyte and decreases the current density per unit area. The porous structure can accommodate the volume change of the Li^+ ion insertion/extraction during the charge-discharge process, which can prevent the active materials falling off the current collector.

Polyhedral magnetite nanocrystals with multiple facets have been researched by combining experimental and computational methods. The multiple facets, including (100), (010), (001), (110), (101), (011) and (111), exposed by the as-prepared magnetite were systematically predicted by DFT calculation and characterised by XRD, FESEM, TEM and HRTEM analysis. Their optical and magnetic properties were studied, which demonstrated surface dependent features. When applied as anode material in lithium ion cells, the as-prepared polyhedral Fe_3O_4 nanocrystals demonstrated a high lithium storage capacity and a satisfactory cycling performance. In particular, they show the tolerance towards charge and discharge at high current densities. At the high current of 1000 mA g^{-1}, the electrode can still deliver a specific capacity of 700 mA h g^{-1} in the first cycle and maintain the capacity satisfactorily within the subsequence cycles. The improved electrochemical performance should be ascribed to the nanoparticle, which can benefit the accessibility of electrolyte, and shorten the diffusion length of Li ions.

Through a simple hydrothermal route, one-dimensional magnetite nanowires were synthesized. As characterised by XRD, FESEM, TEM and HRTEM, it was confirmed the as-prepared Fe_3O_4 nanowires were confirmed to be single crystals that grew along a

uniform preferred direction. The one-dimension structure shortens the diffusion length of Li ions and increase the electron conductivity, allowing it to maintain a discharge capacity of 900 mA h g^{-1} at the current density of 50 mA g^{-1} after 50 cycles. A high initial discharge capacity (1868 mA h g^{-1}) and good capacity retention was still obtained even when current density was increased to 500 mA g^{-1}.

11.1.3 Nanostructure Nickel oxide as Anode Materials for Li-ion batteries

One-dimensional mesoporous nickel oxide nanowires were successfully synthesised by a hydrothermal reaction and subsequent annealing at 400 °C in air. FESEM and HRTEM demonstrated individual NiO nanowire consisted of aggregated nanocrystals, and N_2 sorption analysis revealed its mesoporous feature, inducing a high specific surface area. As measured by the galvanostatic charge/discharge, as-prepared NiO nanowires electrode can deliver 1280 mA h g^{-1} capacity after 100 cycles at 100 mA g^{-1} current density. Mesoporous NiO nanowires demonstrated a high specific capacitance of 348 F g^{-1} as electrode for supercapacitors. The outstanding electrochemical performance is due to the unique advantages of one-dimension architecture and mesoporous structure, such as short pathways for Li ions diffusion, high contact area of electrode/electrolyte and tolerance on the volume change.

Furthermore, mesoporous faceted NiO crystals were synthesised from annealing $Ni(OH)_2$ treatment. TEM analysis identified that NiO crystals had dominantly {110} exposed crystal planes and mesoporous architecture. When applied as anode materials in lithium ion cells, they can deliver a high reversible lithium storage capacity of around 700 mA h g^{-1} in 100 cycles with high Coulombic efficiency at 1 C current rate. The materials also demonstrated an outstanding high rate performance, which mimics supercapacitors for high power delivery. At 40 C, it can obtain 322 mA h g^{-1} capacity

after 1000 cycles. As revealed by the theoretical calculation, {110} facets of NiO have much higher surface energy, which can profit the conversion reaction between the Li ions and NiO, and contributes the high rate performance. *Ex-situ* TEM characterisation clearly illustrated that the mesporous and faceted crystal structure had been retained after long term discharge/charge cycling even at high current rates.

11.1.4 Polymorphs MnO_2 Nanorods as Cathode for Na-ion batteries

α-MnO_2 and β-MnO_2 nanorods have been synthesized by a hydrothermal method. Through the TEM analyses, the nanorod morphology, single crystalline nature, growth habit, and exposed crystal planes were all identified. When applied as cathode materials in Na-ion batteries, both α- and β-MnO_2 nanorods exhibited a high initial discharge capacity (278 mA h g^{-1} and 298 mA h g^{-1}, respectively, at 20 mA g^{-1} current density). β-MnO_2 demonstrated much better capacity retention ability, after 100 cycles, the β-MnO_2 electrode maintained a capacity of 145 mA h g^{-1}. When β-MnO_2 nanorods were tested at high current density, they also showed well-defined capability and cyclability. The satisfactory electrochemical property of β-MnO_2 could be ascribed to the more compact one dimension tunnel-structure, which can facilitate regular intercalation of Na ions during the charge and discharge process. Based on this research, β-MnO_2 nanorods are a promising high capacity cathode material for Na-ion batteries.

11.1.5 SnO_2@graphene Nanocomposites as Anode Materials for Na-ion Battery

As the anode material for the Na-ion batteries, SnO_2@graphene nanocomposites with 3D architecture were synthesized by an *In-situ* hydrothermal method. Homogeneous distribution of octahedral SnO_2 nanocrystals with ~ 60 nm size on

graphene nanosheets were confirmed by FESEM and TEM characterisation. Galvanostatic charge-discharge measurements show the highly reactive nature of SnO_2@graphene nanocomposites towards sodium storage in Na-ion batteries. SnO_2@graphene nanocomposites delivered an average of more than 700 mA h g^{-1} capacity in 100 cycles at 20 mA g^{-1} current density. In particular, they demonstrated an excellent capacity retention capability with almost no capacity fading within 100 cycles (638 mA h g^{-1} after 100 cycles). It was proposed that the excellent cyclability and decent high rate performance could be ascribed to the unique 3D architecture of the nanocomposite. In addition, the graphene matrix, has superior conductivity, large surface areas, and excellent mechanical strength, which can buffer the electrode volume change generated by the expansion and contraction during Na insertion and extraction process. Furthermore, the SnO_2 react with Na based on the alloy reaction is a reversible process which can profit the cyclability also.

11.2 Outlook

The main method and design strategy of synthesising nanostructure electrode material presented here can be extended to the preparation of other analogue cathode or anode materials for both Li-ion batteries and Na-ion batteries. At the same time, many aspects which might affect the electrochemical properties of as-prepared active materials were not evaluated due to the limitation of doctoral duration. Therefore, further research is needed to deeply characterise the relationship between the materials structure and the electrochemcial performance, particularly in relation to factors related to the improvement of capacity (the majority electrode materials cannot achieve their theoretical capacity) and cycliablity.

Although the theoretical calculation based on the DFT method, proved that lithium iron silicate with the $P2_1$ symmetry is an ionic conductor for Li ions with two-dimensional diffusion, and it presents a potential low-cost and environment friendly cathode materials candidate for the Li-ion batteries, the practical synthesis procedure remains a challenge. So far, few convenient methods can successfully prepare the Li_2FeSiO_4 with the $P2_1$ symmetry due to the existence of other polymorphs. Therefore, obtaining a Li_2FeSiO_4 that exhibits its theoretical capacity is critical for the commercialisation of this material.

In addition, the facet dependent properties of the nano electrode materials have been discussed preliminary in this doctoral work. The facet effect is a crucial for the electrochemical performance and greater understanding of this mechanism is essential for fulfilling the potential of the nanomaterials serving as a portable battery or the EVs and HEVs. Alougth it has been studied from a theoretical aspect, the difficulty of direct observation places theories in the black box. A combination of the computational and experimental studies will allow the whole process to be elucidated efficiently.

Moreover, as discussed in this doctoral work, Na-ion batteries are emerging in importance due to abundant raw materials compared with its counterpart Li-ion batteries. Of course, some disadvantages relating to larger ionic diameter and higher ionization potential of the Na limit the practical development of Na-ion batteries. The larger ionic radius presents a steric limitation in numerous host structures that are suitable for the Li-ion batteries, leading to a higher volume expansion upon cycling. Consequently, finding and optimising suitable electrode materials for the application of Na-ion batteries is a meaningful pursuit. Basic research on appropriate

active materials with sufficiently large interstitial space within their crystallographic structure to host Na ions, or development of some other material based on the conversion reaction or alloying-de-alloying mechanisms are main steps to achieve optimal electrochemical performance.

REFERENCES

(1) Etacheri, V.; Marom, R.; Elazari, R.; Salitra, G.; Aurbach, D. *Energy & Environmental Science* **2011**, *4*, 3243.

(2) Thackeray, M.; Johnson, P.; De Picciotto, L.; Bruce, P.; Goodenough, J. *Materials Research Bulletin* **1984**, *19*, 179.

(3) Ohzuku, T.; Kitagawa, M.; Hirai, T. *Journal of the Electrochemical Society* **1990**, *137*, 769.

(4) Tarascon, J.; Guyomard, D. *Electrochimica Acta* **1993**, *38*, 1221.

(5) Poizot, P.; Laruelle, S.; Grugeon, S.; Dupont, L.; Tarascon, J. M. *Nature* **2000**, *407*, 496.

(6) Wang, X.; Yang, Z.; Sun, X.; Li, X.; Wang, D.; Wang, P.; He, D. *Journal of Materials Chemistry* **2011**, *21*, 9988.

(7) Needham, S. A.; Wang, G. X.; Liu, H. K. *Journal of Power Sources* **2006**, *159*, 254.

(8) Wu, M.-S.; Lin, Y.-P. *Electrochimica Acta* **2011**, *56*, 2068.

(9) Su, D.; Kim, H.-S.; Kim, W.-S.; Wang, G. *Chemistry-a European Journal* **2012**, *18*, 8224.

(10) Xia, Y.; Zhang, W.; Xiao, Z.; Huang, H.; Zeng, H.; Chen, X.; Chen, F.; Gan, Y.; Tao, X. *Journal of Materials Chemistry* **2012**, *22*, 9209.

(11) Chen, Z.; Xiao, A.; Chen, Y.; Zuo, C.; Zhou, S.; Li, L. *Materials Research Bulletin* **2012**, *47*, 1987.

(12) Chen, X.; Zhang, N.; Sun, K. *Electrochemistry Communications* **2012**, *20*, 137.

(13) Liu, H.; Wang, G. X.; Liu, J.; Qiao, S. Z.; Ahn, H. J. *Journal of Materials Chemistry* **2011**, *21*, 3046.

(14) Ellis, B.; Makahnouk, W.; Makimura, Y.; Toghill, K.; Nazar, L. *Nature Materials* **2007**, *6*, 749.

(15) Palomares, V.; Serras, P.; Villaluenga, I.; Hueso, K. B.; Carretero-González, J.; Rojo, T. *Energy & Environmental Science* **2012**, *5*, 5884.

(16) Wadia, C.; Albertus, P.; Srinivasan, V. *Journal of Power Sources* **2011**, *196*, 1593.

(17) Ellis, B.; Ramesh, T.; Rowan-Weetaluktuk, W.; Ryan, D.; Nazar, L. *Journal of Materials Chemistry* **2012**, *22*, 4759.

(18) Tarascon, J.-M. *Nature Chemistry* **2010**, *2*, 510.

(19) Tarascon, J.-M. *Philosophical Transactions of the Royal Society A: Mathematical, Physical and Engineering Sciences* **2010**, *368*, 3227.

(20) Ong, S. P.; Chevrier, V. L.; Hautier, G.; Jain, A.; Moore, C.; Kim, S.; Ma, X.; Ceder, G. *Energy & Environmental Science* **2011**, *4*, 3680.

(21) Cao, Y.; Xiao, L.; Sushko, M. L.; Wang, W.; Schwenzer, B.; Xiao, J.; Nie, Z.; Saraf, L. V.; Yang, Z.; Liu, J. *Nano Letters* **2012**, *12*, 3783.

(22) Bruce, P. G.; Scrosati, B.; Tarascon, J. M. *Angewandte Chemie-International Edition* **2008**, *47*, 2930.

(23) Lee, H.; Cho, J. *Nano Letters* **2007**, *7*, 2638.

(24) Kim, M. G.; Jo, M.; Hong, Y. S.; Cho, J. *Chemical Communications* **2009**, 218.

(25) Kang, B.; Ceder, G. *Nature* **2009**, *458*, 190.

(26) Bates, J. B.; Dudney, N. J.; Neudecker, B. J.; Hart, F. X.; Jun, H. P.; Hackney, S. A. *Journal of the Electrochemical Society* **2000**, *147*, 59.

(27) Islam, M. S.; Driscoll, D. J.; Fisher, C. A. J.; Slater, P. R. *Chemistry of Materials* **2005**, *17*, 5085.

(28) Morgan, D.; Van der Ven, A.; Ceder, G. *Electrochemical and Solid State Letters* **2004**, *7*, A30.

(29) Chen, G. Y.; Song, X. Y.; Richardson, T. J. *Electrochemical and Solid State Letters* **2006**, *9*, A295.

(30) Kang, K.; Morgan, D.; Ceder, G. *Physical Review B* **2009**, *79*.

(31) Wei, G.-Z.; Lu, X.; Ke, F.-S.; Huang, L.; Li, J.-T.; Wang, Z.-X.; Zhou, Z.-Y.; Sun, S.-G. *Advanced Materials* **2010**, *22*, 4364.

(32) Armand, M.; Tarascon, J. M. *Nature* **2008**, *451*, 652.

(33) Goodenough, J. B.; Kim, Y. *Chemistry of Materials* **2010**, *22*, 587.

(34) Hayashi, K.; Nemoto, Y.; Tobishima, S.-i.; Yamaki, J.-i. *Electrochimica Acta* **1999**, *44*, 2337.

(35) Zhang, X.; Kostecki, R.; Richardson, T. J.; Pugh, J. K.; Ross, P. N. *Journal of the Electrochemical Society* **2001**, *148*, A1341.

(36) Egashira, M.; Takahashi, H.; Okada, S.; Yamaki, J.-i. *Journal of Power Sources* **2001**, *92*, 267.

(37) Garcia, B.; Lavallée, S.; Perron, G.; Michot, C.; Armand, M. *Electrochimica Acta* **2004**, *49*, 4583.

(38) Markevich, E.; Baranchugov, V.; Aurbach, D. *Electrochemistry Communications* **2006**, *8*, 1331.

(39) Nishimoto, A.; Watanabe, M.; Ikeda, Y.; Kohjiya, S. *Electrochimica Acta* **1998**, *43*, 1177.

(40) Croce, F.; Curini, R.; Martinelli, A.; Persi, L.; Ronci, F.; Scrosati, B.; Caminiti, R. *The Journal of Physical Chemistry B* **1999**, *103*, 10632.

(41) Pradel, A.; Ribes, M. *Materials Chemistry and Physics* **1989**, *23*, 121.

(42) Minami, T.; Hayashi, A.; Tatsumisago, M. *Solid State Ionics* **2006**, *177*, 2715.

(43) Jörissen, L.; Gogel, V.; Kerres, J.; Garche, J. *Journal of Power Sources* **2002**, *105*, 267.

(44) Appetecchi, G. B.; Croce, F.; Marassi, R.; Persi, L.; Romagnoli, P.; Scrosati, B. *Electrochimica Acta* **1999**, *45*, 23.

(45) Persi, L.; Croce, F.; Scrosati, B. *Electrochemistry Communications* **2002**, *4*, 92.

(46) Ye, H.; Huang, J.; Xu, J. J.; Khalfan, A.; Greenbaum, S. G. *Journal of the Electrochemical Society* **2007**, *154*, A1048.

(47) Sirisopanaporn, C.; Fernicola, A.; Scrosati, B. *Journal of Power Sources* **2009**, *186*, 490.

(48) Nagata, K.; Nanno, T. *Journal of Power Sources* **2007**, *174*, 832.

(49) Cho, J.; Liu, M. *Electrochimica Acta* **1997**, *42*, 1481.

(50) Imhof, R.; Novák, P. *Journal of the Electrochemical Society* **1999**, *146*, 1702.

(51) Fuller, J.; Carlin, R. T.; Osteryoung, R. A. *Journal of the Electrochemical Society* **1997**, *144*, 3881.

(52) Fong, R.; von Sacken, U.; Dahn, J. R. *Journal of the Electrochemical Society* **1990**, *137*, 2009.

(53) Yazami, R. *Electrochimica Acta* **1999**, *45*, 87.

(54) Vogdanis, L.; Martens, B.; Uchtmann, H.; Hensel, F.; Heitz, W. *Die Makromolekulare Chemie* **1990**, *191*, 465.

(55) Sloop, S. E.; Pugh, J. K.; Wang, S.; Kerr, J. B.; Kinoshita, K. *Electrochemical and Solid-State Letters* **2001**, *4*, A42.

(56) Jow, T. R.; Ding, M. S.; Xu, K.; Zhang, S. S.; Allen, J. L.; Amine, K.; Henriksen, G. L. *Journal of Power Sources* **2003**, *119–121*, 343.

(57) Wang, Y.; Zaghib, K.; Guerfi, A.; Bazito, F. F. C.; Torresi, R. M.; Dahn, J. R. *Electrochimica Acta* **2007**, *52*, 6346.

(58) Koch, V. R.; Dominey, L. A.; Nanjundiah, C.; Ondrechen, M. J. *Journal of the Electrochemical Society* **1996**, *143*, 798.

(59) Baranchugov, V.; Markevich, E.; Pollak, E.; Salitra, G.; Aurbach, D. *Electrochemistry Communications* **2007**, *9*, 796.

(60) Diaw, M.; Chagnes, A.; Carré, B.; Willmann, P.; Lemordant, D. *Journal of Power Sources* **2005**, *146*, 682.

(61) Kim, G. T.; Jeong, S. S.; Xue, M. Z.; Balducci, A.; Winter, M.; Passerini, S.; Alessandrini, F.; Appetecchi, G. B. *Journal of Power Sources* **2012**, *199*, 239.

(62) Markevich, E.; Baranchugov, V.; Salitra, G.; Aurbach, D.; Schmidt, M. A. *Journal of the Electrochemical Society* **2008**, *155*, A132.

(63) Markevich, E.; Sharabi, R.; Borgel, V.; Gottlieb, H.; Salitra, G.; Aurbach, D.; Semrau, G.; Schmidt, M. A. *Electrochimica Acta* **2010**, *55*, 2687.

(64) Groult, H.; Nakajima, T.; Perrigaud, L.; Ohzawa, Y.; Yashiro, H.; Komaba, S.; Kumagai, N. *Journal of Fluorine Chemistry* **2005**, *126*, 1111.

(65) Stassen, I.; Hambitzer, G. *Journal of Power Sources* **2002**, *105*, 145.

(66) Adachi, G.-y.; Imanaka, N.; Aono, H. *Advanced Materials* **1996**, *8*, 127.

(67) Kim, Y.; Saienga, J.; Martin, S. W. *The Journal of Physical Chemistry B* **2006**, *110*, 16318.

(68) Machida, N.; Maeda, H.; Peng, H.; Shigematsu, T. *Journal of the Electrochemical Society* **2002**, *149*, A688.

(69) Takada, K.; Aotani, N.; Kondo, S. *Journal of Power Sources* **1993**, *43*, 135.

(70) Schoonman, J. *Solid State Ionics* **2000**, *135*, 5.

(71) Feuillade, G.; Perche, P. *Journal of Applied Electrochemistry* **1975**, *5*, 63.

(72) Forsyth, S. A.; Pringle, J. M.; MacFarlane, D. R. *Australian Journal of Chemistry* **2004**, *57*, 113.

(73) Jenkins, H. D. B. *Science progress* **2011**, *94*, 265.

(74) Weis, D. C.; MacFarlane, D. R. *Australian Journal of Chemistry* **2012**, *65*, 1478.

(75) Shin, J.-H.; Henderson, W. A.; Passerini, S. *Electrochemistry Communications* **2003**, *5*, 1016.

(76) Kohjiya, S.; Kitade, T.; Ikeda, Y.; Hayashi, A.; Matsuda, A.; Tatsumisago, M.; Minami, T. *Solid State Ionics* **2002**, *154*, 1.

(77) Whittingham, M. S. *Chemical Reviews* **2004**, *104*, 4271.

(78) Ikeda, H.; Ueno, S.; Saito, T.; Nakaido, S.; Tamura, H. *Denki Kagaku* **1977**, *45*, 391.

(79) Ikeda, H.; Tada, K.; Matsuura, K.; Kawai, Y. *Denki Kagaku* **1977**, *45*, 463.

(80) Ikeda, H.; Saito, T.; Tamura, H. *Denki Kagaku* **1977**, *45*, 314.

(81) Gamble, F. R.; Osiecki, J. H.; Cais, M.; Pisharod.R *Science* **1971**, *174*, 493.

(82) Gamble, F. R.; Thompson, A. H. *Solid State Communications* **1978**, *27*, 379.

(83) Whittingham, M. S. *Science* **1976**, *192*, 1126.

(84) Whittingham, M. S. *Chemtech* **1979**, *9*, 766.

(85) Holleck, G. L.; Driscoll, J. R. *Electrochimica Acta* **1977**, *22*, 647.

(86) Thompson, A. H. *Phys Rev Lett* **1975**, *35*, 1786.

(87) Whittingham, M. S. *Journal of the Electrochemical Society* **1976**, *123*, 315.

(88) Rao, B. M. L.; Francis, R. W.; Christopher, H. A. *Journal of the Electrochemical Society* **1977**, *124*, 1490.

(89) Mizushima, K.; Jones, P. C.; Wiseman, P. J.; Goodenough, J. B. *Materials Research Bulletin* **1980**, *15*, 783.

(90) Amatucci, G. G.; Tarascon, J. M.; Klein, L. C. *Journal of the Electrochemical Society* **1996**, *143*, 1114.

(91) Rossen, E.; Reimers, J. N.; Dahn, J. R. *Solid State Ionics* **1993**, *62*, 53.

(92) Gabrisch, H.; Yazami, R.; Fultz, B. *Journal of the Electrochemical Society* **2004**, *151*, A891.

(93) Ozawa, K. *Solid State Ionics* **1994**, *69*, 212.

(94) Nagaura, T.; Tozawa, K. *Prog. Batteries Solar Cells* **1990**, *9*, 209.

(95) Ellis, B. L.; Lee, K. T.; Nazar, L. F. *Chemistry of Materials* **2010**, *22*, 691.

(96) Ohzuku, T.; Ueda, A. *Journal of the Electrochemical Society* **1994**, *141*, 2972.

(97) Yang, X.; Sun, X.; McBreen, J. *Electrochemistry Communications* **2000**, *2*, 100.

(98) Reimers, J. N.; Dahn, J. *Journal of the Electrochemical Society* **1992**, *139*, 2091.

(99) Amatucci, G.; Tarascon, J.; Klein, L. *Journal of the Electrochemical Society* **1996**, *143*, 1114.

(100) Van der Ven, A.; Aydinol, M. K.; Ceder, G. *Journal of the Electrochemical Society* **1998**, *145*, 2149.

(101) Chen, Z.; Lu, Z.; Dahn, J. *Journal of the Electrochemical Society* **2002**, *149*, A1604.

(102) Wang, H.; Jang, Y. I.; Huang, B.; Sadoway, D. R.; Chiang, Y. M. *Journal of the Electrochemical Society* **1999**, *146*, 473.

(103) Endo, E.; Yasuda, T.; Kita, A.; Yamaura, K.; Sekai, K. *Journal of the Electrochemical Society* **2000**, *147*, 1291.

(104) Chung, K. Y.; Yoon, W. S.; McBreen, J.; Yang, X. Q.; Oh, S. H.; Shin, H. C.; Cho, W. I.; Cho, B. W. *Journal of the Electrochemical Society* **2006**, *153*, A2152.

(105) Amatucci, G.; Tarascon, J.; Klein, L. *Solid State Ionics* **1996**, *83*, 167.

(106) Goodenough, J. B. M., K. *U.S. Patent* **1981**, *4*, 518.

(107) Whittingham, M. S. *Progress in Solid State Chemistry* **1978**, *12*, 41.

(108) Cho, J.; Kim, C. S.; Yoo, S. I. *Electrochemical and Solid-State Letters* **2000**, *3*, 362.

(109) Cho, J.; Kim, Y. J.; Kim, T. J.; Park, B. *Angewandte Chemie* **2001**, *113*, 3471.

(110) Cho, J.; Kim, Y. J.; Park, B. *Chemistry of Materials* **2000**, *12*, 3788.

(111) Cho, J.; Kim, Y. J.; Park, B. *Journal of the Electrochemical Society* **2001**, *148*, A1110.

(112) Wang, Z.; Liu, L.; Chen, L.; Huang, X. *Solid State Ionics* **2002**, *148*, 335.

(113) Wang, Z.; Wu, C.; Liu, L.; Wu, F.; Chen, L.; Huang, X. *Journal of the Electrochemical Society* **2002**, *149*, A466.

(114) Liu, L.; Wang, Z.; Li, H.; Chen, L.; Huang, X. *Solid State Ionics* **2002**, *152*, 341.

(115) Cho, J.; Park, B. *Bordeaux, Abstract* **2003**, *1*.

(116) Chen, Z.; Dahn, J. *Electrochimica Acta* **2004**, *49*, 1079.

(117) Levasseur, S.; Menetrier, M.; Suard, E.; Delmas, C. *Solid State Ionics* **2000**, *128*, 11.

(118) Imanishi, N.; Fujiyoshi, M.; Takeda, Y.; Yamamoto, O.; Tabuchi, M. *Solid State Ionics* **1999**, *118*, 121.

(119) Dahn, J.; von Sacken, U.; Michal, C. *Solid State Ionics* **1990**, *44*, 87.

(120) Rougier, A.; Gravereau, P.; Delmas, C. *Journal of the Electrochemical Society* **1996**, *143*, 1168.

(121) Pouillerie, C.; Suard, E.; Delmas, C. *Journal of Solid State Chemistry* **2001**, *158*, 187.

(122) Ohzuku, T.; Ueda, A.; Nagayama, M. *Journal of the Electrochemical Society* **1993**, *140*, 1862.

(123) Li, W.; Reimers, J.; Dahn, J. *Solid State Ionics* **1993**, *67*, 123.

(124) Rougier, A.; Saadoune, I.; Gravereau, P.; Willmann, P.; Delmasa, C. *Solid State Ionics* **1996**, *90*, 83.

(125) Saadoune, I.; Delmas, C. *Journal of Solid State Chemistry* **1998**, *136*, 8.

(126) Saadoune, I.; Ménétrier, M.; Delmas, C. *Journal of Materials Chemistry* **1997**, *7*, 2505.

(127) Saadoune, I.; Delmas, C. *J. Mater. Chem.* **1996**, *6*, 193.

(128) Zhecheva, E.; Stoyanova, R. *Solid State Ionics* **1993**, *66*, 143.

(129) Chebiam, R.; Prado, F.; Manthiram, A. *Journal of the Electrochemical Society* **2001**, *148*, A49.

(130) Prado, G.; Fournes, L.; Delmas, C. *Journal of Solid State Chemistry* **2001**, *159*, 103.

(131) Prado, G.; Rougier, A.; Fournes, L.; Delmas, C. *Journal of the Electrochemical Society* **2000**, *147*, 2880.

(132) Kanno, R.; Shirane, T.; Inaba, Y.; Kawamoto, Y. *Journal of Power Sources* **1997**, *68*, 145.

(133) Delmas, C.; Menetrier, M.; Croguennec, L.; Levasseur, S.; Peres, J.; Pouillerie, C.; Prado, G.; Fournes, L.; Weill, F. *International Journal of Inorganic Materials* **1999**, *1*, 11.

(134) Pouillerie, C.; Perton, F.; Biensan, P.; Pérès, J. P.; Broussely, M.; Delmas, C. *Journal of Power Sources* **2001**, *96*, 293.

(135) Pouillerie, C.; Croguennec, L.; Delmas, C. *Solid State Ionics* **2000**, *132*, 15.

(136) Bang, H. J.; Joachin, H.; Yang, H.; Amine, K.; Prakash, J. *Journal of the Electrochemical Society* **2006**, *153*, A731.

(137) Lei, J.; McLarnon, F.; Kostecki, R. *The Journal of Physical Chemistry B* **2005**, *109*, 952.

(138) Cho, Y.; Cho, J. *Journal of the Electrochemical Society* **2010**, *157*, A625.

(139) Täubert, C.; Fleischhammer, M.; Wohlfahrt-Mehrens, M.; Wietelmann, U.; Buhrmester, T. *Journal of the Electrochemical Society* **2010**, *157*, A721.

(140) Nakai, I.; Nakagome, T. *Electrochemical and Solid-State Letters* **1998**, *1*, 259.

(141) Park, S. H.; Sun, Y. K.; Park, K. S.; Nahm, K. S.; Lee, Y. S.; Yoshio, M. *Electrochimica Acta* **2002**, *47*, 1721.

(142) Chen, R.; Whittingham, M. S. *Journal of the Electrochemical Society* **1997**, *144*, L64.

(143) Armstrong, A. R.; Bruce, P. G. *Nature* **1996**, *381*, 499.

(144) Whittingham, M. S.; Zavalij, P. Y. *Solid State Ionics* **2000**, *131*, 109.

(145) Capitaine, F.; Gravereau, P.; Delmas, C. *Solid State Ionics* **1996**, *89*, 197.

(146) Chen, R.; Zavalij, P.; Whittingham, M. S. *Chemistry of Materials* **1996**, *8*, 1275.

(147) Chen, R.; Chirayil, T.; Zavalij, P.; Whittingham, M. S. *Solid State Ionics* **1996**, *86*, 1.

(148) Reed, J.; Ceder, G.; Van Der Ven, A. *Electrochemical and Solid-State Letters* **2001**, *4*, A78.

(149) Doeff, M. M.; Richardson, T. J.; Kepley, L. *Journal of the Electrochemical Society* **1996**, *143*, 2507.

(150) Armstrong, A. R.; Huang, H.; Jennings, R. A.; Bruce, P. G. *Journal of Materials Chemistry* **1998**, *8*, 255.

(151) Zhang, F.; Ngala, K.; Whittingham, M. S. *Electrochemistry Communications* **2000**, *2*, 445.

(152) Lu, Z.; Dahn, J. *Chemistry of Materials* **2001**, *13*, 1252.

(153) Lu, Z.; Dahn, J. *Chemistry of Materials* **2001**, *13*, 2078.

(154) Lu, Z.; Dahn, J. *Journal of the Electrochemical Society* **2001**, *148*, A237.

(155) Lu, Z.; Donaberger, R.; Dahn, J. *Chemistry of Materials* **2000**, *12*, 3583.

(156) Dollé, M.; Patoux, S.; Doeff, M. M. *Chemistry of Materials* **2005**, *17*, 1036.

(157) Shaju, K.; Subba Rao, G.; Chowdari, B. *Electrochimica Acta* **2003**, *48*, 2691.

(158) Rossen, E.; Jones, C.; Dahn, J. *Solid State Ionics* **1992**, *57*, 311.

(159) Spahr, M. E.; Novák, P.; Schnyder, B.; Haas, O.; Nesper, R. *Journal of the Electrochemical Society* **1998**, *145*, 1113.

(160) Ohzuku, T.; Makimura, Y. *Chemistry Letters* **2001**, *30*, 744.

(161) Makimura, Y.; Ohzuku, T. *Journal of Power Sources* **2003**, *119–121*, 156.

(162) Zhou, F.; Zhao, X.; Lu, Z.; Jiang, J.; Dahn, J. *Electrochemical and Solid-State Letters* **2008**, *11*, A155.

(163) Yabuuchi, N.; Kim, Y. T.; Li, H. H.; Shao-Horn, Y. *Chemistry of Materials* **2008**, *20*, 4936.

(164) Ammundsen, B.; Paulsen, J. *Advanced Materials* **2001**, *13*, 943.

(165) Yoon, W. S.; Paik, Y.; Yang, X. Q.; Balasubramanian, M.; McBreen, J.; Grey, C. P. *Electrochemical and Solid-State Letters* **2002**, *5*, A263.

(166) Reed, J.; Ceder, G. *Electrochemical and Solid-State Letters* **2002**, *5*, A145.

(167) Miao, S.; Kocher, M.; Rez, P.; Fultz, B.; Ozawa, Y.; Yazami, R.; Ahn, C. C. *The Journal of Physical Chemistry B* **2005**, *109*, 23473.

(168) Islam, M. S.; Davies, R. A.; Gale, J. D. *Chemistry of Materials* **2003**, *15*, 4280.

(169) Venkatraman, S.; Choi, J.; Manthiram, A. *Electrochemistry Communications* **2004**, *6*, 832.

(170) Kang, K.; Ceder, G. *Physical Review B* **2006**, *74*, 094105.

(171) Makimura, Y.; Ohzuku, T. *Journal of Power Sources* **2003**, *119*, 156.

(172) Kang, K.; Meng, Y. S.; Bréger, J.; Grey, C. P.; Ceder, G. *Science* **2006**, *311*, 977.

(173) Schougaard, S. B.; Bréger, J.; Jiang, M.; Grey, C. P.; Goodenough, J. B. *Advanced Materials* **2006**, *18*, 905.

(174) Wu, E. J.; Tepesch, P. D.; Ceder, G. *Philosophical Magazine B* **1998**, *77*, 1039.

(175) Grey, C. P.; Yoon, W. S.; Reed, J.; Ceder, G. *Electrochemical and Solid-State Letters* **2004**, *7*, A290.

(176) Bréger, J.; Meng, Y. S.; Hinuma, Y.; Kumar, S.; Kang, K.; Shao-Horn, Y.; Ceder, G.; Clare, P. *Chemistry of Materials* **2006**, *18*, 4768.

(177) Yabuuchi, N.; Kumar, S.; Li, H. H.; Kim, Y. T.; Shao-Horn, Y. *Journal of the Electrochemical Society* **2007**, *154*, A566.

(178) Ohzuku, T.; Makimura, Y. *Chemistry Letters* **2001**, *30*, 642.

(179) Wang, Z.; Sun, Y.; Chen, L.; Huang, X. *Journal of the Electrochemical Society* **2004**, *151*, A914.

(180) Kim, J. H.; Park, C.; Sun, Y. K. *Solid State Ionics* **2003**, *164*, 43.

(181) Choi, J.; Manthiram, A. *Journal of the Electrochemical Society* **2005**, *152*, A1714.

(182) Zhang, X.; Mauger, A.; Jiang, W. J.; Groult, H.; Julien, C. M. In *Nanostructured Materials for Energy Storage and Conversion*; Zaghib, K., Chiu, W., Ramani, V., Liaw, B. Y., Julien, C., Mustain, W., VanSchalkwijk, W., Eds. 2011; Vol. 35, p 89.

(183) Tan, L.; Liu, H. *Solid State Ionics* **2010**, *181*, 1530.

(184) Petersburg, C. F.; Li, Z.; Chernova, N. A.; Whittingham, M. S.; Alamgir, F. M. *Journal of Materials Chemistry* **2012**, *22*, 19993.

(185) Mei, T.; Zhu, Y.; Tang, K.; Qian, Y. *Rsc Advances* **2012**, *2*, 12886.

(186) Mahesh, K. C.; Manjunatha, H.; Venkatesha, T. V.; Suresh, G. S. *Journal of Solid State Electrochemistry* **2012**, *16*, 3011.

(187) Mahesh, K. C.; Manjunatha, H.; Shivashankaraiah, R. B.; Suresh, G. S.; Venkatesha, T. V. *Journal of the Electrochemical Society* **2012**, *159*, A1040.

(188) Jiang, K.-C.; Xin, S.; Lee, J.-S.; Kim, J.; Xiao, X.-L.; Guo, Y.-G. *Physical Chemistry Chemical Physics* **2012**, *14*, 2934.

(189) Huang, Z.-D.; Liu, X.-M.; Oh, S.-W.; Zhang, B.; Ma, P.-C.; Kim, J.-K. *Journal of Materials Chemistry* **2011**, *21*, 10777.

(190) Hashem, A. M.; El-Taweel, R. S.; Abuzeid, H. M.; Abdel-Ghany, A. E.; Eid, A. E.; Groult, H.; Mauger, A.; Julien, C. M. *Ionics* **2012**, *18*, 1.

(191) Guo, R.; Shi, P.; Cheng, X.; Ma, Y.; Tan, Z. *Journal of Power Sources* **2009**, *189*, 2.

(192) Gao, P.; Li, Y.; Liu, H.; Pinto, J.; Jiang, X.; Yang, G. *Journal of the Electrochemical Society* **2012**, *159*, A506.

(193) Ding, C. X.; Meng, Q. S.; Wang, L.; Chen, C. H. *Materials Research Bulletin* **2009**, *44*, 492.

(194) Koyama, Y.; Makimura, Y.; Tanaka, I.; Adachi, H.; Ohzuku, T. *Journal of the Electrochemical Society* **2004**, *151*, A1499.

(195) Lu, Z.; MacNeil, D.; Dahn, J. *Electrochemical and Solid-State Letters* **2001**, *4*, A200.

(196) Hwang, B.; Tsai, Y.; Carlier, D.; Ceder, G. *Chemistry of Materials* **2003**, *15*, 3676.

(197) Yin, S. C.; Rho, Y. H.; Swainson, I.; Nazar, L. *Chemistry of Materials* **2006**, *18*, 1901.

(198) Kim, J. M.; Chung, H. T. *Electrochimica Acta* **2004**, *49*, 937.

(199) Yabuuchi, N.; Makimura, Y.; Ohzuku, T. *Journal of the Electrochemical Society* **2007**, *154*, A314.

(200) Kobayashi, H.; Emura, S.; Arachi, Y.; Tatsumi, K. *Journal of Power Sources* **2007**, *174*, 774.

(201) Whitfield, P.; Davidson, I.; Cranswick, L.; Swainson, I.; Stephens, P. *Solid State Ionics* **2005**, *176*, 463.

(202) Reale, P.; Privitera, D.; Panero, S.; Scrosati, B. *Solid State Ionics* **2007**, *178*, 1390.

(203) Cahill, L.; Yin, S. C.; Samoson, A.; Heinmaa, I.; Nazar, L.; Goward, G. *Chemistry of Materials* **2005**, *17*, 6560.

(204) Yabuuchi, N.; Ohzuku, T. *Journal of Power Sources* **2003**, *119*, 171.

(205) Wang, Y.; Jiang, J.; Dahn, J. *Electrochemistry Communications* **2007**, *9*, 2534.

(206) Yoon, W. S.; Grey, C. P.; Balasubramanian, M.; Yang, X. Q.; Fischer, D. A.; McBreen, J. *Electrochemical and Solid-State Letters* **2004**, *7*, A53.

(207) Yoon, W. S.; Balasubramanian, M.; Chung, K. Y.; Yang, X. Q.; McBreen, J.; Clare, P.; Fischer, D. A. *Journal of the American Chemical Society* **2005**, *127*, 17479.

(208) Tsai, Y.; Hwang, B.; Ceder, G.; Sheu, H.; Liu, D.; Lee, J. *Chemistry of Materials* **2005**, *17*, 3191.

(209) Yabuuchi, N.; Koyama, Y.; Nakayama, N.; Ohzuku, T. *Journal of the Electrochemical Society* **2005**, *152*, A1434.

(210) Zeng, D.; Cabana, J.; Bréger, J.; Yoon, W. S.; Grey, C. P. *Chemistry of Materials* **2007**, *19*, 6277.

(211) Shinova, E.; Stoyanova, R.; Zhecheva, E.; Ortiz, G.; Lavela, P.; Tirado, J. *Solid State Ionics* **2008**, *179*, 2198.

(212) Nanjundaswamy, K.; Padhi, A.; Goodenough, J.; Okada, S.; Ohtsuka, H.; Arai, H.; Yamaki, J. *Solid State Ionics* **1996**, *92*, 1.

(213) Padhi, A.; Nanjundaswamy, K.; Masquelier, C.; Okada, S.; Goodenough, J. *Journal of the Electrochemical Society* **1997**, *144*, 1609.

(214) Koltypin, M.; Aurbach, D.; Nazar, L.; Ellis, B. *Electrochemical and Solid-State Letters* **2007**, *10*, A40.

(215) MacNeil, D.; Lu, Z.; Chen, Z.; Dahn, J. R. *Journal of Power Sources* **2002**, *108*, 8.

(216) Padhi, A.; Nanjundaswamy, K.; Goodenough, J. B. *Journal of the Electrochemical Society* **1997**, *144*, 1188.

(217) Higuchi, M.; Katayama, K.; Azuma, Y.; Yukawa, M.; Suhara, M. *Journal of Power Sources* **2003**, *119*, 258.

(218) Huang, H.; Yin, S. C.; Nazar, L. *Electrochemical and Solid-State Letters* **2001**, *4*, A170.

(219) Dominko, R.; Bele, M.; Gaberscek, M.; Remskar, M.; Hanzel, D.; Pejovnik, S.; Jamnik, J. *Journal of the Electrochemical Society* **2005**, *152*, A607.

(220) Yamada, A.; Chung, S. C.; Hinokuma, K. *Journal of the Electrochemical Society* **2001**, *148*, A224.

(221) Yang, S.; Zavalij, P. Y.; Stanley Whittingham, M. *Electrochemistry Communications* **2001**, *3*, 505.

(222) Prosini, P. P.; Carewska, M.; Scaccia, S.; Wisniewski, P.; Passerini, S.; Pasquali, M. *Journal of the Electrochemical Society* **2002**, *149*, A886.

(223) Safronov, D. V.; Novikova, S. A.; Kulova, T. L.; Skundin, A. M.; Yaroslavtsev, A. B. *Inorganic Materials* **2012**, *48*, 513.

(224) Nizamidin, P.; Yimit, A.; Wang, J. D. *Current Analytical Chemistry* **2012**, *8*, 557.

(225) Ding, Y.-h.; Zhang, P. *Transactions of Nonferrous Metals Society of China* **2012**, *22*, S153.

(226) Morgan, D.; Van der Ven, A.; Ceder, G. *Electrochemical and Solid-State Letters* **2004**, *7*, A30.

(227) Nishimura, S.; Kobayashi, G.; Ohoyama, K.; Kanno, R.; Yashima, M.; Yamada, A. *Nature Materials* **2008**, *7*, 707.

(228) Li, J.; Yao, W.; Martin, S.; Vaknin, D. *Solid State Ionics* **2008**, *179*, 2016.

(229) Fisher, C. A. J.; Islam, M. S. *Journal of Materials Chemistry* **2008**, *18*, 1209.

(230) Srinivasan, V.; Newman, J. *Journal of the Electrochemical Society* **2004**, *151*, A1517.

(231) Nan, C.; Lu, J.; Chen, C.; Peng, Q.; Li, Y. *Journal of Materials Chemistry* **2011**, *21*, 9994.

(232) Chen, G.; Song, X.; Richardson, T. J. *Electrochemical and Solid-State Letters* **2006**, *9*, A295.

(233) Delmas, C.; Maccario, M.; Croguennec, L.; Le Cras, F.; Weill, F. *Nature Materials* **2008**, *7*, 665.

(234) Lee, K. T.; Kan, W. H.; Nazar, L. F. *Journal of the American Chemical Society* **2009**, *131*, 6044.

(235) Yamada, A.; Koizumi, H.; Nishimura, S.; Sonoyama, N.; Kanno, R.; Yonemura, M.; Nakamura, T.; Kobayashi, Y. *Nature Materials* **2006**, *5*, 357.

(236) Yamada, A.; Koizumi, H.; Sonoyama, N.; Kanno, R. *Electrochemical and Solid-State Letters* **2005**, *8*, A409.

(237) Meethong, N.; Huang, H. Y. S.; Carter, W. C.; Chiang, Y. M. *Electrochemical and Solid-State Letters* **2007**, *10*, A134.

(238) Wagemaker, M.; Borghols, W. J. H.; Mulder, F. M. *Journal of the American Chemical Society* **2007**, *129*, 4323.

(239) Kobayashi, G.; Nishimura, S.; Park, M. S.; Kanno, R.; Yashima, M.; Ida, T.; Yamada, A. *Advanced Functional Materials* **2008**, *19*, 395.

(240) Gibot, P.; Casas-Cabanas, M.; Laffont, L.; Levasseur, S.; Carlach, P.; Hamelet, S.; Tarascon, J. M.; Masquelier, C. *Nature Materials* **2008**, *7*, 741.

(241) Zhang, W. J. *Journal of the Electrochemical Society* **2010**, *157*, A1040.

(242) Liao, X. Z.; Ma, Z. F.; Wang, L.; Zhang, X. M.; Jiang, Y.; He, Y. S. *Electrochemical and Solid-State Letters* **2004**, *7*, A522.

(243) Chung, S. Y.; Bloking, J. T.; Chiang, Y. M. *Nature Materials* **2002**, *1*, 123.

(244) Ravet, N.; Abouimrane, A.; Armand, M. *Nature Materials* **2003**, *2*, 702.

(245) Delacourt, C.; Wurm, C.; Laffont, L.; Leriche, J. B.; Masquelier, C. *Solid State Ionics* **2006**, *177*, 333.

(246) Fisher, C. A. J.; Hart Prieto, V. M.; Islam, M. S. *Chemistry of Materials* **2008**, *20*, 5907.

(247) Wagemaker, M.; Ellis, B. L.; Lützenkirchen-Hecht, D.; Mulder, F. M.; Nazar, L. F. *Chemistry of Materials* **2008**, *20*, 6313.

(248) Delacourt, C.; Poizot, P.; Morcrette, M.; Tarascon, J. M.; Masquelier, C. *Chemistry of Materials* **2004**, *16*, 93.

(249) Dominko, R.; Bele, M.; Gaberscek, M.; Remskar, M.; Hanzel, D.; Goupil, J. M.; Pejovnik, S.; Jamnik, J. *Journal of Power Sources* **2006**, *153*, 274.

(250) Yang, J.; Xu, J. J. *Journal of the Electrochemical Society* **2006**, *153*, A716.

(251) Wang, D.; Buqa, H.; Crouzet, M.; Deghenghi, G.; Drezen, T.; Exnar, I.; Kwon, N. H.; Miners, J. H.; Poletto, L.; Grätzel, M. *Journal of Power Sources* **2009**, *189*, 624.

(252) Ellis, B.; Herle, P. S.; Rho, Y. H.; Nazar, L.; Dunlap, R.; Perry, L. K.; Ryan, D. *Faraday Discussions* **2007**, *134*, 119.

(253) Shiratsuchi, T.; Okada, S.; Doi, T.; Yamaki, J. *Electrochimica Acta* **2009**, *54*, 3145.

(254) Chen, G.; Wilcox, J. D.; Richardson, T. J. *Electrochemical and Solid-State Letters* **2008**, *11*, A190.

(255) Chen, G.; Richardson, T. J. *Journal of the Electrochemical Society* **2009**, *156*, A756.

(256) Park, Y. U.; Kim, J.; Gwon, H.; Seo, D. H.; Kim, S. W.; Kang, K. *Chemistry of Materials* **2010**, *22*, 2573.

(257) Manthiram, A.; Goodenough, J. *Journal of Solid State Chemistry* **1987**, *71*, 349.

(258) Masquelier, C.; Padhi, A.; Nanjundaswamy, K.; Goodenough, J. *Journal of Solid State Chemistry* **1998**, *135*, 228.

(259) Padhi, A.; Nanjundaswamy, K.; Masquelier, C.; Goodenough, J. *Journal of the Electrochemical Society* **1997**, *144*, 2581.

(260) Torardi, C.; Prince, E. *Materials Research Bulletin* **1986**, *21*, 719.

(261) Kim, Y.; Goodenough, J. B. *The Journal of Physical Chemistry C* **2008**, *112*, 15060.

(262) Kim, Y.; Goodenough, J. B. *Electrochemistry Communications* **2008**, *10*, 497.

(263) Nishimura, S.; Nakamura, M.; Natsui, R.; Yamada, A. *ChemInform* **2011**, *42*, no.

(264) Kim, H.; Lee, S.; Park, Y. U.; Kim, J.; Jeon, S.; Kang, K. *Chemistry of Materials* **2011**, *23*, 3930.

(265) Tamaru, M.; Barpanda, P.; Yamada, Y.; Nishimura, S.; Yamada, A. *Journal of Materials Chemistry* **2012**.

(266) Furuta, N.; Nishimura, S.; Barpanda, P.; Yamada, A. *Chemistry of Materials* **2012**, *24*, 1055.

(267) Jain, A.; Hautier, G.; Moore, C.; Kang, B.; Lee, J.; Chen, H.; Twu, N.; Ceder, G. *Journal of the Electrochemical Society* **2012**, *159*, A622.

(268) Zhou, H.; Upreti, S.; Chernova, N. A.; Whittingham, M. S. *Acta Crystallographica Section E: Structure Reports Online* **2011**, *67*, i58.

(269) Clark, J. M.; Nishimura, S.-i.; Yamada, A.; Islam, M. S. *Angewandte Chemie International Edition* **2012**, *51*, 13149.

(270) Dominko, R.; Bele, M.; Gaberscek, M.; Meden, A.; Remskar, M.; Jamnik, J. *Electrochemistry Communications* **2006**, *8*, 217.

(271) Lv, D.; Wen, W.; Huang, X.; Bai, J.; Mi, J.; Wu, S.; Yang, Y. *Journal of Materials Chemistry* **2011**, *21*, 9506.

(272) Su, D.; Ahn, H.; Wang, G. *Applied Physics Letters* **2011**, *99*, 141909.

(273) Armstrong, A. R.; Lyness, C.; Ménétrier, M.; Bruce, P. G. *Chemistry of Materials* **2010**, *22*, 1892.

(274) Keffer, C.; Mighell, A. D.; Mauer, F.; Swanson, H. E.; Block, S. *Inorganic Chemistry* **1967**, *6*, 119.

(275) Zemann, J. *Acta Crystallographica* **1960**, *13*, 863.

(276) Nytén, A.; Abouimrane, A.; Armand, M.; Gustafsson, T.; Thomas, J. O. *Electrochemistry Communications* **2005**, *7*, 156.

(277) Yan, Z.; Cai, S.; Miao, L.; Zhou, X.; Zhao, Y. *Journal of Alloys and Compounds* **2011**.

(278) Zheng, Z.; Wang, Y.; Zhang, A.; Zhang, T.; Cheng, F.; Tao, Z.; Chen, J. *Journal of Power Sources* **2011**.

(279) Huang, X.; Li, X.; Wang, H.; Pan, Z.; Qu, M.; Yu, Z. *Solid State Ionics* **2010**, *181*, 1451.

(280) Huang, X.; Li, X.; Wang, H.; Pan, Z.; Qu, M.; Yu, Z. *Electrochimica Acta* **2010**, *55*, 7362.

(281) Eames, C.; Armstrong, A.; Bruce, P.; Islam, M. *Chemistry of Materials* **2012**, *24*, 2155.

(282) Arroyo-de Dompablo, M.; Armand, M.; Tarascon, J.; Amador, U. *Electrochemistry Communications* **2006**, *8*, 1292.

(283) Larsson, P.; Ahuja, R.; Nytén, A.; Thomas, J. O. *Electrochemistry Communications* **2006**, *8*, 797.

(284) Wu, S.; Zhu, Z.; Yang, Y.; Hou, Z. *Computational Materials Science* **2009**, *44*, 1243.

(285) Liivat, A.; Thomas, J. O. *Solid State Ionics* **2011**, *192*, 58.

(286) Larsson, P.; Ahuja, R.; Liivat, A.; Thomas, J. O. *Computational Materials Science* **2010**, *47*, 678.

(287) Nishimura, S.; Hayase, S.; Kanno, R.; Yashima, M.; Nakayama, N.; Yamada, A. *Journal of the American Chemical Society* **2008**, *130*, 13212.

(288) Kuganathan, N.; Islam, M. *Chemistry of Materials* **2009**, *21*, 5196.

(289) Zhong, G.; Li, Y.; Yan, P.; Liu, Z.; Xie, M.; Lin, H. *The Journal of Physical Chemistry C* **2010**, *114*, 3693.

(290) Nytén, A.; Kamali, S.; Häggström, L.; Gustafsson, T.; Thomas, J. O. *J. Mater. Chem.* **2006**, *16*, 2266.

(291) Zaghib, K.; Ait Salah, A.; Ravet, N.; Mauger, A.; Gendron, F.; Julien, C. M. *Journal of Power Sources* **2006**, *160*, 1381.

(292) Dominko, R. *Journal of Power Sources* **2008**, *184*, 462.

(293) Kokalj, A.; Dominko, R.; Mali, G.; Meden, A.; Gaberscek, M.; Jamnik, J. *Chemistry of Materials* **2007**, *19*, 3633.

(294) Arroyo-deDompablo, M.; Dominko, R.; Gallardo-Amores, J.; Dupont, L.; Mali, G.; Ehrenberg, H.; Jamnik, J.; Moran, E. *Chemistry of Materials* **2008**, *20*, 5574.

(295) Dahn, J. R.; Zheng, T.; Liu, Y. H.; Xue, J. S. *Science* **1995**, *270*, 590.

(296) Poizot, P.; Laruelle, S.; Grugeon, S.; Dupont, L.; Tarascon, J. *Nature* **2000**, *407*, 496.

(297) Novoselov, K.; Geim, A.; Morozov, S.; Jiang, D.; Zhang, Y.; Dubonos, S.; Grigorieva, I.; Firsov, A. *Science* **2004**, *306*, 666.

(298) Geim, A. K.; Novoselov, K. S. *Nature Materials* **2007**, *6*, 183.

(299) Tachikawa, H. *The Journal of Physical Chemistry C* **2008**, *112*, 10193.

(300) Tachikawa, H. *The Journal of Physical Chemistry C* **2007**, *111*, 13087.

(301) Yoo, E. J.; Kim, J.; Hosono, E.; Zhou, H.; Kudo, T.; Honma, I. *Nano Letters* **2008**, *8*, 2277.

(302) Márquez, A.; Vargas, A.; Balbuena, P. B. *Journal of the Electrochemical Society* **1998**, *145*, 3328.

(303) Nakadaira, M.; Saito, R.; Kimura, T.; Dresselhaus, G.; Dresselhaus, M. *Journal of Materials Research* **1997**, *12*, 1367.

(304) Fujita, M.; Wakabayashi, K.; Nakada, K.; Kusakabe, K. *Journal of the Physical Society of Japan* **1996**, *65*, 1920.

(305) Tachikawa, H.; Kawabata, H. *The Journal of Physical Chemistry B* **2008**, *112*, 7315.

(306) Zhou, W.; Yan, H. *Chemical Physics Letters* **2010**, *489*, 225.

(307) Tachikawa, H.; Nagoya, Y.; Fukuzumi, T. *Journal of Power Sources* **2010**, *195*, 6148.

(308) Armand, M.; Tarascon, J.-M. *Nature* **2008**, *451*, 652.

(309) Whittingham, M. S. *Dalton Trans.* **2008**, 5424.

(310) Cabana, J.; Monconduit, L.; Larcher, D.; Palacín, M. *Advanced materials (Deerfield Beach, Fla.)* **2010**, *22*, 92.

(311) Godshall, N. A.; Raistrick, I. D.; Huggins, R. A. *Materials Research Bulletin* **1980**, *15*.

(312) Thackeray, M. M.; Coetzer, J. *Materials Research Bulletin* **1981**, *16*.

(313) Gabano, J.-P. *Google Patents* **1983**.

(314) Kaun, T. D.; Nelson, P. A.; Redey, L.; Vissers, D. R.; Henriksen, G. L. *Electrochimica Acta* **1993**, *38*.

(315) Grugeon, S.; Laruelle, S.; Dupont, L.; Tarascon, J. M. *Solid State Sciences* **2003**, *5*.

(316) John, B. G.; Youngsik, K. *Chemistry of Materials* **2010**, *22*.

(317) Hajime, A.; Shigeto, O.; Yoji, S.; Jun-ichi, Y. *Journal of Power Sources* **1997**, *68*.

(318) Jin, H.; Hong, L.; Xuejie, H. *Electrochemical and Solid-State Letters* **2005**, *8*.

(319) Apostolova, R. D.; Shembel', E. M.; Talyosef, I.; Grinblat, J.; Markovsky, B.; Aurbach, D. *Russian Journal of Electrochemistry* **2009**, *45*.

(320) Zheng-Wen, F.; Ying, W.; Xiao-Li, Y.; Shang-Li, Z.; Qi-Zong, Q. *The Journal of Physical Chemistry B* **2004**, *108*.

(321) Li, H.; Richter, G.; Maier, J. *Advanced Materials* **2003**.

(322) Yu, F. Z.; Kotomin, E. A.; Balaya, P.; Maier, J. *Solid State Sciences* **2008**, *10*.

(323) Yuriy, V. M.; James, R. A. *Journal of the Electrochemical Society* **2004**, *151*.

(324) Souza, D.; Pralong, V.; Jacobson, A.; Nazar, L. *Science (New York, N.Y.)* **2002**, *296*, 2012.

(325) Xingjiang, L.; Hideo, Y.; Masanori, Y. *Journal of Power Sources* **2005**, *146*.

(326) Poizot, P.; Laruelle, S.; Grugeon, S.; Tarascon, J. M. *Journal of the Electrochemical Society* **2002**, *149*.

(327) Mauvernay, B.; Doublet, M. L.; Monconduit, L. *Journal of Physics and Chemistry of Solids* **2006**, *67*.

(328) Jones, C. H. W.; Kovacs, P. E.; Sharma, R. D.; McMillan, R. S. *The Journal of Physical Chemistry* **1990**, *94*.

(329) Barnett, R.; Bergren, E.; Beringer, J.; Bernardi…, G. *Physics Letters B* **2008**.

(330) Plitz, I.; Badway, F.; Al-Sharab, J.; DuPasquier, A.; Cosandey, F.; Amatucci, G. G. *Journal of the Electrochemical Society* **2005**, *152*.

(331) Hirokazu, K.; Kenji, T.; Fuminori, M.; Akitoshi, H.; Kiyoharu, T.; Masahiro, T. *Journal of the Electrochemical Society* **2007**, *154*.

(332) Jae-Won, C.; Gouri, C.; Hyo-Jun, A.; Ki-Won, K.; Jou-Hyeon, A. *Journal of Power Sources* **2006**, *163*.

(333) Ying, W.; Zheng-Wen, F.; Xiao-Li, Y.; Qi-Zong, Q. *Journal of the Electrochemical Society* **2004**, *151*.

(334) Tarascon, J.; Grugeon, S.; Morcrette, M.; Laruelle…, S. *Comptes Rendus ...* **2005**.

(335) Patrick, J. M.; Ronald, A. G. *Journal of Power Sources* **2008**, *178*.

(336) Hui, L.; Lin, M.; Wei-xiang, C.; Jian-ming, W. *Materials Letters* **2009**, *63*.

(337) Silva, D. C. C.; Crosnier, O.; Ouvrard, G.; Greedan, J.; Safa-Sefat, A.; Nazar, L. F. *Electrochemical and Solid-State Letters* **2003**, *6*.

(338) Badway, F.; Pereira, N.; Cosandey, F.; Amatucci, G. G. *Journal of the Electrochemical Society* **2003**, *150*.

(339) Liu, J.; Luo, T.; Meng, F.; Qian, K.; Wan…, Y. *The Journal of Physical ...* **2010**.

(340) Raymond, J.; Brian, B. *Journal of the Electrochemical Society* **1969**, *116*.

(341) Liu, J.; Wang, X.; Liu, Y.; Dong, H. *Chinese Journal of Chemical Physics* **2007**, *20*, 291.

(342) Xiang, J. Y.; Tu, J. P.; Wang, X. L.; Huang, X. H.; Yuan, Y. F.; Xia, X. H.; Zeng, Z. Y. *Journal of Power Sources* **2008**, *185*.

(343) Fred, W. D. *Journal of the Electrochemical Society* **1981**, *128*.

(344) Marie-Liesse, D.; Frédéric, L.; Frédéric, G.; Laure, M. *Chemistry of Materials* **2002**, *14*.

(345) Yusuke, N.; Hirokazu, K.; Akitoshi, H.; Masahiro, T. *Journal of Power Sources* **2009**, *189*.

(346) Boyanov, S.; Bernardi, J.; Bekaert…, E. *Chemistry of ...* **2008**.

(347) Kim, T.; Choi, J.; Ryu, H.; Cho, G.; Kim…, K. *Journal of Power ...* **2007**.

(348) Bonino, F. *Journal of the Electrochemical Society* **1984**, *131*.

(349) Boyanov, S.; Gillot, F.; Monconduit, L. *Ionics* **2008**, *14*.

(350) Hughes, M.; Hampson, N. A.; Karunathilaka, S. A. G. R. *Journal of Power Sources* **1984**, *12*.

(351) Hironosuke, I.; Satoshi, N. *Journal of Power Sources* **1983**, *9*.

(352) Eichinger, G.; Besenhard, J. O. *Journal of Electroanalytical Chemistry and Interfacial Electrochemistry* **1976**, *72*.

(353) Ke, W.; Jun, Y.; Jingying, X.; Baofeng, W.; Zhongsheng, W. *Electrochemistry Communications* **2003**, *5*.

(354) Lee, S.; Kim, Y.; Deshpande, R.; Parilla…, P. *Advanced ...* **2008**.

(355) Julien, C. M. *Materials Science and Engineering: R: Reports* **2003**, *40*.

(356) Hassan, M. F.; Guo, Z. P.; Chen, Z.; Liu, H. K. *Journal of Power Sources* **2010**, *195*.

(357) Chuanqi, F.; Jun, M.; Hua, L.; Rong, Z.; Zaiping, G.; Huakun, L. *Materials Research Bulletin* **2009**, *44*.

(358) Jun, H. K.; Yoon, S. J.; Kyu, T. L.; Chang, H. K.; Seung, M. O. *Journal of the Electrochemical Society* **2009**, *156*.

(359) Jiao, F.; Bao, J.; Bruce, P. G. *Electrochemical and Solid-State Letters* **2007**, *10*, A264.

(360) Kang, J.-G.; Ko, Y.-D.; Park, J.-G.; Kim, D.-W. *Nanoscale Research Letters* **2008**, *3*, 390.

(361) Jung, Y. S.; Lee, S.; Ahn, D.; Dillon, A. C.; Lee, S.-H. *Journal of Power Sources* **2009**, *188*, 286.

(362) Grugeon, S.; Laruelle, S.; Herrera-Urbina, R.; Dupont, L.; Poizot, P.; Tarascon, J. *Journal of the Electrochemical Society* **2001**, *148*, A285.

(363) Larcher, D.; Masquelier, C.; Bonnin, D.; Chabre, Y.; Masson, V.; Leriche, J.-B.; Tarascon, J.-M. *Journal of the Electrochemical Society* **2003**, *150*, A133.

(364) Larcher, D.; Bonnin, D.; Cortes, R.; Rivals, I.; Personnaz, L.; Tarascon, J.-M. *Journal of the Electrochemical Society* **2003**, *150*, A1643.

(365) Hang, B. T.; Okada, S.; Yamaki, J.-i. *Journal of Power Sources* **2008**, *178*, 402.

(366) Bard, A. J.; Parsons, R.; Jordan, J. *Marcel Dekker, Inc., New York, NY* **1985**.

(367) Michael, M. T. *Progress in Solid State Chemistry* **1997**, *25*.

(368) Post, J. E. *Proceedings of the National Academy of Sciences* **1999**, *96*, 3447.

(369) Wu, M.-S.; Chiang, P.-C. J.; Lee, J.-T.; Lin, J.-C. *The journal of physical chemistry. B* **2005**, *109*, 23279.

(370) Jianzhi, Z.; Zhanliang, T.; Jing, L.; Jun, C. *Crystal Growth & Design* **2008**, *8*.

(371) Lavela, P.; Tirado, J. L.; Vidal-Abarca, C. *Electrochimica Acta* **2007**, *52*.

(372) Fan, Q.; Whittingham, M. S. *Electrochemical and Solid-State Letters* **2007**, *10*, A48.

(373) D, P.; N, R.; A, W. *Journal of Power Sources* **2005**, *141*.

(374) Kaifu, Z.; Xin, X.; Bin, Z.; Hong, L.; Zhaoxiang, W.; Liquan, C. *Journal of Power Sources* **2010**, *195*.

(375) Daishu, H.; Junichi, S.; Hiromasa, I.; Yoshiharu, U.; Masataka, W.; Takafumi, M.; Iwao, W. *Journal of Materials Chemistry* **2003**, *13*.

(376) Chunhua, C.; Ning, D.; Long, W.; Yan, Y.; Ingo, L. *Journal of Power Sources* **2009**, *189*.

(377) Li, H.; Balaya, P.; Maier, J. *Journal of the Electrochemical Society* **2004**, *151*, A1878.

(378) Cui, Z.-M.; Jiang, L.-Y.; Song, W.-G.; Guo, Y.-G. *Chemistry of Materials* **2009**, *21*, 1162.

(379) Liu, H.; Wang, G.; Wang, J.; Wexler, D. *Electrochemistry Communications* **2008**, *10*, 1879.

(380) Taberna, P.-L.; Mitra, S.; Poizot, P.; Simon, P.; Tarascon, J.-M. *Nature Materials* **2006**, *5*, 567.

(381) Wang, L.; Yu, Y.; Chen, P.; Zhang, D.; Chen, C. *Journal of Power Sources* **2008**, *183*, 717.

(382) Lee, G.-H.; Park, J.-G.; Sung, Y.-M.; Chung, K. Y.; Cho, W. I.; Kim, D.-W. *Nanotechnology* **2009**, *20*, 295205.

(383) Zhang, W. M.; Wu, X. L.; Hu, J. S.; Guo, Y. G.; Wan, L. J. *Advanced Functional Materials* **2008**, *18*, 3941.

(384) Banov, B.; Ljutzkanov, L.; Dimitrov, I.; Trifonova, A.; Vasilchina, H.; Aleksandrova, A.; Mochilov, A.; Hang, B. T.; Okada, S.; Yamaki, J.-i. *Journal of Nanoscience and Nanotechnology* **2008**, *8*, 591.

(385) Gou, X.; Wang, G.; Kong, X.; Wexler, D.; Horvat, J.; Yang, J.; Park, J. *Chemistry-a European Journal* **2008**, *14*, 5996.

(386) Wu, X.-L.; Guo, Y.-G.; Wan, L.-J.; Hu, C.-W. *The Journal of Physical Chemistry C* **2008**, *112*, 16824.

(387) Chen, J.; Xu, L.; Li, W.; Gou, X.-l. *Advanced Materials* **2005**, *17*, 582.

(388) Liu, J.; Li, Y.; Fan, H.; Zhu, Z.; Jiang, J.; Ding, R.; Hu, Y.; Huang, X. *Chemistry of Materials* **2009**, *22*, 212.

(389) Reddy, M.; Yu, T.; Sow, C.-H.; Shen, Z. X.; Lim, C. T.; Subba Rao, G.; Chowdari, B. *Advanced Functional Materials* **2007**, *17*, 2792.

(390) Tahir, A. A.; Wijayantha, K. U.; Saremi-Yarahmadi, S.; Mazhar, M.; McKee, V. *Chemistry of Materials* **2009**, *21*, 3763.

(391) Zhong, J.; Cao, C.; Liu, Y.; Li, Y.; Khan, W. S. *Chemical Communications* **2010**, *46*, 3869.

(392) Woo, K.; Lee, H. J.; Ahn, J. P.; Park, Y. S. *Advanced Materials* **2003**, *15*, 1761.

(393) Wang, L.; Xu, H.; Chen, P.; Zhang, D.; Ding, C.; Chen, C. *Journal of Power Sources* **2009**, *193*, 846.

(394) An, Z.; Zhang, J.; Pan, S.; Song, G. *Powder Technology* **2011**.

(395) Lian, J.; Duan, X.; Ma, J.; Peng, P.; Kim, T.; Zheng, W. *Acs Nano* **2009**, *3*, 3749.

(396) Cheng, F.; Tao, Z.; Liang, J.; Chen, J. *Chemistry of Materials* **2007**, *20*, 667.

(397) Sun, Z.; Yuan, H.; Liu, Z.; Han, B.; Zhang, X. *Advanced Materials* **2005**, *17*, 2993.

(398) Jiao, F.; Harrison, A.; Jumas, J.-C.; Chadwick, A. V.; Kockelmann, W.; Bruce, P. G. *Journal of the American Chemical Society* **2006**, *128*, 5468.

(399) Liu, L.; Kou, H.-Z.; Mo, W.; Liu, H.; Wang, Y. *The Journal of Physical Chemistry B* **2006**, *110*, 15218.

(400) Qian, H.; Lin, G.; Zhang, Y.; Gunawan, P.; Xu, R. *Nanotechnology* **2007**, *18*, 355602.

(401) Jia, C.-J.; Sun, L.-D.; Luo, F.; Han, X.-D.; Heyderman, L. J.; Yan, Z.-G.; Yan, C.-H.; Zheng, K.; Zhang, Z.; Takano, M. *Journal of the American Chemical Society* **2008**, *130*, 16968.

(402) Wu, C.; Yin, P.; Zhu, X.; OuYang, C.; Xie, Y. *The Journal of Physical Chemistry B* **2006**, *110*, 17806.

(403) Zhang, D.; Li, G.; Yang, X.; Jimmy, C. Y. *Chemical Communications* **2009**, 4381.

(404) Liu, S.; Yu, J.; Jaroniec, M. *Journal of the American Chemical Society* **2010**, *132*, 11914.

(405) Yang, H. G.; Liu, G.; Qiao, S. Z.; Sun, C. H.; Jin, Y. G.; Smith, S. C.; Zou, J.; Cheng, H. M.; Lu, G. Q. *Journal of the American Chemical Society* **2009**, *131*, 4078.

(406) Yang, H. G.; Sun, C. H.; Qiao, S. Z.; Zou, J.; Liu, G.; Smith, S. C.; Cheng, H. M.; Lu, G. Q. *Nature* **2008**, *453*, 638.

(407) Chen, J. S.; Tan, Y. L.; Li, C. M.; Cheah, Y. L.; Luan, D.; Madhavi, S.; Boey, F. Y. C.; Archer, L. A.; Lou, X. W. *Journal of the American Chemical Society* **2010**, *132*, 6124.

(408) Thackeray, M. M.; Baker, S. D.; Coetzer, J. *Materials Research Bulletin* **1982**, *17*.

(409) M, T.; S, B.; K, A.; J, G. *Solid State Ionics* **1985**, *17*.

(410) Poizot, P.; Laruelle, S.; Grugeon, S.; Dupont, L.; Tarascon, J. M. *Ionics* **2000**, *6*.

(411) Obrovac, M. N.; Dunlap, R. A.; Sanderson, R. J.; Dahn, J. R. *Journal of the Electrochemical Society* **2001**, *148*.

(412) Hyun Chul, C.; Sang Yun, L.; Seung Bin, K.; Min Gyu, K.; Min Kyu, L.; Hyun Joon, S.; Jae Sung, L. *The Journal of Physical Chemistry B* **2002**, *106*.

(413) Dedryvère, R.; Laruelle, S.; Grugeon, S.; Poizot, P.; Gonbeau, D.; Tarascon, J. M. *Chemistry of Materials* **2004**, *16*.

(414) Rahman, M.; Wang, J.-Z.; Deng, X.-L.; Li, Y.; Liu, H.-K. *Electrochimica Acta* **2009**, *55*, 504.

(415) Liu, Y.; Mi, C.; Su, L.; Zhang, X. *Electrochimica Acta* **2008**, *53*, 2507.

(416) Wang, X.; Chen, X.; Gao, L.; Zheng, H.; Zhang, Z.; Qian, Y. *The Journal of Physical Chemistry B* **2004**, *108*, 16401.

(417) Yue, W.; Hill, A. H.; Harrison, A.; Zhou, W. *Chemical Communications* **2007**, 2518.

(418) Xu, R.; Wang, J.; Li, Q.; Sun, G.; Wang, E.; Li, S.; Gu, J.; Ju, M. *Journal of Solid State Chemistry* **2009**, *182*, 3177.

(419) Wang, J.; Niu, B.; Du, G.; Zeng, R.; Chen, Z.; Guo, Z.; Dou, S. *Materials Chemistry and Physics* **2011**, *126*, 747.

(420) Chen, J. S.; Zhu, T.; Hu, Q. H.; Gao, J.; Su, F.; Qiao, S. Z.; Lou, X. W. *Acs Applied Materials & Interfaces* **2010**, *2*, 3628.

(421) Barreca, D.; Gasparotto, A.; Lebedev, O. I.; Maccato, C.; Pozza, A.; Tondello, E.; Turner, S.; Van Tendeloo, G. *Crystengcomm* **2010**, *12*, 2185.

(422) Liu, X. H.; Qiu, G. Z.; Li, X. G. *Nanotechnology* **2005**, *16*, 3035.

(423) Wang, X.; Wu, X. L.; Guo, Y. G.; Zhong, Y.; Cao, X.; Ma, Y.; Yao, J. *Advanced Functional Materials* **2010**, *20*, 1680.

(424) Zheng, J.; Liu, J.; Lv, D.; Kuang, Q.; Jiang, Z.; Xie, Z.; Huang, R.; Zheng, L. *Journal of Solid State Chemistry* **2010**, *183*, 600.

(425) Tian, L.; Zou, H.; Fu, J.; Yang, X.; Wang, Y.; Guo, H.; Fu, X.; Liang, C.; Wu, M.; Shen, P. K. *Advanced Functional Materials* **2010**, *20*, 617.

(426) Zhan, F.; Geng, B.; Guo, Y. *Chemistry-a European Journal* **2009**, *15*, 6169.

(427) Lou, X. W.; Deng, D.; Lee, J. Y.; Feng, J.; Archer, L. A. *Advanced Materials* **2008**, *20*, 258.

(428) Du, N.; Zhang, H.; Chen, B.; Wu, J.; Ma, X.; Liu, Z.; Zhang, Y.; Yang, D.; Huang, X.; Tu, J. *Advanced Materials* **2007**, *19*, 4505.

(429) Li, Y.; Tan, B.; Wu, Y. *Nano Letters* **2008**, *8*, 265.

(430) Cheng, H.; Lu, Z. G.; Deng, J. Q.; Chung, C.; Zhang, K.; Li, Y. Y. *Nano Research* **2010**, *3*, 895.

(431) Xia, X.-h.; Tu, J.-p.; Mai, Y.-j.; Wang, X.-l.; Gu, C.-d.; Zhao, X.-b. *Journal of Materials Chemistry* **2011**, *21*, 9319.

(432) Zhang, H.; Wu, J.; Zhai, C.; Ma, X.; Du, N.; Tu, J.; Yang, D. *Nanotechnology* **2007**, *19*, 035711.

(433) Larcher, D.; Sudant, G.; Leriche, J. B.; Chabre, Y.; Tarascon, J. M. *Journal of the Electrochemical Society* **2002**, *149*.

(434) Binotto, G.; Larcher, D.; Prakash, A. S.; Urbina, R. H.; Hegde, M. S.; Tarascon, J. M. *Chemistry of Materials* **2007**, *19*.

(435) Shaju, K.; Jiao, F.; Débart, A.; Bruce, P. *Physical chemistry chemical physics : PCCP* **2007**, *9*, 1837.

(436) Pralong, V. *Solid State Ionics* **2004**, *166*.

(437) Z, F. U.; Y, W.; Y, Z.; Q, Q. I. N. *Solid State Ionics* **2004**, *170*.

(438) Paul, A. C.; John, T. S. I. *Electrochimica Acta* **2002**, *47*.

(439) Ying, W.; Qi-Zong, Q. *Journal of the Electrochemical Society* **2002**, *149*.

(440) Binni, V.; Reddy, M. V.; Zhu, Y.; Chang Sheh, L.; Teo Choon, H.; Rao, G. V. S.; Chowdari, B. V. R.; Andrew Thye Shen, W.; Chwee Teck, L.; Chorng-Haur, S. *Chemistry of Materials* **2008**, *20*.

(441) Xiong, W.; Li; Yan'ge, Z.; Shutao, W.; Zude, Z.; Linfeng, F.; Yitai, Q. *Crystal Growth & Design* **2006**, *6*.

(442) Huang, X. H.; Tu, J. P.; Zhang, B.; Zhang, C. Q.; Li, Y.; Yuan, Y. F.; Wu, H. M. *Journal of Power Sources* **2006**, *161*.

(443) Eiji, H.; Shinobu, F.; Itaru, H.; Haoshen, Z. *Electrochemistry Communications* **2006**, *8*.

(444) Ci, S.; Zou, J.; Zeng, G.; Peng, Q.; Luo, S.; Wen, Z. *Rsc Advances* **2012**, *2*, 5185.

(445) Needham, S. A.; Wang, G. X.; Liu, H. K.; Yang, L. *Journal of Nanoscience and Nanotechnology* **2006**, *6*, 77.

(446) Zhong, J.; Wang, X. L.; Xia, X. H.; Gu, C. D.; Xiang, J. Y.; Zhang, J.; Tu, J. P. *Journal of Alloys and Compounds* **2011**, *509*, 3889.

(447) Huang, X. H.; Tu, J. P.; Zhang, C. Q.; Zhou, F. *Electrochimica Acta* **2010**, *55*, 8981.

(448) Yuan, Y. F.; Xia, X. H.; Wu, J. B.; Yang, J. L.; Chen, Y. B.; Guo, S. Y. *Electrochemistry Communications* **2010**, *12*, 890.

(449) Huang, X. H.; Tu, J. P.; Xia, X. H.; Wang, X. L.; Xiang, J. Y.; Zhang, L.; Zhou, Y. *Journal of Power Sources* **2009**, *188*, 588.

(450) Huang, X. H.; Yuan, Y. F.; Wang, Z.; Zhang, S. Y.; Zhou, F. *Journal of Alloys and Compounds* **2011**, *509*, 3425.

(451) Hosono, E.; Fujihara, S.; Honma, I.; Zhou, H. S. *Electrochemistry Communications* **2006**, *8*, 284.

(452) Mai, Y. J.; Xia, X. H.; Chen, R.; Gu, C. D.; Wang, X. L.; Tu, J. P. *Electrochimica Acta* **2012**, *67*, 73.

(453) Li, X.; Dhanabalan, A.; Wang, C. *Journal of Power Sources* **2011**, *196*, 9625.

(454) Li, X.; Dhanabalan, A.; Bechtold, K.; Wang, C. *Electrochemistry Communications* **2010**, *12*, 1222.

(455) Wang, C.; Wang, D.-L.; Wang, Q.-M.; Chen, H.-J. *Chinese Journal of Inorganic Chemistry* **2010**, *26*, 757.

(456) Huang, X. H.; Tu, J. P.; Zeng, Z. Y.; Xiang, J. Y.; Zhao, X. B. *Journal of the Electrochemical Society* **2008**, *155*, A438.

(457) Mai, Y. J.; Tu, J. P.; Xia, X. H.; Gu, C. D.; Wang, X. L. *Journal of Power Sources* **2011**, *196*, 6388.

(458) Cheng, M.-Y.; Hwang, B.-J. *Journal of Power Sources* **2010**, *195*, 4977.

(459) Huang, Y.; Huang, X.-l.; Lian, J.-s.; Xu, D.; Wang, L.-m.; Zhang, X.-b. *Journal of Materials Chemistry* **2012**, *22*, 2844.

(460) Qiu, D.; Xu, Z.; Zheng, M.; Zhao, B.; Pan, L.; Pu, L.; Shi, Y. *Journal of Solid State Electrochemistry* **2012**, *16*, 1889.

(461) Zou, Y.; Wang, Y. *Nanoscale* **2011**, *3*, 2615.

(462) Xu, C.; Sun, J.; Gao, L. *Journal of Power Sources* **2011**, *196*, 5138.

(463) Linden, D.; Reddy, T. B. *New York* **2002**.

(464) Takashi, I.; Yoshinori, T.; Joji, N.; Hiromichi, O. *Journal of Power Sources* **1980**, *5*.

(465) Bates, R.; Jumel, Y. *Academic Press, London* **1983**.

(466) Podhájecký, P.; Klápště, B.; Novák, P.; Mrha, J.; Moshtev, R.; Manev, V.; Nassalevska, A. *Journal of Power Sources* **1985**, *14*.

(467) Grugeon, S.; Laruelle, S.; Herrera-Urbina, R.; Dupont, L.; Poizot, P.; Tarascon, J. M. *Journal of the Electrochemical Society* **2001**, *148*.

(468) Débart, A.; Dupont, L.; Poizot, P.; Leriche, J. B.; Tarascon, J. M. *Journal of the Electrochemical Society* **2001**, *148*.

(469) Zhang, D. W.; Chen, C. H.; Zhang, J.; Ren, F. *Chemistry of Materials* **2005**, *17*.

(470) Morales, J.; Sánchez, L.; Bijani, S.; Martínez, L.; Gabás, M.; Ramos-Barrado, J. R. *Electrochemical and Solid-State Letters* **2005**, *8*.

(471) Lee, Y. H.; Leu, I. C.; Liao, C. L.; Chang, S. T.; Wu, M. T.; Yen, J. H.; Fung, K. Z. *Electrochemical and Solid-State Letters* **2006**, *9*.

(472) Zhang, C. Q.; Tu, J. P.; Huang, X. H.; Yuan, Y. F.; Chen, X. T.; Mao, F. *Journal of Alloys and Compounds* **2007**, *441*.

(473) Xiang, J. Y.; Tu, J. P.; Yuan, Y. F.; Huang, X. H.; Zhou, Y.; Zhang, L. *Electrochemistry Communications* **2009**, *11*.

(474) Ji Chan, P.; Jeonghan, K.; Hyuksang, K.; Hyunjoon, S. *Advanced Materials* **2009**, *21*.

(475) Hongbo, W.; Qinmin, P.; Jianwei, Z.; Weitao, C. *Journal of Alloys and Compounds* **2009**, *476*.

(476) Chen, L. B.; Lu, N.; Xu, C. M.; Yu, H. C.; Wang, T. H. *Electrochimica Acta* **2009**, *54*.

(477) Fu-Sheng, K.; Ling, H.; Guo-Zhen, W.; Lian-Jie, X.; Jun-Tao, L.; Bo, Z.; Shu-Ru, C.; Xiao-Yong, F.; Shi-Gang, S. *Electrochimica Acta* **2009**, *54*.

(478) Xiang, J. Y.; Tu, J. P.; Zhang, L.; Zhou, Y.; Wang, X. L.; Shi, S. J. *Journal of Power Sources* **2010**, *195*.

(479) Zeng, Q.; Jiang, X.; Yu, A.; Lu, G. *Nanotechnology* **2007**, *18*, 35708.

(480) Ning, Z.; Ran, Y.; Zhong, W.; Rongrong, S.; Haidong, W.; Guanzhou, Q.; Xiaohe, L. *Materials Chemistry and Physics* **2008**, *111*.

(481) Gillot, F.; Monconduit, L.; Doublet, M. L. *Chemistry of Materials* **2005**, *17*.

(482) Oumellal, Y.; Rougier, A.; Nazri, G.; Tarascon, J. M.; Aymard, L. *Nature Materials* **2008**, *7*, 916.

(483) Dey, A. N. *Journal of the Electrochemical Society* **1971**, *118*.

(484) Dey, A. *Journal of the Electrochemical Society* **1971**, *118*, 1547.

(485) Thackeray, M. M.; Vaughey, J. T.; Johnson, C. S.; Kropf, A. J.; Benedek, R.; Fransson, L. M. L.; Edstrom, K. *Journal of Power Sources* **2003**, *113*.

(486) Timmons, A.; Dahn, J. R. *Journal of the Electrochemical Society* **2006**, *153*.

(487) Idota, Y. *Science* **1997**, *276*.

(488) Vaughey, J. T.; Johnson, C. S.; Kropf, A. J.; Benedek, R.; Thackeray, M. M.; Tostmann, H.; Sarakonsri, T.; Hackney, S.; Fransson, L.; Edström, K.; Thomas, J. O. *Journal of Power Sources* **2001**, *97–98*, 194.

(489) Kepler, K. D.; Vaughey, J. T.; Thackeray, M. M. *Electrochemical and Solid-State Letters* **1999**, *2*, 307.

(490) Fransson, L.; Vaughey, J.; Edström, K.; Thackeray, M. *Journal of the Electrochemical Society* **2003**, *150*, A86.

(491) Goward, G. R.; Taylor, N. J.; Souza, D. C. S.; Nazar, L. F. *Journal of Alloys and Compounds* **2001**, *329*.

(492) Wen, C. J.; Robert, A. H. *Journal of Solid State Chemistry* **1981**, *37*.

(493) Weydanz, W. J.; Wohlfahrt-Mehrens, M.; Huggins, R. A. *Journal of Power Sources* **1999**, *81-82*.

(494) Gao, B.; Sinha, S.; Fleming, L.; Zhou, O. *Advanced Materials* **2001**, *13*.

(495) Pimpa, L.; Young-Il, J.; Nancy, J. D.; Yet-Ming, C. *Acta Materialia* **2003**, *51*.

(496) Andreas, N.; Robert, A. H.; Werner, W. *Journal of Power Sources* **2003**, *119-121*.

(497) Obrovac, M. N.; Leif, C. *Electrochemical and Solid-State Letters* **2004**, *7*.

(498) Hatchard, T. D.; Dahn, J. R. *Journal of the Electrochemical Society* **2004**, *151*.

(499) Jing, L.; Dahn, J. R. *Journal of the Electrochemical Society* **2007**, *154*.

(500) Ji Heon, R.; Jae Woo, K.; Yung-Eun, S.; Seung, M. O. *Electrochemical and Solid-State Letters* **2004**, *7*.

(501) Li, H. *Solid State Ionics* **2000**, *135*.

(502) Hong, L. *Electrochemical and Solid-State Letters* **1999**, *2*.

(503) Wei-Ren, L.; Zheng-Zao, G.; Wen-Shiue, Y.; Deng-Tswen, S.; Hung-Chun, W.; Mo-Hua, Y.; Nae-Lih, W. *Journal of Power Sources* **2005**, *140*.

(504) Guo, Z. P.; Wang, J. Z.; Liu, H. K.; Dou, S. X. *Journal of Power Sources* **2005**, *146*.

(505) Cui, L.; Ruffo, R.; Chan, C.; Peng, H.; Cui, Y. *Nano Letters* **2008**.

(506) Berla, L.; Nix, W.; Cui, Y. *Proceedings of the ...* **2012**.

(507) Lee, S. W.; McDowell, M. T.; Choi, J. W.; Cui, Y. *Nano Letters* **2011**, *11*, 3034.

(508) Hui, W.; Yi, C. *Nano Today* **2012**, *7*.

(509) Yan, G.; Fendan, W.; Yong, W. *Advanced Functional Materials* **2013**, *23*.

(510) Ghassemi, H.; Au, M.; Chen, N.; Heiden, P. A.; Yassar, R. S. *Acs Nano* **2011**, *5*, 7805.

(511) Chockla, A. M.; Harris, J. T.; Akhavan, V. A.; Bogart, T. D.; Holmberg, V. C.; Steinhagen, C.; Mullins, C. B.; Stevenson, K. J.; Korgel, B. A. *Journal of the American Chemical Society* **2011**, *133*, 20914.

(512) Steven, A. K.; Ronald, A. R.; Brett, A. C.; Jianwei, L.; Judy, W.; Jun, L. *Journal of Materials Chemistry A* **2013**, *1*.

(513) Nguyen, H.; Yao, F.; Zamfir, M.; Biswas…, C. *Advanced Energy ...* **2011**.

(514) Xu, W.; Vegunta, S. S. S.; Flake, J. C. *Journal of Power Sources* **2011**, *196*, 8583.

(515) Lu, Z.; Zhu, J.; Sim, D.; Shi, W.; Tay, Y. Y.; Ma, J.; Hng, H. H.; Yan, Q. *Electrochimica Acta* **2012**.

(516) Payne, S.; Moore, J.; Boudjouk, P.; Pederson…, L. *... and Solid-State Letters* **2010**.

(517) Chan, C.; Patel, R.; O'Connell, M.; Korgel, B.; Cui, Y. *Acs Nano* **2010**, *4*, 1443.

(518) Huang, R.; Fan, X.; Shen, W.; Zhu, J. *Applied Physics Letters* **2009**, *95*.

(519) Huang, Z.; Geyer, N.; Werner, P.; de Boor, J.; Gösele, U. *Advanced materials (Deerfield Beach, Fla.)* **2011**, *23*, 285.

(520) Wanli, X.; Sri Sai, S. V.; John, C. F. *Journal of Power Sources* **2011**, *196*.

(521) Liu, X.; Zheng, H.; Zhong, L.; Huang, S.; Karki, K.; Zhang, L.; Liu, Y.; Kushima, A.; Liang, W.; Wang, J.; Cho, J.-H.; Epstein, E.; Dayeh, S.; Picraux, S.; Zhu, T.; Li, J.; Sullivan, J.; Cumings, J.; Wang, C.; Mao, S.; Ye, Z.; Zhang, S.; Huang, J. *Nano Letters* **2011**, *11*, 3312.

(522) Riccardo, R.; Seung Sae, H.; Candace, K. C.; Robert, A. H.; Yi, C. *The Journal of Physical Chemistry C* **2009**, *113*.

(523) Chan, C.; Ruffo, R.; Hong, S.; Cui, Y. *Journal of Power Sources* **2009**.

(524) Zhou, S.; Liu, X.; Wang, D. *Nano Letters* **2010**, *10*, 860.

(525) Simon, G. K.; Maruyama, B.; Durstock, M. F.; Burton, D. J.; Goswami, T. *Journal of Power Sources* **2011**, *196*, 10254.

(526) Hwang, T.; Lee, Y.; Kong, B.-S.; Seo, J.-S.; Choi, J. *Nano Letters* **2012**, *12*, 802.

(527) Cui, L.-F.; Hu, L.; Wu, H.; Choi, J. W.; Cui, Y. *Journal of the Electrochemical Society* **2011**, *158*, A592.

(528) Kovalenko, I.; Zdyrko, B.; Magasinski, A.; Hertzberg, B.; Milicev, Z.; Burtovyy, R.; Luzinov, I.; Yushin, G. *Science* **2011**, *334*, 75.

(529) Liu, G.; Xun, S.; Vukmirovic, N.; Song, X.; Olalde-Velasco, P.; Zheng, H.; Battaglia, V. S.; Wang, L.; Yang, W. *Advanced Materials* **2011**, *23*, 4679.

(530) Yao, Y.; McDowell, M. T.; Ryu, I.; Wu, H.; Liu, N.; Hu, L.; Nix, W. D.; Cui, Y. *Nano Letters* **2011**, *11*, 2949.

(531) Ma, H.; Cheng, F.; Chen, J. Y.; Zhao, J. Z.; Li, C. S.; Tao, Z. L.; Liang, J. *Advanced Materials* **2007**, *19*, 4067.

(532) Park, M.-H.; Kim, M.; Joo, J.; Kim, K.; Kim, J.; Ahn, S.; Cui, Y.; Cho, J. *Nano Letters* **2009**, *9*, 3844.

(533) Song, T.; Cheng, H.; Choi, H.; Lee, J.-H.; Han, H.; Lee, D. H.; Yoo, D. S.; Kwon, M.-S.; Choi, J.-M.; Doo, S. G. *Acs Nano* **2011**, *6*, 303.

(534) Song, T.; Xia, J.; Lee, J.-H.; Lee, D. H.; Kwon, M.-S.; Choi, J.-M.; Wu, J.; Doo, S. K.; Chang, H.; Park, W. I. *Nano Letters* **2010**, *10*, 1710.

(535) Aurbach, D. *Journal of Power Sources* **2000**, *89*, 206.

(536) Beaulieu, L.; Hatchard, T.; Bonakdarpour, A.; Fleischauer, M.; Dahn, J. *Journal of the Electrochemical Society* **2003**, *150*, A1457.

(537) Beaulieu, L.; Eberman, K.; Turner, R.; Krause, L.; Dahn, J. *Electrochemical and Solid-State Letters* **2001**, *4*, A137.

(538) Hertzberg, B.; Alexeev, A.; Yushin, G. *Journal of the American ...* **2010**.

(539) Wu, H.; Chan, G.; Choi, J. W.; Ryu, I.; Yao, Y.; McDowell, M. T.; Lee, S. W.; Jackson, A.; Yang, Y.; Hu, L.; Cui, Y. *Nat Nano* **2012**, *7*, 310.

(540) Hu, L.; Wu, H.; Gao, Y.; Cao, A.; Li, H.; McDough, J.; Xie, X.; Zhou, M.; Cui, Y. *Advanced Energy Materials* **2011**, *1*, 523.

(541) Liu, N.; Wu, H.; McDowell, M. T.; Yao, Y.; Wang, C.; Cui, Y. *Nano Letters* **2012**, *12*, 3315.

(542) Anani, A.; Huggins, R. A. *Journal of Power Sources* **1992**, *38*.

(543) Anani, A.; Huggins, R. A. *Journal of Power Sources* **1992**, *38*.

(544) Hansu, K. *Journal of the Electrochemical Society* **1999**, *146*.

(545) Toshihiro, M.; Kozo, W.; Daisuke, T.; Shinichi, M.; Ichiro, N. *Journal of Solid State Chemistry* **2000**, *153*.

(546) Roberts, G. A.; Cairns, E. J.; Reimer, J. A. *Journal of Power Sources* **2002**, *110*.

(547) Wolfenstine, J. *Journal of Power Sources* **2003**, *124*.

(548) Wang, G. X.; Sun, L.; Bradhurst, D. H.; Zhong, S.; Dou, S. X.; Liu, H. K. *Journal of Power Sources* **2000**, *88*.

(549) Il-seok, K. *Electrochemical and Solid-State Letters* **1999**, *3*.

(550) Il-seok, K.; Blomgren, G. E.; Kumta, P. N. *Electrochemical and Solid-State Letters* **2003**, *6*.

(551) Il-seok, K.; Blomgren, G. E.; Kumta, P. N. *Journal of the Electrochemical Society* **2005**, *152*.

(552) Noriyuki, T.; Ryuji, O.; Masahisa, F.; Maruo, K.; Shin, F. *Journal of the Electrochemical Society* **2003**, *150*.

(553) Noriyuki, T.; Ryuji, O.; Masahisa, F.; Shin, F.; Maruo, K.; Ikuo, Y. *Journal of Power Sources* **2002**, *107*.

(554) Beaulieu, L. Y.; Hatchard, T. D.; Bonakdarpour, A.; Fleischauer, M. D.; Dahn, J. R. *Journal of the Electrochemical Society* **2003**, *150*.

(555) Mukaibo, H.; Momma, T.; Shacham-Diamand, Y.; Osaka, T.; Kodaira, M. *Electrochemical and Solid-State Letters* **2007**, *10*.

(556) Keith, D. K. *Electrochemical and Solid-State Letters* **1999**, *2*.

(557) Ou, M. *Journal of the Electrochemical Society* **1999**, *146*.

(558) Fransson, L.; Nordström, E.; Edström, K.; Häggström, L.; Vaughey, J. T.; Thackeray, M. M. *Journal of the Electrochemical Society* **2002**, *149*.

(559) Jun, Y. *Electrochemical and Solid-State Letters* **1999**, *2*.

(560) Yang, J. *Solid State Ionics* **2000**, *133*.

(561) Mario, W.; Jürgen, O. B.; Martin, W. *Journal of Power Sources* **2001**, *94*.

(562) Larcher, D.; Beaulieu, L. Y.; Mao, O.; George, A. E.; Dahn, J. R. *Journal of the Electrochemical Society* **2000**, *147*.

(563) Vaughey, J. T.; Owejan, J.; Thackeray, M. M. *Electrochemical and Solid-State Letters* **2007**, *10*.

(564) Hiroki, S.; Hitohiko, H.; Yuichi, A.; Takao, E. *Journal of Power Sources* **2003**, *119-121*.

(565) Kim, H. *Solid State Ionics* **2001**, *144*.

(566) Dominique, L.; Prakash, A. S.; Juliette, S.; Mathieu, M.; Jean-Marie, T. *Chemistry of Materials* **2004**, *16*.

(567) Larcher, D.; Beaulieu, L. Y.; MacNeil, D. D.; Dahn, J. R. *Journal of the Electrochemical Society* **2000**, *147*.

(568) Ou, M. *Journal of the Electrochemical Society* **1999**, *146*.

(569) Mao, O. *Electrochemical and Solid-State Letters* **1999**, *2*.

(570) Mario, W.; Martin, W.; Jürgen, O. B. *Journal of Power Sources* **2002**, *105*.

(571) Wenji, W.; Yurong, Z. *Solid State Ionics* **1996**, *86-88*.

(572) Jingtian, Y.; Masashi, W.; Seiji, Y.; Kouji, I.; Shigeo, T.; Tetsuo, S. *Journal of the Electrochemical Society* **2003**, *150*.

(573) Ewa, R. n.; Jingtian, Y.; Akiko, K.; Masahi, W.; Shigeo, T.; Tetsuo, S. *Journal of the Electrochemical Society* **2005**, *152*.

(574) Beaulieu, L.; Larcher, D.; Dunlap, R. A.; Dahn, J. R. *Journal of Alloys and Compounds* **2000**, *297*.

(575) Hitomi, M.; Tomohide, S.; Tokihiko, Y.; Toshiyuki, M.; Tetsuya, O. *Electrochemical and Solid-State Letters* **2003**, *6*.

(576) Jingtian, Y.; Masashi, W.; Shigeo, T.; Tetsuo, S. *Journal of the Electrochemical Society* **2004**, *151*.

(577) Beattie, S. D.; Dahn, J. R. *Journal of the Electrochemical Society* **2005**, *152*.

(578) Tarascon, J. M. *Philos T R Soc A* **2010**, *368*, 3227.

(579) Tarascon, J. M. *Nat Chem* **2010**, *2*, 510.

(580) Palomares, V.; Serras, P.; Villaluenga, I.; Hueso, K. B.; Carretero-Gonzalez, J.; Rojo, T. *Energy & Environmental Science* **2012**, *5*, 5884.

(581) Ong, S. P.; Chevrier, V. L.; Hautier, G.; Jain, A.; Moore, C.; Kim, S.; Ma, X. H.; Ceder, G. *Energy & Environmental Science* **2011**, *4*, 3680.

(582) Verónica, P.; Paula, S.; Irune, V.; Karina, B. H.; Javier, C.-G.; Teófilo, R. *Energy & Environmental Science* **2012**, *5*.

(583) Zaghib, K.; Trottier, J.; Hovington, P.; Brochu, F.; Guerfi, A.; Mauger, A.; Julien, C. M. *Journal of Power Sources* **2011**, *196*, 9612.

(584) Tepavcevic, S.; Xiong, H.; Stamenkovic, V. R.; Zuo, X.; Balasubramanian, M.; Prakapenka, V. B.; Johnson, C. S.; Rajh, T. *ACS Nano* **2012**, *6*, 530.

(585) Gocheva, I. D.; Nishijima, M.; Doi, T.; Okada, S.; Yamaki, J.; Nishida, T. *Journal of Power Sources* **2009**, *187*, 247.

(586) Yamada, Y.; Doi, T.; Tanaka, I.; Okada, S.; Yamaki, J. *Journal of Power Sources* **2011**, *196*, 4837.

(587) Berthelot, R.; Carlier, D.; Delmas, C. *Nature Materials* **2011**, *10*, 74.

(588) Doeff, M. M.; Ma, Y. P.; Peng, M. Y.; Visco, S. J.; Dejonghe, L. C. *Energy Environment Economics: 28th Intersociety Energy Conversion Engineering Conference (Iecec-93), Vol 1* **1993**, 1111.

(589) Yabuuchi, N.; Kajiyama, M.; Iwatate, J.; Nishikawa, H.; Hitomi, S.; Okuyama, R.; Usui, R.; Yamada, Y.; Komaba, S. *Nature Materials* **2012**, *11*, 512.

(590) Kim, D.; Lee, E.; Slater, M.; Lu, W. Q.; Rood, S.; Johnson, C. S. *Electrochem Commun* **2012**, *18*, 66.

(591) Komaba, S.; Takei, C.; Nakayama, T.; Ogata, A.; Yabuuchi, N. *Electrochem Commun* **2010**, *12*, 355.

(592) Xia, X.; Dahn, J. R. *Electrochemical and Solid State Letters* **2012**, *15*, A1.

(593) Mendiboure, A.; Delmas, C.; Hagenmuller, P. *Journal of Solid State Chemistry* **1985**, *57*, 323.

(594) Stoyanova, R.; Carlier, D.; Sendova-Vassileva, M.; Yoncheva, M.; Zhecheva, E.; Nihtianova, D.; Delmas, C. *Journal of Solid State Chemistry* **2010**, *183*, 1372.

(595) Hamani, D.; Ati, M.; Tarascon, J.-M.; Rozier, P. *Electrochem Commun* **2011**, *13*, 938.

(596) Recham, N.; Chotard, J. N.; Dupont, L.; Djellab, K.; Armand, M.; Tarascon, J. M. *Journal of The Electrochemical Society* **2009**, *156*, A993.

(597) Ati, M.; Dupont, L.; Recham, N.; Chotard, J. N.; Walker, W. T.; Davoisne, C.; Barpanda, P.; Sarou-Kanian, V.; Armand, M.; Tarascon, J. M. *Chem Mater* **2010**, *22*, 4062.

(598) Barpanda, P.; Chotard, J. N.; Recham, N.; Delacourt, C.; Ati, M.; Dupont, L.; Armand, M.; Tarascon, J. M. *Inorg Chem* **2010**, *49*, 7401.

(599) Reynaud, M.; Barpanda, P.; Rousse, G.; Chotard, J. N.; Melot, B. C.; Recham, N.; Tarascon, J. M. *Solid State Sci* **2012**, *14*, 15.

(600) Cao, Y. L.; Xiao, L. F.; Sushko, M. L.; Wang, W.; Schwenzer, B.; Xiao, J.; Nie, Z. M.; Saraf, L. V.; Yang, Z. G.; Liu, J. *Nano Letters* **2012**, *12*, 3783.

(601) Cao, Y. L.; Xiao, L. F.; Wang, W.; Choi, D. W.; Nie, Z. M.; Yu, J. G.; Saraf, L. V.; Yang, Z. G.; Liu, J. *Advanced Materials* **2011**, *23*, 3155.

(602) Brian, L. E.; Linda, F. N. *Current Opinion in Solid State and Materials Science* **2012**, *16*.

(603) Yazami, R.; Lebrun, N.; Bonneau, M.; Molteni, M. *Journal of Power Sources* **1995**, *54*, 389.

(604) Berthelot, R.; Carlier, D.; Delmas, C. *Nature Materials* **2011**, *10*, 74.

(605) Jean-Jacques, B.; Claude, D.; Claude, F.; Paul, H. *Materials Research Bulletin* **1980**, *15*.

(606) Kikkawa, S.; Miyazaki, S.; Koizumi, M. *Journal of Power Sources* **1985**, *14*.

(607) Tarascon, J. *Solid State Ionics* **1986**, *22*.

(608) Claude, F.; Guy, M.; Jean-Maurice, R.; Paul, H. *Journal of Solid State Chemistry* **1973**, *6*.

(609) Shacklette, L. W. *Journal of the Electrochemical Society* **1988**, *135*.

(610) Berthelot, R.; Carlier, D.; Delmas, C. *Nature Materials* **2010**, *10*, 74.

(611) Marca, M. D. *Journal of the Electrochemical Society* **1993**, *140*.

(612) Bhide, A.; Hariharan, K. *Solid State Ionics* **2011**, *192*, 360.

(613) Carlier, D.; Cheng, J.; Berthelot, R.; Guignard, M.; Yoncheva, M.; Stoyanova, R.; Hwang, B.; Delmas, C. *Dalton Transactions* **2011**, *40*, 9306.

(614) Zhonghua, L.; Dahn, J. R. *Journal of the Electrochemical Society* **2001**, *148*.

(615) Parant, J.-P.; Olazcuaga, R.; Devalette, M.; Fouassier, C.; Hagenmuller, P. *Journal of Solid State Chemistry* **1971**, *3*, 1.

(616) Velikokhatnyi, O.; Chang, C.-C.; Kumta, P. *Journal of the Electrochemical Society* **2003**, *150*, A1262.

(617) Mendiboure, A.; Delmas, C.; Hagenmuller, P. *Journal of Solid State Chemistry* **1985**, *57*, 323.

(618) Yazami, R.; Lebrun, N.; Bonneau, M.; Molteni, M. *Journal of Power Sources* **1995**, *54*.

(619) Marca, M. D. *Journal of the Electrochemical Society* **1994**, *141*.

(620) Kim, D.; Kang, S. H.; Slater, M.; Rood, S.; Vaughey, J. T.; Karan, N.; Balasubramanian, M.; Johnson, C. S. *Advanced Energy Materials* **2011**, *1*, 333.

(621) Shyue Ping, O.; Vincent, L. C.; Geoffroy, H.; Anubhav, J.; Charles, M.; Sangtae, K.; Xiaohua, M.; Gerbrand, C. *Energy & Environmental Science* **2011**, *4*.

(622) Sauvage, F.; Laffont, L.; Tarascon, J. M.; Baudrin, E. *Inorganic Chemistry* **2007**, *46*.

(623) Marca, M. D. *Journal of the Electrochemical Society* **1996**, *143*.

(624) Tevar, A. D.; Whitacre, J. F. *Journal of the Electrochemical Society* **2010**, *157*.

(625) Whitacre, J. F.; Tevar, A.; Sharma, S. *Electrochemistry Communications* **2010**, *12*.

(626) Yamada, A.; Chung, S. C.; Hinokuma, K. *Journal of the Electrochemical Society* **2001**, *148*.

(627) Burba, C.; Frech, R. *Spectrochimica acta. Part A, Molecular and biomolecular spectroscopy* **2006**, *65*, 44.

(628) Moreau, P.; Guyomard, D.; Gaubicher, J.; Boucher, F. *Chemistry of Materials* **2010**, *22*.

(629) Abigail, R. W.; Paul, E. R.; Francis, J. D. *Journal of Solid State Chemistry* **1989**, *81*.

(630) Zaghib, K.; Trottier, J.; Hovington, P.; Brochu, F.; Guerfi, A.; Mauger, A.; Julien, C. M. *Journal of Power Sources* **2011**, *196*.

(631) Lee, K. T.; Ramesh, T.; Nan, F.; Botton, G.; Nazar, L. F. *Chem Mater* **2011**, *23*, 3593.

(632) Barker, J.; Saidi, M.; Swoyer, J. *Electrochemical and Solid-State Letters* **2003**, *6*, A1.

(633) Zhao, J.; He, J.; Ding, X.; Zhou, J.; Ma, Y. o.; Wu, S.; Huang, R. *Journal of Power Sources* **2010**, *195*, 6854.

(634) Zhuo, H.; Wang, X.; Tang, A.; Liu, Z.; Gamboa, S.; Sebastian, P. *Journal of Power Sources* **2006**, *160*, 698.

(635) LIU, Z.-m.; WANG, X.-y.; WANG, Y.; TANG, A.-p.; YANG, S.-y.; HE, L.-f. *Transactions of Nonferrous Metals Society of China* **2008**, *18*, 346.

(636) Massa, W.; Yakubovich, O. V.; Dimitrova, O. V. *Solid State Sciences* **2002**, *4*, 495.

(637) Sauvage, F.; Laffont, L.; Tarascon, J.-M.; Baudrin, E. *Inorganic Chemistry* **2007**, *46*, 3289.

(638) Swafford, S. H.; Holt, E. M. *Solid State Sciences* **2002**, *4*, 807.

(639) Sanz, F.; Parada, C.; Ruíz-Valero, C. *J. Mater. Chem.* **2000**, *11*, 208.

(640) Recham, N.; Chotard, J.-N.; Dupont, L.; Djellab, K.; Armand, M.; Tarascon, J.-M. *Journal of the Electrochemical Society* **2009**, *156*, A993.

(641) Ellis, B. L.; Makahnouk, W. M.; Rowan-Weetaluktuk, W.; Ryan, D.; Nazar, L. F. *Chemistry of Materials* **2009**, *22*, 1059.

(642) Wolfenstine, J.; Allen, J. *Journal of Power Sources* **2005**, *142*, 389.

(643) Okada, S.; Ueno, M.; Uebou, Y.; Yamaki, J.-i. *Journal of Power Sources* **2005**, *146*, 565.

(644) Hasegawa, Y.; Imanaka, N. *Solid State Ionics* **2005**, *176*, 2499.

(645) Hoshina, K.; Dokko, K.; Kanamura, K. *Journal of the Electrochemical Society* **2005**, *152*, A2138.

(646) Kobayashi, E.; Plashnitsa, L. S.; Doi, T.; Okada, S.; Yamaki, J.-i. *Electrochemistry Communications* **2010**, *12*, 894.

(647) Uebou Y, K. T., Okada S, Yamaki J-I. Kyushu University NII-electronic; 2002;16:1., l. s. T. R. I. A. M. S. **2002**, *16*, 1.

(648) Barker, J.; Gover, R.; Burns, P.; Bryan, A. *Electrochemical and Solid-State Letters* **2005**, *8*, A285.

(649) Plashnitsa, L. S.; Kobayashi, E.; Noguchi, Y.; Okada, S.; Yamaki, J.-i. *Journal of the Electrochemical Society* **2010**, *157*, A536.

(650) Chevrier, V.; Ceder, G. *Journal of the Electrochemical Society* **2011**, *158*, A1011.

(651) Komaba, S.; Mikumo, T.; Yabuuchi, N.; Ogata, A.; Yoshida, H.; Yamada, Y. *Journal of the Electrochemical Society* **2010**, *157*, A60.

(652) Alcantara, R.; Jimenez-Mateos, J. M.; Lavela, P.; Tirado, J. L. *Electrochemistry Communications* **2001**, *3*, 639.

(653) Alcantara, R.; Lavela, P.; Ortiz, G. F.; Tirado, J. L. *Electrochemical and Solid State Letters* **2005**, *8*, A222.

(654) Stevens, D. A.; Dahn, J. R. *Journal of the Electrochemical Society* **2000**, *147*, 1271.

(655) Asher, R. *Journal of Inorganic and Nuclear Chemistry* **1959**, *10*, 238.

(656) Ge, P.; Fouletier, M. *Solid State Ionics* **1988**, *28*, 1172.

(657) Stevens, D.; Dahn, J. *Journal of the Electrochemical Society* **2001**, *148*, A803.

(658) Sangster, J. *Journal of Phase Equilibria and Diffusion* **2007**, *28*, 571.

(659) Doeff, M. M.; Ma, Y.; Visco, S. J.; De Jonghe, L. C. *Journal of the Electrochemical Society* **1993**, *140*, L169.

(660) Alcántara, R.; Jiménez-Mateos, J. M.; Lavela, P.; Tirado, J. L. *Electrochemistry Communications* **2001**, *3*, 639.

(661) Alcántara, R.; Lavela, P.; Ortiz, G. F.; Tirado, J. L. *Electrochemical and Solid-State Letters* **2005**, *8*, A222.

(662) Wenzel, S.; Hara, T.; Janek, J.; Adelhelm, P. *Energy & Environmental Science* **2011**, *4*, 3342.

(663) Stevens, D.; Dahn, J. *Journal of the Electrochemical Society* **2000**, *147*, 1271.

(664) Dahn, J.; Zheng, T.; Yinghu, L.; Xue, J. *Science* **1995**, *270*, 590.

(665) Park, S. I.; Gocheva, I.; Okada, S.; Yamaki, J.-i. *Journal of the Electrochemical Society* **2011**, *158*, A1067.

(666) Senguttuvan, P.; Rousse, G. l.; Seznec, V.; Tarascon, J.-M.; Palacin, M. R. *Chemistry of Materials* **2011**, *23*, 4109.

(667) Didier, C.; Guignard, M.; Denage, C.; Szajwaj, O.; Ito, S.; Saadoune, I.; Darriet, J.; Delmas, C. *Electrochemical and Solid-State Letters* **2011**, *14*, A75.

(668) Szajwaj, O.; Gaudin, E.; Weill, F.; Darriet, J.; Delmas, C. *Inorganic Chemistry* **2009**, *48*, 9147.

(669) Hamani, D.; Ati, M.; Tarascon, J.-M.; Rozier, P. *Electrochemistry Communications* **2011**, *13*, 938.

(670) Darwiche, A.; Marino, C.; Sougrati, M.; Fraisse, B.; Stievano, L.; Monconduit, L. *Journal of the American Chemical Society* **2012**, *134*, 20805.

(671) Handbook, A. *ASM International, Materials Park, OH* **1992**, 2.

(672) Xiao, L. F.; Cao, Y. L.; Xiao, J.; Wang, W.; Kovarik, L.; Nie, Z. M.; Liu, J. *Chemical Communications* **2012**, *48*, 3321.

(673) Qian, J.; Chen, Y.; Wu, L.; Cao, Y.; Ai, X.; Yang, H. *Chemical Communications* **2012**, *48*, 7070.

(674) http://mtixtl.com/ThreeZonesSplitTubeFurnace-OTF-1200X-III.aspx.

(675) West, A. R. *Solid state chemistry and its applications*; John Wiley & Sons, 2007.

(676) Goodenough, J.; Kafalas, J.; Longo, J.; Hagenmuller, P. *High Pressure Synthesis* **1972**.

(677) Griffiths, P.; De Haseth, J. A. *Fourier transform infrared spectrometry*; Wiley-Interscience, 2007; Vol. 171.

(678) Skoog, D. A.; West, D. M. *Principles of instrumental analysis*; Saunders College Philadelphia, Pa., 1980.

(679) Anderson, P. W.; Rowell, J. M. *Physical Review Letters* **1963**, *10*, 230.

(680) Bard, A. J.; Faulkner, L. R. *Electrochemical methods: fundamentals and applications*; Wiley New York, 1980; Vol. 2.

(681) Nicholson, R. S.; Shain, I. *Analytical Chemistry* **1964**, *36*, 706.

(682) Heinze, J. *Angewandte Chemie International Edition in English* **1984**, *23*, 831.

(683) Kremer, F.; Schönhals, A. *Broadband dielectric spectroscopy*; Springer Verlag, 2003.

(684) Von Hippel, A. R. *Dielectrics and waves*, 1966.

(685) Volkov, A.; Prokhorov, A. *Radiophysics and quantum electronics* **2003**, *46*, 657.

(686) Hohenberg, P.; Kohn, W. *Physical Review* **1964**, *136*, B864.

(687) Kohn, W.; Sham, L. J. *Self-consistent equations including exchange and correlation effects*; APS, 1965.

(688) Perdew, J. P.; Burke, K.; Ernzerhof, M. *Physical Review Letters* **1996**, *77*, 3865.

(689) Xu, X.; Zhang, Q.; Muller, R. P.; Goddard III, W. A. *Journal of Chemical Physics* **2005**, *122*, Art. No. 014105.

(690) Delley, B. *The Journal of Physical Chemistry A* **2006**, *110*, 13632.

(691) Amadon, B.; Jollet, F.; Torrent, M. *Physical Review B* **2008**, *77*, 155104(1).

(692) Gonze, X.; Amadon, B.; Anglade, P. M.; Beuken, J. M.; Bottin, F.; Boulanger, P.; Bruneval, F.; Caliste, D.; Caracas, R.; Cote, M.; Deutsch, T.; Genovese, L.; Ghosez, P.; Giantomassi, M.; Goedecker, S.; Hamann, D. R.; Hermet, P.; Jollet, F.; Jomard, G.; Leroux, S.; Mancini, M.; Mazevet, S.; Oliveira, M. J. T.; Onida, G.; Pouillon, Y.; Rangel, T.; Rignanese, G. M.; Sangalli, D.; Shaltaf, R.; Torrent, M.; Verstraete, M. J.; Zerah, G.; Zwanziger, J. W. *Comput Phys Commun* **2009**, *180*, 2582.

(693) Gonze, X.; Rignanese, G. M.; Verstraete, M.; Beuken, J. M.; Pouillon, Y.; Caracas, R.; Jollet, F.; Torrent, M.; Zerah, G.; Mikami, M.; Ghosez, P.; Veithen, M.; Raty, J. Y.; V, O.; Bruneval, F.; Reining, L.; Godby, R.; Onida, G.; Hamann, D. R.; Allan, D. C. *Z Kristallogr* **2005**, *220*, 558.

(694) Perdew, J. P.; Wang, Y. *Physical Review B* **1992**, *45*, 13244.

(695) Vanderbilt, D. *Physical Review B* **1990**, *41*, 7892.

(696) Henkelman, G.; Jónsson, H. *The Journal of Chemical Physics* **2000**, *113*, 9978.

(697) Born, M.; Huang, K. *Oxford: University Press* **1954**.

(698) Timothy, S. B.; Julian, D. G.; Catlow, C. R. A.; Peter, D. B. *Journal of Materials Chemistry* **1994**, *4*.

(699) Dick, B.; Overhauser, A. *Physical Review* **1958**, *112*.

(700) Tasker, P. *Journal of Physics C: Solid State Physics* **2001**, *12*, 4977.

(701) Tarascon, J. M.; Armand, M. *Nature* **2001**, *414*, 359.

(702) Padhi, A.; Nanjundaswamy, K.; Goodenough, J. B. d. *Journal of the Electrochemical Society* **1997**, *144*, 1188.

(703) Yamada, A.; Chung, S.; Hinokuma, K. *Electrochem Soc* **2001**, *148*, 224.

(704) Gong, Z. L.; Li, Y. X.; Yang, Y. *Journal of Power Sources* **2007**, *174*, 524.

(705) Armstrong, A. R.; Lyness, C.; Ménétrier, M.; Bruce, P. G. *Chemistry of Materials* **2010**, *22*, 1892.

(706) Kam, K. C.; Gustafsson, T.; Thomas, J. O. *Solid State Ionics* **2011**, *192*, 356.

(707) Fan, X.-Y.; Li, Y.; Wang, J.-J.; Gou, L.; Zhao, P.; Li, D.-L.; Huang, L.; Sun, S.-G. *Journal of Alloys and Compounds* **2010**, *493*, 77.

(708) Nishimura, S.-i.; Hayase, S.; Kanno, R.; Yashima, M.; Nakayama, N.; Yamada, A. *Journal of the American Chemical Society* **2008**, *130*, 13212.

(709) Van der Ven, A.; Ceder, G. *Electrochemical and Solid-State Letters* **2000**, *3*, 301.

(710) Reed, J.; Ceder, G. *Chemical Reviews-Columbus* **2004**, *104*, 4513.

(711) Kang, K.; Morgan, D.; Ceder, G. *Physical Review B* **2009**, *79*, 014305.

(712) Ouyang, C.; Shi, S.; Wang, Z.; Huang, X.; Chen, L. *Physical Review B* **2004**, *69*, 104303.

(713) Fisher, C. A.; Hart Prieto, V. M.; Islam, M. S. *Chemistry of Materials* **2008**, *20*, 5907.

(714) Du, Y. A.; Holzwarth, N. *Physical Review B* **2007**, *76*, 174302.

(715) Vanderbilt, D. *Physical Review B* **1990**, *41*, 7892.

(716) Blöchl, P. E.; Jepsen, O.; Andersen, O. *Physical Review B* **1994**, *49*, 16223.

(717) Anisimov, V. I.; Zaanen, J.; Andersen, O. K. *Physical Review B* **1991**, *44*, 943.

(718) Armstrong, A. R.; Arrouvel, C.; Gentili, V.; Parker, S. C.; Islam, M. S.; Bruce, P. G. *Chemistry of Materials* **2010**, *22*, 6426.

(719) Zhou, F.; Cococcioni, M.; Kang, K.; Ceder, G. *Electrochemistry Communications* **2004**, *6*, 1144.

(720) Wang, L.; Maxisch, T.; Ceder, G. *Physical Review B* **2006**, *73*, 195107.

(721) Zhou, F.; Cococcioni, M.; Marianetti, C. A.; Morgan, D.; Ceder, G. *Physical Review B* **2004**, *70*, 235121.

(722) Jiang, X.; Guo, G. *Physical Review B* **2004**, *69*, 155108.

(723) Osorio-Guillen, J.; Holm, B.; Ahuja, R.; Johansson, B. *Solid State Ionics* **2004**, *167*, 221.

(724) Boultif, A.; Louër, D. *Journal of applied crystallography* **1991**, *24*, 987.

(725) McKinnon, W.; Legrand, A.; Flandrois, S. *NATO ASI Series B* **1987**, *172*, 181.

(726) McKinnon, W.; Bruce, P. *Bruce. PG* **1995**, 163.

(727) Aydinol, M.; Kohan, A.; Ceder, G. *Journal of Power Sources* **1997**, *68*, 664.

(728) Islam, M. S.; Driscoll, D. J.; Fisher, C. A.; Slater, P. R. *Chemistry of Materials* **2005**, *17*, 5085.

(729) Liivat, A.; Thomas, J. *Solid State Ionics* **2009**.

(730) Du, Y. A.; Holzwarth, N. *Journal of the Electrochemical Society* **2007**, *154*, A999.

(731) Vineyard, G. H. *Journal of Physics and Chemistry of Solids* **1957**, *3*, 121.

(732) Van der Ven, A.; Ceder, G. *Physical Review Letters* **2005**, *94*, 45901.

(733) Ensling, D.; Stjerndahl, M.; Nytén, A.; Gustafsson, T.; Thomas, J. O. *Journal of Materials Chemistry* **2009**, *19*, 82.

(734) Politaev, V.; Petrenko, A.; Nalbandyan, V.; Medvedev, B.; Shvetsova, E. *Journal of Solid State Chemistry* **2007**, *180*, 1045.

(735) Dunlap, R.; Mao, O.; Dahn, J. *Physical Review B* **1999**, *59*, 3494.

(736) Huang, J.; Yang, M.; Gu, C.; Zhai, M.; Sun, Y.; Liu, J. *Materials Research Bulletin* **2011**, *46*, 1211.

(737) Zhang, J.; Thurber, A.; Hanna, C.; Punnoose, A. *Langmuir* **2010**, *26*, 5273.

(738) Wang, Z.; Luan, D.; Madhavi, S.; Ming Li, C.; Lou, X. W. *Chemical Communications* **2011**, *47*, 8061.

(739) Teja, A. S.; Koh, P. Y. *Progress in Crystal Growth and Characterization of Materials* **2009**, *55*, 22.

(740) Mahmoudi, M.; Simchi, A.; Imani, M. *JICS* **2010**, *7*, S1.

(741) Tadić, M.; Čitaković, N.; Panjan, M.; Stojanović, Z.; Marković, D.; Spasojević, V. *Journal of Alloys and Compounds* **2011**, *509*, 7639.

(742) Singh, J.; Srivastava, M.; Dutta, J.; Dutta, P. K. *International Journal of Biological Macromolecules* **2011**, *48*, 170.

(743) Wang, G.; Gou, X.; Horvat, J.; Park, J. *Journal of Physical Chemistry C* **2008**, *112*, 15220.

(744) Tahir, A. A.; Upul Wijayantha, K. G.; Saremi-Yarahmadi, S.; Maznar, M.; McKee, V. *Chemistry of Materials* **2009**, *21*, 3763.

(745) Wu, Z.; Yu, K.; Zhangand, S.; Xie, Y. *Journal of Physical Chemistry C* **2008**, *112*, 11307.

(746) Woo, K.; Lee, H. J.; Ahn, J. P.; Park, Y. S. *Advanced Materials* **2003**, *15*, 1761.

(747) Wang, L.; Xu, H. W.; Chen, P. C.; Zhang, D. W.; Ding, C. X.; Chen, C. H. *Journal of Power Sources* **2009**, *193*, 846.

(748) Liu, J.; Wang, R.; Yang, J.; Shi, Y. *Ecological Complexity* **2010**, *7*, 212.

(749) Chen, J.; Xu, L.; Li, W.; Gou, X. *Advanced Materials* **2005**, *17*, 582.

(750) Sun, Z.; Yuan, H.; Liu, Z.; Han, B.; Zhang, X. *Advanced Materials* **2005**, *17*, 2993.

(751) Jiao, F.; Harrison, A.; Jumas, J. C.; Chadwick, A. V.; Kockelmann, W.; Bruce, P. G. *Journal of the American Chemical Society* **2006**, *128*, 5468.

(752) Liu, L.; Kou, H. Z.; Mo, W.; Liu, H.; Wang, Y. *Journal of Physical Chemistry B* **2006**, *110*, 15218.

(753) Bang, J. H.; Suslick, K. S. *Journal of the American Chemical Society* **2007**, *129*, 2242.

(754) Jia, C. J.; Sun, L. D.; Yan, Z. G.; You, L. P.; Luo, F.; Han, X. D.; Pang, Y. C.; Zhang, Z.; Yan, C. H. *Angewandte Chemie* **2005**, *117*, 4402.

(755) Wu, C.; Yin, P.; Zhu, X.; OuYang, C.; Xie, Y. *Journal of Physical Chemistry B* **2006**, *110*, 17806.

(756) Zhang, D.; Li, G.; Yang, X.; Yu, J. C. *Chemical Communications* **2009**, 4381.

(757) Chen, J. S.; Tan, Y. L.; Li, C. M.; Cheah, Y. L.; Luan, D.; Madhavi, S.; Boey, F. Y. C.; Archer, L. A.; Lou, X. W. *Journal of the American Chemical Society* **2010**, *132*, 6124.

(758) Xiao, W.; Chen, J. S.; Lu, Q.; Lou, X. W. *Journal of Physical Chemistry C* **2010**, *114*, 12048.

(759) Sugimoto, T.; Muramatsu, A.; Sakata, K.; Shindo, D. *Journal of Colloid And Interface Science* **1993**, *158*, 420.

(760) Sugimoto, T.; Wang, Y. *Journal of Colloid And Interface Science* **1998**, *207*, 137.

(761) Wang, J.; White, W. B.; Adair, J. H. *Journal of the American Ceramic Society* **2005**, *88*, 3449.

(762) Zhang, J.; Liu, H.; Zhan, P.; Wang, Z.; Ming, N. *Advanced Functional Materials* **2007**, *17*, 1558.

(763) Lee, S. J.; Kim, B.; Lim, G.; Rhie, J. W.; Kang, H. W.; Cho, D. W. 2007, p 91.

(764) Veglió, F.; Passariello, B.; Barbaro, M.; Plescia, P.; Marabini, A. M. *International Journal of Mineral Processing* **1998**, *54*, 183.

(765) Vayssieres, L.; Sathe, C.; Butorin, S. M.; Shuh, D. K.; Nordgren, J.; Guo, J. *Advanced Materials* **2005**, *17*, 2320.

(766) Maier, J. *Nature Materials* **2005**, *4*, 805.

(767) Hu, Y. S.; Kienle, L.; Guo, Y. G.; Maier, J. *Advanced Materials* **2006**, *18*, 1421.

(768) Jamnik, J.; Maier, J. *Physical Chemistry Chemical Physics* **2003**, *5*, 5215.

(769) Liu, J. Q.; He, M. D.; Zhai, X.; Wang, L. L.; Wen, S.; Chen, L.; Shao, Z.; Wan, Q.; Zou, B. S.; Yao, J. *Optics Express* **2009**, *17*, 1859.

(770) Deng, Y.; Qi, D.; Deng, C.; Zhang, X.; Zhao, D. *Journal of the American Chemical Society* **2008**, *130*, 28.

(771) Li, B.; Cao, H.; Shao, J.; Qu, M.; Warner, J. H. *Journal of Materials Chemistry* **2011**, *21*, 5069.

(772) Fengqin, H.; Keith, W. M.; Emily, A. W.; Elise, A. S.-S.; Amanda, L. E.; Thomas, J. M. *Chemical Communications* **2010**, *46*.

(773) Lu, A.-H.; Salabas, E.; Schüth, F. *Angewandte Chemie (International ed. in English)* **2007**, *46*, 1222.

(774) Grass, R. N.; Athanassiou, E. K.; Stark, W. J. *Angewandte Chemie International Edition* **2007**, *46*, 4909.

(775) Laurent, S.; Forge, D.; Port, M.; Roch, A.; Robic, C.; Vander Elst, L.; Muller, R. *Chemical Reviews* **2008**, *108*, 2064.

(776) Cao, S.; Zhu, Y.; Ma, M.; Li…, L. *The Journal of Physical ...* **2008**.

(777) Saravanan, M.; Bhaskar, K.; Maharajan, G.; Pillai, K. *International journal of pharmaceutics* **2004**, *283*, 71.

(778) Lübbe, A.; Bergemann, C.; Huhnt, W.; Fricke, T.; Riess, H.; Brock, J.; Huhn, D. *Cancer research* **1996**, *56*, 4694.

(779) Richardson, J.; Hawkins, P.; Luxton, R. *Biosensors & bioelectronics* **2001**, *16*, 989.

(780) Huh, Y.-M.; Jun, Y.-w.; Song, H.-T.; Kim, S.; Choi, J.-s.; Lee, J.-H.; Yoon, S.; Kim, K.-s.; Shin, J.-S.; Suh, J.-S.; Cheon, J. *Journal of the American Chemical Society* **2005**, *127*, 12387.

(781) Bao, J.; Chen, W.; Liu, T.; Zhu, Y.; Jin, P.; Wang, L.; Liu, J.; Wei, Y.; Li, Y. *Acs Nano* **2007**, *1*, 293.

(782) Nam, J.-M.; Thaxton, C.; Mirkin, C. *Science (New York, N.Y.)* **2003**, *301*, 1884.

(783) Park, H.-Y.; Schadt, M.; Wang, L.; Lim, I. I. S.; Njoki, P.; Kim, S.; Jang, M.-Y.; Luo, J.; Zhong, C.-J. *Langmuir : the ACS journal of surfaces and colloids* **2007**, *23*, 9050.

(784) Yaping, H.; Qinglin, S.; Jianbin, Z.; Minzhi, W.; Bin, L. *Electrochimica Acta* **2011**, *56*.

(785) He, Y. P.; Wang, S. Q.; Li, C. R.; Miao, Y. M.; Wu, Z. Y.; Zou, B. S. *Journal of Physics D: Applied Physics* **2005**, *38*.

(786) Xie, J.; Xu, C.; Xu, Z.; Hou, Y.; Young, K.; Wang, S.; Pourmond, N.; Sun, S. *Chemistry of materials : a publication of the American Chemical Society* **2006**, *18*, 5401.

(787) Nae-Lih, W. *Materials Chemistry and Physics* **2002**, *75*.

(788) Jie, C.; Kelong, H.; Suqin, L. *Electrochimica Acta* **2009**, *55*.

(789) Yanping, Z.; Haibo, L.; Likun, P.; Ting, L.; Zhuo, S. *Journal of Electroanalytical Chemistry* **2009**, *634*.

(790) Yuanzhe, P.; Hyun Sik, K.; Yung-Eun, S.; Taeghwan, H. *Chemical Communications* **2010**, *46*.

(791) Theivanayagam, M.; Arumugam Vadivel, M.; Arumugam, M. *Chemical Communications* **2009**.

(792) Taberna, P.; Mitra, S.; Poizot, P.; Simon, P.; Tarascon, J. M. *Nature Materials* **2006**, *5*, 567.

(793) Wang, L.; Yu, Y.; Chen, P. C.; Zhang, D. W.; Chen, C. H. *Journal of Power Sources* **2008**, *183*.

(794) Hao, L.; Guoxiu, W.; Jiazhao, W.; David, W. *Electrochemistry Communications* **2008**, *10*.

(795) Olson, C.; Nelson, J.; Islam, M. *The journal of physical chemistry. B* **2006**, *110*, 9995.

(796) Yang, H.; Sun, C.; Qiao, S.; Zou, J.; Liu, G.; Smith, S.; Cheng, H.; Lu, G. *Nature* **2008**, *453*, 638.

(797) Sean, F.; Andrew, R.; Mei-Yin, L.; Julian, G.; Gordon, P. *Journal of Crystal Growth* **2000**, *209*.

(798) Roger, C. B.; Hong, Y. *The Journal of Physical Chemistry B* **2003**, *107*.

(799) Donald, M.; Nora, H. d. L. *Journal of Materials Chemistry* **2002**, *12*.

(800) Craig, A. J. F.; Islam, M. S. *Journal of Materials Chemistry* **2008**, *18*.

(801) Parker, S. C.; Leeuw, N. H. d.; Redfern, S. E. *Faraday Discussions* **1999**, *114*.

(802) Zhi-Min, C.; Ling-Yan, J.; Wei-Guo, S.; Yu-Guo, G. *Chemistry of Materials* **2009**, *21*.

(803) Lee, G.-H.; Park, J.-G.; Sung, Y.-M.; Chung, K.; Cho, W.; Kim, D.-W. *Nanotechnology* **2009**, *20*, 295205.

(804) Wei-Ming, Z.; Xing-Long, W.; Jin-Song, H.; Yu-Guo, G.; Li-Jun, W. *Advanced Functional Materials* **2008**, *18*.

(805) Docherty, R.; Clydesdale, G.; Roberts, K.; Bennema, P. *Journal of Physics D: Applied Physics* **1991**, *24*, 89.

(806) Fisher, C. A.; Islam, M. S. *Journal of Materials Chemistry* **2008**, *18*, 1209.

(807) Vayssieres, L.; Sathe, C.; Butorin, S. M.; Shuh, D. K.; Nordgren, J.; Guo, J. *Advanced Materials* **2005**, *17*, 2320.

(808) Sun, Y.; Salamon, M.; Garnier, K.; Averback, R. *Physical Review Letters* **2003**, *91*, 167206.

(809) Sasaki, M.; Jönsson, P.; Takayama, H.; Mamiya, H. *Physical Review B* **2005**, *71*.

(810) Mamiya, H.; Nakatani, I.; Furubayashi, T. *Physical Review Letters* **1999**, *82*.

(811) Mamiya, H.; Nakatani, I.; Furubayashi, T. *Physical Review Letters* **2002**, *88*, 67202.

(812) Masatsugu, S.; Sharbani, F.; Itsuko, S.; Lingyan, W.; Chuan-Jian, Z. *Physical Review B* **2009**, *79*.

(813) Yu, D.; Sun, X.; Zou, J.; Wang, Z.; Wang, F.; Tang, K. *The journal of physical chemistry. B* **2006**, *110*, 21667.

(814) Yang, T.; Shen, C.; Li, Z.; Zhang, H.; Xiao, C.; Chen, S.; Xu, Z.; Shi, D.; Li, J.; Gao, H. *The journal of physical chemistry. B* **2005**, *109*, 23233.

(815) Suqing, W.; Jingying, Z.; Chunhua, C. *Journal of Power Sources* **2010**, *195*.

(816) Laruelle, S.; Grugeon, S.; Poizot, P.; Dollé, M.; Dupont, L.; Tarascon, J. M. *Journal of the Electrochemical Society* **2002**, *149*.

(817) Hu, Y. S.; Kienle, L.; Guo, Y. G.; Maier, J. *Advanced Materials* **2006**, *18*.

(818) Janez, J.; Joachim, M. *Physical Chemistry Chemical Physics* **2003**, *5*.

(819) Chan, C.; Peng, H.; Liu, G.; McIlwrath, K.; Zhang, X.; Huggins, R.; Cui, Y. *Nature nanotechnology* **2008**, *3*, 31.

(820) Jinping, L.; Yuanyuan, L.; Xintang, H.; Ruimin, D.; Yingying, H.; Jian, J.; Lei, L. *Journal of Materials Chemistry* **2009**, *19*.

(821) Lakshmi, B.; Patrissi, C.; Martin, C. *Chemistry of Materials* **1997**.

(822) Muraliganth, T.; Murugan, A. V.; Manthiram, A. *Chemical Communications* **2009**, 7360.

(823) Taberna, L.; Mitra, S.; Poizot, P.; Simon, P.; Tarascon, J. M. *Nature Materials* **2006**, *5*, 567.

(824) Yoon, S. J.; Sangkyoo, L.; Dongjoon, A.; Anne, C. D.; Se-Hee, L. *Journal of Power Sources* **2009**, *188*.

(825) Grugeon, S.; Laruelle, S.; Herrera-Urbina, R.; Dupont, L.; Poizot, P.; Tarascon, J.-M. *Journal of the Electrochemical Society* **2001**, *148*, A285.

(826) Larcher, D.; Masquelier, C.; Bonnin, D.; Chabre, Y.; Masson, V.; Leriche, J.-B.; Tarascon, J.-M. *Journal of the Electrochemical Society* **2003**, *150*, A133.

(827) Larcher, D.; Bonnin, D.; Cortes, R.; Rivals, I.; Personnaz, L.; Tarascon, J. M. *Journal of the Electrochemical Society* **2003**, *150*, A1643.

(828) Larcher, D.; Sudant, G.; Leriche, J. B.; Chabre, Y.; Tarascon, J. M. *Journal of the Electrochemical Society* **2002**, *149*, A234.

(829) Wu, X. L.; Guo, Y. G.; Wan, L. J.; Hu, C. W. *Journal of Physical Chemistry C* **2008**, *112*, 16824.

(830) Duan, X.; Huang, Y.; Cui, Y.; Wang, J.; Lieber, C. M. *Nature* **2001**, *409*, 66.

(831) Huang, Y.; Duan, X.; Cui, Y.; Lieber, C. M. *Nano Letters* **2002**, *2*, 101.

(832) Law, M.; Greene, L. E.; Johnson, J. C.; Saykally, R.; Yang, P. *Nature Materials* **2005**, *4*, 455.

(833) Nordlinder, S.; Nyholm, L.; Gustafsson, T.; Edström, K. *Chemistry of Materials* **2006**, *18*, 495.

(834) Jiao, F.; Shaju, K. M.; Bruce, P. G. *Angewandte Chemie - International Edition* **2005**, *44*, 6550.

(835) Zhou, Y.; Li, H. *Journal of Materials Chemistry* **2002**, *12*, 681.

(836) Nam, K. T.; Kim, D. W.; Yoo, P. J.; Chiang, C. Y.; Meethong, N.; Hammond, P. T.; Chiang, Y. M.; Belcher, A. M. *Science* **2006**, *312*, 885.

(837) Du, N.; Zhang, H.; Chen, B.; Wu, J.; Ma, X.; Liu, Z.; Zhang, Y.; Yang, D.; Huang, X.; Tu, J. *Advanced Materials* **2007**, *19*, 4505.

(838) Park, M.; Suh, K.; Kim, K.; Hur, S. H.; Lee, W. S. *IEEE Electron Device Letters* **2007**, *28*, 750.

(839) Wang, Y.; Cao, G. *Advanced Materials* **2008**, *20*, 2251.

(840) Manthiram, A.; Murugan, A. V.; Sarkar, A.; Muraliganth, T. *Energy & Environmental Science* **2008**, *1*, 621.

(841) Kim, D. H.; Kim, J. *Electrochemical and Solid-State Letters* **2006**, *9*, A439.

(842) Huang, Y. D.; Dong, Z. F.; Jia, D. Z.; Guo, Z. P.; Cho, W. I. *Electrochimica Acta* **2011**, *56*, 9233.

(843) Zhu, Y.; Bai, Y. J.; Han, F. D.; Qi, Y. X.; Lun, N.; Yao, B.; Zhang, J. X. *Materials Letters* **2011**, *65*, 3157.

(844) Tsuda, N.; Nasu, K.; Yanase, A.; Siratori, K. **1991**.

(845) He, Y.; Huang, L.; Cai, J.; Zheng, X.; Sun, S. *Electrochimica Acta* **2010**.

(846) Dedryvere, R.; Laruelle, S.; Grugeon, S.; Poizot, P.; Gonbeau, D.; Tarascon, J. M. *Chemistry of Materials* **2004**, *16*, 1056.

(847) Li, X. F.; Dhanabalan, A.; Wang, C. L. *Journal of Power Sources* **2011**, *196*, 9625.

(848) Grugeon, S.; Laruelle, S.; Dupont, L.; Tarascon, J. M. *Solid State Sciences* **2003**, *5*, 895.

(849) Balaya, P.; Li, H.; Kienle, L.; Maier, J. *Advanced Functional Materials* **2003**, *13*.

(850) Tarascon, J.; Armand, M. *Nature* **2001**, *414*, 359.

(851) Peter , G. B.; Bruno, S.; Jean-Marie, T. *Angewandte Chemie* **2008**, *120*.

(852) Bruce, P.; Scrosati, B.; Tarascon, J.-M. *Angewandte Chemie (International ed. in English)* **2008**, *47*, 2930.

(853) Janos, H. F.; Fiona, C. M. *Advanced Materials* **1995**, *7*.

(854) Zhou, W.; Yao, M.; Guo, L.; Li, Y.; Li, J.; Yang, S. *Journal of the American Chemical Society* **2009**, *131*, 2959.

(855) Lee, Y.; Yi, H.; Kim, W.-J.; Kang, K.; Yun, D.; Strano, M.; Ceder, G.; Belcher, A. *Science (New York, N.Y.)* **2009**, *324*, 1051.

(856) Min-Sik, P.; Guo-Xiu, W.; Yong-Mook, K.; David, W.; Shi-Xue, D.; Hua-Kun, L. *Angewandte Chemie* **2007**, *119*.

(857) Mai, L. Q.; Hu, B.; Chen, W.; Qi, Y. Y.; Lao, C. S.; Yang, R. S.; Dai, Y.; Wang, Z. L. *Advanced Materials* **2007**, *19*.

(858) Lou, X. W.; Deng, D.; Lee, J. Y.; Feng, J.; Archer, L. A. *Advanced Materials* **2008**, *20*.

(859) Lei, Z.; Yang, X.; Dong, J.; Yi, X. *Chemistry of Materials* **2009**, *21*.

(860) Dengyu, P.; Song, W.; Bing, Z.; Minghong, W.; Haijiao, Z.; Yong, W.; Zheng, J. *Chemistry of Materials* **2009**, *21*.

(861) Guoxiu, W.; Xiaoping, S.; Jane, Y.; Jinsoo, P. *Carbon* **2009**, *47*.

(862) Kim, H.; Cho, J. *Nano Letters* **2008**, *8*, 3688.

(863) Ji, X.; Lee, K.; Nazar, L. *Nature Materials* **2009**, *8*, 500.

(864) Xiong Wen, L.; Da, D.; Jim Yang, L.; Lynden, A. A. *Journal of Materials Chemistry* **2008**, *18*.

(865) Nahong, Z.; Gaojun, W.; Yan, H.; Bin, W.; Baodian, Y.; Yuping, W. *Chemistry of Materials* **2008**, *20*.

(866) Li, D.; Zhou, H.; Honma, I. *Nature Materials* **2004**, *3*, 65.

(867) Shaju, K. M.; Bruce, P. G. *Advanced Materials* **2006**, *18*.

(868) Jiao, F.; Bruce, P. G. *Advanced Materials* **2007**, *19*.

(869) Wang, K.; Wei, M.; Morris, M. A.; Zhou, H.; Holmes, J. D. *Advanced Materials* **2007**, *19*.

(870) Feng, J.; Kuthanapillil Mani, S.; Peter, G. B. *Angewandte Chemie* **2005**, *117*.

(871) Feng, J.; Kuthanapillil Mani, S.; Peter, G. B. *Angewandte Chemie International Edition* **2005**, *44*.

(872) Jia-yan, L.; Yong-gang, W.; Huan-ming, X.; Yong-yao, X. *Chemistry of Materials* **2007**, *19*.

(873) Li, X.; Cheng, F.; Guo, B.; Chen, J. *The journal of physical chemistry. B* **2005**, *109*, 14017.

(874) Guoxiu, W.; Hao, L.; Jian, L.; Shizhang, Q.; Gaoqing Max, L.; Paul, M.; Hyojun, A. *Advanced Materials* **2010**, *22*.

(875) Yu, R.; Laurence , J. H.; Peter , G. B. *Angewandte Chemie* **2010**, *122*.

(876) Yu, R.; Laurence , J. H.; Peter , G. B. *Angewandte Chemie International Edition* **2010**, *49*.

(877) Guoxiu, W.; Hao, L.; Josip, H.; Bei, W.; Shizhang, Q.; Jinsoo, P.; Hyojun, A. *Chemistry - A European Journal* **2010**, *16*.

(878) Hyesun, K.; Jaephil, C. *Journal of Materials Chemistry* **2008**, *18*.

(879) Liu, H.; Wang, G.; Liu, J.; Qiao, S.; Ahn, H. *Journal of Materials Chemistry* **2011**, *21*, 3046.

(880) Wenbo, Y.; Xiaoxiang, X.; John, T. S. I.; Pierrot, S. A.; Chong, L.; Heyong, H.; Dongyuan, Z.; Wuzong, Z. *Chemistry of Materials* **2009**, *21*.

(881) Kavan, L.; Rathouský, J.; Grätzel, M.; Shklover, V.; Zukal, A. *Microporous and Mesoporous Materials* **2001**, *44-45*.

(882) Li, T.; Hongli, Z.; Junxiang, F.; Xianfeng, Y.; Yi, W.; Hongliang, G.; Xionghui, F.; Chaolun, L.; Mingmei, W.; Pei Kang, S.; Qiuming, G. *Advanced Functional Materials* **2010**, *20*.

(883) Guoxiu, W.; Xiaoping, S.; Josip, H.; Bei, W.; Hao, L.; David, W.; Jane, Y. *The Journal of Physical Chemistry C* **2009**, *113*.

(884) Pang, H.; Lu, Q.; Zhang, Y.; Li, Y.; Gao, F. *Nanoscale* **2010**, *2*, 920.

(885) Chen, J. S.; Tan, Y. L.; Li, C. M.; Cheah, Y. L.; Luan, D. Y.; Madhavi, S.; Boey, F. Y. C.; Archer, L. A.; Lou, X. W. *Journal of the American Chemical Society* **2010**, *132*, 6124.

(886) Xie, X.; Li, Y.; Liu, Z.-Q.; Haruta, M.; Shen, W. *Nature* **2009**, *458*, 746.

(887) Hu, L.; Peng, Q.; Li, Y. *Journal of the American Chemical Society* **2008**, *130*, 16136.

(888) Wang, X.; Li, X.; Sun, X.; Li, F.; Liu, Q.; Wang, Q.; He, D. *Journal of Materials Chemistry* **2011**, *21*, 3571.

(889) Wang, Y.; Zhang, H. J.; Wei, J.; Wong, C. C.; Lin, J.; Borgna, A. *Energy & Environmental Science* **2011**, *4*, 1845.

(890) Tasker, P. W. *J Phys C Solid State* **1979**, *12*, 4977.

(891) Zhang, J. H.; Liu, H. Y.; Zhan, P.; Wang, Z. L.; Ming, N. B. *Advanced Functional Materials* **2007**, *17*, 1558.

(892) Rumplecker, A.; Kleitz, F.; Salabas, E. L.; Schuth, F. *Chemistry of Materials* **2007**, *19*, 485.

(893) Shaju, K. M.; Jiao, F.; Debart, A.; Bruce, P. G. *Physical Chemistry Chemical Physics* **2007**, *9*, 1837.

(894) Balaya, P.; Li, H.; Kienle, L.; Maier, J. *Advanced Functional Materials* **2003**, *13*, 621.

(895) Wang, G. X.; Shen, X. P.; Yao, J.; Park, J. *Carbon* **2009**, *47*, 2049.

(896) Fang, B.; Kim, M. S.; Kim, J. H.; Lim, S.; Yu, J. S. *Journal of Materials Chemistry* **2010**, *20*, 10253.

(897) Ni, S. B.; Li, T.; Yang, X. L. *Materials Chemistry and Physics* **2012**, *132*, 1108.

(898) Mai, Y. J.; Shi, S. J.; Zhang, D.; Lu, Y.; Gu, C. D.; Tu, J. P. *Journal of Power Sources* **2012**, *204*, 155.

(899) Huang, Y.; Huang, X. L.; Lian, J. S.; Xu, D.; Wang, L. M.; Zhang, X. B. *Journal of Materials Chemistry* **2012**, *22*, 2844.

(900) Lebedeva, N. P.; Koper, M. T. M.; Feliu, J. M.; van Santen, R. A. *Journal of Physical Chemistry B* **2002**, *106*, 12938.

(901) Zhang, D. Q.; Wen, M. C.; Zhang, P.; Zhu, J.; Li, G. S.; Li, H. X. *Langmuir* **2012**, *28*, 4543.

(902) Chen, J. S.; Liu, H.; Qiao, S. Z.; Lou, X. W. *Journal of Materials Chemistry* **2011**, *21*, 5687.

(903) Dupont, L.; Laruelle, S.; Grugeon, S.; Dickinson, C.; Zhou, W.; Tarascon, J. M. *Journal of Power Sources* **2008**, *175*, 502.

(904) Xiong, H.; Slater, M. D.; Balasubramanian, M.; Johnson, C. S.; Rajh, T. *J. Phys. Chem. Lett* **2011**, *2*, 2560.

(905) Kim, D.; Lee, E.; Slater, M.; Lu, W.; Rood, S.; Johnson, C. S. *Electrochemistry Communications* **2012**, *18*, 66.

(906) Komaba, S.; Takei, C.; Nakayama, T.; Ogata, A.; Yabuuchi, N. *Electrochemistry Communications* **2010**, *12*, 355.

(907) Xia, X.; Dahn, J. *Electrochemical and Solid-State Letters* **2011**, *15*, A1.

(908) Tepavcevic, S.; Xiong, H.; Stamenkovic, V. R.; Zuo, X.; Balasubramanian, M.; Prakapenka, V. B.; Johnson, C. S.; Rajh, T. **2011**.

(909) Zaghib, K.; Trottier, J.; Hovington, P.; Brochu, F.; Guerfi, A.; Mauger, A.; Julien, C. *Journal of Power Sources* **2011**, *196*, 9612.

(910) Gocheva, I. D.; Nishijima, M.; Doi, T.; Okada, S.; Yamaki, J.-i.; Nishida, T. *Journal of Power Sources* **2009**, *187*, 247.

(911) Yamada, Y.; Doi, T.; Tanaka, I.; Okada, S.; Yamaki, J.-i. *Journal of Power Sources* **2011**, *196*, 4837.

(912) Caballero, A.; Hernán, L.; Morales, J.; Sánchez, L.; Peña, J. S.; Aranda, M. *Journal of Materials Chemistry* **2002**, *12*, 1142.

(913) Sauvage, F.; Laffont, L.; Tarascon, J. M.; Baudrin, E. *Inorganic Chemistry* **2007**, *46*, 3289.

(914) Doeff, M. M.; Richardson, T. J.; Kepley, L. *Journal of the Electrochemical Society* **1996**, *143*, 2507.

(915) Hosono, E.; Matsuda, H.; Honma, I.; Fujihara, S.; Ichihara, M.; Zhou, H. *Journal of Power Sources* **2008**, *182*, 349.

(916) Caballero, A.; Hernan, L.; Morales, J.; Sanchez, L.; Pena, J. S.; Aranda, M. A. G. *Journal of Materials Chemistry* **2002**, *12*, 1142.

(917) Stoyanova, R.; Carlier, D.; Sendova-Vassileva, M.; Yoncheva, M.; Zhecheva, E.; Nihtianova, D.; Delmas, C. *Journal of Solid State Chemistry* **2010**, *183*, 1372.

(918) Doeff, M. M.; Peng, M. Y.; Ma, Y.; De Jonghe, L. *Journal of the Electrochemical Society* **1994**, *141*, L145.

(919) Shen, X. F.; Ding, Y. S.; Liu, J.; Cai, J.; Laubernds, K.; Zerger, R. P.; Vasiliev, A.; Aindow, M.; Suib, S. L. *Advanced Materials* **2005**, *17*, 805.

(920) Chen, W.-M.; Qie, L.; Shao, Q.-G.; Yuan, L.-X.; Zhang, W.-X.; Huang, Y.-H. *Acs Applied Materials & Interfaces* **2012**, *4*, 3047.

(921) Ghodbane, O.; Pascal, J. L.; Favier, F. *Acs Applied Materials & Interfaces* **2009**, *1*, 1130.

(922) Xiao, W.; Wang, D. L.; Lou, X. W. *Journal of Physical Chemistry C* **2010**, *114*, 1694.

(923) Ponrouch, A.; Marchante, E.; Courty, M.; Tarascon, J.-M.; Rosa Palacin, M. *Energy & Environmental Science* **2012**, *5*, 8572.

(924) Goodenough, J. B. *Journal of Solid State Electrochemistry* **2012**, *16*, 2019.

(925) Ellis, B. L.; Nazar, L. F. *Curr Opin Solid St M* **2012**, *16*, 168.

(926) Barpanda, P.; Nishimura, S.-i.; Yamada, A. *Advanced Energy Materials* **2012**, *2*, 841.

(927) Lu, Y.; Wang, L.; Cheng, J.; Goodenough, J. B. *Chemical Communications* **2012**, *48*, 6544.

(928) Xia, X.; Obrovac, M. N.; Dahn, J. R. *Electrochemical and Solid State Letters* **2011**, *14*, A130.

(929) Senguttuvan, P.; Rousse, G.; Seznec, V.; Tarascon, J.-M.; Rosa Palacin, M. *Chemistry of Materials* **2011**, *23*, 4109.

(930) Xiong, H.; Slater, M. D.; Balasubramanian, M.; Johnson, C. S.; Rajh, T. *J Phys Chem Lett* **2011**, *2*, 2560.

(931) Xu, Y.; Zhu, Y.; Liu, Y.; Wang, C. *Advanced Energy Materials* **2012**, 128.

(932) Hummers, W. S.; Offeman, R. E. *Journal of the American Chemical Society* **1958**, *80*, 1339.

(933) Wang, J. W.; Liu, X. H.; Mao, S. X.; Huang, J. Y. *Nano Letters* **2012**, *12*, 5897.

(934) Ellis, L. D.; Hatchard, T. D.; Obrovac, M. N. *Journal of the Electrochemical Society* **2012**, *159*, A1801.

(935) Datta, M. K.; Epur, R.; Saha, P.; Kadakia, K.; Park, S. K.; Kumta, P. N. *Journal of Power Sources* **2013**, *225*, 316.

(936) Xu, Y.; Zhu, Y.; Liu, Y.; Wang, C. *Advanced Energy Materials* **2013**, *3*, 128.

APPENDIX: LIST OF ABBREVIATIONS

Abbreviation	Full name
EVs	electric vehicles
HEVs	hybrid electrical vehicles
ICEs	internal combustion engines
E_g	the energy separation
LUMO	The lowest unoccupied molecular orbital
HOMO	The highest occupied molecular orbital
μ_A	Cathode electrochemical potentials
μ_C	Anode electrochemical potentials
ε_F	Fermi energies
V_{oc}	open circuit voltage
Λ	The capacity of reversible charge transfer per unit weight between the anode and cathode
ΛV_{oc}	The energy density,
σ_{Li}	Li^+ ion conductivity
σ_e	electronic conductivity
PC	propylene carbonate
EC	ethylene carbonate
DEC	diethyl carbonate
DMC	dimethyl carbonate
EMC	ethylmethyl carbonate
SEI	Solid electrolyte-interface
RTILs	Room-temperature ionic liquids

PEOs	polyethylene oxides
MEEGE	(2-methoxyethoxy) ethyl glycidyl ether composition
OCV	Open circuit voltage
XPS	X-ray photoelectron spectroscopy
XAS	X-ray absorption spectroscopy
EELS	electron energy loss spectroscopy
ED	electron diffraction
ESD	electrostatic spray deposition
PPy	polypyrrole
VLS	vapour-liquid-solid
SFLS	scalable supercritical fluid-liquid-solid
NWs	Nanowires
AES	Auger electron spectroscopy
LiTFSI	lithium bis(trifluoromethylsulfonyl)imide
EDS	Energy dispersive spectroscopy
UV-Vis	ultraviolet-visible
TGA–DTA	thermogravimetric and differential thermal analysis
Å	angstroms
FWHM	Full width at half maximum
FEG	Field emission guns
BF	Bright field image
FT-IR	Fourier Transform Infrared Spectroscopy
ZFC	Zero-field-cooled
FCC	Field-cooled upon cooling the sample
FCW	Field-cooled upon warming the sample

a.u.	Arbitrary unit
BET	Brunauer Emmett Teller
BJH	Barrett-Joyner-Halenda
CV	Cyclic voltammetry
hcp	hexagonal close-packed
ccp	cubic close packed
fcc	face-centred cubic
i	Current
E	Potential
SCE	Calomel reference electrode
C	Specific capacitance
E_m	Migration energy barrier
E_g	Band gap
CB	Carbon black
EES	Electrical energy storage
cm	Centimeter
1D	One-dimension
2D	Two-dimension
3D	Three-dimension
CMC	Dimethyl carbonate
C-rate	Current rate
EC	Ethylene carbonate
EIS	Electrochemical impedance spectroscopy
AC	Alternating current
DC	Direct current

MP2	Møller-Plesset perturbation theory
DFT	Density functional theory
GGA	Generalized gradient approximations
LDA	Local-density approximation
PBE	Perdew, Burke and Ernzerhof
USPP	Ultra-soft pseudopotential
NEB	Nudged Elastic Band method
PDOS	Partial density of states
DOS	Density of states
VCA	Virtual crystal approximation
$\overline{V}$	average intercalation voltage
U	Energy density
E_s	Specific energy
Eq.	Equation
CTAB	Cetyltrimethylammonium bromide
FESEM	Field emission scanning electron microscopy
MEM	Maximum entropy method
FFT	Fast-Fourier-Transform
PVP	Poly vinyl pyrrolidone
EG	Ethylene glycol
GO	Graphite oxide
GE	Graphene
FTIR	Fourier transform inferior red spectroscopy
EVs	Electric vehicles
HEVs	Hybrid electric vehicles

HF	Hydrofluoric acid
JCPDS	Joint committee on powder diffraction standards
Li	Lithium
nm	Nanometer
NMP	1-methyl-2-pyrrolidinone
OCP	Open circuit potential
PC	Propylene carbonate
PVDF	Polyvinylidene fluoride
SAED	Selected area electron diffraction
SEI	Solid electrolyte interphase
SEM	Scanning electron microscopy
TEM	Transmission electron microscopy
HRTEM	High resolution transmission electron microscopy
TGA	Thermogravimetric analysis
XRD	X-ray diffraction